

BIOLOGICAL PERFORMANCE OF NOVEL PHOSPHATE-BASED GLASS MICROSPHERES FOR MESENCHYMAL STEM CELL THERAPY IN OSTEOPOROTIC PATIENTS

DHANAK GUPTA, B. Tech, MSc.

Thesis submitted to the University of Nottingham for the degree of Doctor of Philosophy

November 2016

अज्ञान तिमिरान्धस्य ज्ञानाञ्जन शलाकया।

चक्षुरुन्मीलितं येन तस्मै श्री गुरवे नमः॥

(I salute that Guru, who through knowledge

opens the eye of those blinded by the gloom of ignorance)

Dedicated to:

The Divine,

Papa, Mama, Nani, Nanu,

Raghav, Nirwan

and other family members

Abstract

In this study, degradable phosphate-based bulk or porous glass microspheres (BGMS or PGMS), with nominal molar compositions of P45-($45P_2O_5$-16CaO-24MgO-$11Na_2O$-$4Fe_2O_3$) and P40-($40P_2O_5$-16CaO-24MgO-$20Na_2O$), were evaluated for cytotoxicity, cytocompatibility and osteogenic potential for Mesenchymal stem cell (MSC)-based therapy in osteoporotic patients.

Evaluations were performed using direct-contact and indirect-contact bone marrow derived human MSC (hMSC)-based experiments, in addition to material characterisations such as morphology, elemental composition and degradation behaviour, which were correlated to the hMSC experiments.

Degradation of microspheres (MS) was measured using a novel method where Scanning Electron micrographs was used to assess the number of MS with surface damage (cracks and peeling effect), over 42 days of degradation in culture medium. Results showed that after 42 days, 2%, 46% and 29% of P45 BGMS, P40 BGMS and P40 PGMS, respectively, had cracks or peeling off surfaces. The results for direct-contact hMSC-experiments showed that P45 BGMS supported 1.4 times more hMSCs than P40 BGMS over 31 days of culture period. However, P45 BGMS were not osteoinductive, possibly due to hydrophobic nature of this glass and its slower dissolution rate. On the other hand, in comparison to P45 BGMS, hMSCs seeded on P40 BGMS showed up to 1.7 times higher alkaline phosphatase (ALP) activity on Day 7, up to 1.5 times more collagen and at least 6 times more Ca deposited in extracellular matrix, in addition to osteocalcin on Day 21 of culture, which strongly indicated the osteoinductive nature of P40 BGMS. This effect was also confirmed through indirect-contact experiments where there was higher collagen and Ca production by hMSCs was observed after 25 days of culture in P40 BGMS-conditioned medium as compared to control (no MS) or P45-conditioned medium.

Elemental analysis using Energy Dispersive X-Ray Spectroscopic (EDS) analysis revealed that the Ca-based porogen used in the manufacturing of PGMS, may have been retained on the edges of the pores in PGMS. Therefore, an acid-washing step was introduced at the end of manufacturing process in order to remove the porogen and limit the possible cytotoxic effect of porogen and excess calcium. Characterisation results indicated that acid washing changed the physicality of these microspheres without changing their chemical composition. For example, mean and mode pore window sizes on the surface of PGMS increased from 2.63 μm to 2.73 μm and from 1.15 μm to 1.53 μm, respectively, and closed porosity decreased by 27%, as a result of acid washing. However, more detailed EDS analysis revealed that the Ca-based porogen was not being completely removed from PGMS even after acid washing and this may need further investigation. Cytotoxicity evaluations over 7 days of elution (indirect-contact hMSC experiments) suggested that there was marked improvement in hMSC membrane integrity and metabolic activity in PGMS neat extracts after acid washing. Moreover, direct-contact hMSC experiments also showed higher DNA content on acid washed (AW) P40 PGMS over 7 days of culture. Therefore, based on these results, it was hypothesised that acid washing may have opened up some of the pores and removed some of the glass fragments from PGMS surface, which may have been responsible for cytotoxicity in non-AW PGMS.

Direct-contact experiments also showed that over 42-day culture period, there was up to 1.6 times higher hMSC numbers in AW P40 PGMS as compared to P40 BGMS. However, this increase was much lower than the expected range as there was more than 10-fold increase in surface area after the introduction of porosity. This was probably due to presence of <5 μm and <10 μm pore window sizes and interconnection sizes, respectively, in these microspheres, which allowed limited penetration of hMSCs into the porous structures. There was also evidence of at least 2 times more ALP activity up to day 42 of culture and up to 1.7 times more collagen

production by day 21 of culture, in case of AW P40 PGMS as compared to P40 BGMS, which strongly indicated a positive effect of porosity on osteogenesis. Interestingly, there was also lower Ca and P deposited by hMSCs in porous microspheres, which was in line with the observations made through indirect-contact experiments, where there was lower collagen and Ca production by hMSCs in P40 PGMS-conditioned medium as compared to P40 BGMS-conditioned medium. This negative effect of PGMS was hypothesised due to excess release of glass fragments/particulates and calcium ions into the medium, possibly leading to cytotoxicity.

Based on the results shown here, there is a potential of P40 BGMS and AW P40 PGMS for hMSC-based bone repair therapy. However, future work needs to be done in order to limit the delamination of glass surfaces and release of glass fragments/particulates from these MS, as a result of degradation.

Conference Presentations

D Gupta, KMZ Hossain, I Ahmed, DM Grant and V Sottile "*Biological Evaluation of Degradable Phosphate-Based Glass Microspheres for Stem Cell Therapy*", European Chapter Meeting of the Tissue Engineering and Regenerative Medicine International Society (TERMIS-EU) 2016, 28 Jun – 30 Jun 2016, Uppsala, Sweden. (***Poster***)

D Gupta, KMZ Hossain, I Ahmed, DM Grant and V Sottile "*Behaviour and Osteogenic Differentiation of Human Mesenchymal Stem Cells on 2D and 3D Culture Environments*", UK Society of Biomaterials (UKSB), 01 Jul 2016, London, UK. (***Rapid fire Oral***)

Acknowledgements

The pages of this thesis will fall short if I were to explain in detail the contributions from various researchers at University of Nottingham in this study. However, I will try to soulfully explain my gratitude towards some of the most contributing people.

From the bottom of my heart, I thank my supervisors Professor David M. Grant and Dr. Virginie Sottile, for giving me the opportunity to work under their esteemed supervision. My PhD work remains as much theirs as it is mine. I will always remember their kindness and unconditional support throughout the years of my research work.

I am also indebted to Dr. Ifty Ahmed and Dr. Kazi Md. Zakir Hossain for kindly providing glass microspheres used for this work and also for their expert advice on glass materials. I am hopeful that this PhD work will be highly beneficial for their ongoing research work on novel phosphate-based microspheres.

I am highly grateful to 'Vice Chancellors Scholarship for Excellence in Research' provided by the University of Nottingham for funding my PhD research work. I am also thankful Dr. Colin Scotchford for motivating me during the difficult times and also for providing technical advice on cytocompatibility studies. His contribution has been invaluable for this research work.

I am thankful to current and former members of Adult Stem Cell Research group at Centre for Bimolecular Sciences (CBS) and Advanced Materials Research group at Wolfson Building, for helping maintain a healthy and friendly work environment in labs. I especially wish to thank Stephanie, Alex, Amy, Richard, Shelanah, Azaz, Amal, Katherine, Sarah, Zubair, Uresha, Brian and Yang for making those never ending hours in labs entertaining and full of fun.

I thank Glen Kirkham, Penny Howick, Maria Barbadillo-munoz, Teresa Marshall, Paula Olson and Jayson Bispham at CBS; and Keith Dinsdale, Martin Roe, Julie Thompson, Nikki Weston, Nigel Neate, Dhruma Thakkar and Tom Buss at Wolfson Building for their guidance and technical assistance in the experimental part of this project. I would like to specially mention the following researchers for their invaluable motivation, support and advice- Dr. Martin Roe and Dr. Emily Smith (XPS), Dr. Christopher Parmenter (Cryo FIB/SEM), Dr. Martin Corfield (Micro CT), Dr. Lee Stevens (BET), Mark Hardy (Laser diffraction), Dr. Alan Parish (image analysis), Dr. Glen Kirkham (mouse calvarial tissue and immunostaining) and the lovely Denise Mclean (cryo-sectioning and histology). I am also deeply thankful to Caroline Reffin for her concern and timely help with a number of administrative matters during my PhD.

I am obliged to my parents and my grandparents (Nani and Nanu) for eternity who have dedicated their lives for me and my brother's careers; and also to my brother (Raghav), who is the Niles to the Frasier in me (for those who watched the famous American television series *Frasier*). Finally, I will never forget the sacrifices my husband (Nirwan) had to make for me to complete my PhD work with full dedication.

Table Of Contents

ABSTRACT ..... **III**

CONFERENCE PRESENTATIONS ..... **VI**

ACKNOWLEDGEMENTS ..... **VII**

LIST OF TABLES ..... **XIV**

LIST OF FIGURES ..... **XV**

ABBREVIATIONS ..... **XXIV**

CHAPTER 1 INTRODUCTION AND REVIEW OF LITERATURE **1**

1.1 ORGANISATION OF LITERATURE REVIEW 1

1.2 OSTEOPOROSIS – THE 'SILENT EPIDEMIC' 2

1.2.1 Current treatments for bone fracture *3*

1.3 BONE ARCHITECTURE 5

1.4 BONE REMODELLING 8

1.4.1 Osteoclastogenesis-bone resorption-concavity formation *11*

1.4.2 Osteoblastogenesis-mineralisation in lacunae-bone formation *12*

1.4.3 Bone matrix deposition *13*

1.5 MESENCHYMAL STEM CELLS (MSCS) 13

1.5.1 Plasticity, Sources and Frequency of MSCs *14*

1.5.2 MSCs enhance bone formation in vivo *16*

1.5.3 Clinical studies with MSCs *18*

1.6 BIOACTIVE MATERIALS 19

1.6.1 Phosphate-based glasses *23*

1.7 OSTEOINDUCTIVITY OF BIOACTIVE GLASSES 27

1.8 POROSITY AS A STRATEGY FOR BONE TISSUE ENGINEERING 30

1.8.1 Bone formation in porous structures *31*

1.8.2 Optimal pore size for bone formation *35*

1.8.3 Interconnectivity of pores *40*

1.8.4 Porosity at the nanoscale *41*

1.9 CONCAVE/CONVEX RADII OF CURVATURE AND CELL MORPHOLOGY AS CRITICAL DETERMINANT OF MSC-FATE 44

1.10 TWO-DIMENSIONAL AND THREE-DIMENSIONAL CULTURE SYSTEMS 47

1.11 MICROSPHERES AS A 3D SUBSTRATE FOR CELLS 50
1.11.1 Microspheres for bone tissue engineering 52
1.12 AIMS AND OBJECTIVES OF THE WORK 58
CHAPTER 2 MATERIALS AND METHODS 59
2.1 INTRODUCTION 59
2.2 MATERIAL CHARACTERISATION 61
2.2.1 Major axis length and Sphericity measurements 61
2.2.2 Laser diffraction 61
2.2.3 Sieving of particles 62
2.2.4 Surface area analysis 62
2.2.5 Micro Computational Tomography (μ CT) 63
2.2.6 Cryo-Focused Ion Beam/Scanning Electron Microscopy (Cryo-FIB/SEM) 63
2.2.7 Pore window measurements 64
2.2.8 Relative Density 64
2.2.9 Tapped density 65
2.2.10 Electron Dispersive Spectroscopy (EDS) 65
2.2.11 Fourier Transform Infrared (FTIR) Spectroscopy 65
2.2.12 Degradation studies 66
2.3 CYTOCOMPATIBILITY STUDIES 67
2.3.1 Human Mesenchymal Stem Cell (hMSC) culturing 67
2.3.2 Cell seeding on microspheres 70
2.3.3 Design of direct-contact experiments 71
2.3.4 Design of indirect-contact experiments 77
2.3.5 Cell metabolic activity assay 80
2.3.6 DNA assay 81
2.3.7 Cell counts 81
2.3.8 Assessment of microsphere agglomeration 82
2.3.9 FDA/PI staining 82
2.3.10 Neutral Red uptake (NRU) assay 83
2.3.11 Alkaline Phosphatase (ALP) activity 84
2.3.12 Sectioning of 3D agglomerates 84
2.3.13 Sirius Red staining 84
2.3.14 Alizarin Red staining 85
2.3.15 Osteocalcin (OCN) immunostaining 86
2.3.16 Haematoxylin and Eosin (H&E) staining 87

2.3.17 X-Ray Photon Spectroscopy (XPS) of 3D samples 87
2.3.18 Sample preparation for SEM 88
2.3.19 Sample preparation for Environmental SEM (ESEM) 88
2.3.20 Micro CT for visualising cells on PGMS 88
2.4 STATISTICAL ANALYSES 89

CHAPTER 3 MATERIAL CHARACTERISATION 91
3.1 INTRODUCTION 91
3.2 PARTICLE GEOMETRY ANALYSES 91
3.2.1 Angular-shaped particles 91
3.2.2 Borosilicate glass microspheres 93
3.2.3 Phosphate based glass bulk microspheres 95
3.2.4 Phosphate based glass porous microspheres 99
3.3 SURFACE AREA OF PARTICLES 105
3.4 POROSITY ANALYSES 106
3.4.1 Porosity, pore size and pore interconnectivity 106
3.4.2 Pore window size distribution on PGMS 111
3.5 PARTICLE COMPOSITIONAL ANALYSES 114
3.5.1 Relative density measurements 114
3.5.2 Tapped density measurements 115
3.5.3 Elemental compositional analyses 118
3.5.4 Glass chemistry after acid washing 130
3.6 DEGRADATION OF PARTICLES 131
3.6.1 Degradation in water 131
3.6.2 Degradation in culture medium for 42 days 132
3.7 DISCUSSION 135
3.7.1 Effect of spheroidisation on particles 135
3.7.2 Effect of acid washing on PGMS 140
3.7.3 Particulates on glass surface: a source of cytotoxicity 141
3.7.4 Degradation of microspheres 142
3.8 CONCLUSIONS 144

CHAPTER 4 2D VS. 3D CULTURE SYSTEM 146
4.1 INTRODUCTION 146
4.2 CELL HEALTH ANALYSIS 146
4.2.1 Cell attachment 148
4.2.2 Cell growth 150

4.2.3 Cell viability *153*
4.3 OSTEOGENIC DIFFERENTIATION 157
4.3.1 Alkaline Phosphatase activity *157*
4.3.2 Collagen production *160*
4.3.3 Mineral deposition *165*
4.3.4 Osteocalcin Expression *169*
4.3.5 Extracellular Matrix formation *172*
4.4 DISCUSSION 174
4.4.1 Batch-to-batch variability in BSG *174*
4.4.2 Metabolic differences exist in 2D and 3D *174*
4.4.3 Geometrical control of hMSCs-survival *176*
4.4.4 Geometrical control of osteogenesis *181*
4.5 CONCLUSIONS 185
CHAPTER 5 PHOSPHATE-BASED GLASS MICROSPHERES 186
5.1 INTRODUCTION 186
5.2 ANGULAR VS. SPHERICAL PARTICLES 186
5.3 ACID WASHED VS. NON-WASHED PGMS 190
5.4 BATCH-TO-BATCH VARIABILITY 192
5.5 HUMAN MSC ATTACHMENT ON MICROSPHERES 196
5.6 PARTICLE AGGREGATION 197
5.7 HUMAN MSC VIABILITY ON MICROSPHERES 200
5.8 HUMAN MSC GROWTH ON MICROSPHERES 203
5.8.1 Effect of degradation products on cell growth *206*
5.9 HUMAN MSC MORPHOLOGY ON MICROSPHERES 208
5.10 ALKALINE PHOSPHATASE ACTIVITY ON MICROSPHERES 213
5.10.1 Effect of degradation products on ALP activity *216*
5.11 COLLAGEN PRODUCTION 217
5.11.1 Qualitative assessment *217*
5.11.2 Quantitative assessment *217*
5.11.3 Effect of degradation products on collagen production *220*
5.12 CA AND P DEPOSITION ON MICROSPHERES 222
5.12.1 Effect of degradation products on Ca production *225*
5.13 OSTEOCALCIN PRODUCTION ON MICROSPHERES 226
5.14 EXTRACELLULAR MATRIX FORMATION (ECM) ON MICROSPHERES 229
5.15 CYTOTOXICITY OF MICROSPHERES 232
5.15.1 Indirect contact test *232*

5.15.2 Elution for 1 day *236*
5.15.3 Elution for 7 days *238*
5.15.4 Cytotoxicity of spent culture medium *243*
5.16 DISCUSSION 245
5.16.1 Angular shaped vs. regular shaped particles *245*
5.16.2 Batch-to-batch variability *246*
5.16.3 Effect of acid washing on hMSC response *247*
5.16.4 Cytocompatibility of P45 BGMS *248*
5.16.5 Cell growth on P40 BGMS *249*
5.16.6 Differentiation on P40 BGMS *252*
5.16.7 Cell growth on porous microspheres *253*
5.16.8 Differentiation on porous microspheres *256*
5.16.9 Limited penetration of hMSCs in PGMS *257*
5.16.10 Cytotoxicity of porous microspheres *259*
5.16.11 Re-precipitation of ions on bulk microspheres *260*
5.17 CONCLUSIONS 262
FINAL DISCUSSION AND OTHER APPLICATIONS **264**
FUTURE DIRECTIONS **267**
REFERENCES **269**
APPENDICES **311**
APPENDIX 1 311
APPENDIX 2 312
APPENDIX 3 315
APPENDIX 4 316
APPENDIX 5 317

List Of Tables

Table 1-1: Role of metal ions in bone metabolism..... 29

Table 1-2: Studies investigating effect of pore size 36

Table 1-3: Summary of commercially available microspheres for cell expansion. 52

Table 2-1: Nominal glass compositions (mol%) 60

Table 2-2: Batches of particles used in this study. 60

Table 2-3: Parameters for Micro Computational Tomography analysis. 63

Table 2-4: Details of direct-contact experiments 72

Table 2-5: Details of indirect-contact experiments 77

Table 2-6: Parameters for Micro Computational Tomography analysis for microspheres with cells..... 89

Table 2-7: Statistical analyses in different experiments. 90

Table 3-1: Summary of morphology: laser diffraction, sphericity and major axis length measurements of particles..... 104

Table 3-2: Surface area measurements..... 105

Table 3-3: Summary of density and closed porosity measurements of particles. 118

Table 3-4: Summary of elemental composition of particles using EDS analysis. 130

Table 4-1:Effect of cell seeding density on hMSC growth in 2D and 3D. 151

List Of Figures

Figure 1-1: Degeneration of bone in osteoporosis. 2

Figure 1-2: Hierarchy of bone structure in compact bone..... 6

Figure 1-3: Trabecular bone structure. 8

Figure 1-4: The basic multicellular unit of bone remodelling..... 10

Figure 1-5: Osteoclast activity. 12

Figure 1-6: Relationship between hMSCs and age. 15

Figure 1-7: *In vivo* bone formation in MSC loaded scaffolds. 17

Figure 1-8: Mechanism of bioglass-tissue bond formation. 20

Figure 1-9: Bioactivity spectrum for bioceramic implants.. 21

Figure 1-10: SEM image of human bone marrow stem cells cultured for 10 days on different ceramic materials.. 25

Figure 1-11: Osteoinductivity of bioglass. 28

Figure 1-12: Effect of porosity on *in vivo* bone formation..... 31

Figure 1-13: Examples illustrating the role of concavity in bone formation. 34

Figure 1-14: Effect of interconnectivity on *in vivo* bone formation. 40

Figure 1-15: Effect of nano pit arrangement on hMSC fate after 4 weeks of culture 42

Figure 1-16: Effect of cell morphology on hMSC fate. 46

Figure 1-17: Adhesive, topographical, mechanical, and soluble cues in 2D and 3D. 48

Figure 2-1: Identification of particles using Image J. 61

Figure 2-2: Identification of pore windows using Image J. 64

Figure 2-3: Methodology for quantification of MS with apparent cracks and peeling surfaces..... 67

Figure 2-4: Schematic view of the areas explored using hMSC-based experiments on MS. 69

Figure 2-5: A monolayer of MS prepared for hMSC seeding..... 71

Figure 2-6: Experimental design for cytotoxicity evaluation of MS through a transwell insert. 79

Figure 3-1: Morphology of AG1 P45 BGMP.. 92

Figure 3-2: SEM images of BSG. 93

Figure 3-3: Morphology of BSG. 94

Figure 3-4: Morphology of AG1 P45 BGMS. 96

Figure 3-5: Morphology of P45 PGMS and P40 BGMS. 97

Figure 3-6: Particle size distribution of P45 BGMS batches and P40 BGMS batches. 98

Figure 3-7: Morphology of AG1 P45 PGMS.. 100

Figure 3-8: SEM images of sieved fractions of AG1 P45 PGMS. ... 101

Figure 3-9: Morphology of AG5 P40 PGMS AW, AG6 P40 PGMS and AG6 P40 PGMS AW.. 103

Figure 3-10: Micro CT analysis of AG1 P45 PGMS.. 108

Figure 3-11: Micro CT analysis of AG1 P45 PGMS 200-300 µm. .. 109

Figure 3-12: Structural analysis of AG1 P45 PGMS 200-300 µm using micro CT. 110

Figure 3-13: Internal pore structure of AG6 P40 PGMS AW using Cryo-FIB SEM.. 111

Figure 3-14: Major axis length measurements of sieved fractions of AG1 P45 PGMS. 112

Figure 3-15: Major axis length and sphericity measurements of AG5 P40 PGMS AW, AG6 P40 PGMS and AG6 P40 PGMS AW.. 113

Figure 3-16: Relative density measurements. 116

Figure 3-17: Tapped density measurements.. 117

Figure 3-18: Elemental composition of AG1 P45 BGMP, AG1 P45 BGMS and AG1 P45 PGMS using EDS..... 119

Figure 3-19: Compositional analysis for AG1 P45 BGMS as an effect of MS diameter. 120

Figure 3-20: Retention of porogen in AG1 P45 PGMS. Scale bar- 20 µm. 120

Figure 3-21: EDS mapping analysis of AG1 P45 BGMP, AG1 P45 BGMS and AG1 P45 PGMS. 121

Figure 3-22: Elemental composition of BSG Batch 1 and BSG Batch 2 using EDS. 122

Figure 3-23: EDS mapping analysis of BSG Batch 1 and BSG Batch 2. 123

Figure 3-24: Elemental composition of P45 BGMS Batches 1, 2 and 3 and P40 BGMS Batches 1, 2 and 3 using EDS. 124

Figure 3-25: EDS mapping analysis of P45 BGMS Batches 1, 2 and 3. 126

Figure 3-26: EDS mapping analysis of P40 BGMS Batches 1, 2 and 3. 127

Figure 3-27: Elemental composition of AG5 P40 PGMS AW, AG6 P40 PGMS and AG6 P40 PGMS AW. 128

Figure 3-28: Retention of porogen in AG6 P40 PGMS and AG6 P40 PGMS AW.. 128

Figure 3-29: EDS mapping analysis of AG5 P40 PGMS AW, AG6 P40 PGMS and AG6 P40 PGMS AW.. 129

Figure 3-30: FTIR analysis of glasses before and after acid washing. 131

Figure 3-31: Degradation of MS in water 132

Figure 3-32: Progression of surface damage on bulk and porous MS as a result of degradation in culture medium over 42 days... 133

Figure 3-33: Quantification of degradation of MS in culture medium. 134

Figure 4-1: Batch-to-batch reproducibility of BSG..... 147

Figure 4-2: Cell attachment of hMSCs in 2D and 3D..... 149

Figure 4-3: Growth of hMSCs in 2D and 3D. 152

Figure 4-4: SEM images of 3D agglomerates..... 154

Figure 4-5: Viability of hMSC in 2D and 3D. 156

Figure 4-6: Alkaline phosphatase (ALP) activity measurements of hMSCs in 2D and 3D in standard culture (SC) medium and osteogenic (OS) medium. 159

Figure 4-7: Qualitative assessment of collagen production by hMSCs in standard culture (SC) medium and osteogenic culture medium (OS) after 7 days and 21 days of differentiation in 2D. 162

Figure 4-8: Qualitative assessment of collagen production by hMSCs grown in standard culture (SC) medium and osteogenic culture medium (OS) after 7 days and 21 days in 3D.. 163

Figure 4-9: Quantification of collagen produced by hMSCs seeded in 2D and 3D in standard culture (SC) medium and osteogenic (OS) medium.. 164

Figure 4-10: Qualitative assessment of mineral production by hMSCs in 2D and 3D systems in standard culture (SC) medium and osteogenic (OS) medium on Day 7 and 21 of differentiation. 167

Figure 4-11: Quantification of mineral production by hMSCs in 2D and 3D systems in standard culture (SC) medium and osteogenic (OS) medium on Day 21 of differentiation. 168

Figure 4-12: Controls for Osteocalcin staining in 2D and 3D..... 170

Figure 4-13: Osteocalcin (OCN) expression by hMSCs in 2D and 3D in Experiments OCN01..... 171

Figure 4-14: ECM formation by hMSCs in 3D in Experiment ECM01 173

Figure 4-15: Cells sense surface curvature on 3D matrix. 180

Figure 4-16: Proposed model for geometrical regulation of *in vivo* bone formation..... 185

Figure 5-1: Effect of particle shape on hMSC metabolic activity. . 187

Figure 5-2: ESEM images of hMSCs AG1 P45 BGMP and AG1 P45 BGMS after 7 days of culture in Experiment-PRE01. 188

Figure 5-3: ESEM images of hMSCs on AG1 P45 PGMS after 7 days of culture in Experiment-PRE01.. 189

Figure 5-4: Effect of acid washing of PGMS on hMSC growth..... 191

Figure 5-5: Effect of acid washing of bulk glass microspheres on hMSC attachment and growth. 192

Figure 5-6: Batch-to-batch variability in P45 BGMS in terms of hMSC growth. 193

Figure 5-7: Batch-to-batch variability in P40 BGMS in terms of hMSC growth. 194

Figure 5-8: Batch-to-batch variability in P40 PGMS AW in terms of hMSC growth..... 195

Figure 5-9: Human MSC attachment on different glass microspheres..... 198

Figure 5-10: FITC channel and overlay (FITC + Bright field) images of live hMSCs on different microsphere conditions after 1 days of culture..... 199

Figure 5-11: Human MSC spread and microsphere agglomeration during initial 24 h of culture. 200

Figure 5-12: Percentage hMSC viability in fields of view (normalised to cells in 2D) on day 1 and day 4 of culture on different glass microspheres..... 201

Figure 5-13: Representative images of live and dead hMSCs on day 1, 4 and 7 of culture. 202

Figure 5-14: Representative images of live and dead hMSCs on day 21 of culture from top, bottom and cross-sectional views of different 3D agglomerates..... 203

Figure 5-15: Human MSC growth on microspheres over shorter culture periods. 204

Figure 5-16: Human MSC growth on MS over longer culture periods 205

Figure 5-17: Effect of degradation products of glass microspheres on hMSC metabolic activity..... 207

Figure 5-18: Effect of degradation products of glass microspheres on hMSC proliferation. 208

Figure 5-19: SEM images of cells growing on different glass MS in Experiment-CP07 210

Figure 5-20: Micro CT of cell-PGMS agglomerate after 7 days in culture..... 211

Figure 5-21: Cell colonisation inside PGMS. 212

Figure 5-22: Alkaline phosphatase activity (ALP) activity of hMSCs on different microspheres. 215

Figure 5-23: Effect of degradation products of glass microspheres on hMSC Alkaline phosphatase (ALP) activity 216

Figure 5-24: Qualitative analysis of collagen deposition by hMSC on different glass microspheres using Sirius Red staining, after 21 of culture. 218

Figure 5-25: Collagen production by hMSCs on different glass microspheres on Day 21 of culture after cell seeding at 2,500 cells cm^{-2}. 219

Figure 5-26: Collagen production by hMSCs on different glass microspheres on Day 21 of culture after cell seeding at 10,000 cells cm^{-2}. 220

Figure 5-27: Effect of degradation products of glass microspheres on collagen deposition by hMSCs..... 221

Figure 5-28: Ca and P deposition by hMSCs on different microspheres on Day 21 in Experiment-MIN06 223

Figure 5-29: Ca and P deposition by hMSCs on different microspheres on Day 7, 14 and 21 of culture in Experiment-MIN07 224

Figure 5-30: Effect of degradation products of glass microspheres on Ca deposition by hMSCs..... 225

Figure 5-31: Osteocalcin staining on neural stem cells and detection of auto fluorescence and non-specific primary or secondary antibody staining in different microsphere conditions..... 226

Figure 5-32: Osteocalcin (OCN) expression (FITC) by hMSC on different microspheres after 21 of culture in SC (Standard culture) medium. 227

Figure 5-33: Osteocalcin (OCN) expression (FITC) by hMSC on different microsphere after 21 of culture in OS (osteogenic stimulation) medium. 228

Figure 5-34: Extracellular matrix (ECM) formation by hMSCs on different glass microspheres after 21 of culture.. 230

Figure 5-35: Typical H&E stained 3D cryo-section of P40 PGMS AW cultured with hMSCs for 21 days. 231

Figure 5-36: Indirect contact cytotoxicity evaluation for glass microspheres (MS) using a transwell in Experiment-TOX01.. 232

Figure 5-37: Indirect contact cytotoxicity evaluation for glass microspheres (MS) using a transwell in Experiment-TOX02.. 233

Figure 5-38: Images taken on day 3 of Experment-TOX02. 234

Figure 5-39: Characterisation of floating particulates collected in Experiment-TOX02..... 235

Figure 5-40: Extract tests of MS after 1 day of elution in medium in Experiment-TOX03..... 237

Figure 5-41: Neutral Red uptake by hMSCs in Experiment-TOX03. 238

Figure 5-42: Extract tests of MS after 7 day of elution in medium without medium changes in Experiment-TOX04. 240

Figure 5-43: Extract tests of MS after 7 day of elution in medium with medium changes in Experiment-TOX05..... 241

Figure 5-44: Neutral red uptake by hMSCs in Experiment-TOX05 242

Figure 5-45: Cytotoxicity of spent medium removed from hMSC-loaded MS on day 7, 14 and 21 of culture 244

Figure 5-46: Floating glass particulates in P40 BGMS and P40 PGMS AW-spent medium in Experiment-TOX06 and TOX07. 245

Figure A-1: Measurement of pH of media eluted with different glass MS over 22 days of conditioning. 311

Figure A-2: Validation of DNA quantification on 2D and 3D.....313

Figure A-3: Validation of ALP activity measurements in 2D and 3D systems..... 314

Figure A-4: Trypsinisation of cells on 3D samples.....315

Figure A-5: Collagen standard curve and validation of Sirius Red quantification on 3D samples.....316

Figure A-6: Barium loading on hMSCs.....317

Abbreviations

2D-	2-dimensional
3D-	3-dimensional
AG-	Ahmed Generation
AW-	Acid-washed
ALP-	Alkaline Phosphatase
BET-	Brunauer–Emmett–Teller
BGMP-	Bulk Glass Microparticles
BGMS-	Bulk Glass Microspheres
BSG-	Borosilicate glass microspheres
CPC-	Calcium phosphate cement
DMEM-	Dulbecco's Modified Eagle's Medium
ECM-	Extracellular Matrix
EDS-	Energy Dispersive X-ray Spectroscopy
ESEM-	Environmental Scanning Electron Microscopy
FTIR-	Fourier transform infrared spectroscopy
GFP-	Green Fluorescent Protein
hMSC-	Human mesenchymal stem cell
H&E-	Haematoxylin and Eosin
MAL-	Major axis length
MS-	Microspheres
MSC-	Mesenchymal Stem Cells
NRU-	Neutral Red uptake
OCN-	Osteocalcin
OS-	Osteogenic stimulation
PBG -	Phosphate-based glass
PGMS-	Porous Glass Microspheres

SC-	Standard culture
SEM-	Scanning Electron Microscopy
XPS-	X-Ray Photon Spectroscopy

Chapter 1 Introduction And Review Of Literature

1.1 Organisation of Literature Review

This PhD thesis reports a strategy for bone repair and reinforcement using bioactive glass materials. The work presented here focuses on human bone marrow derived mesenchymal stem cell (MSC) responses to smooth and porous geometries of phosphate based glass (PBG) microspheres (MS) from two major perspectives; (1) effect of chemical formulation and (2) effect of introduction of porosity; for end application in bone repair and reinforcement in osteoporotic patients. Based on a literature review, this is the first study that reports the development of porous PBG MS for bone repair.

This chapter embarks upon the current literature relevant to the present study in the following order–an introduction of osteoporosis (Section 1.2), adult bone architecture (Section 1.3) and bone remodelling process (Section 1.4), followed by an insight into MSCs and their clinical applications, with special focus on studies showing MSC seeded implants perform better than un-seeded implants *in vivo* (Section 1.5). Then, bioactive glasses (Section 1.6) and their mechanism of osteoinductivity (Section 1.7) are reviewed in detail, which leads on to a review on how porosity has been identified as an essential geometrical cue for bone formation at macro, micro and nano scales (Section 1.8). Further, in Section 1.9, effect of concave and convex radii of curvature on hMSC is discussed, leading on to a brief introduction that compares the traditional monolayer culture system to three dimensional culture system (Section 1.10). Then MS as cell-substrates are introduced and previous studies focusing on smooth and porous MS for bone repair applications have been discussed (Section 1.11). Finally, the aims and objectives of this PhD thesis are presented (Section 1.12).

1.2 Osteoporosis – the 'silent epidemic'

The International Osteoporosis Foundation (IOF) describes osteoporosis as the condition of 'porous bones' (Kanis et al. 1994). It involves significantly reduced bone mineral density and therefore, increased fragility, making the bones susceptible to fractures (Figure 1-1).

Osteoporosis is an age-related disorder that occurs when the delicate balance between bone formation and bone resorption in the adult bone marrow is disrupted. This imbalance usually occurs in post menupausal women and in men over 50 years of age. Based on current statistics reported by IOF, 200 million women curently suffer from osteoporosis and one in three women and one in five men over 50 years of age will experience a fracture (Kanis et al. 2013). It is estimated that an osteoporotic fracture occurs every 3 seconds, totalling 8.9 million incidents every year (Currey et al. 1996; Zioupos & Currey 1998; Lam 2008). As a result, countries with ever increasing aging population are destined to be under socio-economic pressure in the coming years. For these reasons, osteoporosis is now referred to as a 'silent epidemic' (Iacono 2007; Rachner et al. 2011; Lerner 2006).

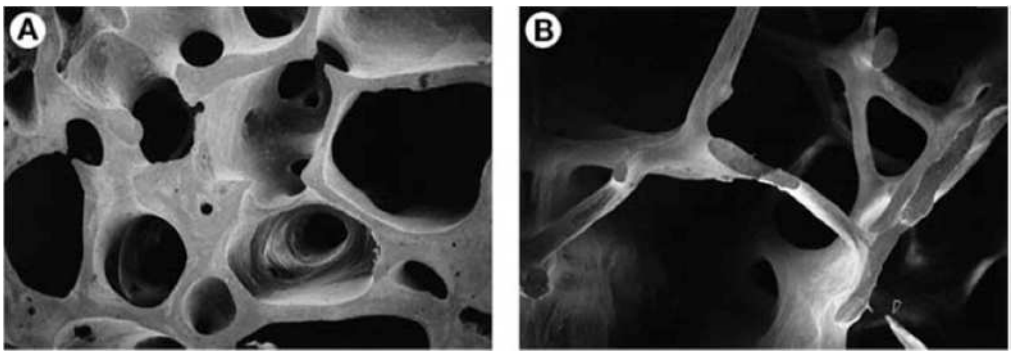

Figure 1-1: Degeneration of bone in osteoporosis. Scanning electron micrographs of (A) normal and (B) osteoporotic cancellous bone from human iliac crest. Taken from (Dempster et al. 1986).

The fractures occurring due to osteoporosis are commonly in the hip and spine but other regions such as knee, wrist, pelvis, arms, etc. are also prone. A hip fracture often necessitates surgery and can

result in disability (50% cases) or loss of life (20% mortality rate), while a vertebral fracture can result in loss of height, severe back pain and deformity. In the European Union alone, the cost of osteoporosis is estimated at €37 billion per year (Kanis et al. 2013).

Current available cures for age-related osteoporosis are mostly in the form of preventive therapy, combined with lifestyle changes to minimise the risk of fracture. Preventive treatments include anabolic agents such as growth hormone (GH) and parathyroid hormone (PTH) and anti-resorptive agents such as bisphosphonates, strontium renelate, denosumab and raloxifene. GH plays a positive role in fracture healing but has safety issues related to optimal dose (Tran et al. 2009). PTH enhances bone regeneration, bone mass, mechanical bone strength and bone-mineral density with side effects under investigation (Tzioupis & Giannoudis 2006). Bisphosphonates reduce the activity of osteoclasts and induce their apoptosis but also leads to side effects such as osteonecrosis (McClung 2015). Strontium renelate is an alternative to biosulphonates and acts on both bone formation and resorption (O'Donnell et al. 2006). Denosumab selectively inhibits osteoclastogenesis by targeting the receptor activator of nuclear factor- κB ligand (RANKL) (Zaheer et al. 2015) and raloxifene is a selective estrogen receptor modulator (SERM) that helps maintain bone density and reduces the risk of fracture, especially in the spine (Nagatoya et al. 2014).

1.2.1 Current treatments for bone fracture

In the event of a bone fracture, several therapeutic strategies are available depending upon the site of fracture (Roberts & Rosenbaum 2012). The common approaches include distraction osteogenesis and bone transport (Green et al. 1992; Aronson 1997) and different bone-grafting methods such as autologous bone grafts, allografts and bone-graft substitutes with or without growth factors (Giannoudis & Einhorn 2009; Roberts & Rosenbaum 2012).

In bone grafting, autologous bone transplant is considered a 'gold standard' grafting material since it incorporates all the properties of a successful material namely *osteoinduction* (bone morphogenetic proteins (BMPs) and other growth factors), *osteogenesis* (osteoprogenitor cells) and *osteoconduction* (scaffold), together with being histocompatible and non-immunogenic (Dodd et al. 1988; Bauer & Muschler 2000; Roberts & Rosenbaum 2012).

However, harvesting these grafts requires an additional surgical procedure with well-documented complications including risk of wound infection, increased blood loss, prolonged anaesthetic time, increased costs and limited available volume (about $20cm^3$) together with general discomfort for the patient (Burchardt 1983). This increases the costs of the therapy (Nandi et al. 2010; Matassi et al. 2011; Zimmermann & Moghaddam 2011). Additionally, the efficacy of bone auto-grafting in elderly patients is yet to be fully explored as these patients not only have limited availability of autografts but the grafting material may also contain fewer mesenchymal stem cells and stimulatory factors, vital for bone regeneration (Tollemar et al. 2012).

The second option available is the use of allogeneic grafts. They can be harvested from living donor cadavers in various shapes and sizes. They have variable *osteoinductive* and *osteoconductive* properties with lack of osteogenic properties; and come in various forms including, demineralised bone matrix (DBM), morselized and cancellous chips, corticocancellous and cortical grafts, and osteochondral and whole-bone segments (Zimmermann & Moghaddam 2011; Tollemar et al. 2012). The concern of transmission of infectious diseases is eliminated through tissue processing and sterilization. However, there have been some documented cases of transmission of human immunodeficiency virus (HIV), hepatitis C virus (HCV), bacterial contaminations and some unknown viruses (Dodd et al. 1988; Bauer & Muschler 2000; Roberts & Rosenbaum 2012).

Allografts, like autografts again have limited availability and cannot alone suffice the ever-increasing global demand for grafting materials. For this reason, new synthetic grafting technologies for bone tissue engineering and bone regeneration are being investigated.

Biomaterials address some of the limitations of traditional grafting materials, especially with respect to availability and patient discomfort. They are made from all classes of materials such as natural and synthetic polymers, ceramics, metals, composites and bioactive glasses in general (Kolk et al. 2012). They are also sometimes used in combination with osteoinductive factors such as BMPs and osteogenic factors such as MSCs and osteoblasts, to enhance the bone regeneration (Dimitriou et al. 2011; Squillaro et al. 2016).

1.3 Bone architecture

Biomaterial scaffolds act by providing *osteoconductive* and *osteoinductive* mechanisms for cells to form bone. However, osteogenesis finally occurs when the cells seeded on scaffolds or recruited from the neighbouring host tissue establish new centres for bone formation (Karageorgiou & Kaplan 2005). For this to work, the scaffolds must mimic bone morphology, structure and function so as to integrate the scaffold with host tissue. It is therefore essential to understand the basic bone architecture in our bodies.

The bone is comprised of the compact or cortical bone and the cancellous or trabecular bone. The compact bone forms the cortex or an outer shell that protects the inner parts of the bone and consists of cortical series of solid structures named haversian canals (2500-12,000 μm^2 cross-sectional area), resulting in total porosity of 3-12% and typical density value of 1.85±0.06 g cm^{-3} (Karageorgiou & Kaplan 2005). See Figure 1-2 for illustration.

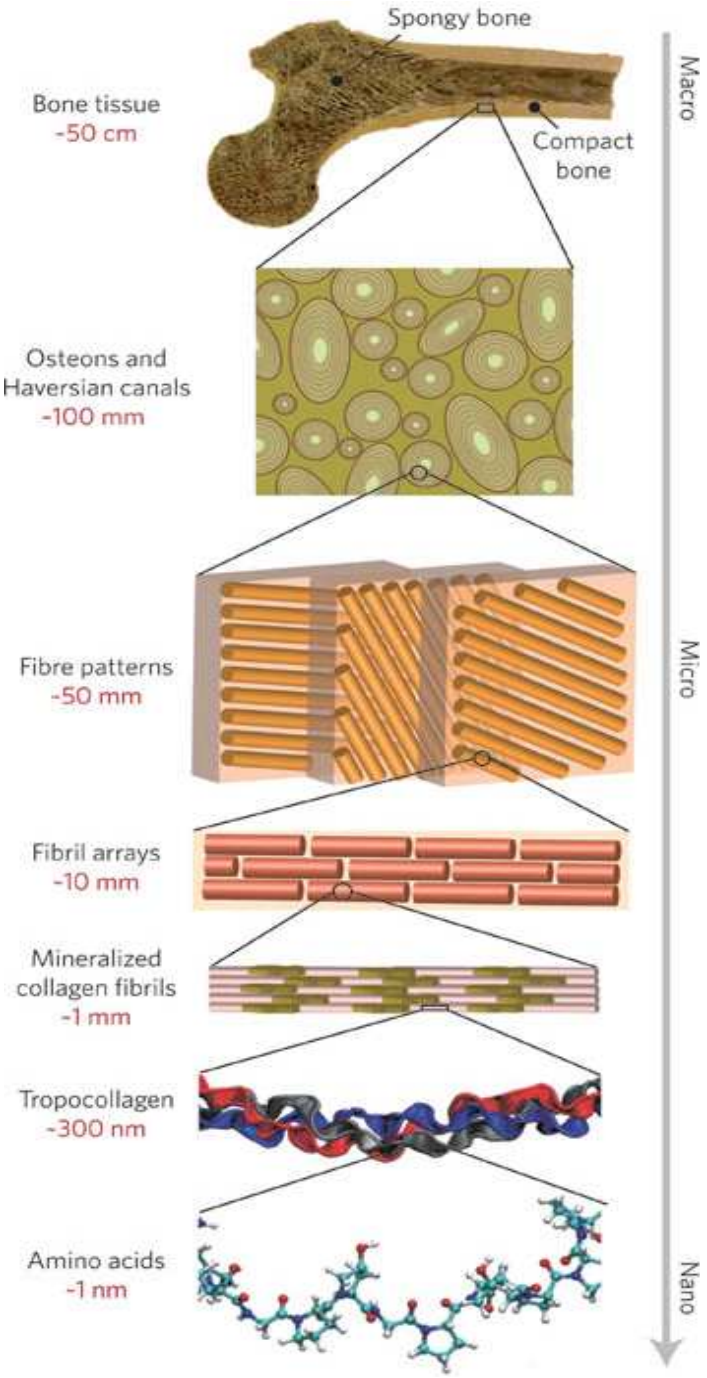

Figure 1-2: Hierarchy of bone structure in compact bone. Three polypeptide chains intertwine to form the tropocollagen molecules that get mineralised with hydroxyapatite by osteoblasts. The tropocollagen tightens through the mechanisms of molecular uncoiling and intermolecular sliding to from collagen fibrils. The fibrils align to form fibril array and fibril patterns. These fibril patterns form the osteons and haversion canals in trabecular and cortical bones. Adapted from (Ritchie 2011).

The cancellous bone is a spongy-type of bone, which is present at the ends of all long bones such as femur and tibia, and also found within flat and irregular bones, such as the sternum, pelvis and spine (Keaveny et al. 2001). The trabecular bone consists of 50-90% porosity with 1 mm diameter as minimum pore size (Keaveny et al. 2001), which supports bone marrow cells and vasculature (see Figure 1-3) The typical density value for proximal tibial trabecular bone is 0.30±0.10 g cm^{-3} (Karageorgiou & Kaplan 2005). However,

there is variation reported in the trabecular bone density from different sources of the body. For example, trabecular bone from the calcaneus was measured at 1.14±0.15 g cm^{-3}, while trabecular bone from the iliac crest was measured at 1.10±0.08 g cm^{-3} (Follet et al. 2004; Karageorgiou & Kaplan 2005). The mechanical properties of trabecular bone also vary both in modulus and strength, from region to region. For example, compressive modulus can vary 100-fold from one location to another within a single proximal tibia, and strength can vary 5-fold within the proximal femur and across sites. Moreover, the ultimate stress in trabecular bone is seen to reduce by 7% and 11% per decade for human proximal femur and spine, respectively, from ages 20–100 years. Recapitulating this heterogeneity and anisotropy in the trabecular architecture is the key for the performance of a biomimetic scaffold implanted *in vivo*.

At the molecular level, bone is a composed of hydroxyapatite (HA) ($Ca_{10}(PO_4)_6(OH)_2$) crystals deposited within an organic (collagenous) matrix (Ritchie 2011) (see Figure 1-2). In adults, the extracellular matrix (ECM) formation and mineral deposition is performed by the osteoblasts derived from MSCs during the bone remodelling process (discussed in next section); and the stiffness and compressive strength of the cancellous bone is found to be directly proportional to the mineralisation of the bone in ECM (Follet et al. 2004).

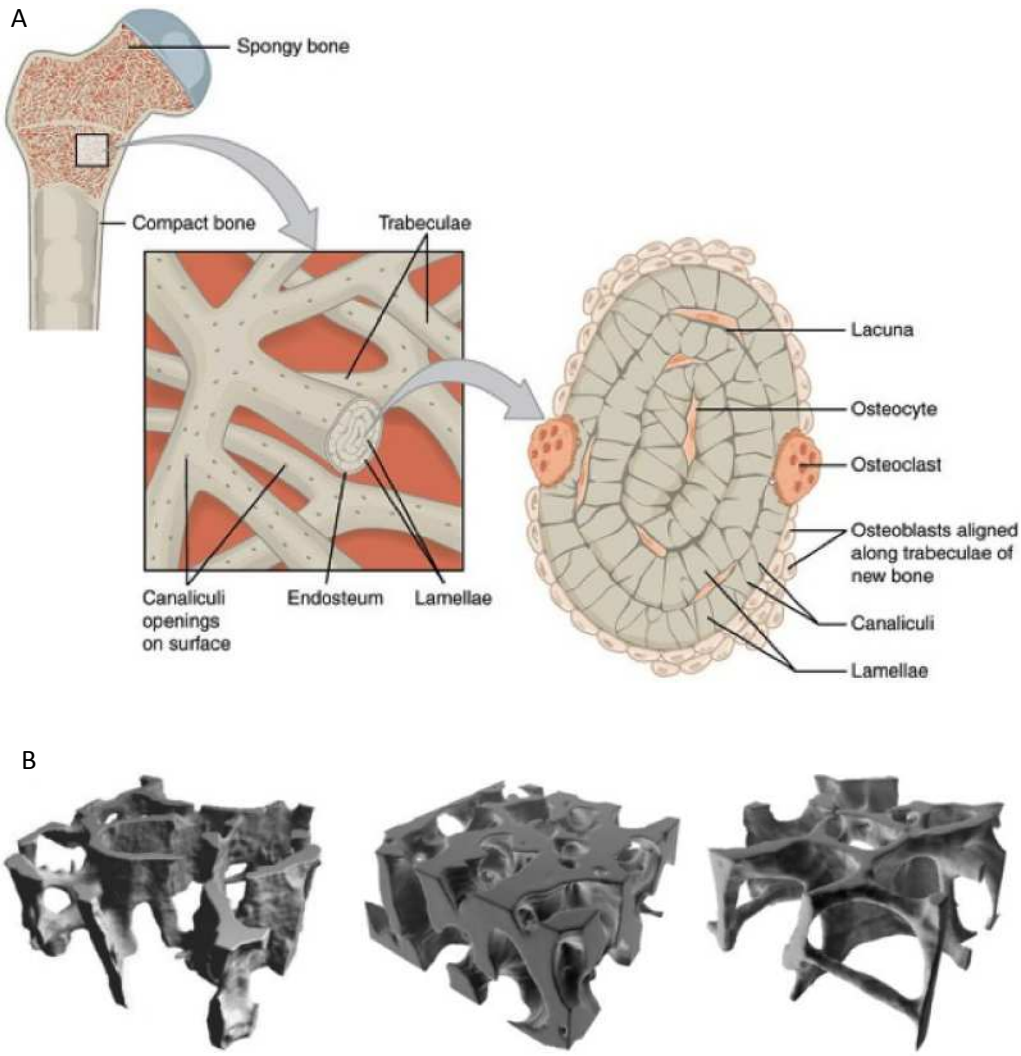

Figure 1-3: Trabecular bone structure. (A) A typical long bone showing the location of cancellous (trabecular) bone and its lamellae structure, which houses osteocytes and osteoclasts while being surrounded by osteoblasts. (B) Volume rendering (20 μm resolution) of human proximal tibia, human femoral neck, and human vertebral trabecular bone (left to right). Specimens have the same bulk dimensions (3 X 3 X 1 mm^3) and demonstrate heterogeneity in trabecular bone architecture. Adapted from (Keaveny et al. 2001).

1.4 Bone remodelling

At the molecular level, it is the process of osteogenesis that lies at the heart of bone repair process. Therefore, to achieve bone regeneration, it is essential to identify the key factors that influence the same.

Bone remodelling is a dynamic process that keeps the bones healthy and fully functional. In the homeostatic bone remodelling system,

there is a delicate balance between the rate of osteoblast activity and the rate of osteoclast activity, such that there is 25% of trabecular bone and 3% of cortical bone turnover per year. This process is highly regulated by hormones, vitamins and cytokines at gene level (Teitelbaum 2000; Dimitriou et al. 2005; Olszta et al. 2007).

Unfortunately, this homeostatic state is short-lived and both men and women start losing bone density in the fourth decade of their life, caused by excessive osteoclast activity and decreased osteoblasts differentiation, due to a decline in MSC numbers in bone marrow and periosteum (Weitzmann 2013). This loss is accelerated in women who experience menopause and have decreased estrogen levels in blood for 5-10 years, leading to faster bone resorption and more susceptibility to bone fractures (osteoporosis). In men, the rate of bone loss has linear relationship with time, due to progressive decline in sex steroids. This persistent loss correlated to ageing leads to osteopenia (low bone mass) and ultimately to osteoporosis (Bellantuono et al. 2009).

At the cellular level, the underlying temporary anatomical structure that brings about bone remodelling is called the basic multicellular unit (BMU), see Figure 1-4. This unit comprises of osteoclasts, osteoblasts, bone lining cells and osteocytes, which work together in an orchestrated fashion. In short, the osteoclasts resorb the bone to form concavities and osteoblasts produce and mineralize new bone matrix in these concavities. The osteocytes act as mechanical sensors that help maintain the balance between bone resorption and bone formation. Finally, bone lining cells take part in osteoclast or osteoblast differentiation depending upon bone physiology (Crockett et al. 2011; Kular et al. 2012; Florencio-Silva et al. 2015). The osteoclastic and osteoblastic activities are discussed in greater detail below.

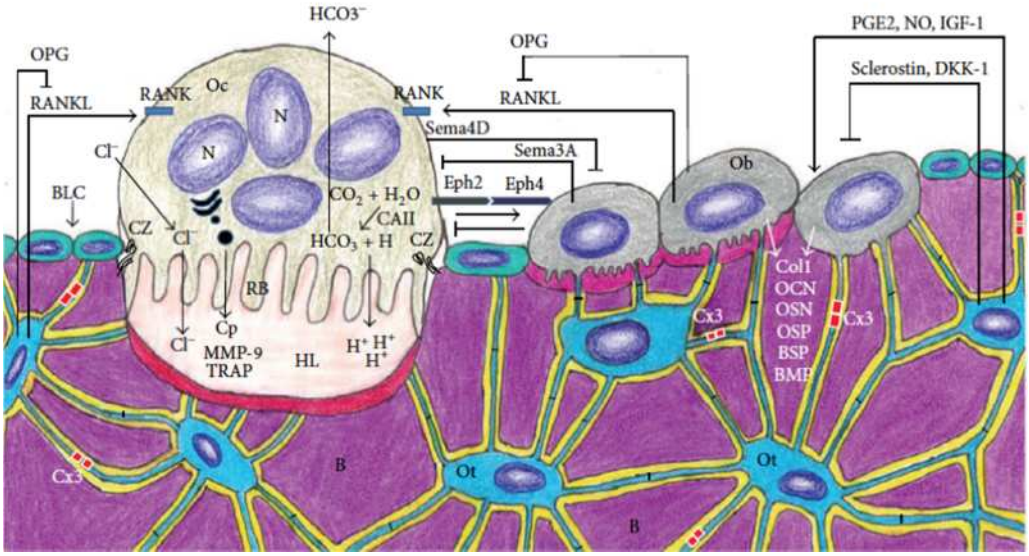

Figure 1-4: The basic multicellular unit of bone remodelling. Osteoclast (Oc) is activated by binding of Receptor activator of nuclear factor kappa-β ligand (RANKL) to RANK receptor on osteoclast plasma membrane. This leads to polarization of osteoclast creation specialized regions of the ruffled border (RB) and clear zone (CZ) on the plasma membrane, as the osteoclast resorbs the bone to form Howship lacuna (HL). The hydroxyapatite and collagen in the bone surface adjacent to RF is dissolved due to pumping of hydrogen ions (H+), carbonic anhydrase II (CAII), cathepsin (Cp), matrix metalloproteinase-9 (MMP-9) and tartrate-resistant acid phosphatase (TRAP). EphrinB2 (Eph2) present in osteoclast membrane binds to ephrinB4 (Eph4) in osteoblast (Ob) precursor membrane, promoting its differentiation, whereas the reverse signalling (ephrinB4/ephrinB2) inhibits osteoclastogenesis. Ob forms the organic matrix by secreting collagenous (Col1) and non-collagenous proteins such as osteocalcin (OCN), osteopontin (OSP), osteonectin (OSN), bone sialoprotein (BSP), and bone morphogenetic proteins (BMP). Osteocytes (Ot) located within lacunae surrounded by mineralized bone matrix (B) have cytoplasmic processes that connect with cytoplasmic processes of other neighbouring osteocytes processes by gap junctions via connexin 43 (Cx3). This networking amongst Ot forms the lacunocanalicular system, which facilitates intercellular transport of small signalling molecules such as prostaglandins, nitric oxide, oxygen and nutrients, since the network is in close proximity to the blood supply. The osteocytes are able to sense the mechanical pressures and enable the adaptation of bone matrix with the external mechanical forces. They also regulate the osteoblast and osteoclast activities by release appropriate factors including RANKL, osteoprotegerin (OPG), prostaglandin E2 (PGE2), nitric oxide (NO), insulin-like growth factor (IGF), sclerostin and dickkopf WNT signalling pathway inhibitor (DKK-1). Taken from (Florencio-Silva et al. 2015).

1.4.1 Osteoclastogenesis-bone resorption-concavity formation

The osteoclast is a tissue-specific macrophage that is differentiated from monocyte/macrophage precursor cells on or near the bone surface. The two haematopoietic factors, tumour necrosis factor (TNF)-related cytokine RANK ligand (RANKL, secreted by osteoblasts, osteocytes, and stromal cells) and the polypeptide growth factor colony-stimulating factor-1 (CSF-1), secreted by osteoprogenitor mesenchymal cells present in surrounding stroma, activate RANK on the surface of precursor cells. Calciotropic hormones and pro-resorptive cytokines also induce the expression of RANKL on osteogenic stromal cells to initiate this process.

The precursor cells fused to the bone, undergo cell division and 10-20 individual cells fuse together to form one mature polykaryon osteoclast expressing tartrate-resistant acid phosphatase (TRAP), cathepsin K (CATK), calcitonin receptor and the β_3-integrin, characteristic of late osteoclastogenesis. This also stimulates secretion of protons and lytic enzymes through a signalling cascade inside the cytoplasm, into a sealed resorption vacuole formed between the basal surface of the mature osteoclast and the bone surface. Vacuole formation leads to activation of TRAP and CATK that ultimately degrade the mineral and collagen matrices of the bone. The degraded products (collagen fragments and solubilized calcium and phosphate) are processed by osteoclasts and then released into the blood circulation. The degrading activity of osteoclasts can leave pits up to 50 µm deep and 100 µm wide (Roodman 1999; Väänänen et al. 2000; Boyle et al. 2003; Nakamura et al. 2012; Florencio-Silva et al. 2015), see Figure 1-5.

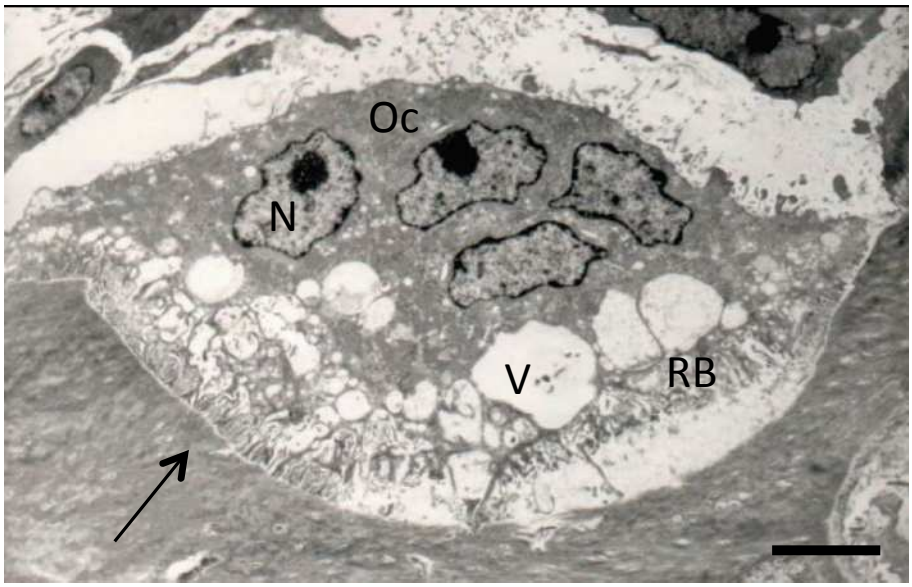

Figure 1-5: Osteoclast activity. Transmission electron micrograph of multinucleated osteoclast (Oc) with vacuoles adjacent to ruffled border (RB) near the excavated bone surface. The osteoclast resorbs the bone to create a resorption pit/concavity (arrow), later to be filled by osteoblasts. N-nucleus, scale bar-4 µm. Adapted from (Florencio-Silva et al. 2015).

1.4.2 Osteoblastogenesis-mineralisation in lacunae-bone formation

Specialised cells known as osteoblasts perform the function of bone formation. These cells are polarised and secrete osteoid only towards the bone matrix or substrate they are present on. As protein synthesising cells, they also have large Golgi apparatus and abundant rough endoplasmic reticulum and secretory vesicles. Osteoblasts are differentiated from MSCs in the bone marrow through the process of osteoblastogenesis. This process is initiated by establishing the expression of Runx2, which also triggers the ColIA1 expression. Then MSCs enter into a proliferative state, where alkaline phosphatase (ALP) activity is enhanced and the cells are considered pre-osteoblasts. As the pre-osteoblasts progress to mature osteoblasts stage, there is an increase in the Osterix expression, which leads to bone matrix deposition (Hadjidakis & Androulakis 2006; Crockett et al. 2011; Dimitriou et al. 2011; Kular et al. 2012; Florencio-Silva et al. 2015; Lieben 2016).

1.4.3 Bone matrix deposition

The bone matrix formation inside the lacunae occurs in two stages. In the first stage, proteins (including type I collagen, osteocalcin, osteonectin, BSP II, osteopontin), and proteoglycans (including decorin and biglycan) are released by mature osteoblasts and form the organic matrix. In the next stage, mineralisation of this organic matrix takes place in two further phases. Phase one is the vesicular phase, in which the osteoblasts release Ca^{2+} ions containing matrix vesicles via the apical membrane domain of the cell membrane on to the organic matrix. The sulphated proteoglycans (negatively charged) immobilize the Ca^{2+} ions inside the vesicles and when the osteoblasts secrete the enzymes that degrade proteoglycans, the Ca^{2+} ions are released. At the same time, ALP degrades the phosphate-containing compounds, releasing Pi inside the matrix vesicles. The P_i and Ca^{2+} inside the vesicles then nucleate to form hydroxyapatite (HA) crystals. In the second phase or the fibrillar phase, the P_i and Ca^{2+} inside the vesicles supersaturate, leading to the rupture of these vesicles and the hydroxyapatite crystals are released and deposited on the surrounding matrix. The osteoblasts may show cytoplasmic processes towards the bone matrix indicating mineralisation. In the final stage, the osteoblasts may undergo apoptosis or become osteocytes or bone lining cells (Hadjidakis & Androulakis 2006; Crockett et al. 2011; Dimitriou et al. 2011; Kular et al. 2012; Florencio-Silva et al. 2015; Lieben 2016).

1.5 Mesenchymal Stem Cells (MSCs)

Bone marrow derived MSCs are the cells with osteogenic potential and play a key role in bone regeneration by giving rise to osteoblasts.

Friedenstein et al. (1966; 1974; 1988) first discovered the presence of mesenchyme derived stromal stem cells in the bone marrow. He observed that these cells adhered to plastic, were spindle-shape in appearance and were clonogenic. They could also serve as feeder

layers for haematopoietic stem cell culture over a period of several weeks to months *in vitro* and could also form differentiated colonies like that of bone or cartilage cells. Friedenstein discovered that these cells were heterogeneous population and that after serial subculturing, they became more homogeneously fibroblastic in appearance. In 1991, Caplan renamed these cells from stromal stem cells to mesenchymal stem cells due to their capacity to give rise to tissues of mesodermal origin including bone, fat and cartilage (Caplan 1987; Caplan 1988; Caplan 1991; Bruder et al. 1994; Jaiswal et al. 1997; Johnstone et al. 1998).

1.5.1 Plasticity, Sources and Frequency of MSCs

Unique MSCs markers are currently unknown. However, the *International Society for Cytotherapy* has suggested the minimal requirement for a population of cells to qualify as MSCs (Pittenger 1999; Bobis et al. 2006; Liu et al. 2009):

(1) The plastic adherence of the isolated cells in culture.
(2) Positive expression of CD 105, CD 73 and CD 90 in more than 95% of cells and lack of expression of CD 34, CD 45, CD 14 or CD 11b, CD 79α or CD 19 and HLA-DR in more than 95% of the culture. However, the expression level of these markers may vary depending upon culture conditions, donor age, and differentiation stages of cells, tissue sources and species differences.
(3) The differentiation of the MSCs into bone, fat and cartilage. However, in recent years, MSCs have also been discovered to differentiate into myoblasts, connective stromal cells, hepatocytes, lung cells, gut cells, neurons, glia and skin cells, through the process of trans-differentiation (Krabbe et al. 2005).

MSCs are not just limited to bone marrow but have now been isolated from non-marrow tissues. These include skeletal muscle, adipose tissue, skin, thymus, periosteum, synovium, synovial fluid, lung, dental pulp of deciduous baby teeth, the circulatory system,

amniotic fluid, umbilical cord blood as well as fetal blood and liver (Klingemann et al. 2008).

In the bone marrow, MSCs are found in low numbers and their titres depend upon the age of the donor (see Figure 1-6). A study showed that there is three orders of magnitude decrease in MSC titres between new-born and 80-year-old (Caplan 2009). At the same time, MSCs also lose their self-renewal ability with age. For example, MSCs have maximum lifespan from 30-40 population doublings in young donor to 20 population doublings in older donors. This has been found to be due to telomere shortening and increased number of MSCs undergoing senescence (Stenderup et al. 2003; Baxter et al. 2004).

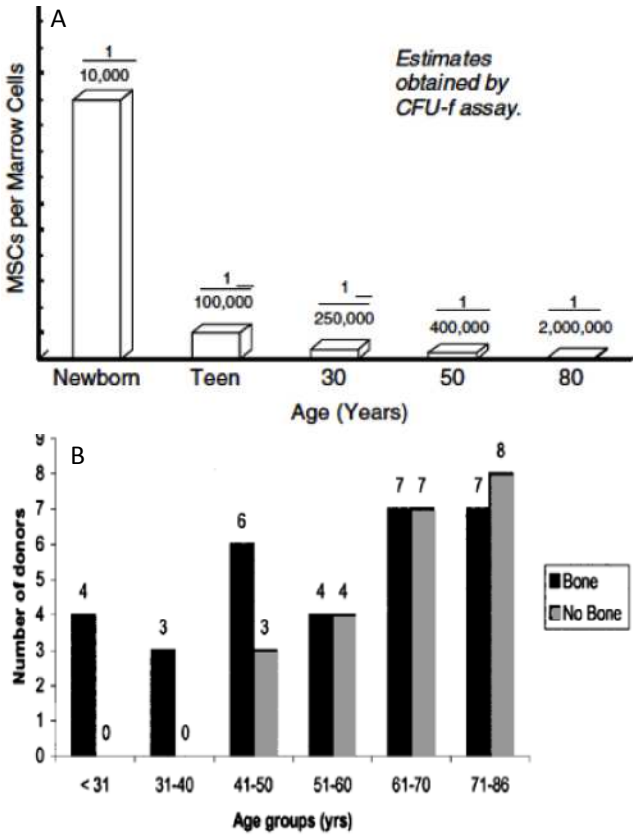

Figure 1-6: Relationship between hMSCs and age. Top- colony forming unit-fibroblasts assay used as measure of hMSC titres in bone marrow of different ages. There was a decline in hMSC titres with age. Taken from (Caplan 2009). Bottom-effect of age on bone forming potential of hMSCs from bone marrow in nude mice. There were more regions devoid of new bone in mice transplanted with hMSC from donors of more than 40 years of age. Taken from (Mendes et al. 2002).

Age-related changes in the differentiation potential of MSCs have also been investigated (Bellantuono et al. 2009). Nonetheless, there is no consistent evidence that shows age-related loss of osteogenic potential of MSCs. For instance, Mendes et al. (2002) showed that when MSCs from 53 donors of various age were seeded on calcium phosphate scaffolds and implanted under the skin of nude mice, the bone forming potential was found to decline with age. Nearly 67%, 50% and 46% of the cultures were able to form bone in 41–50 years, 51–70 years and beyond 70 years of age groups, respectively. On the other hand, Stenderup et al. (2003) obtained osteoblasts from hMSCs donated by young (24-30 years, n=5) and old (71-81 years, n=5) individuals and implanted them in immunodeficient mice. Results showed no difference in bone forming potential between hMSCs from young and old donors.

1.5.2 MSCs enhance bone formation *in vivo*

A number of studies have shown bone forming potential of MSCs (Pittenger 1999; Orozco et al. 2013; Bruder et al. 1998; Bellantuono et al. 2009; Bruder et al. 1998; Bobis et al. 2006; Orozco et al. 2011; Liebergall et al. 2013; Kern et al. 2006; Giuliani et al. 2013; Caplan 1991; Neelam Jaiswal et al. 1997) and in this sub-section some of the *in vivo* studies have been reviewed.

Dong et al. (2001) developed a novel porous HA scaffold with 77% porosity, 500 μm as average pore diameter and 200 μm wide interconnecting paths. The scaffolds seeded with or without bone marrow derived osteoblasts (BMO) were implanted into subcutaneous sites of syngeneic rats. After two week of implantation, the HA scaffold with BMO had significantly more ALP activity, osteocalcin content and mineralised collagen matrix as compared to HA scaffolds implanted without BMO. Cowan et al. (2004) used PLGA or poly(lactic-co-glycolic acid) scaffolds and seeded them with adipose derived adult stromal cells, bone marrow stromal cells, calvarial-derived osteoblasts or dura mater cells (all from adult or juvenile sources) before implanting in mice to heal

critical-size mouse calvarial defects. After four weeks, presence of stem cells significantly enhanced bone repair *in vivo* as compared to implants not seeded with cells before implantation; and Juvenile cells showed more potential for mineralisation and bone repair *in vivo* than the adult sources, see Figure 1-7 A).

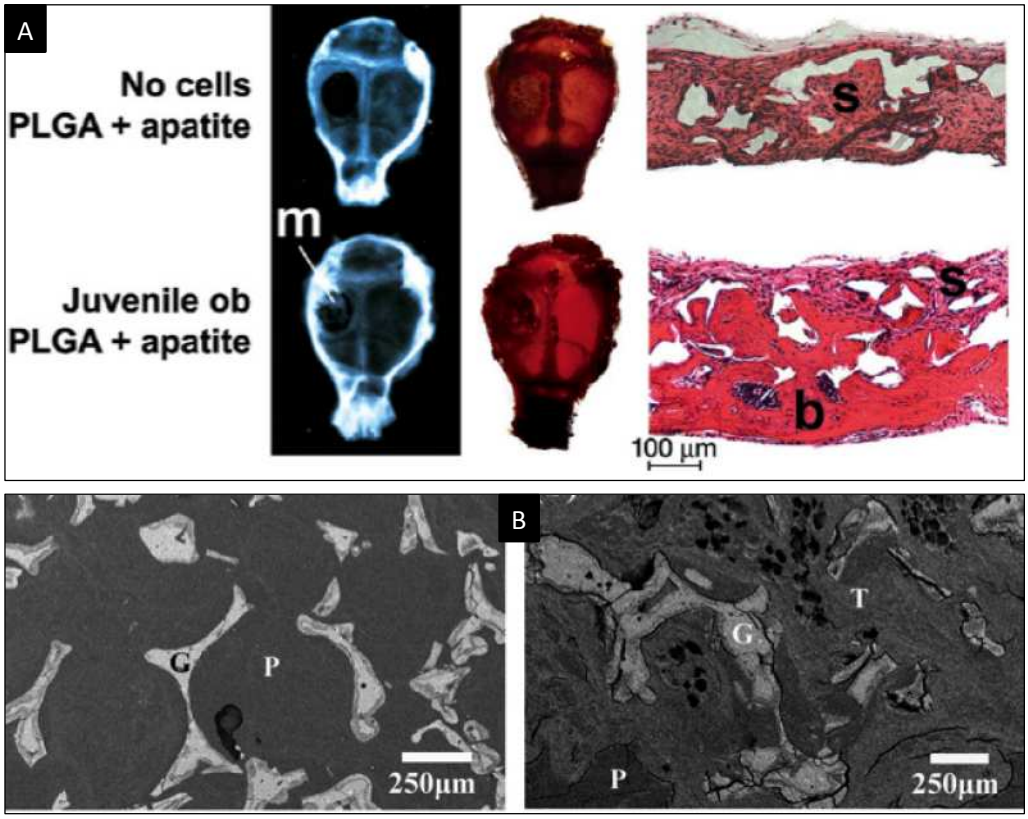

Figure 1-7: *In vivo* bone formation in MSC loaded scaffolds. (A) X-Ray, alizarin red and histological analysis (left to right) after 4 weeks of implantation of apatite coated PLGA scaffolds with or without juvenile osteoblasts in critical-sized calvarial defects. There is no bone formation in scaffolds without cells and robust bone formation is visible in scaffolds seeded with juvenile cells. s-scaffolds, b-bone, m-mineral. Adapted from (Cowan et al. 2004). (B) Backscattered electron images of trabecular shaped bioglass implants (left) without MSCs and (right) seeded with MSCs. G-glass; T-tissue; P-PMMA. Adapted from (Fu et al. 2010).

Meinel et al. (2005) studied the bone formation potential of silk porous scaffolds seeded with or without hMSCs, differentiated or undifferentiated under osteogenic induction medium. After 8 weeks of implantation in rat femur critical sized defects, substantial bone formation was observed in scaffolds previously seeded with hMSCs and differentiated before implantation as compared to scaffolds without cells or the empty defects. In another study, Fu et al.

(2010) showed that the *in vivo* bone formation was significantly enhanced in case of 13-93 bioactive porous scaffolds, when seeded with MSCs and implanted in subcutaneous pockets in the dorsum of rats. These scaffolds had columnar or trabecular shaped pores in the range of 90-110 μm and total porosity of 65% (see Figure 1-7 B).

These studies collectively suggest a significant improvement in bone repair when implants are pre-seeded with MSCs before implantation into the defect. Such studies have spurred nearly 94 MSC-based clinical trials for bone and cartilage diseases worldwide (Squillaro et al. 2016; Trounson & McDonald 2015).

1.5.3 Clinical studies with MSCs

Some clinical studies have also shown that MSC administration improves bone formation. Some examples include, treatment of distal tibia non-reunion fractures (50% improvement in healing time reported after MSC administration) (Liebergall et al. 2013); degenerative disc disease with severe low back pain (85% pain and disability relief in 3 months in MSC administered patients) (Orozco et al. 2011); knee osteoarthritis (78% improvement of algofunctional indices reported after 1 year of MSC administration) (Orozco et al. 2013) and severe osteogenesis imperfecta in foetus (*in utero* MSCs administrated led to normal psychomotor development and growth of foetus) (Le Blanc & Pittenger 2005).

According to the US National Institutes of Health, there are currently 493 MSC-based clinical trials in total. For example, Prochymal MSCs are now used to treat steroid resistant severe paediatric GVHD (graft versus host disease) in Canada and New Zealand. MSCs are used for supressing myocardial infraction (MI) and suggested for application post-MI. The anti-fibrotic effects of autologous MSCs have been explored in patients with alcohol liver cirrhosis. Clinical trials with patients suffering from type II diabetes are currently ongoing. Due to the neuroregulatory activity of MSCs, clinical trials for stroke, ALS and MS are underway (Squillaro et al. 2016;

Trounson & McDonald 2015). Some *in vitro* and *in vivo* studies (Kasper et al. 2007; Schumann et al. 2009) have confirmed the role of MSCs in promoting angiogenesis by paracrine factors during fracture healing; suggested their potential to home in injured tissues (Granero-moltó et al. 2012); and demonstrated their ability to supress T-cell proliferation and cytokine production (De Bari & Dell'Accio 2007). This makes them popular candidates as adjunct grafts for clinical studies involving allogeneic grafting for containment of immune rejection.

1.6 Bioactive materials

The first generation of biomaterials included stainless steel and cobalt-chrome alloys, plastics, Ti and Ti-based alloys, alumina and zirconia and polymers such as silicone rubber and acrylic resins. These materials were chosen on the basis of their inertness and corrosion resistance *in vivo,* so as to minimise formation of scar tissue at the interface with host tissue. However, it was not long before when it was realised that no material is truly bio-inert and can elicit a response in the patient that may lead to rejection of the implanted material.

In 1969, Professor Larry L. Hench discovered Bioglass®, which was the first synthetic material that formed a living bond with the host tissue, without immune rejection. This gave rise to second generation of biomaterials (Hench 2006) and today, they are commercially available in the form of products such as 45S5 Bioglass® powder by NovaBone (Jones 2013).

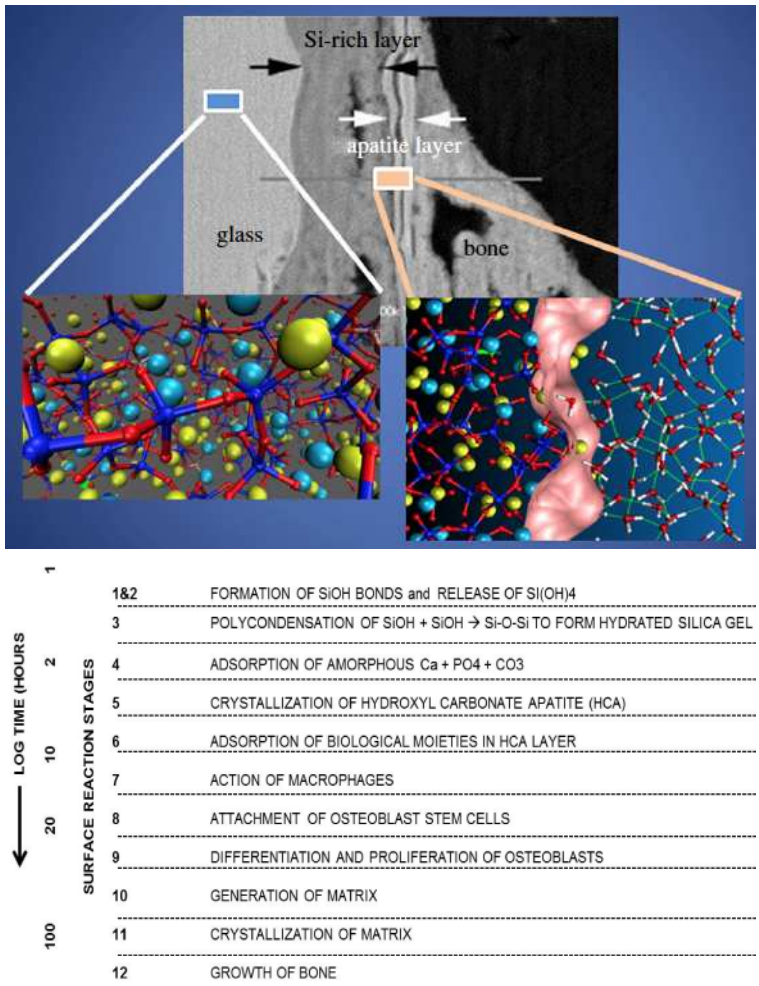

Figure 1-8: Mechanism of bioglass-tissue bond formation. Top: Scanning electron micrograph showing the interface between glass and bone with corresponding atomic models of bulk glass and the interface with liquid water. Bottom: 12-stage process of bond formation of Bioglass® with host tissue. Adapted from (Cormack & Tilocca 2012) and (Hench 2013).

Early *in vivo* investigations using the glass formulation of 45%SiO_2-24.5%Na_2O-24.5%CaO-6%P_2O_5 (mol%, 45S5 Bioglass®) provided the first evidence that small rectangular-shaped Bioglass® implants could form an interfacial bond with the bone in a rat femoral implant model after 6 weeks (Hench & Paschall 1973). To investigate the mechanism behind this bonding, *in vitro* tests were conducted. The authors suggested that the controlled release of Ca, P and Na ions from 45S5 Bioglass® surface, produced an alkaline pH. This induced development of an HA layer on glass surface that chemically bonded to the layers of collagen fibrils, which were produced at the glass-tissue interface by the osteoblasts (Hench & Paschall 1973). Follow-up studies in rat femur and tibia, canine femur, monkey bones,

primate and swine mandibular and maxillary bones, later helped to elucidate the underlying mechanism of *bioactivity*, which is described below and also in Figure 1-8.

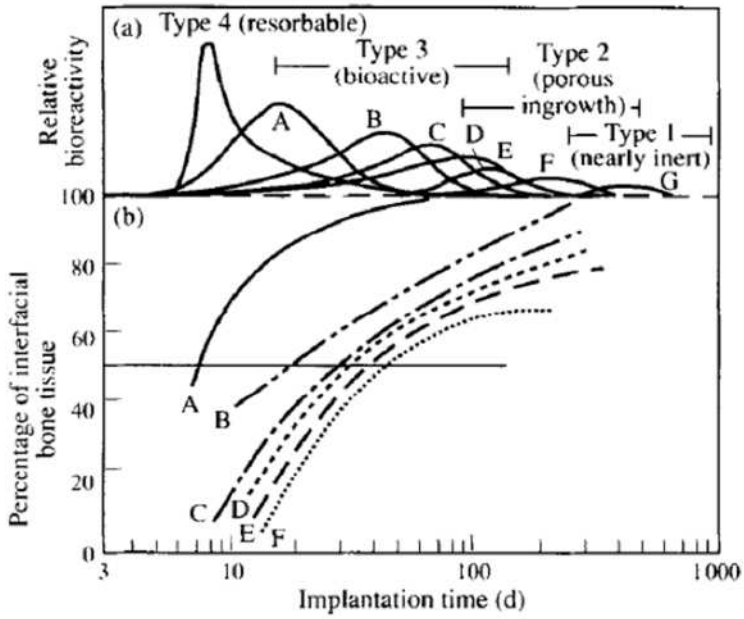

Figure 1-9: Bioactivity spectrum for bioceramic implants. (a) Relative rate of bioactivity and (b) time dependence of formation of bone bonding at an implant interface. (A) 4585 Bioglass‟, (B) Mina13 Ceravital®,(C) 55S4.3 Bioglass®, (D)A/W glass-ceramic, (E) HA, (F) KGy213 Ceravital®. Adapted from (Cao & Hench 1996).

Briefly, initial stages of bioactivity involve ion exchange of Na ions with proton and hydronium ions. The silanols formed undergo a condensation reaction forming a silica gel. In the next stage calcium and phosphorous from body fluids along with the ions released from the glass, form an amorphous calcium phosphate rich phase on the silica gel. The calcium phosphate crystallizes while incorporating carbonate ions from the solution to form polycrystalline hydroxyl-carbonate apatite (HCA) crystals that bond to collagen from the host tissue. This reaction layers of silica gel and HCA recruit growth factors and macrophages to prepare the site for tissue repair, paving the way for stem cell attachment, proliferation and differentiation into mature osteoblasts, which is absent on bio-inert materials due to lack of ionic stimuli. These osteoblasts release extracellular matrix, including collagenous proteins and finally mineralize this matrix, leaving mature osteocytes encased in a

collagen-HCA matrix (Hench 2013; Hench 2015). Based on the active bond formation with host tissue, biomaterials are now categorized as described in Figure 1-9.

Studies have shown that the bioactive glasses with low solubility, for example 45S5F (fluorine containing bioglass), completely separate from the bone after six weeks of implantation, as in the case of inert implant materials such as alumina (Karlsson & Hupa 2008). On the other hand, faster solubilizing bioglass ceramics such as 45S5 Bioglass®, with more surface activity, elicit a higher histological response and integrate better with the bone (Karlsson & Hupa 2008). For example, Oonishi et al. (1997; 2000) showed that 45S5 Bioglass®, porous apatite-wollastonite glass-ceramic and synthetic HAp, all granulated between 100-300 μm, had variation in bone formation in femoral rabbit model. The order of bone ingrowth rate into the spaces of three bioactive particles was Bioglass > A-W glass ceramic > synthetic HA at all time points up to 12 weeks and the resorption rate also followed the same order. In another similar study, Oonishi et al. (1999) also showed the bone formation was of order- low-crystalline HAp and OCP (orthocalcium phosphate) > TeCP (tetra calcium phosphate), TeDCPD (TeCP with dicalcium phosphate dihydrate), TeDCPA (TeCP with dicalcium phosphate anhydrate) > α-TCP, β-TCP and again this was also the order of resorption rate of these ceramics. Later, Fujibayashi et al. (2003) used $Na_2O–CaO–SiO_2$ glass system and showed that the depth of *in vivo* bone ingrowths among glass particles increases in proportion to the glass' capacity to support apatite formation *in vitro.* Together, these studies strongly suggest that the dissolution rate is a critical determinant for bioactivity and bone ingrowth.

Based on dissolution rate, glasses are further divided into two categories: Class A (up to 52% SiO_2, wt%)-both *osteoconductive* and *osteoproductive* materials and release ions such as Si^{4+}, Ca^{2+}, P^{5+} and Na^{+} at critical concentrations that give rise to both intracellular and extracellular responses at the interface of the glass with tissue; Class B (>52% SiO_2)- are *osteoconductive* but due to

slow dissolution rates and surface reactions, extracellular responses are limited to bone tissue only at the interface. These glasses do not bond with soft tissues and there is much delay in bond formation with bone as well (Cao & Hench 1996; Hench 2006; Hench 2013). Due to availability of a wide range of bone forming bioglass formulations, these bioglasses have been clinically used for a number of orthopaedics, craniofacial and dental-maxillofacial-ENT applications (Hench 2006; Hench 1991; Hench 2013).

1.6.1 Phosphate-based glasses

Phosphate-based glasses (PBGs) represent the next generation of bioactive glasses. Though the 45S5 Bioglass® is the benchmark for performance of silica-based glasses, there are now studies reporting issues with the long-term effects of silica (Anderson 2001; Abou Neel et al. 2009; Fu et al. 2012). For example, in a recent study, Fu et al. (2012) immersed 45S5 glass–ceramic MS (75–150 μm size range) for ten years at 25^0C in K_2HPO_4 solution with a concentration of 0.01 M or 1.0 M and starting pH of 7.0 or 9.5. They reported that after 10 years the conversion of these MS into HA-like material was incomplete and predicted that these MS may take up to 45 years to completely disappear from the body (based on a kinetic model of 45S5c conversion to HA at 37–60 ^{0}C).

Nagase et al. (1992) showed that the mortality rate of mice increased with increasing silica content from 0, 5, 10, 15 and 40-mole % in calcium phosphate glass within 30 days of implantation. They also showed that apatite-wollastonite glass ceramic inserted in C57BL/6, C3H and A/J mice (750 mg/kg) induced death in mice within 2 to 6 days and the reason for death was the material itself and not the supernatant of the ceramic powder (Nagase et al. 1987). During the same time period, Li et al. (1991) discovered that decreasing the Si content in bioactive glass powders (synthesised via sol-gel process) and increasing the CaO and P_2O_5 content in the same, resulted in enhanced rate of HA film formation in Tris-

buffered solution. These studies instigated a shift in the current research paradigm towards silica-free bioactive glasses.

More recently, the relationship between sintering window, composition and bioactivity has been understood (Jones 2013). The network connectivity should be ~2 for a glass to be bioactive, but conventional bioglasses such as Bioglass® have small sintering windows (Brink 1997), making it hard to process and fabricate these glasses in to 3D scaffolds (Hench & Jones 2015). One of the ways to increase the sintering window is by increasing the MgO, P_2O_5, B_2O_3 contents while decreasing Na_2O content in a silica-free glass system (Zhang et al. 2009) and PBG is an outcome of the same.

PBGs are currently under intense investigation as they are known to be highly tuneable in terms of their degradation properties and associated ion release (Knowles 2003). Similar to bioglass®, PBGs are also expected to make a mark in the domains of dental, maxillofacial and orthopaedic implants (Abou Neel et al. 2009).

PBGs are formed from inorganic phosphate-network linkages between the PO_4^{3-} tetrahedral units. The pure P_2O_5 can be introduced with oxides such as Na_2O, MgO, CaO, Fe_2O_3, B_2O_3, CuO, CoO, Al_2O_3, TiO_2, ZnO, AgO, Ga_2O_3 and SrO to produce PBGs of different compositions that vary in degradation rates, associated ion-release and bioactivity, depending upon the end application. Earlier studies mostly focused on binary and ternary PBG systems and with realisation of short degradation time scales of binary and ternary PBG systems with limited biocompatibility properties, the investigations shifted towards more complex, quaternary and quinary PBG systems.

In this PhD work, P_2O_5-CaO-MgO-Na_2O glass system with or without Fe_2O_3 has been used. Therefore, in the next sub-section, studies investigating role of CaO, Fe_2O_3, Na_2O and MgO in degradation and cytocompatibility of PBGs, have been reviewed.

1.6.1.1 Fe, Na and Mg containing PBGs

In $Na_2O–CaO–P_2O_5$ glass system, an inverse relationship between CaO content and dissolution rate is clearly seen, when P_2O_5 content is fixed at 45 mole% (Franks et al. 2000). Moreover, the glasses with lowest dissolution rate but with relatively more Ca^{2+} release rate, upregulated cell proliferation and expression of osteonectin, bone sialopeotein and fibronectin (Salih et al. 2000). Ahmed et al. (2004a; 2004b), exploring the characteristics of $Na_2O–CaO–P_2O_5$ glass fibers also showed that there was decrease in solubility with increase in CaO content. Gough et al. (2002) showed that the sodium phosphate (ternary) glasses have minimal macrophage activation and high osteoblast cytocompatibility.

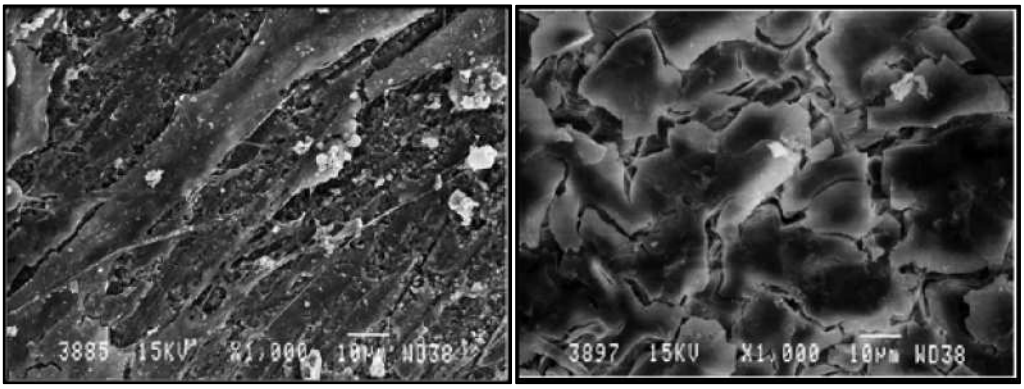

Figure 1-10: SEM image of human bone marrow stem cells cultured for 10 days on different ceramic materials. (A) Hydroxyapatite, (B) Phosphate-based glass ($50P_5O_5$-48CaO-$2Na_2O$ in mol%). The glass surface contains a number of cracks and has lost its integrity. As a result, there is absence of live hMSCs on glass surface. Scale bars- 10 µm. Adapted from (Skelton et al. 2007).

Skelton et al. (2007) used the P_2O_5(50)–CaO(50-X)–Na2O(X) system, where X is either 2, 4, 6, 8 or 10, and assessed the proliferation, differentiation and death of adult human bone marrow stromal cells and human fetal osteoblast 1.19 cells on these glasses. All formulations except with highest CaO mole% (called C48), exhibited high cell death compared to HA and tissue culture plastic after 10 days in culture, see Figure 1-10. Further investigation showed that there was significant appearance of cracks and peeling surface on PBGs and the C48 glass had deleterious effect on cells and their osteocalcin mRNA expression.

Franks et al. (2002) showed that introduction of MgO from 0 to 22% at fixed Na_2O and P_2O_5 mol% (23 and 45%, respectively) into the $Na_2O–CaO–P_2O_5$ system, led to decrease in the degradation rate of the glasses with increasing MgO content in a non-linear fashion. Moreover, increased MG63 proliferation after 5 days in culture was reported in case of medium eluted with 7mol% MgO or more. Knowles et al. (2001) also showed that increases in K_2O content in the $Na_2O–CaO–P_2O_5$ system, from 0, 15, 20 and 25 mole % at fixed P_2O_5 45 mol% and fixed CaO content at either 20, 24 or 28 mol%, resulted in an increase in the solubility of the glasses.

Lin et al. (1994) developed $Fe_2O_3–CaO–P_2O_5$ glass fibres of 20 μm diameter. These fibers displayed dissolution rates of 0.001, 0.0005 and 0.0001 μg mm^{-2} h^{-1} at pH 7.4 in PBS, with increasing Fe_2O_3 content from 5, 10 and 15 mol%, respectively, at fixed P_2O_5 mole% of 79%. Transplantation of these glass fibers in rabbit tibia showed no inflammation and very little bony ingrowth after 9 weeks. In another study Yu et al. (1997) developed P_2O_5-Fe_2O_3-Na_2O glasses and found that with increasing Fe_2O_3 and Na_2O content, the density of these glasses increased and thermal expansion coefficient and dissolution rate decreased. Mossbauer and XPS results indicated Fe(II) and Fe(III) both were present in glasses and durability improved with increasing Fe(III) concentration. This was attributed to the replacement of P-O-P bond by chemically resistant P-O-Fe(II) and P-O-Fe(III) bonds.

Since 1997, a number of other studies have now shown decrease in degradation rate of glass with increasing Fe content. For example, Parsons et al. (2004) showed that degradation rate in sodium iron phosphate glasses decreases with increase in Fe content from 1% to 15%. The authors also showed that glasses with ≤10% Fe degraded too quickly and in 15% and 20% Fe glasses, there was low macrophage activation, in addition to significantly lower osteoblast cells on 20% Fe glasses as compared to 15% Fe glasses. Ahmed et al. (2004) developed iron-phosphate glass fibres using $CaO–Na_2O–Fe_2O_3–P_2O_5$ system and showed decrease in dissolution rates for the

bulk glass and glass fibres with increase in CaO mol% (from 30, 35 to 40 %), along with an increase in Fe_2O_3 mol% (from 1, 2, 3, 4 to 5%). Biocompatibility studies using muscle precursor cells showed 4-5 mol% Fe_2O_3 in these glass fibers were more efficient in supporting cell attachment and differentiation into myotubes as compared to glasses with lower mol% Fe_2O_3.

More recently, Hasan et al. (2012) investigated six PBG formulations in the system P_2O_5-CaO-MgO-Na_2O-Fe_2O_3 with fixed Mg and Ca content at 24% and 16%, respectively and varying P_2O_5 and Fe_2O_3 content between 40-50% and 0-4%, respectively. They reported an increase in T_g (glass transition temperature) and decrease in degradation rate with increasing P_2O_5 and Fe_2O_3 content in the glasses. Cytocompatibility studies showed that MG63 cells grew on all formulations over 7 days in culture, except for on P50Fe4 glass, which had decreased cell growth after 2 days in culture. A decrease in alkaline phosphatase activity was also observed with increasing P_2O_5 and Fe_2O_3 content over 7 days in culture and when MG63 cells were grown for 24 h in medium conditioned with these formulations no cytotoxicity was detected.

1.7 Osteoinductivity of bioactive glasses

Though bioactive glasses have been investigated since 1969, it wasn't until the end of the century when the osteoinductive nature of Bioglass® was understood. One *in vivo* study that clearly demonstrated the osteopromotive nature of silica containing bioactive glasses was by Ylänen et al. (2000) cited in (Karlsson & Hupa 2008). He used flame sprayed α-wallostonite spheres (wt% 6 Na_2O, 11 K_2O, 5 MgO, 22 CaO, 1 B_2O_3, 2 P_2O_5 and 53 SiO_2) and sintered narrow fractions of the glass spheres (250-300 μm) to form porous, conical implants. This porous scaffold and a reference sample made from titanium were implanted into rabbit tibia. In the titanium implant, there was bone formation only after 12 weeks of implantation and in bioglass implant, the same happened after 6 weeks of implantation. Moreover, while the titanium implant showed

osteoconductivity, the bioglass implant showed both osteoconductivity as well osteoinductivity due to formation of bone in ectopic regions (see Figure 1-11).

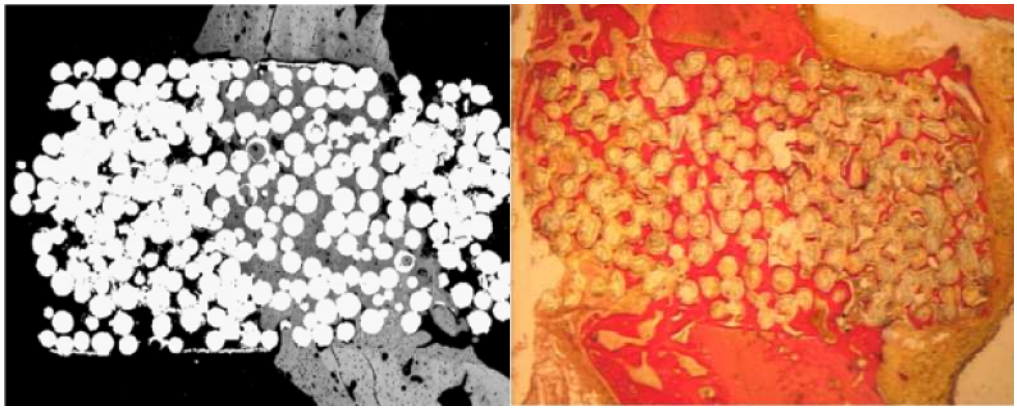

Figure 1-11: Osteoinductivity of bioglass. Optical micrographs of van Gieson stained porous titanium implant (top) and porous bioactive glass implant (bottom) after 12 and 6 weeks, respectively of implantation in tibia of rabbit. Adapted from (Karlsson & Hupa 2008).

Since then, several studies have tried to elucidate the molecular mechanisms behind osteoinductivity of bioactive glasses. Pioneering study by Xynos et al. (2000) showed the osteoinductive effect on Bioglass® compared to bioinert (plastic) substrates over a period of 12 days in culture *in vitro*. They found that the human primary osteoblasts had enhanced proliferation and osteoblastic differentiation markers such as ALP activity, osteocalcin with also presence of mineralised collagen matrix, over 12 days. In a follow up study, Xynos et al. (2000) studied the expression levels of insulin-like growth factor II (IGF-II), metalloproteinase-2 and cathepsin-D in human primary osteoblasts grown in medium conditioned with or without 45S5 Bioglass®. The results showed significantly higher expression of all three proteins in culture medium conditioned with bioglass and the ionic release from bioglass was held responsible for induction of osteoblast proliferation via IGF-II. In more extensive studies performed on different cell lines including primary human osteoblasts, foetal human osteoblasts, murine embryonic stem cells and human embryonic stem cells and also organ cultures of murine foetal long bones; gene array analyses suggested upregulation of genes

associated with transcription factors and cell cycle regulators, DNA synthesis, repair and recombination, apoptotic regulators, growth factors and cytokines, cell surface antigens and receptors and extra cellular matrix compounds, after exposure to medium conditioned with Bioglass® (Xynos et al. 2001; Hench 2009).

Since then, increasing number of studies have now shown that the released ionic products from bioactive glasses may play a critical role in osteopromotive nature of the bioactive glasses and this has been reviewed by Hoppe et al. (2011) and also in Table 1-1. Some of the released ionic species such as Si^{4+},B^{3+}, P^{5+}, Ca^{2+}, Na^{+}, Fe^{3+}, Fe^{2+} and Mg^{2+} are known to be of therapeutic value as they play a role in bone metabolism by acting as enzyme co-factors that influence various signalling pathways associated with bone tissue.

Table 1-1: Role of metal ions in bone metabolism. Adapted from (Hoppe et al. 2011) and (Beattie & Avenell 1992).

Ions	Function
Si^{4+}	It is essential for metabolic processes, formation and calcification of bone tissue Dietary intake of Si increases bone mineral density (BMD) Aqueous Si induces HAp precipitation $Si(OH)_4$ stimulates collagen I formation and osteoblastic differentiation
B^{3+}	It stimulates RNA synthesis in fibroblast cells Dietary boron stimulates bone formation
Ca^{2+}	It favours osteoblast proliferation, differentiation and extracellular matrix (ECM) mineralization It activates Ca-sensing receptors in osteoblast cells, increases expression of growth factors, e.g. IGF-I or IGF-II
P^{5+}	It stimulates expression of matrix gla protein (MGP) a key regulator in bone formation
Na^{+}	High salt intake is associated with risk of osteoporosis
Mg^{2+}	It stimulates new bone formation It increases bone cell adhesion and stability (probably due to interactions with integrins)
Fe^{3+}/Fe^{2+}	It is part of biosynthetic precursors of collagen Severe Fe deficiency leads to decrease in bone formation and bone resorption High iron dietary intake is associated with accelerated bone loss and risk of osteoporosis

1.8 Porosity as a strategy for bone tissue engineering

In the present work, development of novel porous PBG MS has been reported. Therefore, this section is dedicated to the current state of knowledge on porosity and its impact on bone formation in different biomaterial implants.

Porosity is the percentage of void space in a solid and is a morphological property that is independent of the material type (Karageorgiou & Kaplan 2005). There are two main components of porosity- pore size and pore interconnectivity, and both are essential for the bone healing process. Pore size directly relates to bone ingrowth, since it provides surface and space for cell adhesion and osteogenesis; while pore interconnectivity allows the cells to migrate and distribute evenly for efficient regeneration and repair, facilitated by vascularisation vital for nutrient supply (Mastrogiacomo et al. 2006).

Smart self-inducing biomaterials matrices with porosity are the hallmark of third generation biomaterial implants. The effect of porosity on bone formation is perhaps, best illustrated in studies comparing solid or smooth surfaced implants with porous implants. For example, Kuboki et al. (1998) investigated three forms of HA loaded with BMP cocktails- solid particles (SPHAP), porous particles (PPHAP), and coral-replicated porous tablets (coral-HAP); and implanted them subcutaneously into rats. They showed that both PPHAP and coral-HAP systems induced osteogenesis 2 weeks after implantation. However, no evidence of osteogenesis or chondrogenesis was observed in SPHAP. This indicated that the geometry of the interconnected porous structure in PPHAP and coral-HAP lead to osteogenesis, while the smooth structure and close contact of particles in SPHAP failed to promote the same.

In another study, Chang et al. (1998) investigated three different implants (10 X 6 X 5 mm)-Ti-6Al-4V smooth-sided implant, Ti

plasma spray–coated Ti-6Al-4V implant (coated layer had 380 μm pores and 58% average porosity) and open pore structure made from pure Ti (60% porous and 170 μm as average pore size). The implants were fitted in dog femoral condyles and after 24 weeks of implantation bone formation was assessed. The authors showed that the smooth lines implant did not integrate with the host tissue; in case of Ti plasma spray coated implants, there was thickening of lamellar bone; but in case of the open porous implant, abundant bone growth into the Ti fiber mesh was observed that resulted in the complete integration/fixation of the implant with the host tissue (see Figure 1-12).

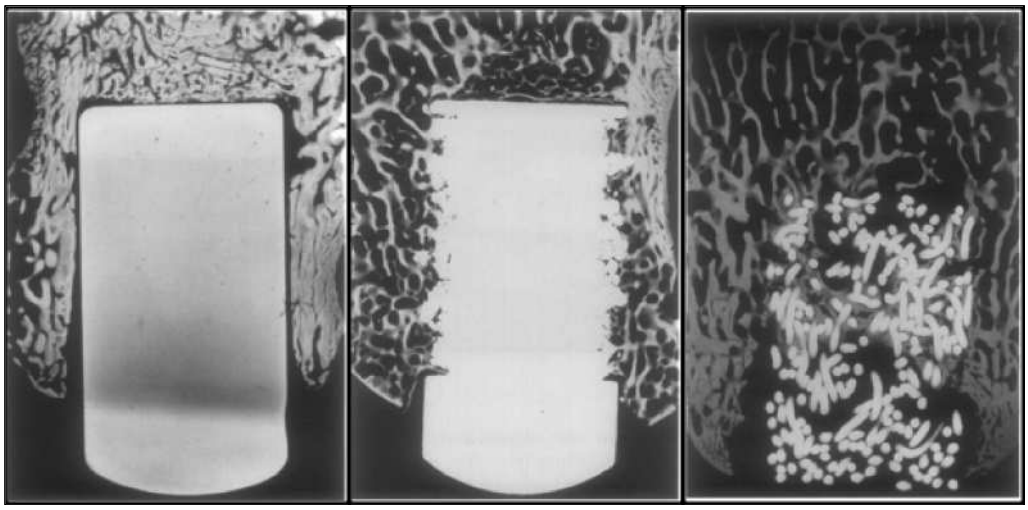

Figure 1-12: Effect of porosity on *in vivo* bone formation. Left to right: bone formation in smooth-sided Ti alloy implant, Ti plasma spray-coated Ti alloy implant and open pore structure pure Ti implant. Adapted from (Chang et al. 1998).

1.8.1 Bone formation in porous structures

Effect of porosity on osteogenesis is beautifully demonstrated in some of the studies that show ectopic bone formation in scaffolds. For example, Yuan et al. (2001) implanted cylindrical (5 X 6 mm) porous scaffolds (100-600 μm pore size range) made form 45S5 Bioglass® in dog muscles (n=16) and investigated *de novo* bone formation after 3 months. They found that the outer layer of the glass implants was only covered with connective tissue near the host tissue. However, there was substantial mineralisation with soft

tissue and bone vessel formation inside the inner pores of the scaffold. Yuan et al. (2001; 2002) showed preferential bone ingrowth (including Haversian system) in macropores of HA as well as TCP porous scaffolds (both with pores 100-800 μm wide and with 51 and 41 % total porosity, respectively) after 2.5 years of implantation in dog muscles. Le Nihouannen et al. (2005) also show ectopic bone formation only in the pores of biphasic calcium phosphate ceramic particles (1-2 mm diameter) after 6 months of implantation in back muscles of sheep. Furthermore, studies by Ripamonti (1996; 2003; 2009) also showed *de novo* bone formation preferentially in the porous spaces of coral-derived HA discs (200 and 500 μm pore size) when implanted in the *rectus abdominis* muscle of baboon for 90 days.

Preferential bone formation in pores has also been reported in metallic and polymeric implants. Fujibayashi et al. (2004) first reported bone induction in non-osseous site in dorsal muscles of mature beagle dogs by Ti metal porous blocks (300-500 μm pore diameter, 40% total porosity) and by Ti fibre mesh cylinders (250 μm fiber diameter and 50% total porosity) both in absence of osteogenic cells or osteoinductive agents. In the regions of new bone, they also showed that the lamellae structure were restricted to the inner surface of pores of the implant. When these porous Ti implants were implanted in rabbit femur, again bone ingrowth was observed inside the pore structures only (Takemoto et al. 2005).

Damien et al. (2003) implanted cylindrical porous hydroxyapatite (400-600 μm pore size range) implants with or without growth factor-I and also observed preferential mineralisation in the curvatures of the pores by osteoblasts in rabbit femur. Scarano et al. (2014) studied the bone response around the dental implants in rabbit tibia over 8 weeks. They used thread-shaped M implants (thread shaped- implants with screw-like threads; M-machine implant surface that has considered to have minimally rough surface) blasted with apatitic calcium phosphate particles and HA-coated implants made of Ti alloy. This suggested preferential bone

formation in concavities during early stages of bone repair because there was more bone formation in concavities compared to convexities of the implant after 1, 2 and 4 weeks of culture. Kim and Valentini (2002), developed hyaluronic acid derived porous scaffolds (80–90% porosity and pores range of 100 -600 μm) and used them as delivery vehicle for BMP-2 to enhance osteogenic differentiation by murine pluripotent cell line C3H10T1 *in vitro*. The results from SEM and fluorescent images taken over 28 days of culture, showed significant cell growth (T1/2 cells) near the curvatures of the pores.

Recently composite biomaterials have been used to develop 3D scaffolds incorporating all the advantages of the composite materials and effect of porosity has been demonstrated on these scaffolds as well. Attawia et al. (1995) fabricated 3D degradable biodegradable PLAGA-ceramic scaffolds (100 μm pore size) and seeded them with rat primary osteoblasts. The cells inside the scaffold expressed significantly higher ALP activity and osteocalcin after 7 days in culture as compared to control (Devin et al. 1996). Lew Androwski et al. (2003) investigated a bioresorbable bone graft substitutes made from the unsaturated polyester poly(propylene fumarate) mixed with varying ratios of autograft and pore sizes of 50 to 1000 μm. After 6-week implantation in rat tibia, they showed that amount of new bone formation was independent of the amount of autograft loading and report bone formation occurring primarily within pores. Some of these examples have been shown in Figure 1-13.

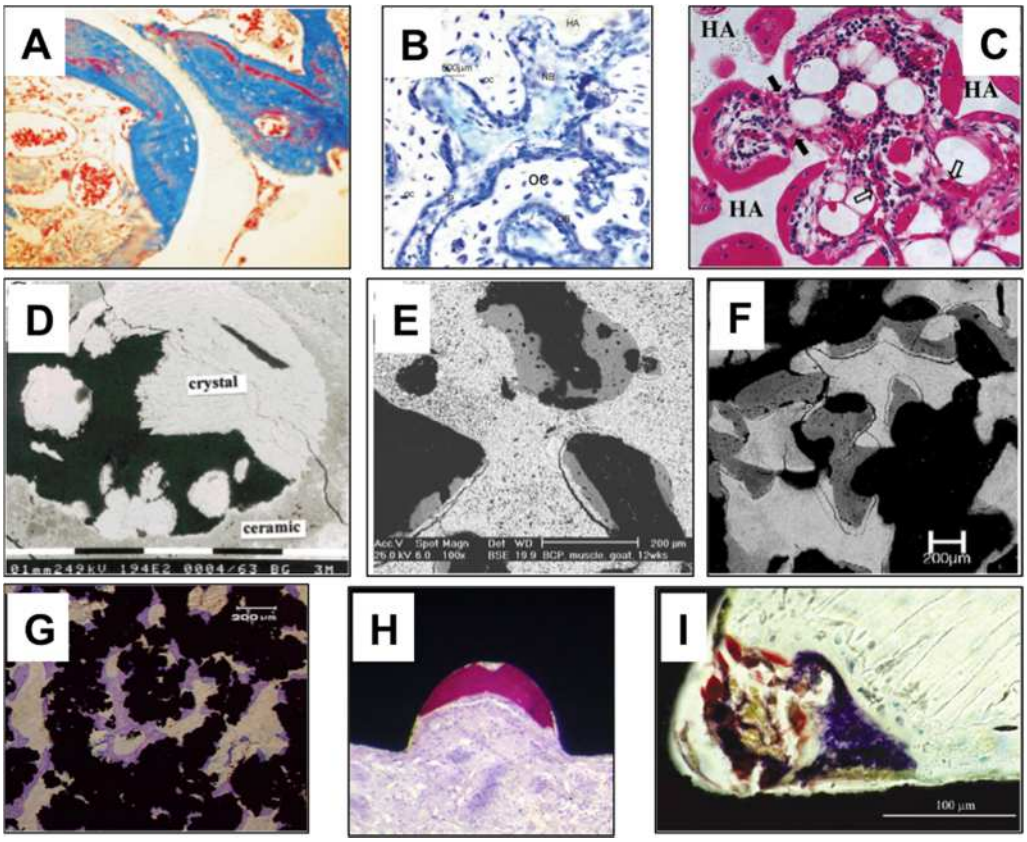

Figure 1-13: Examples illustrating the role of concavity in bone formation. (A) Porous HA matrices 90 days after implantation in the rectus abdominis muscle of adult baboons contain blue regions of newly formed bone (Ripamonti 2009), (B) IGF-I-treated porous HA-implant showing woven bone formation 3 weeks after implantation in rabbit femur. NB, new bone; OB, osteoblast; OC, osteocyte; P, primary bone. Scale bar 500 μm (Damien et al. 2003), (C) Photomicrograph (mag-X40) of interconnected porous calcium HA ceramic 6 weeks after implantation in rabbit femur. The newly formed bone is rimmed by cuboidal active osteoblasts through the interconnections (black arrows) and there is also presence of blood vessels (open arrows)(Tamai et al. 2002). (D) BSE image of the crystals formed in an inner pore after 3 months implantation of porous glass ceramic (prepared from bioglass®) in dog thigh muscles (Yuan, De Bruijn, et al. 2001). (E) BSE image of bi-calcium phosphate implants after 12 weeks implantation in sheep back muscles. Bar-200 μm (Yuan et al. 2002). (F) BSE image of bi-calcium phosphate granules after intramuscular implantation for 6 months into the back muscles of sheep. Bar-200 μm (Le Nihouannen et al. 2005). (G) Optical microscopy photograph showing massive newly formed bone with a lamella structure on the inner surface of the pores of bioactive titanium implant after 12 months implantation in dorsal dog muscles. Bar-200 μm (Fujibayashi et al. 2004). (H) Newly formed bone and many osteoblasts producing osteoid matrix directly on the surface of thread-shaped M implants, blasted with apatitic CaP, 4 weeks after implantation in rabbit tibia (magnification X100) (Scarano et al. 2014). (I) Alkaline phosphatase positive cells (blue) and Acid phosphatase positive cells indicate coupling status of bone remodeling in pore cavity of screw shaped Ti implant after 6 weeks implantation in rabbit tibia. Bar=100 mm. (Sul et al. 2002).

1.8.2 Optimal pore size for bone formation

The Table 1-2 details a list of various *in vivo* and *in vitro* studies performed on different biomaterials in order to determine the optimal range of pore size for maximum bone regeneration. Collectively these studies suggest the following:

(1) Except a few *in vivo* studies such as (Ayers et al. 1999; Flautre et al. 2001; Itälä et al. 2001; von Doernberg et al. 2006), the majority of the studies indicate that the larger the pore size, more is the bone ingrowth and blood vessel formation *in vivo*.
(2) There may be a minimum threshold of 30 μm, below which no bone formation or bone related marker expression takes place (Klawitter et al. 1976; Wilkinson et al. 2011).
(3) Overall, the optimal size range of pores for maximum bone formation and vascularisation is 100-750 μm and further increase in pore diameter does not significantly enhance bone infiltration (Bobyn et al. 1980; Hing et al. 1999; Kasten et al. 2008; Feng et al. 2011; Zhao et al. 2016).

Table 1-2: Studies investigating effect of pore size *in vivo* and *in vitro*.

Material	Pore sizes tested (μm)	Model	Time (weeks)	Optimal pore size	Observations and suggestions	Source
In vivo						
Calcium aluminate ceramic material	10-44, 44-75, 75-100 μm	Canine femur	4	75-100 μm	Connective tissue only in 10-75 μm pores, initiation of bone (osteon) in 75-100 μm pores.	(Hulbert et al. 1970)
Calcium aluminate ceramic material	44-75, 75-100, 100-150 and 150-200 μm	Canine femur	11	150-200 μm	- 10%, 50% and 50% calcified bone matrix in 75-100, 100-150 and 150-200 μm pores. - Order of lamellae and blood vessels formation: 150-200 μm>100-150 μm >75-100 μm pores.	(Hulbert et al. 1970)
Polyethylene rods (Porex Division, Glasrock Products, Inc., Fairburn, Ga.)	230-3,500 μm (mean values)	Femur of mongrel dogs	4, 8, 16	100-135 μm, with 40 μm as minimum threshold	- increase in bone formation with increase in pore size beyond 100-135 μm pores. -Atleast 8 to 16 weeks required complete infiltration of bone into pores of 100 μm.	(Klawitter et al. 1976)
Cobalt-base alloy spherical particles with porous surface	20-50, 50-200, 200-400 and 400-800 μm	Canine femurs	4, 8, 12	50-400 μm	- a pore size range of approximately 50 to 400 μm provided the optimum fixation strength (17 MPa) in the shortest time period (8 weeks)	(Bobyn et al. 1980)
Coralline hydroxyapatite bone substitutes	200 or 500 μm	Rabbit femur	12, 26	500 μm	- No new bone in 200 μm pores - 500 μm pores had substantial new bone.	(Kühne et al. 1994)
Biphasic calcium phosphate ceramic	300 or 565 μm	Rabbit femur	8	565 μm	- 565 μm peripheral or deep pores had new bone.	(Gauthier et al. 1998)
Hydroxyapatite (HA) scaffolds	500, 750 or 1500 μm	Rabbit femur	1.5	750 μm	Order of bone ingrowth was 750>1500>500 μm.	(Hing et al. 1999)
NiTi implants	353, 218 and 178 μm	Rabbit cranial bone	6	No difference	- no significant difference in the %age bone and void/soft tissue composition of the implants with different pore sizes.	(Ayers et al. 1999)
HA scaffolds	- Cylindrical-type parallel liner pores-50,	Rabbit tibia	4, 8	>300 μm	-50 μm pores supported only osteoconduction - more new bone and blood vessels in 300 and 500 μm cylindrical-type pores than	(Chang et al. 2000)

	100, 300 or 500 µm. - Sponge-type pores-250 µm - Cross-type linear pores-100 X 120 µm				sponge-type and cross type pores or smaller cylindrical-type pores.	
HA scaffolds	500 or 1500 µm	Rabbit femur	5, 13, 26	1500 µm	Bone ingrowth was lower in 500 µm pores on all time points.	(Hing et al. 2002)
Ti plates 250 or 500 µm thick	50, 75, 100 and 125 µm	Rabbit femur	12	No difference	-the median value for bone ingrowth varied between 64 and 78%.	(Itälä et al. 2001)
HA porous ceramics	175-260, 260-350 and 350-435 µm	Rabbit femur	12	No difference	-the occupied bone tissue volume (OBTV) inside pores had an inverse trend with pore size but there was no effect on the occupied mineralized bone tissue volume (OMBTV) inside pores	(Flautre et al. 2001)
HA and β-tricalcium phosphate (TCP) cylinders	45-80, 80-140, 140- 200, and 200-250 µm	Rabbit femur	16, 52	> 80 µm	-higher rate of bone formation in TCP than into the HA ceramics with the same pore size ranges. -45-80 µm pores have lowest new bone up to 120 days. -no differences were observed for large pore sizes until 4 months or 1 year.	(Galois & Mainard 2004)
β-TCP blocks	150, 260, 510 µm and 1220 mm	Cancellous bone in sheep	6, 12, 24	No difference	- specimens with 510 µm pores degraded faster than specimens with 150 and 260 µm pores. -The faster degrading specimens had lower bone content and a higher soft tissue content after 6 weeks only.	(von Doernberg et al. 2006)
biphasic calcium phosphate particles	40–70, 70–140, 140–210 and 210– 280 µm	Mice calvariae	4	>140 µm	-functional capillary density was higher in pores >140 µm. - Bone deposition increased with increasing pore size	(Klenke et al. 2007).
β-TCP scaffold	<5-50 µm (TCP	SCID Mice	8	TCP 65	- Scaffolds loaded with undifferentiated hMSC	(Kasten et

	25), <5-200 µm (TCP 65), 200-600 µm (TCP 75)	(subcutaneously)			were implanted -More ALP and protein content in TCP65, then TCP75 and least in TCP25 groups. -Higher calcification in TCP65 and TCP75 groups.	al. 2008)
porous TCP cylinders	300–400 µm, 400–500 µm, 500–600 µm and 600–700 µm	Bilateral perivertebral *fascia lumbodorsalis* in rabbits	8	> 400 µm	-more vascularization in scaffolds with pores > 400 µm.	(Feng et al. 2011)
In vitro						
β-TCP scaffold	<5-50 µm (TCP 25), <5-200 µm (TCP 65), 200-600 µm (TCP 75)	Human MSCs in osteogenic medium	3	TCP 65	-Higher ALP activity and protein content in TCP65 and TCP75 groups.	(Kasten et al. 2008)
collagen glycosaminoglycan scaffolds	85, 120, 164, 190 and 325 µm	MC3T3-E1 cells in normal growth medium	1	>325 µm	-cell number was also seen in scaffolds with a mean pore size of 120 µm at time points up to 48 hours post-seeding -cell proliferation was significantly higher on scaffolds with 325 µm pore size after 1, 2 and 7 days of culture. -improved cell migration provided by scaffolds with pores above 300 µm.	(Murphy et al. 2010)
Micropatterend topography polymethymethacrylate	pits of 20, 30 or 40 µm diameter and 300 nm depth	Human osteoblastic cells in normal growth medium	3, 4	30 µm	-higher nodule formation with positive osteocalcin in 30 µm pits than planar surface and other pits - thicker actin stress fibers with more intense vinculin staining was observed on pitted surfaces than planar surfaces	(Wilkinson et al. 2011)
Ti discs	312, 130 or 62	Osteogenic cells	2	62 µm	-order of cell proliferation (days 3, 7, 10) was	(Teixeira et

	µm	derived from human alveolar bone in osteogenic medium			312>130> 62 µm -order of *RUNX2, ALP, BSP, COL* and *OPN* expression was 62>130>312 µm (day 14)	al. 2012)
NiTi Alloys discs	277, 334 or 567 µm	Human osteoblast cells in normal growth medium	1.5	334 and 567 µm	- more cells present on discs with 567 and 334 µm pores. - all porous discs supported higher ALP activity compared to controls(cpTi or polystyrene plate)	(Jian et al. 2015)
3D porous PCL scaffolds subjected to hydrolysis (for 1 or 2 h) or aminolysis (for 0.25 or 2 h).	100–200, 200–300 and 300–450 µm	Human MSC in normal growth medium for growth studies and osteogenic /chondrogenic medium for differentiation studies	1	200-300 µm	-more growth on 200–300 µm pores with hydrolysis (1 or 2 h). - best osteogenic differentiation on 200–300 µm pores with hydrolysis for 1 h. -best chondrogenic differentiation on 300–450 µm pores with aminolysis for 1 h. -Synergetic effect of pore size and chemistry is suggested.	(Zhao et al. 2016).

1.8.3 Interconnectivity of pores

Some studies have also investigated effect of interconnectivity in bone formation. For example, Flautre et al. (2001) intensively studied the relationship between pore size and pore interconnection by testing bone formation in rabbit femur cancellous bone implanted for 12 weeks. They tested HA porous ceramics with four interconnection sizes (30, 60, 100 and 130 μm) at constant pore size of 175-260 μm. They reported that the occupied bone tissue volume (OBTV) inside pores had a linear trend with increasing interconnection size (see Figure 1-14) but this trend was not as robust in case of mineralised bone tissue volume (OMBTV) inside pores. The best osteoconduction was obtained in the centre of the ceramic by means of a 130 μm interconnection size.

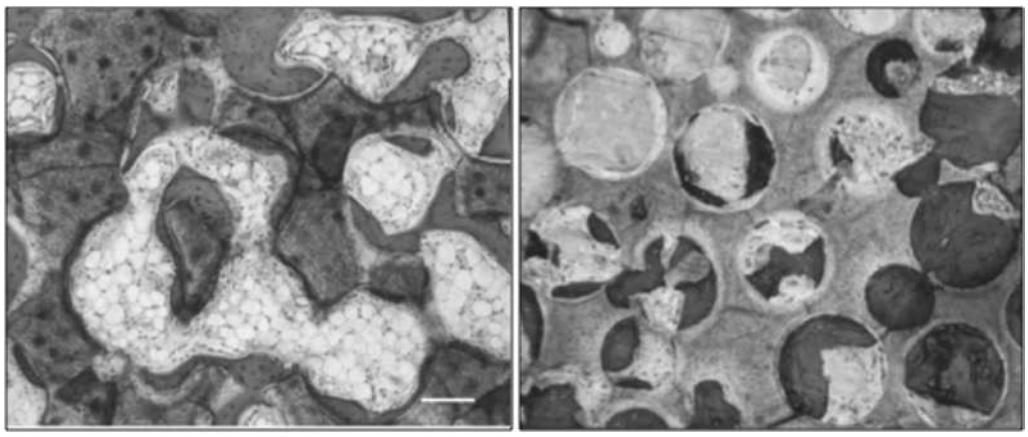

Figure 1-14: Effect of interconnectivity on *in vivo* bone formation. Stained sections (Picro-Fuschine van Gieson) after 12 weeks implantation in cancellous rabbit bone. The pore size in both sections are 175-260 μm and interconnection size is 130 μm on left and 30 μm on right (Flautre et al. 2001).

In an older study, Lu et al. (1999) reported slower osteoblast growth in HA and TCP porous discs (100-300 μm pores with 50-52% total porosity and 30-100 μm interconnections) compared to blank wells in normal growth medium over 31 days of culture. Moreover, significantly higher cells on HA discs (0.94 m^2g^{-1}) than on TCP discs (4.00 m^2g^{-1}) was seen only on the later time points of day 21 ad 31 of culture. The authors also reported preferential penetration of osteoblasts in interconnections over 40 μm (Lu et al. 1999). The

authors also inserted HA or TCP cylinders with same porosity characteristics in rabbit femurs for 12 and 24 weeks and found that '*interconnection density'* (the quantity of links between pores of porous materials) and pore density were more important factors than the size of the pores. They showed that a 20 μm interconnection size only allows cell penetration; however the size of the interconnections must be over 50 μm to favour new bone ingrowth inside the pores.

1.8.4 Porosity at the nanoscale

Many groups, for example Dalby 2007; Turner & Dalby 2014, have demonstrated that even nanotopographies (such as, created using electron beam lithography) in form of pits, grooves and columns; can affect cell characteristics including cell spreading, attachment, proliferation, centromere positioning and cell fate. However, most of these have been *in vitro* and on two-dimensional culture systems.

Cells have been seen to respond differently to different sized nano pits as well as to the order and symmetry of these nano pits. When fibroblast cells were seeded on nano pits with 35, 75 and 120 nm diameters, the cell spread area on 35 nm pits was same as that of planar control but significantly lower than in 120 and 75 nm pits. Moreover, mean number of filopodia was more on the surface with nano pits and showed a linear increase with increasing pit size (Dalby et al. 2004). Curtis et al. (2004) found significantly more cell spread in 120 nm pits (with 300 nm pitch) compared to orthogonally arranged 35 nm, 75 nm wide pits and hexagonally arranged 80 nm wide pits with 100, 200 and 300 nm pitches, respectively. Moreover, cell adhesion on nano-pitted surfaces was again found to be significantly lower when compared to planar surfaces. A later study showed that nano pits influenced osteoblast–substrate adhesion directly or indirectly by affecting adhesion complex formation, a phenomenon which is dependent on nano pit dimension and conformation (Biggs et al. 2006).

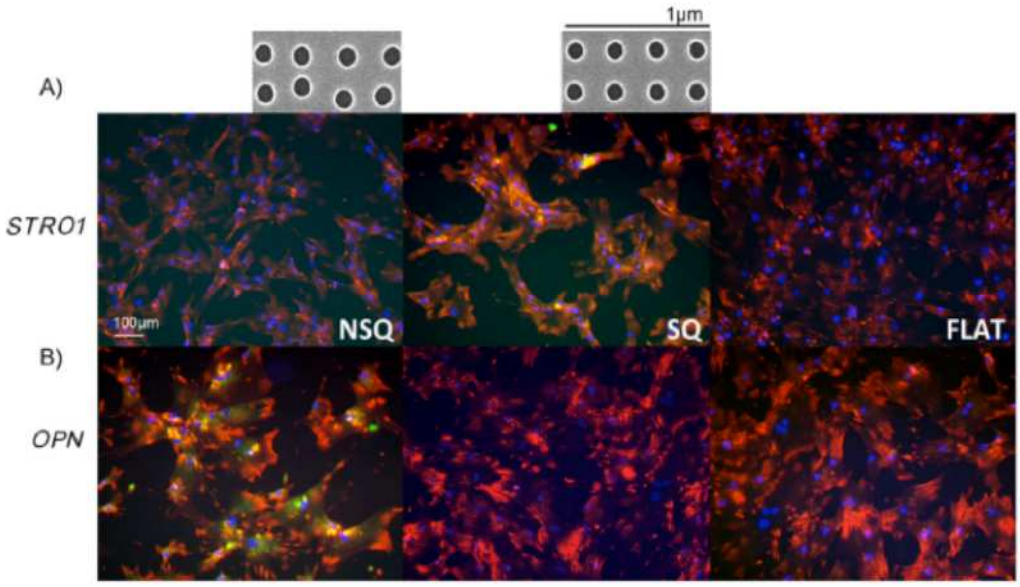

Figure 1-15: Effect of nano pit arrangement on hMSC fate after 4 weeks of culture. (A) Only hMSCs on the square nano-pit (SQ) configuration were STRO-1+. (B) Only hMSCs cultured on nearly square nano pit (NSQ50) configuration showed strong expression of osteopontin (OPN). Red-actin; green-STRO-1 or OPN; blue-nucleus (McMurray et al. 2010).

Cell fate is also affected by arrangement of same sized nano pits. Preliminary investigations showed that the expression of osteogenic markers such as osteocalcin and osteopontin, can be affected by semi-ordered and random nano topographies (Dalby et al. 2006). Later in a more intensive study, four nano pit configurations were compared to planar surface for human MSC response (see Figure 1-15). The nano pits were 120 nm in diameter (100 nm deep, 300 nm centre-centre spacing) and after 21 days of culture (in normal growth medium and in absence of non-osteogenic supplements), nodule formation with positive osteocalcin and osteopontin expressions, were observed on nano pits with near-square configuration but no on planar surface or surface with square, displaced-square and random-nano pit placements (Dalby et al. 2007). This osteogenic induction of near square configuration is not only seen in bone marrow derived MSCs but also from recently discovered MSCs from human olfactory mucosa (Johnstone et al. 2015). Further investigation showed that differentiation of skeletal cells on near-square nano-topographical structures is mediated via ERK signalling (Kantawong et al. 2009). On the other hand, the

more ordered square configuration has been shown to maintain the stemness character in MSC over prolonged cultures (up to 8 weeks), which was lost in case of planar surfaces during same time period (McMurray et al. 2011; Tsimbouri et al. 2013; Wang et al. 2014; Yang et al. 2014).

Another study by Ball et al. (2008) investigated the effect surface roughness and order of topographies present on Ti-alloy surface on osteoblast-like cells cultured in normal growth medium. They used Ti-alloy samples containing random discontinuities with roughness average, R_a=0.54 and 1.75 (created by bombarding them with 150–300 μm glass beads or 100 μm sized silicon carbide powder, respectively) and Ti-alloy samples with ordered grooves and R_a=0.49 (created by grounding on using 240 grade silicon carbide sandpaper) and compared them to relatively polished (planar) surface with R_a<0.05 (created by grounding on using 240 grade silicon carbide sandpaper and 1 μm grade diamond powder paper). These surfaces were further coated with 1 μm thick layer of hydroxyapatite to provide similar surface chemistry. The authors observed a decrease in cell proliferation by day 2 of culture (using Ki-67 immunostaining) and an increase in extracellular matrix formation (identified through type 1 collagen immunostaining) after 7 days of culture on the surfaces with random discontinuities as compared to other samples. This study combined with Dalby et al. (2005) strongly suggests that the random pit arrangements on polymeric or HA-coated surfaces created using photolithography or surface bombardment, may direct the cells towards differentiation and possibly osteogenic fate.

The effect of nanotopographies has also been demonstrated using 3D scaffolds *in vivo*. For example, Wang et al. (2013) developed four different bioglass scaffolds. Sample A- scaffold with nano-macro dual pores, sample B- scaffold with negligible nanopores, sample C- scaffold with nanopores but no macropores and sample D- scaffold with no nanopores or macropores. These disk-shaped scaffolds (12 mm diameter and 2 mm thickness) were implanted subcutaneous

into New Zealand rabbits and evaluated histologically after 1 and 2 weeks of implantation. There was significantly more penetration of cells into the macropores of sample A as compared to sample B after 1 and 2 weeks of implantation. Moreover, there was full integration of sample C to the surrounding tissue, however, interstitial spaces remained between sample D and surrounding tissue, indicating relatively poor scaffold integration. This study suggested that nanotopography alone can significantly affect the biological performance of engineered glass tissue scaffolds.

1.9 Concave/convex radii of curvature and cell morphology as critical determinant of MSC-fate

Lo et al. (2016) recently investigated the effect of monodispersed pores and homogeneous spherical geometries using 3D scaffolds (made from gelatin) with four different mean pore diameters, 47±2 μm (Group I), 84±11 μm (Group II), 148±7 μm (Group III) and 199±9 μm (Group IV). The ratio of surface negative curvature (curvature of concave surfaces) was 12:6:4:3, respectively and all four types of scaffolds had same porosity of 70±2%. The authors showed that the MSC viability was similar in all four scaffolds (98-99%) and in the same range as 2D flat gel (98%), after 1 day of culture in normal growth medium. Thus, the concave radius of curvature did not have an effect on the cell survival. A similar pattern was also observed through the MTS assay on day 1, 2, 3, 4, and 5 of culture in the 3D scaffolds. However, cell morphology analysis revealed that the MSCs in Groups II and III were stretched and elongated, had significantly higher aspect ratio of 8.9 ± 2.7 and 9.1 ± 2.2, respectively, with p-myosin and FA (focal adhesion) sizes at the extreme ends of cell body. On the other hand, the MSCs in Group IV were flattened and attached to the walls with reduced an AR value of 6.6 ± 2.3 and MSCs in Group I had a nearly spherical shape with a small AR of 2.1 ± 0.4. There was also 1.5- to 2- fold higher alkaline phosphatase activity, *Runx2, Col1A1* and *osteonectin*

expression, in addition to mineral deposition, in Groups II and III as compared to Groups I and IV, over 28 days of culture in osteogenic medium. This suggested that concave radius of curvature in Groups II and III had greatest potential to accelerate osteogenic differentiation of MSCs. This hypothesis was also strengthened by higher expression of vinculin and F-actin, in addition to *a2* and *a5 integrin*s, in MSCs present on Groups II and III.

Werner et al., (2016) recently designed cell substrates with containing convex and concave spherical structures with diameters ranging from 250 μm (principle curvature (κ) = 1/125 μm^{-1}) to 750 μm (κ = 1/375 μm^{-1}). Human MSC migration speed on concave spherical surfaces (3.7±0.2 nm s^{-1}) was significantly cell higher than on convex (2.8±0.3 nm s^{-1}) structures and cell flat surfaces (2.7 0.3 nm s^{-1}). The authors hypothesised that this increase was due to a peculiar cell movement observed in concave structures resulting from an upward-lift of the cell body that minimised the contact area with the substrate. These observations are also in line with the chord model presented by Bidan et al. (2013; 2013a), that defines cells as tensile elements that are stretched upward between the focal adhesions on concave surfaces, while being pulled downward toward the surface on convex substrates. Werner et al. also go on to show that osteocalcin expression was highest in convex surfaces (350 μm diameter) as compared to concave (350 μm diameter) and flat surfaces, despite lower/weak F-actin intensity on the same convex surfaces. Moreover, the osteocalcin expression increased with increase in surface curvature (convex as well as concave) on day 10 of culture in osteogenic or normal culture conditions.

The work from above two studies can be directly correlated to some of the older studies by McBeath et al. (2004) and Kilian et al. (2010), who cultured MSCs on micropatterned surfaces and investigated the effect of cell morphology on MSCs fate at single cell level. They showed that cells with rounded morphology (such as with radius of curvature as 6 μm) undergo adipogeneisis, while the

cells with spider-like extended morphology, under go osteogenesis; when hMSCs are grown in medium containing 1:1 ratio of osteogenic and adipogenic factors. It has been hypothesised that the geometric features (membrane curvatures) that increase acto-myosin contractility in MSCs (increased expression of myosin IIa), similar to *in vivo* environment, promote osteogenesis over adipogenesis (see Figure 1-16). This is attributed to c-Jun N-terminal kinase (JNK) and extracellular related kinase (ERK1/2) activation in conjunction with elevated Wnt signalling, a RhoA-independent mechanism for osteogenesis (Kilian et al. 2010).

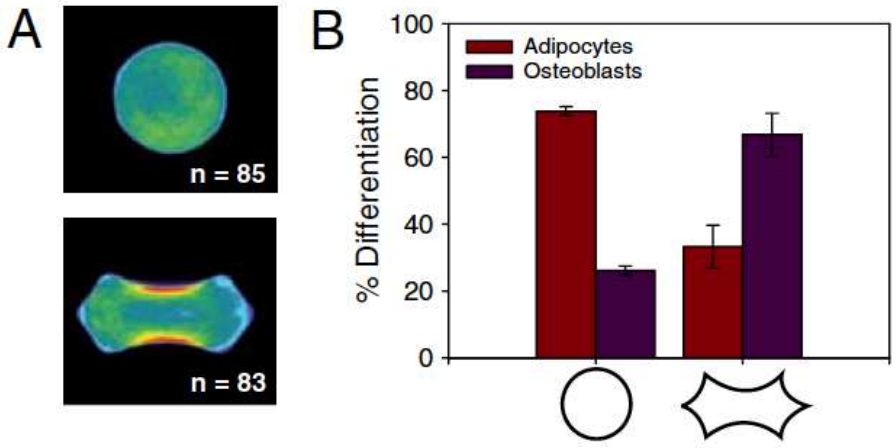

Figure 1-16: Effect of cell morphology on hMSC fate. (A) Myosin IIa immunofluorescent heat maps of >80 cells cultured in circles or holly shapes (micro-patterns). (B) Corresponding differentiation of cells in both shapes after exposure to mixed media containing both osteogenic and adipogenic induction factors. Taken from (Kilian et al. 2010).

Other than MSCs, effect of cell morphology and radii of curvature is also illustrated on chondrocytes (terminally differentiated cells that produce and maintain cartilage matrix and are difficult to expand *in vitro* due to their ability to dedifferentiate on 2D). Yuan et al. (2015) developed biomimetic collagenous ‘‘basket’’ enveloping individual chondrocytes within the circular patterns having diameters of 20, 40, and 80 μm. The cell spread was inversely proportional to the radius of curvature, with significantly higher collagen II in 40 μm patterns compared to 20 and 80 μm patterns and unpatterned substrates. They also showed that the cells in 40 μm patterns maintained a constant cell volume (after an initial decrease), which

may be due to their flexible cytoskeleton, enabling these cells to modulate the matrix tension toward chondrogensis. It was observed that in 40 μm patterns, previously dedifferentiated cells, redifferentiated into chondrocyte phenotypes, which was attributed to the deposited collagen II matrix in those patterns that created more physiological-like microenvironments, enhancing the retaining and regaining of differentiated phenotype.

All these studies strongly indicate a role of radii of curvatures, resulting cell morphology and MSC fate.

1.10 Two-dimensional and three-dimensional culture systems

Many cell-based studies are performed by growing cells as monolayers. However, one of the drawbacks of this methodology is the resulting cell environment that does not truly represent the *in vivo* conditions and may be leading to changes in the cell behaviour.

Cells adhere to their matrix via integrins, which forms a link between the ECM and the acto-myosin cytoskeleton present inside the cell and enable the bi-directional transmission of forces across the plasma membrane (Evans & Calderwood 2007; Harburger & Calderwood 2009). Each of these molecules, contain two heterodimeric transmembrane glycoproteins called the α and β subunits. The extracellular integrin domain binds to the tripeptide sequence arginine-glycine-aspartic acid (RGD), in the other ECM proteins such as fibronectin, vitronectin, fibrinogen or laminin. On the other hand, the intracellular domains bind to the focal adhesion protein network consisting of talin, tension, vinculin, α-actinin, paxillin, FAK (focal adhesion kinase), which are further connected to the acto-myosin cytoskeleton (Berrier & Yamada 2007; Brüggemann et al. 2014).

The idea of comparing 2D (monolayers) and 3D (three-dimensional) geometries arises on the basis of integrin-mediated adhesions to the

extracellular matrix (ECM), see Figure 1-17. In 2D, the cell adheres to the underlying matrix on one plane of the cell but in 3D, adhesion is across a number of planes (Baker & Chen 2012). This affects cell morphology, which leads to differences in organisation of plasma membrane, cytoskeletal architecture, nucleus structure and position as well as motility. These changes ultimately lead to different cell fates via changes in signalling pathways (Abbott 2003; Lutolf et al. 2009; Baker & Chen 2012).

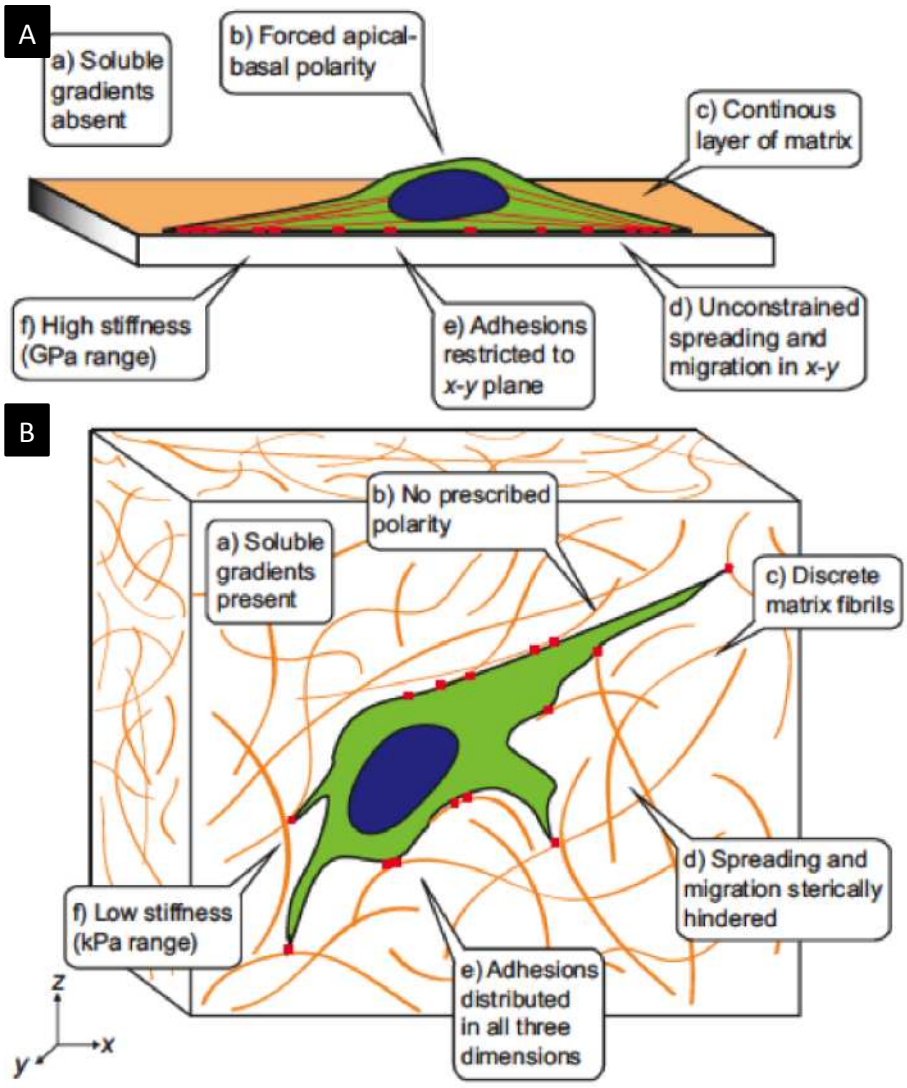

Figure 1-17: Adhesive, topographical, mechanical, and soluble cues in (A) 2D and (B) 3D. The cues encountered by a cell are strikingly different between the two systems. Adapted from (Baker & Chen 2012).

In the last two decades, there has been a growing body of evidence that demonstrates notable differences between the 2D and 3D culture systems effecting gene expression which ultimately affects

cellular responses such as proliferation, viability and differentiation (Wang et al. 1998; Weaver et al. 1997; Abbott 2003; Pampaloni et al. 2007).

Effects of 3D culture environments were initially encountered in cancer biology. For example, growth of human breast tumour cells was arrested due to down-modulation of β1-integrin signalling only in 3D basement membrane assay and not in monolayers (Wang et al. 1998). Sung et al. (2013) more recently demonstrate that human mammary fibroblasts secrete more paracrine factors in 3D than in 2D and these factors are capable of increasing the invasive behaviour of breast cancer cells.

The difference between 2D and 3D cell culture systems has also been demonstrated in cell motility. On 2D matrix, cells are known to undergo lamellipodia-based movement, propagated by actomyosin contractility, after polarisation and adhesion of cells to matrix. However, there is another type of cell movement in 3D that is absent in 2D, and is called high-pressure migration (Petrie & Yamada 2015). It relies on formation of a high intracellular pressure that is created towards the front of the cell.

Considerable progress has also been towards developing *in vitro* models of whole-organ development mimicking intestine, pituitary, retina and brain *in vivo* environments. Lancaster et al. (2014) recently developed cerebral organoids that model human brain. These organoids contained discrete and interdependent brain regions, including cerebral cortex, that displayed an organisation similar to the early developing human brain, i.e., characteristic progenitor zone organization with abundant outer radial glial stem cells, which is not reported in a 2D set up yet.

Human MSCs, which are currently the most lucrative source of regenerative cells due to their self-renewal and multipotent regenerative capacity, are also responsive to 2D and 3D environments. For example, Wang et al. (2009) used a uniformly

engineered 3D spheroid system where cells were cultured on patterned micro-domains of 100 µm coated with photosensitized poly(ethylene glycol) and investigated the adipogenic and osteogenic differentiation efficacy of 3D spheroids of MSCs in induction medium. After 26 days of culture, 100% MSCs on 3D spheroids (even at the core) showed positive staining for Nile Red staining whereas only 22±5% of cells in 2D stained positively. After 16 days of culture, almost all cells in 3D spheroids stained positive for alizarin red but in 2D, the number of positive cells was again significantly less. Gene expression through RT-PCR studies also showed nearly 2-fold (Day 1) and 14-fold (Day 6) increase in PPAR-γ and 3-fold (Day 1) and 4-fold (Day 6) increase in Runx2. Moreover, oligo DNA microarray analysis showed higher low-density lipoprotein receptor-related protein 2 precursor, fatty acid- binding protein, lipoprotein lipase, adipophilin expressions in adipogenic induction medium and alkaline phosphatase, Bone morphogenetic protein 2, osteopontin and SOX9 in osteogenic induction medium in 3D spheroids than in monolayers.

Thus, there is considerable evidence generated across different cell biology domains that clearly indicate significant differences in 2D and 3D culture systems. These studies provided the impetus for this study to investigate the differences between MSCs in monolayers (2D) and microsphere 3D system.

1.11 Microspheres as a 3D substrate for cells

Microsphere (MS) or microcarrier culture systems came into prevalence when the two-Dimensional (2D) *in vitro* culture system was identified to be inefficient to suffice the growing needs of clinical applications in terms of cell numbers (Malda and Frondoza, 2006). Since the invention of microcarrier system in 1967 by van Wezel (van Wezel 1967), this system has been used for mass production of viral vaccines and biological products using mammal cells (Giard et al. 1977), as it makes cell expansion cheaper by providing enhanced surface area compared to 2D. For example, 3 g of 150-200 µm

sized-smooth plastic microcarriers (SoloHill, USA) or 1 g of 200-280 µm sized Cytopore 1 porous microcarriers (made of cellulose) provide surface area comparable to fifteen 75 cm^2 culture flasks and a simple microcarriers suspension culture can yield up to 200 million cells per ml using non-porous Cytodex microcarriers (GE Healthcare) (Malda & Frondoza 2006). For these reasons, MS in stirred suspension bioreactors are commonly used for large scale mammalian stem cell expansion for transplantation purposes (Jung et al. 2012; Panchalingam et al. 2015). A wide variety of microcarriers are now commercially available for a variety of biological products at the analytical and industrial scales (Malda & Frondoza 2006). Some of the commercially available MS for cell expansion are given in Table 1-3.

Other than cell cultivation, MS are now being tested for applications in cell delivery, drug delivery and defect filling (Park et al. 2013). They can be easily injected into the defect using a syringe for targeted cell-therapy with minimal invasive procedures (Saralidze et al. 2010; Park et al. 2013). Examples of some commercially available MS used as fillers are Cerasorb® (β-TCP), Hydros (brushite calcium phosphate) and Calcibon® (precipitated HA).

Some studies have reported development of more complex MS such as dexamethasone (DEX) loaded poly(lactic- co -glycolic acid) (PLGA) MS coated with Arg-Gly-Asp (RGD) peptide and bone morphogenic protein 2 (BMP-2) for MSC based-osteogenic repair *in vivo* (Park et al. 2010); DEX-loaded PLGA MS coated with basic fibroblast growth factor (bFGF)-loaded nanoparticles for dual release of growth factors *in vivo* for the purpose of MSC differentiation into nucleus pulposus-like cells and also to reduce the inflammatory response for intervertebral disc tissue engineering (Liang et al. 2012); glucose containing alginate MS for prolonging the viability of MSCs in suspension cultures (Gálvez et al. 2014); bioactive glass MS (BGMs) for bone tissue regeneration using MSC (Lei et al. 2011); injectable collagen MS encapsulating MSC for bone regeneration (Chan et al. 2010) and titanium PBG MS as a bioreactor substrate

for large scale cell expansion and guided differentiation of MSC (Lakhkar et al. 2012). These research studies reflect the application potential of MS culture system in stem cell therapy, tissue engineering and regenerative medicine.

1.11.1 Microspheres for bone tissue engineering

The numbers of studies reporting development of bulk, porous and hollow MS have significantly increased this century. They have been developed from ceramics, polymers, glasses as well as composite materials. They offer different advantages based on their size, surface area, porosity, surface characteristics and degradation rate. Where polymer-based MS have largely been investigated for drug release and as delivery vehicles for therapeutic components such as BMPs, most of the MS studies for bone tissue engineering are based on ceramic, composite and glass materials. Some of them have been reviewed below.

Table 1-3: Summary of commercially available MS for cell expansion (Malda & Frondoza 2006).

Name	Company	Size (μm)	Surface area (cm^2g^{-1})	Pores	Material
Cytodex 1	Amersham Biosciences, Sweden	147–248	4400	–	Dextran matrix with substituted N, N-dimethylamino ethyl groups
Cytodex 2	Amersham Biosciences, Sweden	135–200	3300	–	Dextran matrix with a surface layer of N,N,N-trimethyl-2-hydroxyaminop ropyl groups
Hillex	SoloHill, USA	150–210	350	–	Dextran matrix with treated surface
Plastic coated	SoloHill, USA	150–210	380	–	Plastic coated with denaturated collagen
PlasticPlus coated	SoloHill, USA	150–210	380	–	Plastic coated with denatured collagen, promoting fast

					attachment
Cytoline 2	Amersham Biosciences, Sweden	400–2500	>1000	+	Polyethylene and silica
Glass-coated	SoloHill, USA	150–210	380	–	Plastic with glass coating
Cytopore 1	Amersham Biosciences, Sweden	200–280	~1200	+	Cellulose
Cultispher G	Percell Biolitica, Sweden	130–380	n/a	+	Cross-linked porcine gelatin
Cultispher S	Percell Biolitica, Sweden	130–380	n/a	+	Cross-linked porcine gelatin
Cytodex 3	Amersham Biosciences, Sweden	141–211	2700	–	Dextran matrix with thin layer of denatured pig skin-derived collagen
Cellagen	MP Biomedicals, USA	100–400	n/a	+	Highly cross-linked bovine collagen type I

1.11.1.1 Ceramic and composite microspheres

The majority of the MS developed for bone repair have been made from HA-based materials. Fischer et al. (2003) first reported development of dense (non-porous) and microporous HA spherical particles and seeded them with goat bone marrow derived MSCs. After 7 days in osteogenic medium, the particles were then implanted in subcutaneous pockets at each side of the spine for 4 weeks. The *de novo* bone formation was abundant in the case of dense or microporous particles (212-300 μm) with no significant differences between them and no bone formation was seen in case of dense 500-716 μm particles. Moreover, microporous HA MS were also found to be associated with macrophages and multinucleated cells absent in all other conditions. *In vitro* assessment showed slower cell growth on microporous particles compared to dense particles on day 4 and 7 of culture in osteogenic medium but no difference on days 12 and 20 of culture. Barrias et al. (2004) also

reported fabrication of HA MS with 550 μm mean diameter and microporosity less than 5 μm. Human osteoblast-like MG63 cells showed efficient adherence and viability over 7 days culture in normal growth medium on these MS. Sun et al. (2009) developed hollow HA MS (mean size 5 μm) by using a simple spray drying method. They used ammonium bicarbonate as a porogen, which produced carbon dioxide and ammonia gas bubbles during the spraying, and thus created a hollow inner structure in the resultant MS with open pores (0.2–1.5 μm) on their surface.

Composite HA MS have also been widely reported. The following are examples based on ceramic and synthetic or natural polymers: Devin et al. (1996) fabricated porous MS composed poly(lactide/glycolide) reinforced-calcium phosphate cement with interconnected pores of approximately 100 μm diameter. Four polymer/ceramic ratios were used in matrix fabrication: 1:0, 1:1, 2.5:1, and 5:1 and increased HA matrix content from 0% to 50% translated into increased compressive elastic moduli from 0.30 X 10^3 MPa to 1.46 X 10^3 MPa and decreased rates of matrix degradation from 50% to 20%, respectively. Due to their macroporosity and cytocompatibility, these MS were suggested for bone repair applications.

Fluorine ions in HA structure stimulates bone cell proliferation and increase new mineral deposition in cancellous bone; hence, Komlev et al. (2003) developed porous HA-fluorapatite MS with 50-200 μm diameter and 43-62% porosity. Granja et al. (2004) used a combination of chitosan and HA to develop MS (200-500 μm) with varying porosities. Increased HA content led to decreased pore size but increased the MS size and homogeneity in size distribution. Wu et al. (2004) also developed HA MS with reconstituted fibrous collagen, which allowed the growth of osteoblast cells for 8 days in culture. Barrias et al. (2005) developed calcium titanium MS (550 μm mean diameter and microporosity less than 5 μm) that showed higher ALP and osteocalcin expression by bone marrow stromal cells over 3 weeks compared to tissue culture plastic MS (250 μm mean

diameter). Perez et al. (2011) developed HA and gelatin/HA MS using water oil emulsion of a calcium phosphate cement (CPC) to form entangled network of HA crystals with pore sizes 0.5-5 μm and Saos-2 cells showed enhanced adhesion and proliferation over 14 days of culture in case of gelatin/HA MS as compared to HA MS.

In more recent years, Park et al. (2014) fabricated calcium phosphate cement and alginate MS which allowed osteoblastic cells to be cultured on their surface with an active proliferative and osteogenic potential during 14 days of culture. Soriano-Souza et al. (2015) developed Chlorhexidine-loaded HA MS as an antimicrobial delivery system and studied their *in vivo* response in rat calvarial tissue after 7 and 21 days of implantation. These MS were toxic to osteoblast cells at higher concentrations of chlorhexidine and prevented bone formation *in vivo*. A threshold of 0.9±0.17 μg CHX/cm^2 HA was identified to balance the anti-microbial activity and *in vivo* bone formation. Xiong et al. (2015) developed BMP2 leaded hollow HA MS (100 μm) and showed enhanced osteoinduction and osteogenicity in large bone defects in rats compared to unloaded HA MS.

Altogether HA and HA-based MS come in ranging size, porosity and osteoconductive properties and offer advantages such as ease of injection via minimal invasive procedures, these materials are slower degrading and less bioactive than the glass materials (Cao & Hench 1996) and also involve time-consuming and expensive manufacturing processes (Hossain et al. 2014).

1.11.1.2 Polymer-based microspheres

Polymer-based MS have received considerable attention due to their controlled drug release characteristics either by leaching the drug components from the polymer or by degradation of the polymer matrix (Kim & Pack 2006; Hossain et al. 2014). The natural polymers such as collagen, alginate, etc. undergo degradation either due to enzymatic activity and synthetic polymers such as polylactic

acid (PLA), polycaprolactone (PCL), polyglycolic acid (PGA) and polylactic-co-glycolic acid (PLGA) undergo degradation due to hydrolytic activity. A number of methods have been used to fabricate polymer MS including emulsion-solvent evaporation, spray drying, electro-spinning, gelation followed by emulsification, suspension polymerisation, ultrasonication and phase separation for a number of biomedical applications as reviewed by Hossain et al. (2014).

As example, Kim et al. (2006) fabricated open porous (pores up to 25 μm) biodegradable PLGA MS (200-800 μm) using water-in-oil-in-water double emulsion solvent evaporation method. NIH3T3 cells were homogeneously adhered onto the surface in the early culture period and entered the porous structures after 7 days. Bock et al. (2011) developed non-porous PCL MS (10-20 μm diameter) using electrospraying method. They showed highly spherical morphology and homogeneously embossed texture and their degraded products were non-cytotoxic. Patel et al. (2008) investigated the effects of controlled dual delivery of vascular endothelial growth factor (VEGF) and bone morphogenetic protein-2 (BMP-2) for bone regeneration in a rat cranial critical size defect using spherical gelatine microparticles in poly(propylene fumarate) scaffolds. Histological analysis showed significantly higher bone formation with vascularisation over 12 weeks of implantation in case of these MS as compared to other control groups.

Despite significant success in development of polymeric MS, they often have too low an elastic modulus for bone applications, for example, PDLLA (film or disk), PLLA (film or disk), PGA (fibre), PLGA, poly(anhydrides) and poly(ortho-esters) have modulus of 1.9-2.4 GPa, 1.2-3.0 GPa, 7-14 GPa, 1.4-2.8 GPa, 0.14-1.4 GPa, 2.5-4.4 GPa, respectively (Rezwan et al. 2006); release cytotoxic debris, crystalline by-products and acidic degradation products (Saralidze et al. 2010) and also cause inflammatory response dependent on their rate of release of acidic by-products (Vacanti et al. 1988).

1.11.1.3 Glass microspheres

Bioactive glasses have potential for bone repair applications due to their *osteoconductive*, *osteostimulatory* and *osteoinductive* properties (Hench 2006). A number of studies have reported development of MS made from silicate-based glasses, phosphate-based glasses and borate-based glasses (Gerhardt & Boccaccini 2010; Rahamana et al. 2013; Jones 2013; Hossain et al. 2014). The common methodologies used to manufacture glass MS include dropping crushed glass particles down a vertical tube furnace, pouring molten glass onto stainless steel plates to create droplets, sol–gel method and spray drying of sols and via the flame spheroidisation process (Hossain et al. 2014).

These MS have been explored and tested in a number of *in vivo* and *in vitro* environments. For example, Ylänen et al. (2000) developed bioglass MS with diameter of 250-300 μm and sintered them to generate porous scaffolds. They reported double rate of silica-rich layer formation on MS compared to flat surfaced same glass. Itälä et al. (2003) also fabricated smooth and microroughened surface bioactive (13-93) glass MS (215–350 μm) and tested their *in vivo* response in rat tibia after 1, 2 and 8 weeks. The results showed that microroughened bioactive surface could enhance the expression of genes associates with bone resorption. Conzone et al. (2002) fabricated bulk dysprosium lithium-borate (DyLB) glass MS with a diameter range between 5-15 μm to prevent particulate leakage during radiation synovectomy for the treatment of rheumatoid arthritis. *In vivo* evaluation in the stifle joint of a rat and *in vitro* studies showed that as the MS degraded non-uniformly due to the soluble (Li and B) and insoluble (Dy) constituents of the glass. Porous DyLB glass MS, ranging from 45-150 μm in diameter with open porosity (pores of 30 nm wide) have also been developed and suggested for bone tissue engineering (Conzone & Day 2008). Liang et al. (2008) fabricated sodium calcium borate glass MS (90-425 μm size range) with smooth or microporous surface and showed that these MS could support osteogenic cells on their surface.

In more recent years, Lakhkar and co-workers (Guedes et al. 2012; Lakhkar et al. 2012; Lakhkar et al. 2015) reported the development of bulk MS with titanium phosphate glasses $0.5P_2O_5$–0.4CaO–(0.1–x) Na_2O–$xTiO_2$ where x=0.00, 0.01, 0.03, 0.05 and 0.07 mole fraction, using flame spheroidisation method. The MS diameter ranged from ~10–200 μm and had a high sphericity. They were found to be non-cytotoxic and allowed the growth of MG63 cells over 7 days in culture.

These studies emphasise the growing potential of bioactive glass MS for therapeutic applications ranging from cancer therapy, arthritis to bone regeneration.

1.12 Aims and Objectives of the work

The aim of the work was to provide deeper understandings of 3D culture system and also hMSC-PBG microsphere direct and indirect interactions.

The objectives were:

(1) Investigate differences in cell growth and bone formation potential of hMSCs in 2D and MS culture system.
(2) Characterise chemically different PBG MS and also their degradation, to examine the sensitivity of degradation and their influence in 3D culture systems.
(3) Investigate influence of the spheres, their degradation and degradation products, on hMSC growth and osteogenic differentiation *in vitro* using direct contact (cells on microspheres) and indirect contact experiments (conditioning experiments and cytotoxicity evaluations).
(4) Study the influence of introduction of porosity in PBG MS on hMSC growth and osteogenic differentiation *in vitro* using direct contact (cells on microspheres) and indirect contact experiments (conditioning experiments and cytotoxicity evaluations).

Chapter 2 Materials and Methods

2.1 Introduction

This study focuses on the biological performance of phosphate based glass (PBG) microspheres (MS) for osteoporotic bone repair.

A total of 3 different types of particles have been used to study cellular responses in this study, including irregular shaped particles, smooth/bulk MS and porous MS. Since, borosilicate glass is known to be non-degradable under physiological conditions (Manikandan et al. 2006), it was used as a control MS system in all investigations.

The porous and non-porous bulk spheres in this study were kindly provided by Dr. Kazi Md. Zakir Hossain and Dr. Ifty Ahmed at University of Nottingham, UK. The phosphate glasses of different compositions were prepared using NaH_2PO_4, $CaHPO_4$, $MgHPO_4$, P_2O_5 and Fe_2O_3 (Sigma-Aldrich, UK) as starting materials. The precursors were weighed according to the P45 or P40 compositions in Table 2-1 and then placed into a 100 ml volume Pt/5%Au crucible. The crucible containing the precursors was then placed into a furnace at 350°C for 30 min (for drying) prior to melting in another furnace at 1150°C for 90 min. The molten glass was then poured into a metal mould to room temperature in order to obtain the bulk glass.

The bulk glasses were then ground into glass microparticles utilising a Retsch PM100 milling machine. For bulk MS, microparticles were further sieved into the size range of interest (63-150 μm), flame spheroidised using an oxygen/acetylene flame utilising a flame spray gun (Metallisation Ltd, U.K.) and collected post spheroidisation (Lakhkar et al. 2012). Borosilicate glass microspheres (BSG) were produced by crushing standard laboratory glass vials (SAMCO, UK), followed by same flame spheroidisation process. The porous spheres manufacture was subject to IP restrictions however the method, which incorporates a blowing

agent, has been patented (patent WO 2016027110 A1) (Ahmed 2016).

For acid washing, glass MS or discs were acid washed using 5 M acetic acid, in the ratio of 1g of material per 10 ml of acid solution for 2.5 min. This was followed by washing with running distilled water for 2 min, before finally drying overnight at 50^0C. The detailed list of MS-batches used in this study, has been provided in Table 2-2. Half of the BSG Batch 1, P45 BGMS Batch 1, P45 BGMS Batch 1 and AG6 P40 PGMS batches were acid-washed (AW) and used to evaluate effect of acid washing.

Table 2-1:Nominal glass compositions (mol %) used in this study.

Glass	P_2O_5	CaO	MgO	Na_2O	Fe_2O_3	SiO_2	B_2O_3	Al_2O_3
P45	45	16	24	11	4	0	0	0
P40*	40	16	24	20	0	0	0	0
BSG#	0	1.7	0	7.1	0	78.6	9.5	3.1

*Fe is absent in P40 formulation, #composition from SAMCO, UK. BSG-borosilicate glass MS.

Table 2-2:Batches of particles used in this study.

Microsphere type	Names of batches used
BSG	BSG Batch 1 BSG Batch 1 AW BSG Batch 2
P45 BGMP	AG1 P45 BGMP
P45 BGMS	AG1 P45 BGMS P45 BGMS Batch 1 P45 BGMS Batch 1 AW P45 BGMS Batch 2 P45 BGMS Batch 3
P40 BGMS	P40 BGMS Batch 1 P40 BGMS Batch 1 AW P40 BGMS Batch 2 P40 BGMS Batch 3
P45 PGMS	AG1 P45 PGMS
P40 PGMS	AG5 P40 PGMS AW AG6 P40 PGMS AG6 P40 PGMS AW

BSG-borosilicate glass microspheres, AG1- Ahmed Generation, P45/P40-glass compositions, BGMP- bulk glass microparticles, BGMS- bulk glass microspheres, PGMS- porous glass microspheres, AW- Acid washed.

2.2 Material Characterisation

2.2.1 Major axis length and Sphericity measurements

The particles were mounted on Aluminium stubs using Carbon adhesive tabs and sputter coated with 15-21 nm of gold before visualising under JEOL 6400 SEM at 20 kV. The acquired SEM images were thresholded to remove background and major axis length (MAL) and sphericity of particles in at least five fields of view were measured using Image J 1.48t (see Figure 2-1). Particles on the edges of the image or overlapping particles were not selected for quantification (Li et al. 2005).

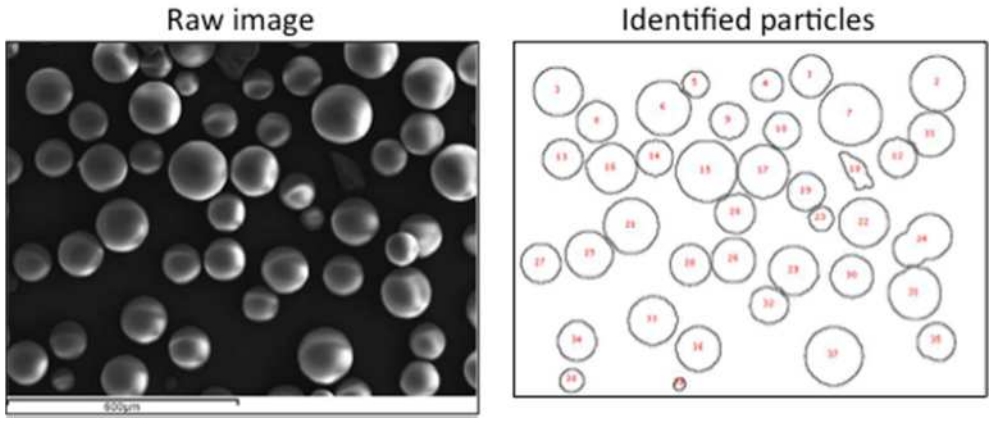

Figure 2-1: Identification of particles using Image J. The raw image (left) was thresholded to identify particles present in the field of view (right). The red digits signify unique identification number of each particle. Incomplete particles on the edges of image or overlapping particles were not selected for quantification.

2.2.2 Laser diffraction

Particle size was measured using Mastersizer 3000 instrument (Malvern, UK) based on principle of laser diffraction. The particles were dispersed in a stream of gas and then passed through a laser beam to produce a scattering pattern. The intensity of light scattered was used to measure size of particles (Li et al. 2005). Measurements were taken in the range between 0.020 to 2000.000 µm, under the following conditions: particle refractive index 1.500, particle absorption coefficient 0.1, Dispersant 1.000, and general calculation model for irregular particles. Two measurements per

batch were taken and analysed using the Mastersizer 3000, ver. 3.40 software.

2.2.3 Sieving of particles

MS were added to stacked sieves (Test sieve with stainless steel frame 200 x 50 mm stainless steel metal wire cloth, VWR International) of mesh sizes 45, 100, 200, 250, 300 and 500 µm with a holder at the bottom, beneath 45 µm sieve. The sieves were then shaken for 30 min with amplitude knob setting at 5, using Sieve Shaker (Octagon Digital).

2.2.4 Surface area analysis

For AG1 P45 BGMP, AG1 P45 BGMS and AG1 P45 PGMS (un-sieved or sieved fractions), the surface area was measured using Quantachrome BET instrument, model number- Autosorb-1 AS1MPLP2. Multipoint BET was performed at constant temperature of 77.4 K, using Nitrogen as the adsorbate. The samples were outgassed at 300 °C under high vacuum for 12 h to remove moisture and other adsorbed gases and then analysed from 0.06 to 0.27 relative pressure (P/Po) at -167 °C in liquid Nitrogen. Isotherms were analysed using Autosorb 1 version 1.55 B Quantachrome Instruments to calculate BET specific surface areas. The measurements for AG1 P45 BGMP, AG1 P45 BGMS and AG1 P45 PGMS (un-sieved) were found to be significantly higher than the theoretical or expected surface areas (Malda & Frondoza 2006) with poor correlation coefficients of 0.9956, 0.9807 and 0.9980, respectively. Therefore, for sieved fractions of AG1 P45 PGMS measurements were performed using Krypton as adsorbate.

For all other MS batches, BET specific surface areas were carried out on a Micromeritics ASAP 2420, using Krypton as the adsorbate. The samples were outgassed as described above. Isotherms were analysed using Microactive V4.03.01 software.

2.2.5 Micro Computational Tomography (μ CT)

Micro CT analyses were carried out for un-sieved AG1 P45 PGMS and 200-300 μm AG1 P45 PGMS using XRADIA Versa XRM–500 microscope as described in Table 2-3.

Table 2-3: Parameters for Micro Computational Tomography analysis.

Parameter	Un-sieved AG1 P45 PGMS	AG1 P45 PGMS 200-300 μm
Sample mass (approx.) in mg	5	3
Resolution (nm)	1000	500
Binning	2	2
Image size (pixels)	1024	1024
Field of view (mm^3)	1.024	0.512
Optical magnification	4X	20X
Source Voltage (kV)	80	80
Power (W)	7	7
Current (μA)	87	88
Source distance (mm)	15	10
Detector distance (mm)	85	16
Exposure time (s)	10	5.5
Projections	1600	1600

The 2D X-Ray images were stacked, filtered, thresholded and cleaned to remove noise (also called purification step) before generating a 3D reconstruction or before measuring porosity (Bone J plugin of Image J). For pore size and strut size measurements, a small section from the 3D reconstruction of AG1 P45 PGMS 200-300 μm was randomly selected and measurements were performed using Bone J plugin (version 1.3.11) of Image J 1.48t (Doube et al. 2010).

2.2.6 Cryo-Focused Ion Beam/Scanning Electron Microscopy (Cryo-FIB/SEM)

The internal porous structure of AG6 P40 PGMS AW was visualised using an FEI Quanta 200 3D (FEI, Portland, OR) equipped with a Quorum PPT 2000 (Quorum Technologies Ltd, Loughton, UK) cryostage and an in-house custom-built sledge. SEM secondary electron and backscattered images were acquired at 15 kV

accelerating voltage with current of 0.14 nA. Ion milling was performed at 20 kV with currents between 1 nA and 30 pA. The ion beam distance was set at 15 mm with 3.5 as spot size and all sections were cut at tilt angle of 52^0.

2.2.7 Pore window measurements

Porous MS were mounted on Aluminium stubs using Carbon adhesive tabs and sputter coated with 15-21 nm of gold before visualising under JEOL 6400 SEM at 20 kV. The acquired images were thresholded to remove background and major axis length (MAL) and roundness of pores in at least five fields of view for each PGMS batch, using Image J 1.48t (see Figure 2-2). Incomplete pores on the edges of the image or wrongly identified pores were not selected for quantification (Li et al. 2005).

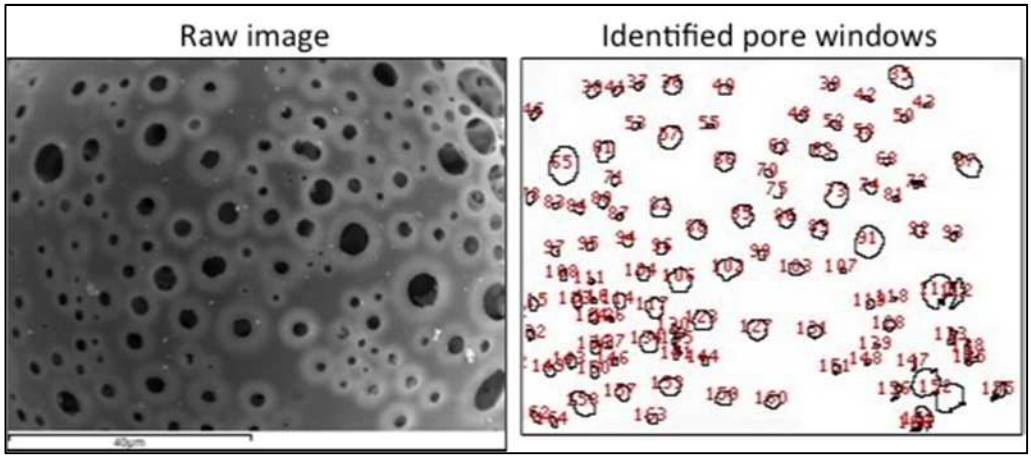

Figure 2-2: Identification of pore windows using Image J. The raw image (left) was thresholded and to identify pore windows present in the field of view (right). The red digits signify unique identification number of each pore. Incomplete pores on the edges of the image or wrongly identified pores were not selected for quantification.

2.2.8 Relative Density

Relative density was measured using Micromeritics AccuPyc 1330 Gas Pycnometer (Norcross, GA, USA). Before measuring the density of samples, a straight-line equation was plotted between the true volume and measured volume values using empty container (with zero true volume) and a reference sphere (of known true volume).

Once the measured volume values of the samples were obtained, true volume values were calculated using the straight-line equation formed earlier. The density of the sample was then calculated by dividing the true volume by mass of sample, weighed using a 4 decimal places sensitive balance (Ohaus Analytical standard AS 200).

2.2.9 Tapped density

The tapped density was measured using Quantachrome Autotap machine. Sample of known mass was added to a container, which was tapped until the height of the sample in container became constant (100 taps). The final volume was used to calculate the tapped density of the sample.

2.2.10 Electron Dispersive Spectroscopy (EDS)

The samples were embedded in a cold resin setting that cured at room temperature, then ground on Silicon Carbide grinding discs and polished using polishing cloth embedded with microparticles down to 1 μm. These polished blocks were then coated with 20 nm of vacuum-evaporated carbon. Elemental analysis was performed using an Oxford Instruments INCA Energy-dispersive X-ray spectroscopy Microanalysis System. Standards used for analysis were jadeite (for Na), gallium phosphide (for P), wollastonite (for Ca), MgO (for Mg), pyrite (for Fe). Backscattering was performed at working distance of 10 mm with a beam voltage of 20 kV. The X-ray beam current was optimized by increasing the spot size to obtain a minimum acquisition rate of 4000 counts s^{-1} while maintaining an acquisition dead time of <30%.

2.2.11 Fourier Transform Infrared (FTIR) Spectroscopy

Bruker Tensor Fourier transform infrared spectrometer with an attenuated total reflectance attachment was used for all IR absorption measurements of the samples. For borosilicate glass, flat

glass pieces with or without acid washing were used; and for PBGs, flat glass discs with or without acid washing were used. A spectral resolution of 4 cm^{-1} over the wavenumber range 500−4000 cm^{-1} was set. All spectra obtained represent the average of 64 scans over the sample area. The IR spectra were processed and analysed using the OPUS spectroscopy software.

2.2.12 Degradation studies

Degradation studies on BSG Batch 2, P45 BGMS Batch 3, P40 BGMS Batch 3 and AG6 P40 PGMS AW samples were performed using two methodologies.

2.2.12.1 Degradation in water for 1 day

Five milligrams of MS were degraded in 10 ml of Milli Q water (at pH 6.8) for 24 h and then left overnight for drying in cell culture hood. After drying, the samples were sputter coated with 15-21 nm of gold and then visualised under JEOL 6400 SEM at 20 kV.

2.2.12.2 Degradation in culture medium for 42 days

For this, MS were prepared in the same way as for cell culture detailed in Section 2.3.1. Briefly, MS were cleaned with Industrial Methylated Spirit (IMS), dried overnight, then washed with phosphate-buffered saline (PBS) and then again washed with culture medium, before finally leaving them in 200 µl $well^{-1}$ culture medium for next 42 days. The resulting material to medium ratio was 22.5 g to 1 ml of culture medium. Medium changes were performed after 1 day and then subsequently, every 2-3 days, up to 42 days of degradation.

On each time point, culture medium was removed; MS were collected from wells, sputter coated with 15-21 nm of gold before visualising under JEOL 6400 SEM at 20 kV. Five fields of view for each MS type were captured at every time point at 100 X. MS with cracks or peeling visible on their surfaces were manually counted

per field of view (see Figure 2-3 as an example) and degradation was presented as percentage MS with apparent cracks or peeling.

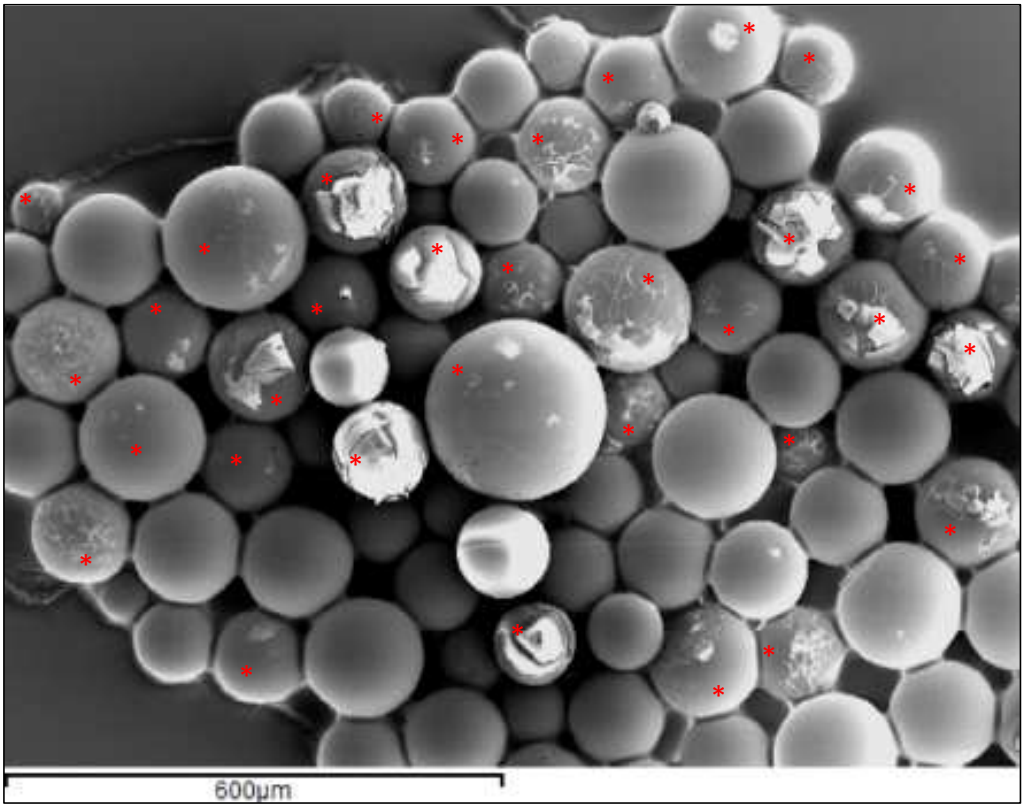

Figure 2-3: Methodology for quantification of MS with apparent cracks and peeling surfaces. MS with * have cracks or peeling surface where as other MS do not have these features. As an example, 53% MS in this image have surface changes on them.

2.3 Cytocompatibility studies

The cytocompatibility studies have been divided into two main categories: cell-material direct-contact interactions and cell-material indirect-contact interactions; which have been explained in following subsections and the schematic diagram in Figure 2-4.

2.3.1 Human Mesenchymal Stem Cell (hMSC) culturing

Adult human bone marrow-derived human immortalised mesenchymal stem cells (hMSCs) were used in this study. These cells have the potential for adipogenic, osteogenic and chondrogenic differentiation and are known to express mesenchymal markers

such as CD29, CD105, CD106, p75, CD90, CD44 and SSEA4 (Okamoto et al. 2002; Rashidi et al. 2012; France et al. 2012; Harrison et al. 2016). In some experiments, Green Fluorescent Protein (GFP) expressing hMSCs were used, which were created using established protocol of stable transfection via electroporation (Peister et al. 2004).

These cells were cultured in standard culture medium (SC) containing Dulbecco's Modified Eagle Medium (DMEM, Life Technologies) supplemented with 10% (v/v) foetal calf serum (FCS, Life Technologies), 1% (v/v) non-essential amino acids (Life Technologies), 1mM L-glutamine (Life Technologies) and 0.5% (v/v) Penicillin/Streptomycin (Life Technologies) and maintained at 37 ^{0}C in humidified atmosphere with 5% CO_2. At 70-90% confluency in T25 flask, the culture medium was removed; cells were then washed with 5 ml PBS and then harvested using 500 µl of 0.05% Trypsin solution in 0.53 mM EDTA (Life Technologies). The cells were seeded at different cell densities as monolayers (2D) or on MS with a final volume of 500 µl per well in 24-well plate and 200 µl per well in 96-well plate, respectively.

2.3.1.1 Osteogenic differentiation

For osteogenic differentiation, after 24 h of cell seeding (considered as Day 0 of differentiation), medium was changed to either standard culture (SC) medium or osteogenic stimulation (OS) medium. The OS medium was the SC medium supplemented with 100 nM DEX (Sigma-Aldrich, Gillingham, UK), 10 mM β-glycerophosphate (Sigma-Aldrich) and 0.05 mM L-ascorbic acid-2-phosphate (Sigma Aldrich). Subsequently medium changes were performed every 2-3 days for up to 3 weeks of culture (France et al. 2012).

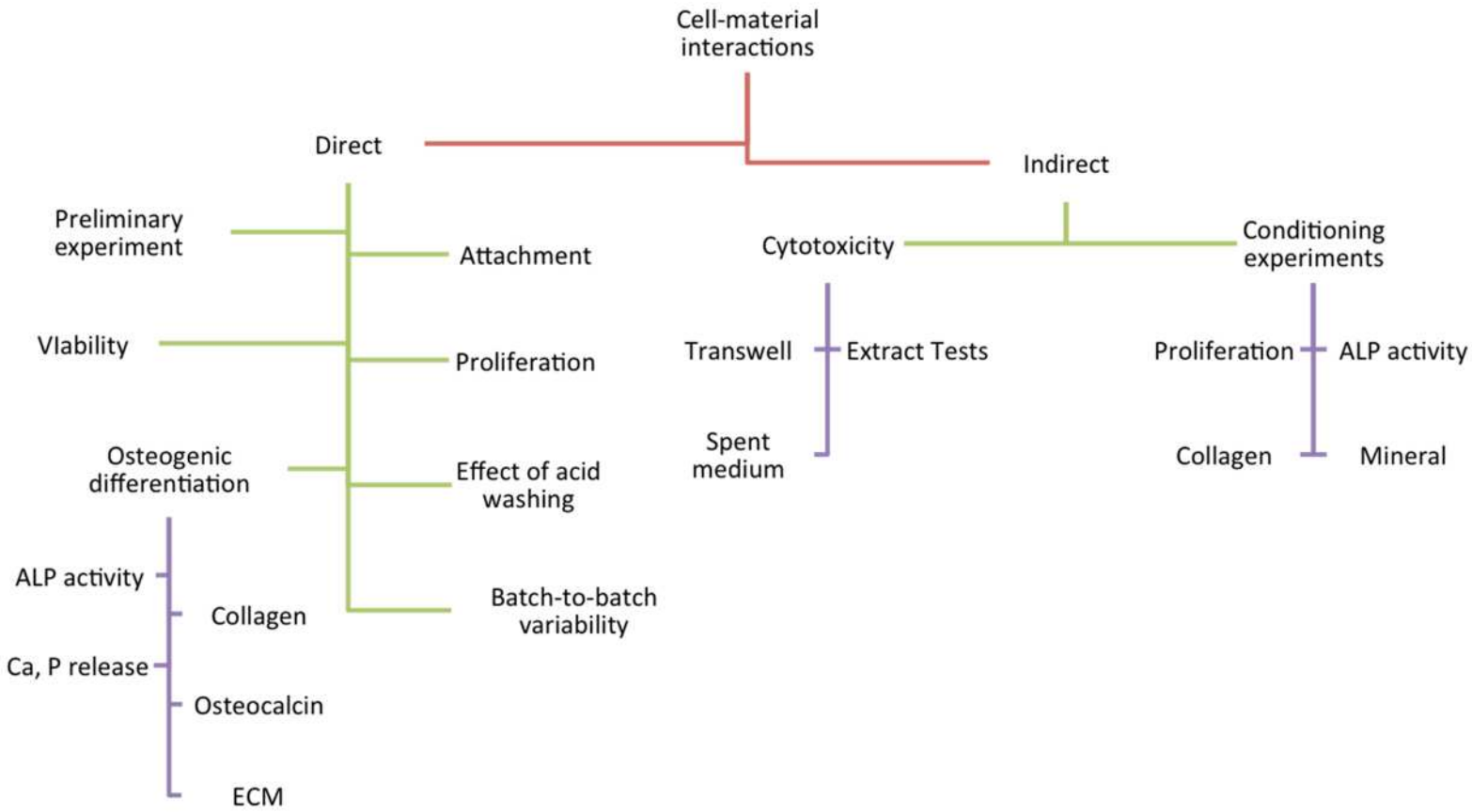

Figure 2-4: Schematic view of the areas explored using hMSC-based experiments on MS. ECM-Extracellular matrix, ALP-Alkaline phosphatase.

2.3.2 Cell seeding on microspheres

In order to grow cells in 2D (covered with glass coverslips from SLS, unless otherwise mentioned), cells were added to each well in a non-treated 24-well plate or 96-well plate. For 3D culturing, the MS were weighed to 2 cm^2 (unless otherwise mentioned) and added into tubes. Particles were then cleaned with IMS for 2 h at constant agitation at 30 rpm before air-drying overnight in cell culture hood. Then particles were washed three times with PBS and three times with culture medium (see Section 2.3.1 for composition), before incubating them for 30 min at room temperature (RT) in culture medium. At this stage, particles (while in medium) were transferred to wells previously coated with 100 µl solution of 10 mg ml^{-1} pHEMA or poly(2-hydroxyethyl methacrylate) (Sigma-Aldrich, UK) solution in 95% ethanol to make ultra-low cell attachment conditions on 96-well flat bottom plate (for preferential attachment of cells to MS only). The MS formed a monolayer at the bottom of the well ready to be seeded with hMSCs (see Figure 2-5). Finally, culture medium was removed and fresh culture medium containing desired cells was added. In Experiment-PRE01, particles were not transferred to well plates and hMSCs were cultured on particles while in tubes. In Experiments-CP04 and CP09, MS were weighed to 12 cm^2 and seeded with hMSCs in 24-well plate coated with pHEMA.

After adding cells, the plates or tubes were further agitated at 45 rpm for 5 min at RT, followed by 30 min static incubation at 37 ^0C and 5% CO_2. This regime was repeated 5 times before undisturbed incubation overnight in 37 ^0C and 5% CO_2 (Lakhkar et al. 2012; Ahmadi et al. 2011). Medium change was performed 24 h after cell seeding and subsequently every 2-3 days for the length of experiment.

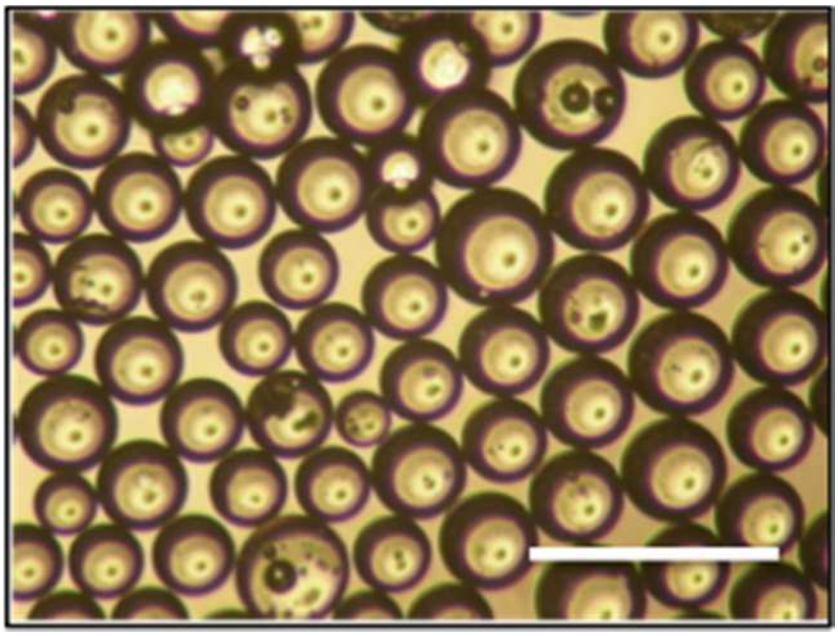

Figure 2-5: A monolayer of MS prepared for hMSC seeding. Scale bar- 250 µm.

2.3.3 Design of direct-contact experiments

In Table 2-4, a detailed description is provided for all the direct-contact experiments performed in this study. In all experiments, except COL01, COL02, OCN01, OCN02, ECM01, ECM02, GFP-hMSCs were used. In Experiment-CV02, non-GFP hMSCs were used for day 1, 4 and 7 time points but for day 21, samples with both non-GFP hMSCs and GFP-hMSCs were prepared.

Table 2-4:Details of direct-contact experiments performed in the study.

Experiment	Platform for cell culture	Assessment(s) performed	Seeding density (cells cm^{-2})	Time point (day)	Medium	Microspheres (MS) used
Preliminary experiment						
PRE01	Particles (3 μm^3)	Metabolic activity	1700€	1, 4, 7	SC	AG1 P45 BGMP, AG1 P45 BGMS, AG1 P45 PGMS (all un-sieved fractions)
Effect of acid washing						
AW01	MS (2 cm^2)	DNA, metabolic activity	2,500	1, 4, 7	SC	AG6 P40 PGMS, AG6 P40 PGMS AW
AW02	MS (2 cm^2)	DNA	2,500	7	SC	AG6 P40 PGMS, AG6 P40 PGMS AW
AW03	MS (2 cm^2)	DNA	500, 1000, 2000, 3000	1	SC	BSG Batch 1, BSG Batch 1 AW, P45 BGMS Batch 1, P45 BGMS Batch 1 AW, P40 BGMS Batch 1, P40 BGMS Batch 1 AW
AW04	MS (2 cm^2)	DNA, metabolic activity	2,500	1, 4, 7	SC	P40 BGMS Batch 1, P40 BGMS Batch 1 AW
Batch-to-batch variability						
BR01	MS (2 cm^2)	DNA, metabolic activity	2,500	1, 4, 7	SC	BSG Batch 1, BSG Batch 2
BR02	MS (2 cm^2)	DNA	2,500	7	SC	BSG Batch 1, BSG Batch 2
BR03	MS (2 cm^2)	DNA, metabolic activity	2,500	1, 4, 7	SC	P45 BGMS Batch 1, P45 BGMS Batch 2
BR04	MS (2 cm^2)	Cell counts	2,500	1, 3, 5, 7	SC	P45 BGMS Batch 1, P45 BGMS Batch 2
BR05	MS (2 cm^2)	DNA, metabolic activity	2,500	1, 4, 7	SC	P40 BGMS Batch 1, P40 BGMS Batch 2
BR06	MS (2 cm^2)	Cell counts	2,500	1, 3, 5, 7	SC	P40 BGMS Batch 1, P40 BGMS Batch 2
BR07	MS (2 cm^2)	DNA, metabolic activity	2,500	1, 4, 7	SC	AG5 P40 PGMS AW, AG6 P40 PGMS AW
BR08	MS (2 cm^2)	DNA	2,500	7	SC	AG5 P40 PGMS AW, AG6 P40 PGMS AW

Cell attachment						
CA01	2D (2 cm^2), MS (2 cm^2)	DNA, metabolic activity	625, 1,250, 2,500, 5,000, 10,000	1	SC	BSG Batch 1
CA02	2D (2 cm^2), MS (2 cm^2)	Metabolic activity	625, 1,250, 2,500, 5,000, 10,000	1	SC	BSG Batch 2
CA03	MS (2 cm^2)	DNA, metabolic activity, live cell imaging	625, 1,250, 2,500, 5,000, 10,000	1	SC	BSG Batch 1, P45 BGMS Batch 1, P40 BGMS Batch 1, AG6 P40 PGMS AW
CA04	MS (2 cm^2)	Metabolic activity, live cell imaging	625, 1,250, 2,500, 5,000, 10,000	1	SC	BSG Batch 2, P45 BGMS Batch 3, P40 BGMS Batch 3, AG6 P40 PGMS AW
Microsphere aggregate formation						
AG01	MS (2 cm^2)	Live cell imaging#	2,500	1	SC	BSG Batch 2, P45 BGMS Batch 3, P40 BGMS Batch 3, AG6 P40 PGMS AW
AG02	MS (2 cm^2)	Live cell imaging#	10,000	1	SC	BSG Batch 2, P45 BGMS Batch 3, P40 BGMS Batch 3, AG6 P40 PGMS AW
Cell proliferation						
CP01	2D (2 cm^2), MS (2 cm^2)	DNA, metabolic activity	2,500	1, 4, 7, 14, 21, 31, 42	SC	BSG Batch 2
CP02	2D (2 cm^2)$^{\$}$, MS (2 cm^2), 2D' (0.33 cm^2)$^{\$}$	Cell counts, metabolic activity	2,500 (2D and 3D), 15,624 (2D')	1, 3, 5, 7	SC	BSG Batch 1

CP03	2D (2 cm^2), MS (2 cm^2)	DNA	10,000	7, 14, 21	SC	BSG Batch 2
CP04	MS (12 cm^2)	DNA	167	1, 7, 14, 21	SC	BSG Batch 1
CP05	MS (2 cm^2)	DNA	2,500	1, 4, 7	SC	BSG Batch 1, P45 BGMS Batch 1, P40 BGMS Batch 1, AG5 P40 PGMS AW
CP06	MS (2 cm^2)	DNA	2,500	1, 4, 7	SC	BSG Batch 2, P45 BGMS Batch 2, P40 BGMS Batch 2, AG6 P40 PGMS AW
CP07	MS (2 cm^2)	DNA	2,500	1, 4, 7, 14, 21, 31, 42	SC	BSG Batch 2, P45 BGMS Batch 3, P40 BGMS Batch 3, AG6 P40 PGMS AW
CP08	MS (2 cm^2)	DNA	10,000	7, 14, 21	SC	BSG Batch 2, P45 BGMS Batch 3, P40 BGMS Batch 2, AG6 P40 PGMS AW
CP09	MS (12 cm^2)	DNA	167	1, 7, 14, 21	SC	BSG Batch 1, P45 BGMS Batch 1, P40 BGMS Batch 1, AG6 P40 PGMS AW
Cell viability						
CV01	2D (2 cm^2), MS (2 cm^2)	FDA/PI staining	2,500	1*, 4*, 7, 21	SC	BSG Batch 2
CV02	MS (2 cm^2)	FDA/PI staining	2,500	1*, 4*, 7, 21	SC	BSG Batch 2, P45 BGMS Batch 3, P40 BGMS Batch 3, AG6 P40 PGMS AW
Early osteogenic differentiation						
CD01	2D (2 cm^2), MS (2 cm^2)	ALP activity	10,000	7, 14, 21	SC, OS	BSG Batch 2
CD02	2D (2 cm^2), MS (2 cm^2)	ALP activity	10,000	7, 21	SC, OS	BSG Batch 2
CD03	2D (2 cm^2), MS (2 cm^2)	ALP activity	2,500	7, 21	SC, OS	BSG Batch 2
CD04	2D (2 cm^2), MS (2 cm^2)	ALP activity	2,500	7, 14, 21	SC, OS	BSG Batch 2
CD05		ALP activity	2,500	1, 4, 7,	SC	BSG Batch 2, P45 BGMS Batch 3, P40 BGMS

	MS (2 cm^2)			14, 21, 31, 42		Batch 3, AG6 P40 PGMS AW
CD06	MS (2 cm^2)	ALP activity	2,500	7, 21	SC	BSG Batch 2, P45 BGMS Batch 3, P40 BGMS Batch 3, AG6 P40 PGMS AW
CD07	MS (2 cm^2)	ALP activity	10,000	7, 14, 21	SC	BSG Batch 2, P45 BGMS Batch 3, P40 BGMS Batch 3, AG6 P40 PGMS AW
CD08	MS (12 cm^2)	ALP activity	167	1, 7, 14, 21	SC	BSG Batch 1, P45 BGMS Batch 1, P40 BGMS Batch 1, AG6 P40 PGMS AW
Collagen production						
COL01	2D (2 cm^2), MS (2 cm^2)	Sirius Red#	2,500, 10,000	21	SC, OS	BSG Batch 2
COL02	MS (2 cm^2)	Sirius Red#	2,500, 10,000	21	SC	BSG Batch 2, P45 BGMS Batch 3, P40 BGMS Batch 3, AG6 P40 PGMS AW
COL03	2D (2 cm^2), MS (2 cm^2)	Sirius Red	10,000	7, 21	SC, OS	BSG Batch 1
COL04	2D (2 cm^2), MS (2 cm^2)	Sirius Red	2,500	7, 14, 21	SC, OS	BSG Batch 2
COL05	MS (2 cm^2)	Sirius Red	2,500	21	SC	BSG Batch 2, P45 BGMS Batch 2, P40 BGMS Batch 2, AG6 P40 PGMS AW
COL06	MS (2 cm^2)	Sirius Red	2,500	21	SC	BSG Batch 2, P45 BGMS Batch 3, P40 BGMS Batch 3, AG6 P40 PGMS AW
COL07	MS (2 cm^2)	Sirius Red	2,500	21	SC	BSG Batch 2, P45 BGMS Batch 3, P40 BGMS Batch 3, AG6 P40 PGMS AW
COL08	MS (2 cm^2)	Sirius Red	10,000	21	SC	BSG Batch 2, P45 BGMS Batch 3, P40 BGMS Batch 3, AG6 P40 PGMS AW
COL09	MS (2 cm^2)	Sirius Red	10,000	21	SC	BSG Batch 2, P45 BGMS Batch 3, P40 BGMS Batch 3, AG6 P40 PGMS AW
COL10	MS (2 cm^2)	Sirius Red	10,000	21	SC	BSG Batch 2, P45 BGMS Batch 3, P40 BGMS Batch 3, AG6 P40 PGMS AW
Mineral deposition						

MIN01	2D (2 cm^2), MS (2 cm^2)	Alizarin Red#	2,500, 10,000	7, 21	SC, OS	BSG Batch 2
MIN02	2D (2 cm^2), MS (2 cm^2)	Alizarin Red	10,000	21	SC, OS	BSG Batch 2
MIN03	MS (2 cm^2)	Alizarin Red	10,000	21	SC, OS	BSG Batch 2
MIN04	2D (2 cm^2), MS (2 cm^2)	Alizarin Red	2,500	21	SC, OS	BSG Batch 2
MIN05	2D (2 cm^2), MS (2 cm^2)	Alizarin Red	2,500	21	SC, OS	BSG Batch 2
MIN06	MS (2 cm^2)	XPS	2,500	21	SC	BSG Batch 1, P45 BGMS Batch 1, P40 BGMS Batch 1
MIN07	MS (2 cm^2)	XPS	2,500	7, 14, 21	SC	BSG Batch 2, P45 BGMS Batch 3, P40 BGMS Batch 3, AG6 P40 PGMS AW
Osteocalcin expression						
OCN01	2D (2 cm^2), MS (2 cm^2)	Immunostaining#	2,500, 10,000	21	SC, OS	BSG Batch 2
OCN02	MS (2 cm^2)	Immunostaining#	2,500, 10,000	21	SC, OS	BSG Batch 2, P45 BGMS Batch 3, P40 BGMS Batch 3, AG6 P40 PGMS AW
Extracellular matrix formation						
ECM01	MS (2 cm^2)	H&E staining#	2,500, 10,000	21	SC, OS	BSG Batch 2
ECM02	MS (2 cm^2)	H&E staining#	2,500, 10,000	21	SC	BSG Batch 2, P45 BGMS Batch 3, P40 BGMS Batch 3, AG6 P40 PGMS AW

€-cells μm^{-3}, # qualitative assessment, *both qualitative and quantitative assessments, $ coverslips not used.

2.3.4 Design of indirect-contact experiments

In Table 2-5, a detailed description is provided for all the indirect-contact experiments performed in the present study.

Table 2-5:Details of indirect-contact experiments performed in the study.

Experiment	Assessment(s) performed	Microspheres (MS) used
CON01	Metabolic activity (Day 25), DNA (all time points), ALP activity (all time points), collagen (Day 25), mineral (Day 16, 25)	BSG Batch 2, P45 BGMS Batch 3, P40 BGMS Batch 3, AG6 P40 PGMS AW
CON02	Metabolic activity (all time points), DNA (all time points), ALP activity (all time points), collagen (Day 16, 25), mineral (Day 16, 25)	BSG Batch 2, P45 BGMS Batch 3, P40 BGMS Batch 3, AG6 P40 PGMS AW
TOX01	Metabolic activity (before treatment, Day 1 and 3), neutral red uptake (Day 3)	BSG Batch 2, P45 BGMS Batch 3, P40 BGMS Batch 3, AG6 P40 PGMS AW, AG6 P40 PGMS
TOX02	Metabolic activity (before treatment, Day 1 and 3), neutral red uptake (Day 3)	P40 BGMS Batch 3, AG6 P40 PGMS AW, AG6 P40 PGMS
TOX03	DNA, metabolic activity, neutral red uptake	BSG Batch 2, P45 BGMS Batch 3, P40 BGMS Batch 3, AG6 P40 PGMS AW, AG6 P40 PGMS
TOX04	DNA, metabolic activity, neutral red uptake	BSG Batch 2, P45 BGMS Batch 3, P40 BGMS Batch 3, AG6 P40 PGMS AW, AG6 P40 PGMS
TOX05	DNA, metabolic activity, neutral red uptake	BSG Batch 2, P45 BGMS Batch 3, P40 BGMS Batch 3, AG6 P40 PGMS AW, AG6 P40 PGMS
TOX06	Neutral red uptake	BSG Batch 2, P45 BGMS Batch 2, P40 BGMS Batch 2, AG5 P40 PGMS AW
TOX07	Neutral red uptake	BSG Batch 2, P45 BGMS Batch 2, P40 BGMS Batch 2, AG6 P40 PGMS AW

2.3.4.1 Conditioning experiments

In Experiments-CON01 and CON02, 10 mg of MS (n=3, weighed in SLS tubes) and three empty tubes (control with no MS), were cleaned with IMS for 2 h, then washed three times with PBS and three times with culture medium (see Section 2.3.1 for composition), before 30 min incubation in culture medium. Then

medium was removed and replaced with 10 ml of fresh growth medium at 37 ^{0}C and 5% CO_2 (ISO 10993-14:2009). Next day (Day 1 of conditioning), medium was removed to store at -20 ^{0}C and fresh medium was added. This was then repeated on Days, 4, 7, 10, 13, 16, 19 and 22 of conditioning. The medium collected on every time point was later used for pH measurements (shown in Appendix 1) and also for hMSC culture.

GFP-hMSCs were seeded at 5,000 cells well^{-1} in a total volume of 100 µl in a 96-well flat bottom plate. On Day 1 of culture, medium was removed and replaced with conditioned medium collected on Day 1 of conditioning. Subsequent medium changes were performed every 3 days using the conditioned medium collected on Day 4, 7, 10, 13, 16, 19 and 22 of conditioning.

2.3.4.2 Cytotoxicity experiments

In Experiments-TOX01 to TOX05, 100 mg of MS (n=3, weighed in SLS tubes) and three empty tubes (control with no MS), were cleaned in IMS for 2 h, then washed three times with PBS, three times with culture medium (see Section 2.3.1 for composition) and then incubated in culture medium for 30 min. Then the medium was removed and MS were finally incubated in culture medium in the ratio of 1 ml per 100 mg of material at 37^{0}C in 5% CO_2, based on ISO standard for irregular shaped porous devices (ISO 10993-12:2009).

For all of above experiments, cells grown in fresh DMEM+10% FCS (positive control), fresh DMEM+5% FCS, fresh DMEM+0% FCS and fresh DMEM+DMSO were used as controls. In Experiments-TOX01 and TOX02, medium changes for these control conditions were performed every day.

Cytotoxicity was evaluated using 4 methodologies as described below.

(1) In Experiments-TOX01 and TOX02, materials were loaded on a transwell (6.5 mm polycarbonate membrane insert with 0.4 µm pore size, Corning) and immersed in medium while simultaneously being exposed to hMSCs (seeded at 8,000 cells well^{-1} in 24 well plate, Transwell®, Corning) for 3 days (see Figure 2-6). No medium change was performed for Control (no MS) or other test conditions during 3 days of elution.

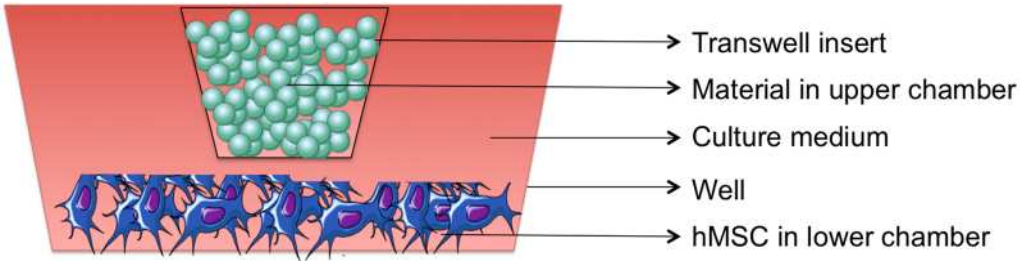

Figure 2-6: Experimental design for cytotoxicity evaluation of MS through a transwell insert.

(2) In Experiments-TOX03, materials were immersed in medium for one day and extracts collected on day 1 of elution were tested for cytotoxicity using hMSCs seeded at 3,000 cells well^{-1} in a 96-well plate, after 24 h exposure.

(3) In Experiment-TOX04, materials were immersed in medium for 7 days without medium changes and extracts collected on day 7 of elution were tested for cytotoxicity using hMSCs seeded at 3,000 cells well^{-1} in a 96-well plate, after 24 h exposure.

(4) In Experiment-TOX05, materials were immersed in medium for 7 days with medium changes on day 1 and 4 of elution. The extracts collected on day 7 of elution were tested for cytotoxicity, either as neat or after filtering through polycarbonate 0.4 µm-filter (STARLITECH), using hMSCs were seeded at 3,000 cells well^{-1} in a 96-well plate, after 24 h exposure.

2.3.4.3 Cytotoxicity of spent medium

In Experiments-TOX06 and TOX07, spent medium collected from day 7, 14 and 21 of culture in Experiments-CP07 and CP08. Human MSCs were seeded at 3,000 cells well^{-1} in a 96-well plate and after

24 h exposure to spent medium, cytotoxicity was assessed using Neutral red uptake assay (Section 2.3.10). BSG-spent medium condition was treated as control for each time point.

2.3.5 Cell metabolic activity assay

In Experiment-PR01, AlamarBlue™ assay (Invitrogen) was used, while in all other experiments, PrestoBlue® assay (Invitrogen) was used. Cell metabolic activity measurements were performed according to manufacturer's instructions.

Briefly, medium was removed and cells were washed with PBS before adding AlamarBlue™ or PrestoBlue® working solution (1:9 Reagent:warm Hanks Balanced Salt Solution/HBSS, Invitrogen) to each test well (n≥3) and three blank wells. The initial volume added to 2D and 3D, in 24-well plate and 96-well plate, was 500 µl and 200 µl, respectively (which was same volume as culture medium). Cells were then incubated at 37^0C and 5% CO_2 until colour change and reaction time was noted.

In Experiment-PR01, two 80 µl extracts from each well and in all other direct-contact experiments, 100 µl extracts from each well, were transferred to a clear 96-well plate (Costar) and fluorescence reading was measured 530 nm excitation and 590 nm emission filters on Tecan Infinite M200 microplate reader (Tecan, Reading, UK). Cell metabolic activity was expressed after subtracting unreduced (blank) reagent from fluorescence and normalising to reaction time (minutes). In all 2D vs. 3D experiments, measurements were further normalised to the initial volume of reagent added.

For in-direct contact experiments, 100 µl of PrestoBlue® working solution was added per well and after colour change, fluorescence reading was measured using plate reader as described above. Unreduced PrestoBlue® was subtracted and cell metabolic activity was expressed per minute.

2.3.6 DNA assay

For 2D vs. 3D experiments and other direct contact experiments, samples were lysed by freeze thawing three times at – 80^0C. The 3D samples were further sonicated using Bioruptor®, Diagenode, USA. The cell lysates (n≥3) were then diluted and 100 µl of test solution was added to a flat 96-well plate (Costar). Since different methodologies were used for lysing cells in 2D and 3D systems, a validation study was performed as detailed in Appendix 2. For in-direct contact experiments, cells (n≥3) were lysed by freeze thawing cycles only as described above.

DNA content was quantified using Quant-iTM PicoGreen® dsDNA Assay kit (ThermoFisher), according to manufacturer's instruction. To each 100 µl of test solution, equal volume of diluted PicoGreen® reagent solution was added to each test well and incubated for 5 min at RT, protected from light. Florescence intensity readings were taken on Tecan Infinite M200 microplate reader (Tecan, Reading, UK) at 480 nm excitation and 520 nm emission. The DNA concentration was extrapolated using a standard curve prepared from calf thymus standard DNA provided with the assay kit.

2.3.7 Cell counts

For detaching cells from MS and TC-plastic, cells were first washed with PBS, then trypsinised for 2 min at RT using 50 µL of 0.05% Trypsin solution in 0.53 mM EDTA solution (Life Technologies). When cells started to detach, sample was pipetted to help release the attached cells from the MS and then 150 µl of medium was added to each well. While slightly tilting the well plate (to allow particles to settle on one side of well), detached cells in medium were transferred to another well and counted using haemocytometer (n≥3). Appendix 3 shows that trypsination was able to remove almost all cells from the 3D samples. For cells on TC-plastic in 24-well plate, 50 µL of trypsin was used and cells were resuspended in

480 µL of fresh medium before counting using haemocytometer (n≥3).

2.3.8 Assessment of microsphere agglomeration

In Experiment-CA01 and CA02, after 24 h of cell seeding, live cell images were taken through the FITC channel using JuLI™ FL (NanoEnTek). In Experiments-AG01 and AG02, live cell images were taken through the FITC channel using JuLI™ FL (NanoEnTek) over initial 24 h of culture at regular intervals of 15 min.

2.3.9 FDA/PI staining

The cell viability assessment was performed based on cell membrane integrity using Fluorescein diacetate (FDA, binds to live cell, CALBIOCHEM) and propidium iodide (PI, binds to dead cell, SIGMA) (Karaoz et al. 2010; Shi et al. 2011). In Experiments CV01 and CV02, cells were washed with PBS and then DMEM containing 8 µg ml^{-1} FDA and 20 µg ml^{-1} PI was added. Cells were incubated at RT for 5 minutes in the dark, then after removing DMEM containing dyes, fresh DMEM only was added. On Days 1, 4, 7 and 21 images were acquired using Nikon TS100 Inverted fluorescence microscope with filters for Texas Red and FITC. On day 21, separate 3D samples were also imaged using FITC and Texas Red channels of Leica TCS LSI Confocal macroscope.

Imaging using above two microscopes revealed live/dead cells at the bottom and top faces (facing towards bottom and lid of well plate, respectively) of 3D agglomerates. Therefore, for visualising cell viability inside the 3D agglomerates on Day 21, GFP-hMSCs loaded samples were first incubated in DMEM containing 20 µg ml^{-1} PI for 5 min, then fixed in 4% paraformaldehyde (PFA) in PBS (at 4^0C) for 10 min, before cryo-sectioning (Section 2.3.12). The stained sections were then visualised under ECLIPSE 90i Fluorescent Nikon Microscope using Texas Red and FITC channels.

Quantification was also performed on days 1 and 4 of both experiments. The fluorescent images (n≥4) were used to quantify red and green signals using Image J. Percentage cell viability was calculated by dividing the green pixels with total pixels (green + red) in the same field of view, before finally normalising to 2D of same time point.

In both experiments, hMSCs fixed in PFA were used as negative control (dead cells) and freshly seeded live hMSCs were used as positive control at all time points.

2.3.10 Neutral Red uptake (NRU) assay

For stock solution, 0.2 g of NR was added to 50 ml of sterile distilled water. This was further diluted to 1 in 80 ratio in DMEM for working solution of Neutral Red (NR) medium, which was syringe filtered using 0.2 filter, before using for evaluating cell viability (Repetto et al. 2008).

For cell viability assessments, culture medium was removed and cells were washed with PBS before adding (1 ml $well^{-1}$ in 24-well plate or 100 µl in 96-well plate) NR dye medium (n≥3) to test wells and three blank wells. Cells were further incubated at 37 ^{0}C and 5% CO_2 for 3 h, then NR medium was discarded and one PBS wash was performed. At this stage, images were taken using Nikon Eclipse TS100.

For quantification, NR desorbing solution (49% Ethanol, 1% glacial acetic acid, 50% water) was added to cells (same volume as used for NR dye medium) and after 10 min incubation at RT, NR absorption was measured at an optical density (OD) of 540 nm using Tecan Infinite M200 microplate reader (Tecan, Reading, UK). Neutral red uptake (cell viability) was calculated by subtracting the blank values and normalising to the control medium for each time point. Viability less than 70% was considered to be cytotoxic, as outlined by ISO standard for biological evaluation of medical devices (ISO 10993-5:2009).

2.3.11 Alkaline Phosphatase (ALP) activity

On specific time points, ALP activity was measured using SIGMAFAST™ p-Nitrophenyl phosphate tablets (substrate) (SIGMA). Briefly, 100 µl of cell lysates (or sterile distilled water for 3 blank wells) and 100 µl of substrate was added to each assay well and absorbance at 405 nm was measured on Tecan Infinite M200 microplate reader (Tecan, Reading, UK). The ALP activity is expressed as absorbance/min/µg of DNA ($n \geq 3$) after removing background and normalising to reaction time and DNA content. A validation study for ALP activity measurements in 2D and 3D was also performed as described in Appendix 2.

2.3.12 Sectioning of 3D agglomerates

On day 21, medium was removed and the 3D agglomerates were fixed in 4% PFA in PBS (at 4^0C) for 10 min. Then the agglomerates were washed with PBS for 5 min followed by immersion in 15% sucrose solution in PBS, until the agglomerates sank. The agglomerates were then transferred to a custom mould and embedded in OCT medium and stored in -20 ^{0}C until sectioning. Agglomerates were sectioned (20 µm section size) at cryostat chamber temperature of -20^{0}C. The sections were then dried overnight at RT and stored at 4^0C. These sections were then used to perform PI staining, Sirius Red staining, Haematoxylin and Eosin (H&E) staining and osteocalcin immunostaining.

2.3.13 Sirius Red staining

For staining, a working solution of 0.1 % Sirius red (Direct Red 80, SIGMA-ALDRICH) was prepared in 100 ml of saturated picric acid (SIGMA) (Lareu et al. 2010; Kliment et al. 2011).

For qualitative assessment in Experiments-COL01 and COL02, samples were incubated in working solution for 30 min with occasional agitation every 10 min. In case of 3D cryo-sections, the excess stain was removed by blot drying and mounted using DPX

before visualising under ECLIPSE 90i Nikon Microscope. In case of 2D coverslips, imaging was performed using Nikon Eclipse TS100. Mouse calvarial tissue was used as a positive control for collagen staining under both microscopes.

For quantification in Experiments COL03-COL10, intact 3D agglomerates or 2D coverslips (n≥3) were used and for quantification in Experiments-CON01 and CON02, cells in 96-well plate were used. Medium was aspirated, samples were washed with PBS for 5 min two times and then fixed in 4% PFA in PBS (4^0C) for 15 min. After removing the fixative, working solution of Sirius Red (same volume as culture medium) was added for 30 min at RT with occasional agitation. Then stain was removed and samples were washed with distilled water, followed by detaining solution (1:1 0.1 N NaOH:Methanol, same volume as culture medium) for 30 min with occasional agitation. Finally, 100 µl volume extracts were used to measure OD at 540 nm using Tecan Infinite M200 microplate reader (Tecan, Reading, UK). The background was subtracted from the absorbance readings of three blank wells and total collagen per sample was extrapolated using a standard curve prepared from Rat-tail collagen type 1 (SIGMA, Appendix 4).

2.3.14 Alizarin Red staining

To assess the extent of mineral production, Alizarin Red staining was performed both qualitatively and quantitatively. For qualitative analysis, medium was aspirated, cells were washed three times with PBS and fixed in 4% PFA in PBS (at 4^0C) for 15 min. After removing the fixative, cells were stained with 1% Alizarin red solution (same volume per well as culture medium) for 10 minutes at RT with occasional agitation. Excess stain was removed with distilled water. For 3D samples, the agglomerates from top were crushed slightly using a fine spatula before imaging using Nikon Eclipse TS100. The 2D coverslips were also imaged under same microscope immediately after staining.

For quantification analysis, after staining, de-staining solution (20% methanol and 10% acetic acid in dH_2O) was further added (same volume as culture medium) for 15 min. Then OD was measured for 100 µl extracts at 540 nm using Tecan Infinite M200 microplate reader (Tecan, Reading, UK) ($n \geq 3$). Mineral content was expressed as absorbance units after subtracting background using three blank wells and DNA content. In 2D vs. 3D experiments, measurements were further normalised to the initial volume of de-staining solution added.

2.3.15 Osteocalcin (OCN) immunostaining

Samples were permeablised with 0.1% Triton X-100 in PBS for 40 min, then washed three times for 5 min with PBS before blocking with 3% goat serum (SIGMA) in 1% Bovine Serum Albumin (BSA, Sigma-Aldrich) in PBS for 30 min. After removing the blocking solution, the samples were incubated with anti-osteocalcin primary antibody, rabbit polyclonal (Millipore) 1:200 dilution in 1% BSA in PBS, at 4^0C. Next day, samples were washed twice in PBS for 5 min. Then 1:200 dilution in 1% BSA in PBS of Alexa Fluor 488 (green) goat anti-rabbit IgG (Invitrogen) was added and incubated at RT for 2 h before performing three 5 min PBS washes. Finally, 1 µg/ml Hoechst (Sigma) in 1% BSA in PBS was added for 15 min at RT, followed by three 5 min PBS washes. The samples were then mounted using DABCO (1-4-Diazabicyclo-2-2-2-octane) Fluorescence Mounting Medium (SIGMA) and imaged under ECLIPSE 90i Fluorescent Nikon Microscope. Monolayers only (on coverslips) or MS with cells were used to exclude auto-fluorescence. Controls with primary Ab only and secondary Ab only (on both monolayers and MS with cells) were also used to exclude non-specific Ab binding. For negative control, human neural stem cells were used. Due to high auto-fluorescence of mouse calvarial tissue, it could not be used as a positive control for OCN staining.

2.3.16 Haematoxylin and Eosin (H&E) staining

The samples were stained in haematoxylin for 5 min, then with tap water, followed by a quick wash in 0.5% acid alcohol for 10 sec, then with tap water, followed by a wash with Scott's tap water for 1 min and then tap water, then stained with Eosin for 5 min and finally again washed with tap water. The samples were dehydrated in graded alcohol 50%, 70%, 90%, 100% and finally in Xylene, before mounting them with DPX (Dibutyl Phathalate Xylene) and imaging under ECLIPSE 90i Nikon Microscope. Mouse calvarial tissue was used as a positive control for H&E staining.

2.3.17 X-Ray Photon Spectroscopy (XPS) of 3D samples

On each time point, 3D agglomerate samples were analysed using the Kratos AXIS ULTRA with a mono-chromated Al kα X-ray source (1486.6eV) operated at 10 mA emission current and 12 kV anode potential (120 W). Samples were mounted on a microscope slide with double sided tape and then on the standard Kratos sample bar. Three wide (survey) scans were acquired for each sample. The chamber pressure remained better than 5 x 10^{-9} Torr after overnight pump down in the vacuum airlock. Charge neutralisation was required as the samples were non-conducting. Data were processed using CASAXPS. The elemental atomic % at the surface region of the samples was estimated from the peak areas in the wide scans using Kratos RSFs, the high-resolution spectra were charge corrected to C 1s at 285 eV and the peaks fitted with model components to ascertain the chemical environment of the atoms. The results have been expressed as Ca/N, P/N and Ca/P ratios. MS without cells were included to validate that quantification was performed with signals only from ECM and not glass material.

2.3.18 Sample preparation for SEM

For secondary electron imaging of 3D agglomerates, samples were first fixed in 4% PFA in PBS (at 4^0C) and then incubated in 100 µl $well^{-1}$ of 1% Osminin tetroxide for 45 min at RT, followed by dehydration by washing with increasing concentrations of ethanol (20%, 40%, 60%, 70%, 80%, 90% and up to 100%) and finally, Hexamethyldisilazane (HMDS) for approximately 5 minutes each. After washings, the samples were mounted on Aluminium stubs using Carbon adhesive tabs and left overnight in HMDS, to air dry in fume hood. Next day, samples were sputter-coated in platinum and secondary electron images were acquired using JEOL 6400 SEM or Philips (FEI) XL (30)-w SEM at electron beam of 5-10 kV.

The 3D agglomerates were also sectioned using a non-invasive method, where a fine spatula was used to segment the agglomerate into two halves without penetrating or touching the inside the agglomerate. The sectioned samples were again coated with platinum before visualising under SEM.

2.3.19 Sample preparation for Environmental SEM (ESEM)

Biological samples were fixed in 4% PFA in PBS, washed with distilled water three times and then added onto the sample holder with some moisture on, before visualising under the Philips XL30 FEG ESEM. The chamber pressure and temperature conditions were maintained such that the water vapour environment of the specimen became saturated and dehydration was prevented. ESEM images were acquired at electron beam of 5-10 kV.

2.3.20 Micro CT for visualising cells on PGMS

To study the 3D agglomerates formed from porous MS and hMSCs micro CT analysis was performed. For this, GFP-hMSCs were seeded at 10,000 cells cm^{-2} on AG6 P40 PGMS AW (2 cm^2) and cultured for 7 days. On day 4, fresh medium containing barium sulphate (1.5

µl/ml) was added (Chakrabarti et al. 1992) and on day 7, cells were fixed in 4% PFA in PBS (at 4^0C) for 10 min. After washing with PBS and cells were imaged under XRADIA Versa XRM–500. The imaging was performed using setting described in Table 2-6. Before performing this investigation, a validation study of barium loading on GFP-hMSCs was also performed as described in Appendix 5.

Table 2-6: Parameters for Micro Computational Tomography analysis for MS with cells.

Parameter	Lower magnification	Higher magnification
Resolution (nm)	2700	500
Binning	2	2
Image size (pixels)	1024	1024
Field of view (mm^3)	2.764	0.512
Optical magnification	4X	20X
Source Voltage (kV)	40	50
Power (W)	3	7
Current (µA)	75	80
Source distance (mm)	9	10
Detector distance (mm)	13	16
Exposure time (sec)	2	15
Projections	1600	1600

2.4 Statistical analyses

All statistical analyses were performed using IBM SPSS Statistics 22 and R version 3.3.1 (R Core Team 2016). Mean, standard deviation and standard errors were computed for at least three replicate samples in all experiments. For comparisons of relative density and tapped density, one-way ANOVA was performed. For comparison of elemental compositions, two-way ANOVA was performed. Detailed description of statistical models used in different experiments is provided in Table 2-7. For pairwise comparisons, post-hoc analyses using Least Significant Difference (LSD), equivalent to no adjustments, were carried out. P values <0.05 were considered significant.

Table 2-7:Statistical analyses in different experiments.

Experiment	Statistical analysis
BR01, BR03, BR04, BR05, BR06, BR07 AW01, AW03, AW04 PRE01, CP01, CP02, CP03, CP05, CP06, CP07, CP08, CP09 CV01, CV02 CD01, CD02, CD03, CD04*, CD05, CD06, CD07, CD08 COL03, COL04 MIN07 CON01 (DNA, ALP activity, collagen production, mineral production) CON02 (DNA, metabolic activity, ALP activity, collagen production, mineral production) TOX06, TOX07	Two-way ANOVA with MS-type and day as two fixed factors.
BR02, BR08 AW02 COL05, COL06, COL07, COL08, COL09, COL10 MIN02, MIN03, MIN04, MIN05, MIN06 CON01 (metabolic activity) TOX01, TOX02 (Day 3 readings) TOX03, TOX04	One-way ANOVA with MS-type as one fixed factor.
CA01, CA02, CA03, CA04	Two-way ANOVA with MS-type and cell seeding density as two fixed factors.
TOX05	Two-way ANOVA with MS-type and medium-type as two fixed factors.
TOX06 and TOX07 combined results	Generalized Linear Mixed Model with MS-type and day as two fixed factors and DNA content in CP07 and CP08 as random factor.

*In CD04, analysis was carried out twice.

Chapter 3 Material Characterisation

3.1 Introduction

The present work revolves around biological evaluation of degradable bulk and porous phosphate based glass (PBG) microspheres (MS) for bone tissue engineering applications. However, it is important to understand the physical and chemical composition and degradation properties of these MS, so that it can be related to the mesenchymal stem cell responses in subsequent chapters. This chapter presents the material characterisation analysis for the various particles used in this study.

In Section 3.2, the physical geometry of the particles is presented; followed by Section 3.3 and Section 3.4, where surface area of different particles and the porosity of porous MS are explored, respectively; leading on to Section 3.5 and Section 3.6, where the compositional characteristics of different particles and degradation studies, respectively are detailed. Finally, in Section 3.7 and Section 3.8, the results from all characterisation assessments have been discussed and concluded, respectively.

3.2 Particle geometry analyses

In order to evaluate the size of the different particles, laser diffraction (LD) was carried out as described in Section 2.2.2. In case of some MS batches, LD measurements were compared to major axis length (MAL) measurements, performed using image analysis (IA) as described in Section 2.2.1. Sphericity of particles was also measured using image analysis as described in Section 2.2.1.

3.2.1 Angular-shaped particles

A single batch of angular shaped particles was used in this study called AG1 P45 BGMP (AG-Ahmed generation, P45-glass formulation

and BGMP-bulk glass microparticles). SEM examination (see Figure 3-1 a-b) showed that particles in this batch had very sharp edges and contained finer particulates deposited on their surface, which were less than 10 µm in size. The LD measurement showed a bimodal size distribution for these particles with two peaks at 10 µm and 79 µm, respectively (see Figure 3-1 c). The sphericity measurements showed a low mean sphericity of 0.64±0.01 for these particles (see Figure 3-1 d).

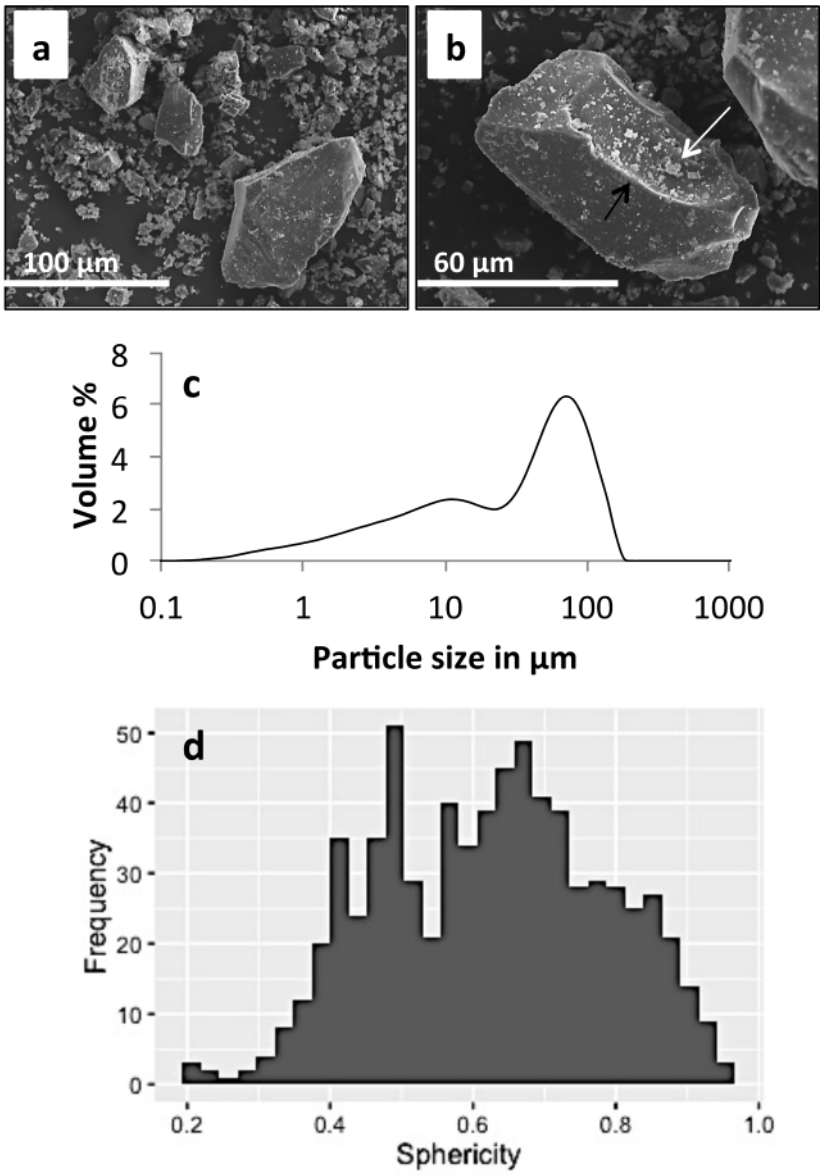

Figure 3-1: Morphology of AG1 P45 BGMP. (a-b) SEM images that AG1 P45 BGMP contained angular-shaped particles with sharp edges (black arrow) and particulates less than 10 µm in size (white arrow), on their surface. (c) Laser diffraction measurements showing bimodal distribution. (d) Sphericity measurements. AG-Ahmed generation, P45-glass formulation, BGMP-bulk glass microparticles.

3.2.2 Borosilicate glass microspheres

Due to processing difficulties, two batches of borosilicate glass microspheres (BSG), BSG Batch 1 and BSG Batch 2, were used in the study. SEM examination (see Figure 3-2) showed that both batches contained spherical particles with few particulates (<10 µm in size) deposited on their surface.

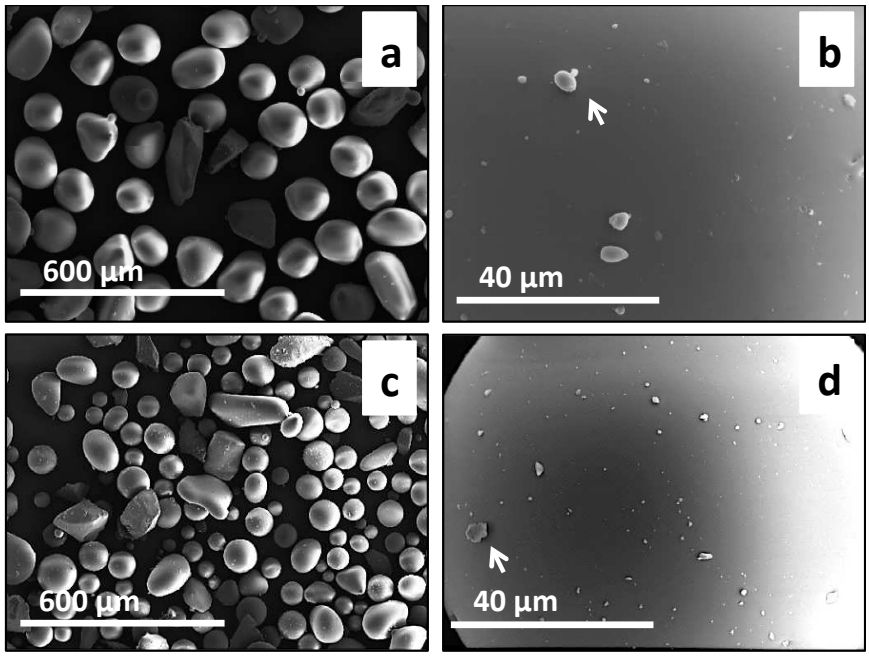

Figure 3-2: SEM images of BSG. The BSG Batch 1 (a, b) and BSG Batch 2 (c, d) contained particles with spherical morphology with finer particulates (<10 µm) deposited on their surface (indicated as arrows).

LD measurements, see Figure 3-3 a, showed that the volume weighted mean size (D[4,3]) of BSG Batch 1 was more than BSG Batch 2, with values of 139 µm and 107 µm, respectively, with measurement error of 1%. This trend was also visible through MAL measurements, see Figure 3-3 b, where mean MAL of BSG Batch 1 and BSG Batch 2 were 125±2 µm and 72±3 µm, respectively. Despite these differences, both batches had similar sphericity distribution of 0.82±0.01 and 0.83±0.01, respectively (see Figure 3-3 c).

Comparison of LD measurements of the BSG Batch 1 and BSG Batch 1 AW showed D[4,3] values of 139 µm and 124 µm, respectively,

with measurement error of 1%, see Figure 3-3 a. This suggested a slight decrease in size of BSG after acid washing.

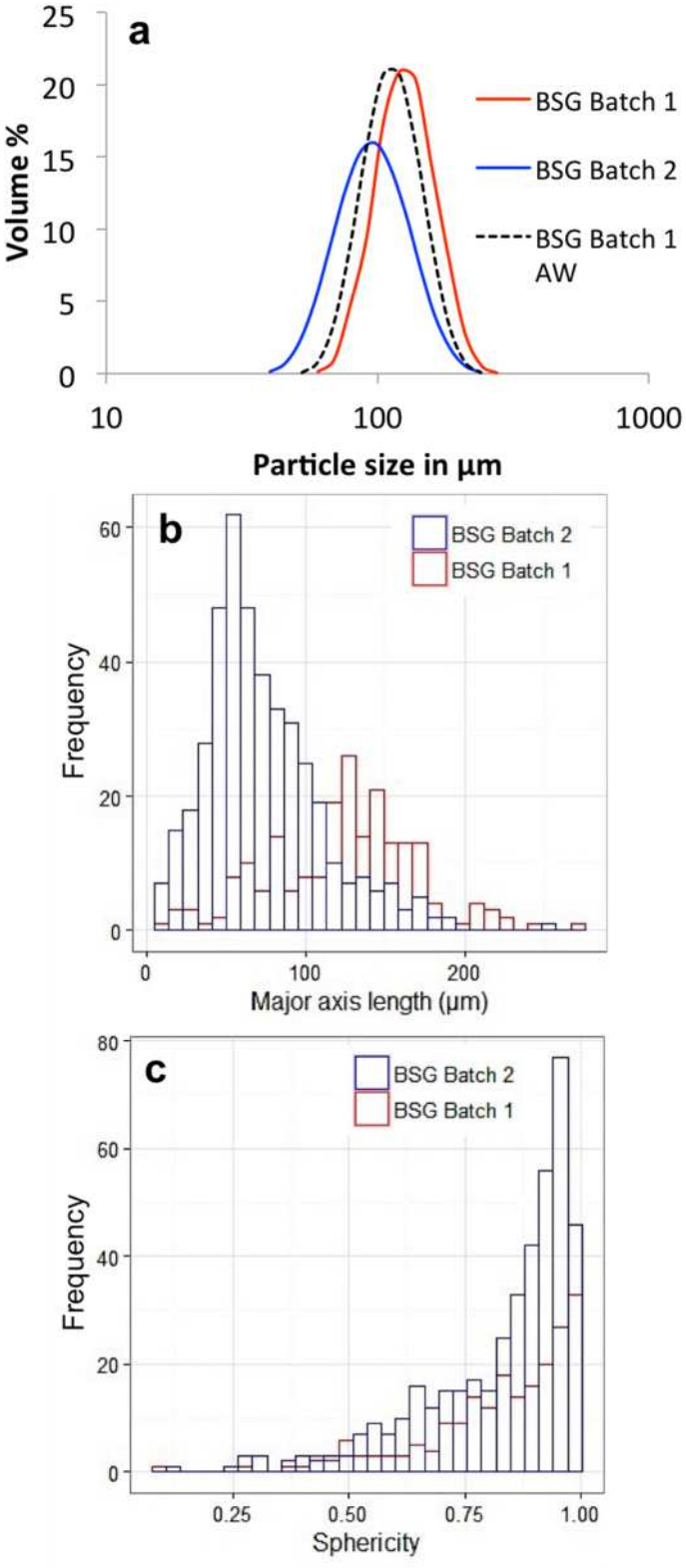

Figure 3-3: Morphology of BSG. (a) Laser diffraction, (b) Major axis length and (c) Sphericity measurements of different BSG batches.

3.2.3 Phosphate based glass bulk microspheres

Seven batches of PBG bulk MS were used in the present study.

The first batch was AG1 P45 BGMS (AG-Ahmed generation, P45-glass formulation and BGMS-bulk glass microspheres) and it contained particles both with spherical morphology as well as angular shapes (see Figure 3-4 a-d). At the same time, there was also presence of some aggregated particles in this batch. The D[4,3] and mean sphericity for this batch was 139 μm (with 1% measurement error) and 0.85±0.01, respectively, both significantly more in comparison to AG1 P45 BGMP, see Figure 3-4 e-f.

The next six batches of PBG bulk MS included- three batches with P45 formulation (P45 BGMS Batch 1, P45 BGMS Batch 2 and P45 BGMS Batch 3) and three batches with P40 formation (P40 BGMS Batch 1, P40 BGMS Batch 2 and P40 BGMS Batch 3).

SEM examination, see Figure 3-5 a-j, showed that these batches also contained particles with spherical morphology (all with mean sphericity of ca. 0.9. Moreover, unlike BSG and AG1 P45 BGMP, there were only a few particulates (<10 μm in size) deposited on their surface.

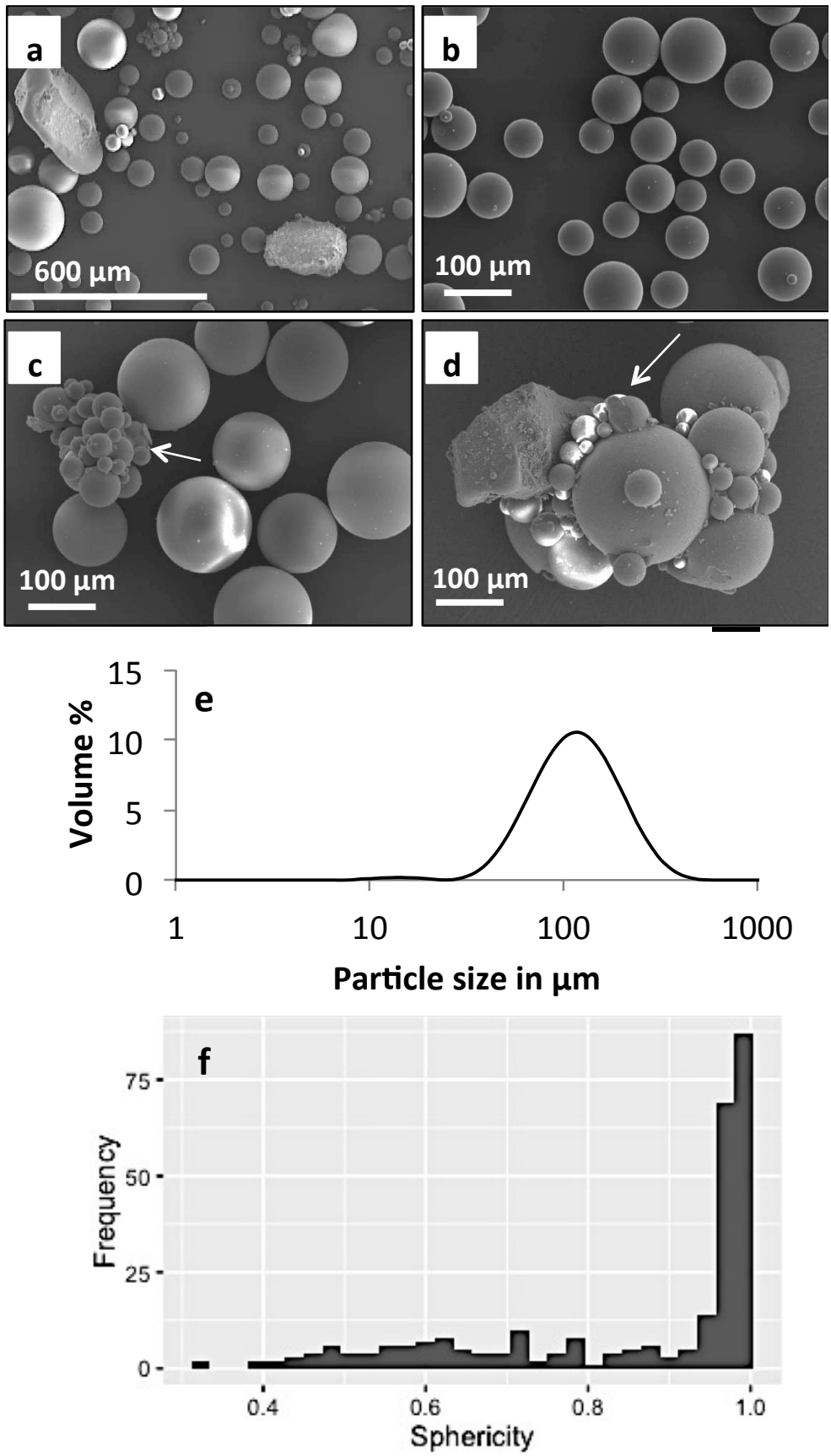

Figure 3-4: Morphology of AG1 P45 BGMS. (a-d) SEM images, arrows indicate agglomerated particles. (e) Laser diffraction measurements. (f) Sphericity measurements.

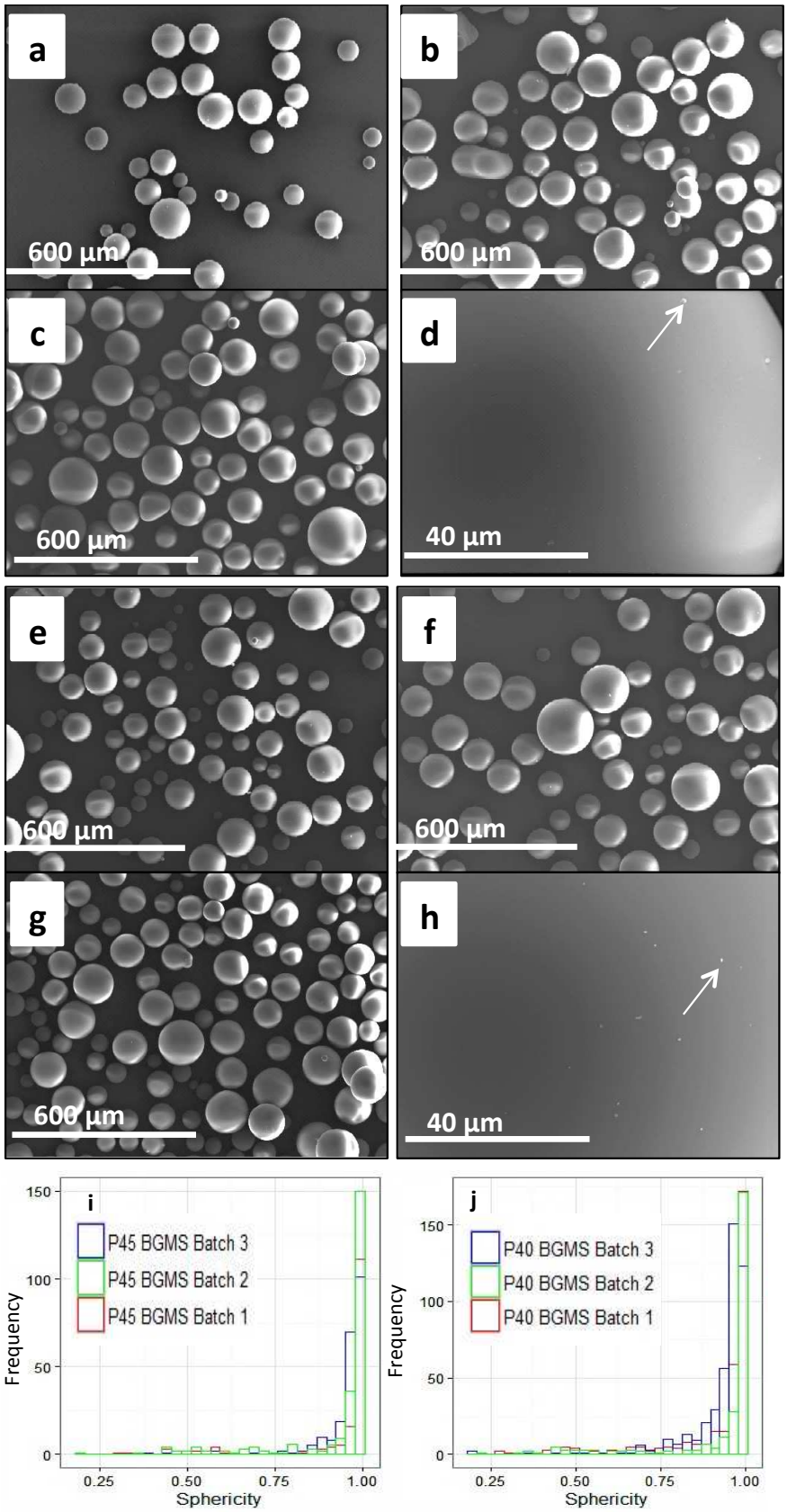

Figure 3-5: Morphology of P45 PGMS and P40 BGMS. SEM images of (a) P45 BGMS Batch 1, (b) P45 BGMS Batch 2, (c, d) P45 BGMS Batch 3, (e) P40 BGMS Batch 1, (f) P40 BGMS Batch 2, (g, h) P40 BGMS Batch 3. Sphericity measurements of (i) P45 BGMS batches and (j) P40 BGMS batches. Arrows indicate particulates deposited on glass surface.

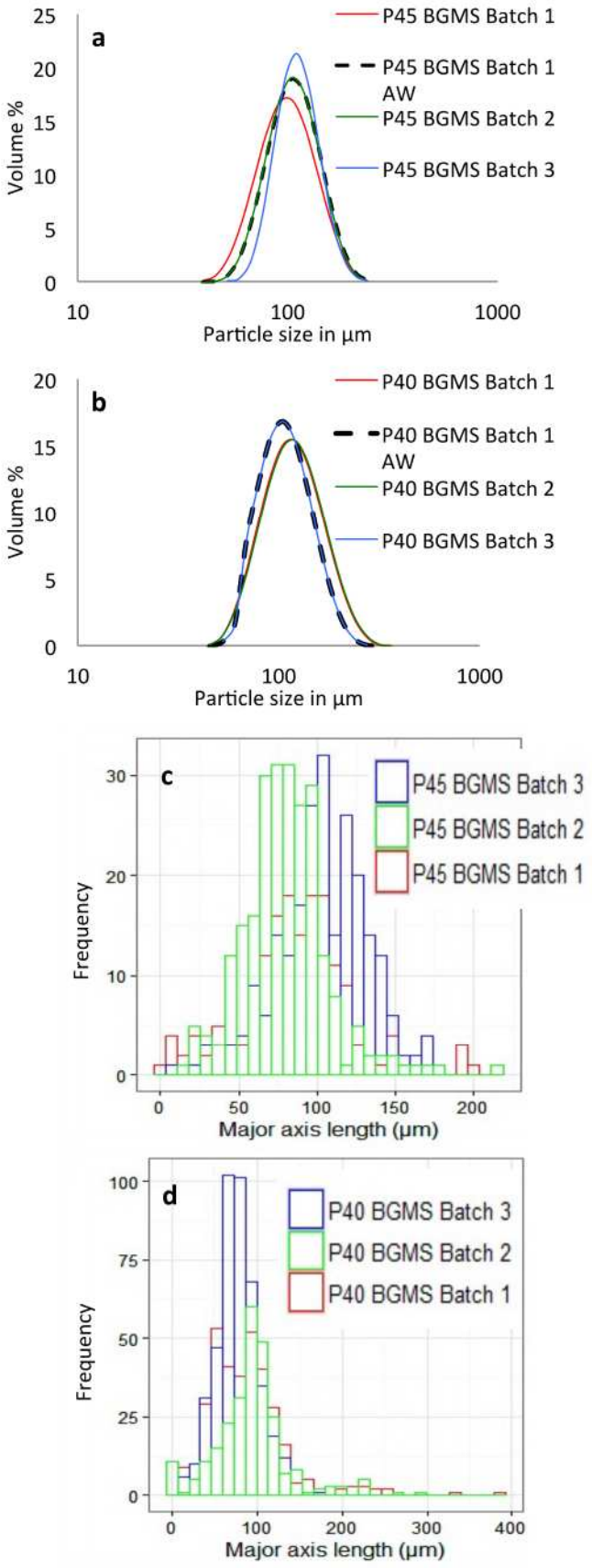

Figure 3-6: Particle size distribution of P45 BGMS batches and P40 BGMS batches. (a, b) Laser diffraction measurements and (c, d) major axis length measurements.

LD and MAL measurements, see Figure 3-6, showed that P45 BGMS Batches 1, 2 and 3 had D[4,3] of 111 µm, 118 µm and 121 µm, respectively, with estimated error of 1%, and mean MAL of 86±3 µm, 80±2 µm and 104±2 µm, respectively. Moreover, P40 BGMS Batches 1, 2 and 3 had D[4,3] of 132 µm, 134 µm and 117 µm, respectively, with estimated error of 1% and mean MAL of 89±3 µm, 94±3 µm and 78±1 µm, respectively. These results suggested subtle size variations from batch-to-batch for P45 BGMS and P40 BGMS.

Finally, comparison of D[4,3] values of P45 BGMS Batch 1 (111 µm) to P45 BGMS Batch 1 AW (119 µm) and of P40 BGMS Batch 1 (132 µm) to P40 BGMS Batch 1 AW (136 µm), showed subtle increase in the size of particles after the acid wash, see Figure 3-6 a-b.

3.2.4 Phosphate based glass porous microspheres

Three batches of porous PBG MS were used in this study. The first batch included heterogeneous AG1 P45 PGMS (AG-Ahmed generation, P45-glass formulation and PGMS-porous glass microspheres). SEM examination (Figure 3-7 a-b) showed that this batch contained particles with spherical morphology and pores on their surface. Further examination of cross-sectioned MS (Figure 3-7 c-d) showed that these pores were not limited to outer surface but were also present on the inside of these MS; however, most of the internal pores seemed to be closed from the outside. There was also evidence of pore interconnectivity in the form of tunnels (approximately 4 µm to 30 µm wide) inside these MS. The LD measurements showed a bimodal distribution for this batch with two peaks at 17 µm and 120 µm and D[4,3] of 137 µm (Figure 3-7 e). The mean sphericity for this batch was 0.92±0.01.

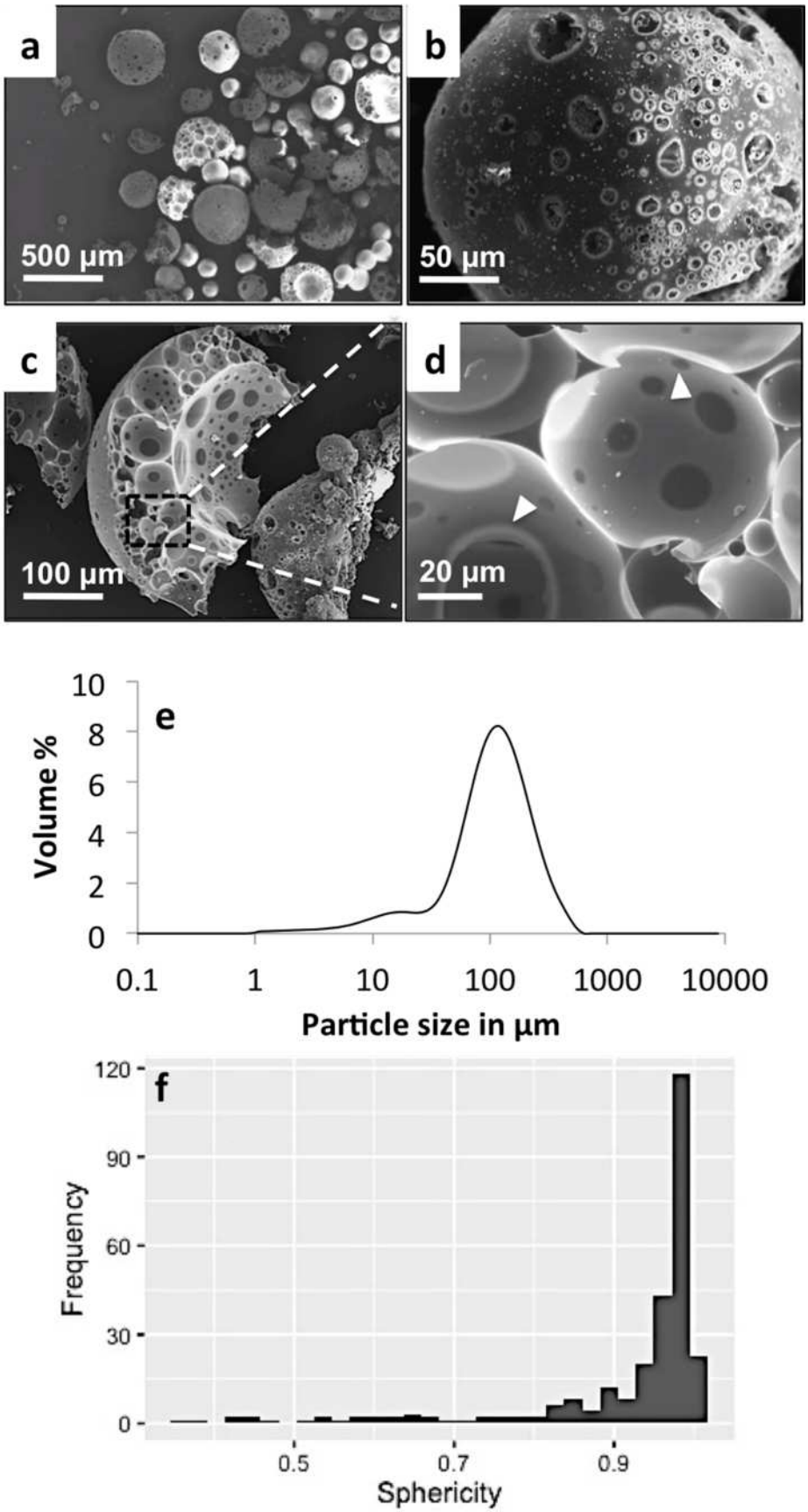

Figure 3-7: Morphology of AG1 P45 PGMS. (a) SEM images. (b) Laser diffraction measurement. (c) Sphericity measurement. Arrow-heads indicate pore interconnectivity.

When AG1 P45 PGMS were sieved (as described in Section 2.2.3), particles were collected in the size ranges of 0-45 µm, 45-100 µm, 100-200 µm, 200-250 µm, 250-300 µm and 300-500 µm. SEM examination, see Figure 3-8, showed that some particles in 0-45 µm fraction were angular-shaped and others were spherical but none of them contained pores on their surface. In the 45-100 µm size range, majority of the particles were spherical with no pores and a few angular shaped particles had pores on their surface. In the size ranges of >100 µm, majority of the particles were spherical and contained pores on their surface. Due to variability observed in porosity in different size ranges, these fractions were further characterised for surface area and pore window sizes, shown in Section 3.3 and Section 3.4.2, respectively.

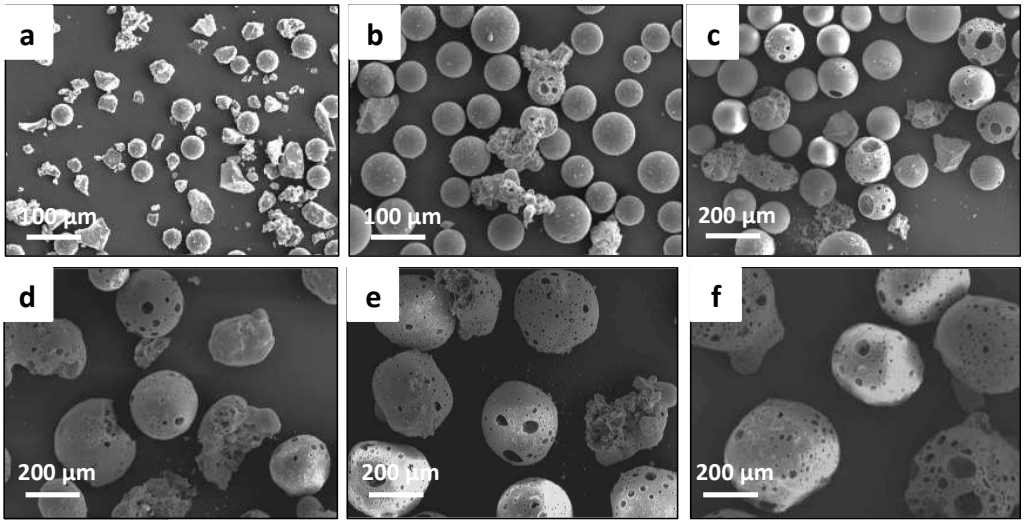

Figure 3-8: SEM images of sieved fractions of AG1 P45 PGMS. (a) 0-45 µm, (b) 45-100 µm, (c) 100-200 µm, (d) 200-250 µm, (e) 250-300 µm and (f) 300-500 µm.

The next batches of porous MS included-AG5 P40 PGMS AW, AG6 P40 PGMS and AG6 P40 PGMS AW (AG-Ahmed generation, P40-glass formulation and PGMS-porous glass microspheres and AW-acid washed).

SEM examination (see Figure 3-9 a) showed that AG5 P40 PGMS AW, AG6 P40 PGMS AW and AG6 P40 PGMS batches contained spherical particles with pores on their surface. Moreover, closer

examination showed that some of the pores were closed on the surface of AG6 P40 PGMS but not on AG5 P45 PGMS AW or AG6 P45 PGMS AW, which indicated that the acid washing may have opened up some pores. More precise measurements of pore windows, present on the surface of these MS, have been described in Section 3.4.2.

MAL and LD measurements, see Figure 3-9 b-c, showed that AG5 P40 PGMS AW, AG6 P40 PGMS and AG6 P40 PGMS AW had mean MAL of 102±2 µm, 118±4 µm and 138±3 µm, respectively and D[4,3] values of 118 µm, 139 µm and 140 µm, respectively, within the error of measurement of 1%. These results suggested batch-to-batch variability and increase in MAL of PGMS after the acid wash.

Finally, AG5 P40 PGMS AW, AG6 P40 PGMS and AG6 P40 PGMS AW had sphericity values of 0.89±0.01, 0.80±0.01 and 0.87±0.01, which indicated no batch-to-batch variability but increase in sphericity after the acid wash in AG6 batch (see Figure 3-9 d).

A summary of the LD, MAL and sphericity measurements for all of particles used in this study is tabulated in Table 3-1.

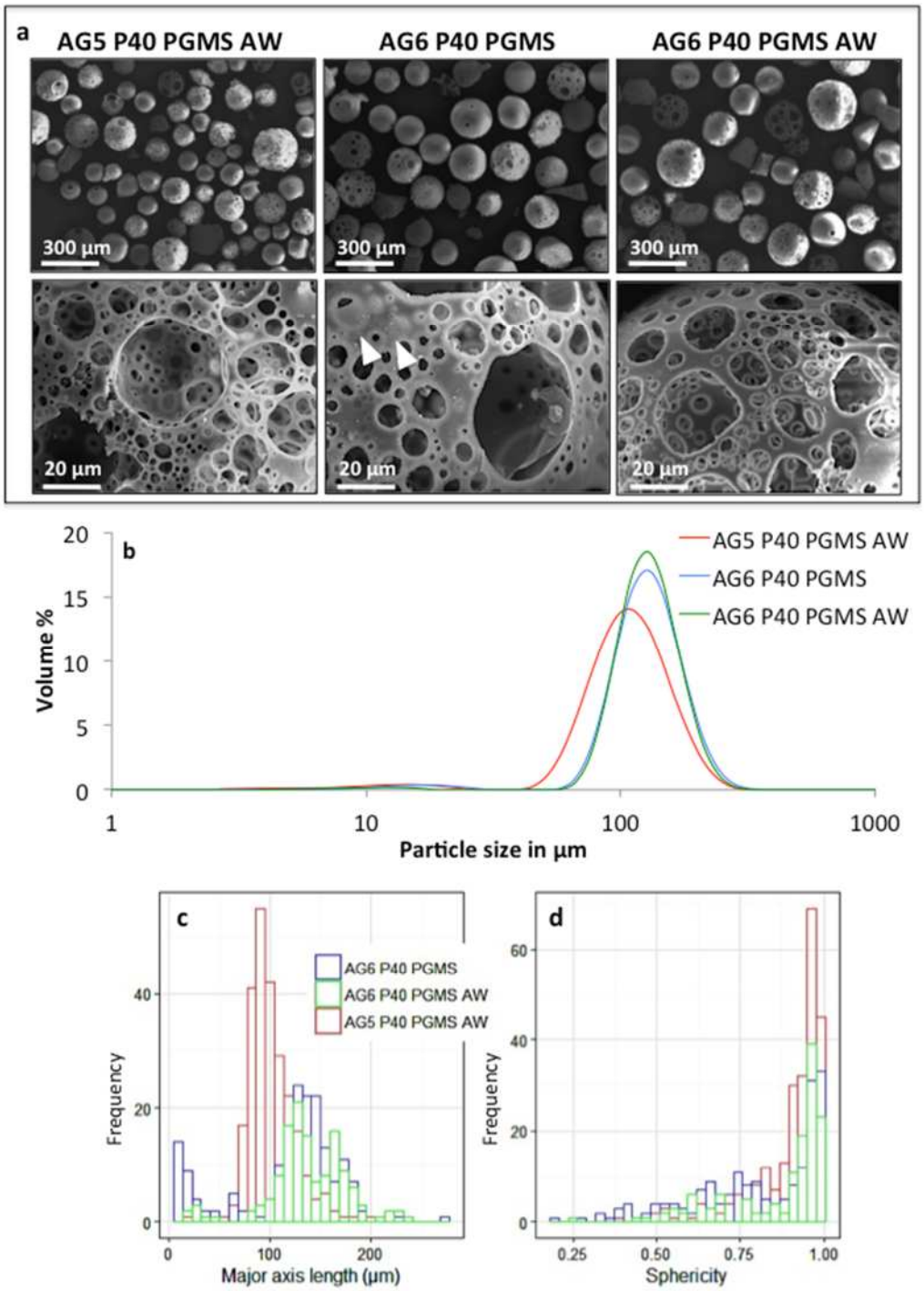

Figure 3-9: Morphology of AG5 P40 PGMS AW, AG6 P40 PGMS and AG6 P40 PGMS AW. (a) SEM images. (b) Laser diffraction measurements. (c) Major axis length measurements. (d) Sphericity measurements. Arrow-heads indicate closed pores on the surface of MS.

Table 3-1: Summary of morphology: laser diffraction, sphericity and major axis length (MAL) measurements of particles.

Sample	Laser diffraction	Image analysis			
	D[4,3] (µm) ± 1% error	N	MAL (µm)		Sphericity
			Range	Mean ± S.E.	Mean ± S.E.
AG1 P45 BGMP	48	746	-	-	0.64±0.01
AG1 P45 BGMS	139	285	-	-	0.85±0.01
AG1 P45 PGMS	137	274	-	-	0.92±0.01
BSG Batch 1	139	208	14-270	125±3	0.82±0.01
BSG Batch 2	107	423	8-256	72±2	0.83±0.01
BSG Batch 1 AW	124	-	-	-	-
P45 BGMS Batch 1	111	162	8-197	86±3	0.92±0.01
P45 BGMS Batch 2	118	241	18-216	80±2	0.92±0.01
P45 BGMS Batch 3	121	229	9-170	104±2	0.94±0.01
P45 BGMS Batch 1 AW	119	-	-	-	-
P40 BGMS Batch 1	132	343	8-387	89±3	0.90±0.01
P40 BGMS Batch 2	134	251	19-290	94±3	0.92±0.01
P40 BGMS Batch 3	117	441	13-178	78±1	0.93±0.01
P40 BGMS Batch 1 AW	136	-	-	-	-
AG5 P40 PGMS AW	118	253	15-206	102±2	0.89±0.01
AG6 P40 PGMS	139	184	8-272	118±4	0.80±0.01
AG6 P40 PGMS AW	140	132	17-241	138±3	0.87±0.01

3.3 Surface area of particles

Surface area measurements for all particles were performed as described in Section 2.2.4 and results are tabulated in Table 3-2.

Table 3-2: Surface area measurements.

Sample	Surface area ($cm^2\ g^{-1}$) ± S.D.*
45-100 µm AG1 P45 PGMS	648
100-200 µm AG1 P45 PGMS	2611
200-250 µm AG1 P45 PGMS	2798
250-300 µm AG1 P45 PGMS	3108
300-500 µm AG1 P45 PGMS	4276
BSG Batch 1	523±149
BSG Batch 2	926±44
P45 BGMS Batch 1	429±13
P45 BGMS Batch 2	524±229
P45 BGMS Batch 3	226±8
P40 BGMS Batch 1	335±141
P40 BGMS Batch 2	203±21
P40 BGMS Batch 3	423±194
AG5 P40 PGMS AW	6470±200
AG6 P40 PGMS	10267±287
AG6 P40 PGMS AW	11075±368

*S.D. was calculated using two measurements per sample. For AG1 batch only one measurement was taken. The measurement error for analysis was 11%.

Surface area measurements for 45-100 µm, 100-200 µm, 200-250 µm, 250-300 and 300-500 µm sieved fractions of AG1 P45 PGMS showed that all sieved fractions had an order of magnitude higher surface area as compared to 45-100 µm sieved fraction. Moreover, the surface area also seemed to increase with increasing size range of porous MS with 100-200 µm, 200-250 µm, 250-300 and 300-500 µm sieved fractions at ca. 2.6 x 10^4 cm^2g^{-1}, 2.8 x 10^4 cm^2g^{-1}, 3.1 x 10^4 $cm^2g^{-1}$and 4.3 x 10^4 cm^2g^{-1}, respectively. These results are in line with the SEM images in Figure 3-8 b-f, where larger-sized porous MS showed more pores on their surface.

Next, all other batches of bulk and porous MS were also analysed for surface area. Comparison of BSG Batches showed that BSG Batch 2 had nearly 1.5 times the surface area as compared to BSG Batch 1.

In case of P40 BGMS and P45 BGMS batches, however, they were all in similar range within the error of analysis, which was 11%. The AG6 P40 PGMS with and without acid wash had high surface areas of $>10^5$ $cm^2\,g^{-1}$, indicating no significant change in surface area after the acid wash. However, these values were significantly higher than the AG5 P40 PGMS AW at ca. 6.5 x 10^4 $cm^2\,g^{-1}$, showing batch-to-batch variability.

3.4 Porosity analyses

Porosity, pore size distribution and interconnecting tunnel measurements of porous MS were performed using Micro CT/image analysis and Cryo-FIB/SEM as described in Sections 2.2.5 and 2.2.6, respectively. Moreover, the MAL and roundness of pore windows present on the surface of porous MS were also measured as described in Section 2.2.7.

3.4.1 Porosity, pore size and pore interconnectivity

The 3D reconstruction of un-sieved AG1 P45 PGMS has been shown in Figure 3-10 and the image analysis gave a porosity value of 45±10%. The Micro CT scan for this sample was carried out for 2 hours and due to low S/N (signal to noise ratio), the porosity measurement may have affected. In order to increase the S/N further, the scan was extended to 3 h for a smaller field of view for 200-300 µm AG1 P45 PGMS and this resulted in higher-resolved greyscale images, illustrated in Figure 3-11. The 3D tomography of this gave a porosity value of 82±10%.

Next, a region from this 3D tomography was randomly selected and pore size measurements were performed as described in Section 2.2.5. The results, see Figure 3-12, showed a mean±S.D. pore diameter of 17.3±6.5 µm (ranging from 1.0-30 µm) and a mean±S.D trabecular thickness (strut size of material) of 3.7±1.2 µm (ranging from 1.0-7.7 µm) for the selected section.

Confirmatory Cryo-FIB/SEM was carried out on AG6 P40 PGMS AW and images in Figure 3-13 showed that the pores in this batch were also interconnected but the size of interconnections was <5 μm in diameter.

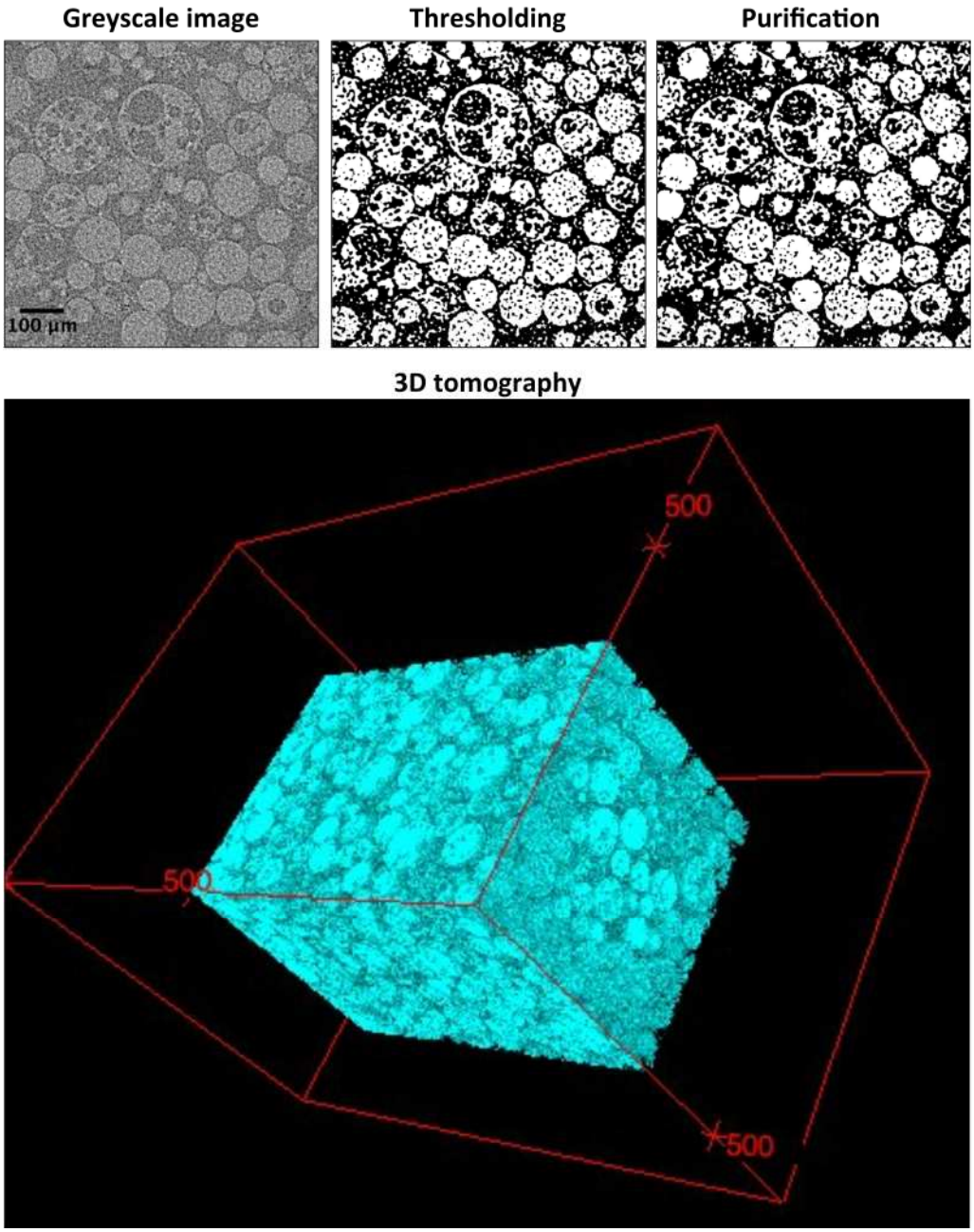

Figure 3-10: Micro CT analysis of AG1 P45 PGMS. Greyscale images or raw images were generated after X-ray imaging, which were then thresholded to separate the material from the background signal and further cleaned (purified) to remove noise. The purified images were then used to generate the 3D tomography (cyan colour represents material) and perform porosity measurements. The 3D reconstruction had a porosity of 45±10% and the markings on red cubes indicate scale in µm.

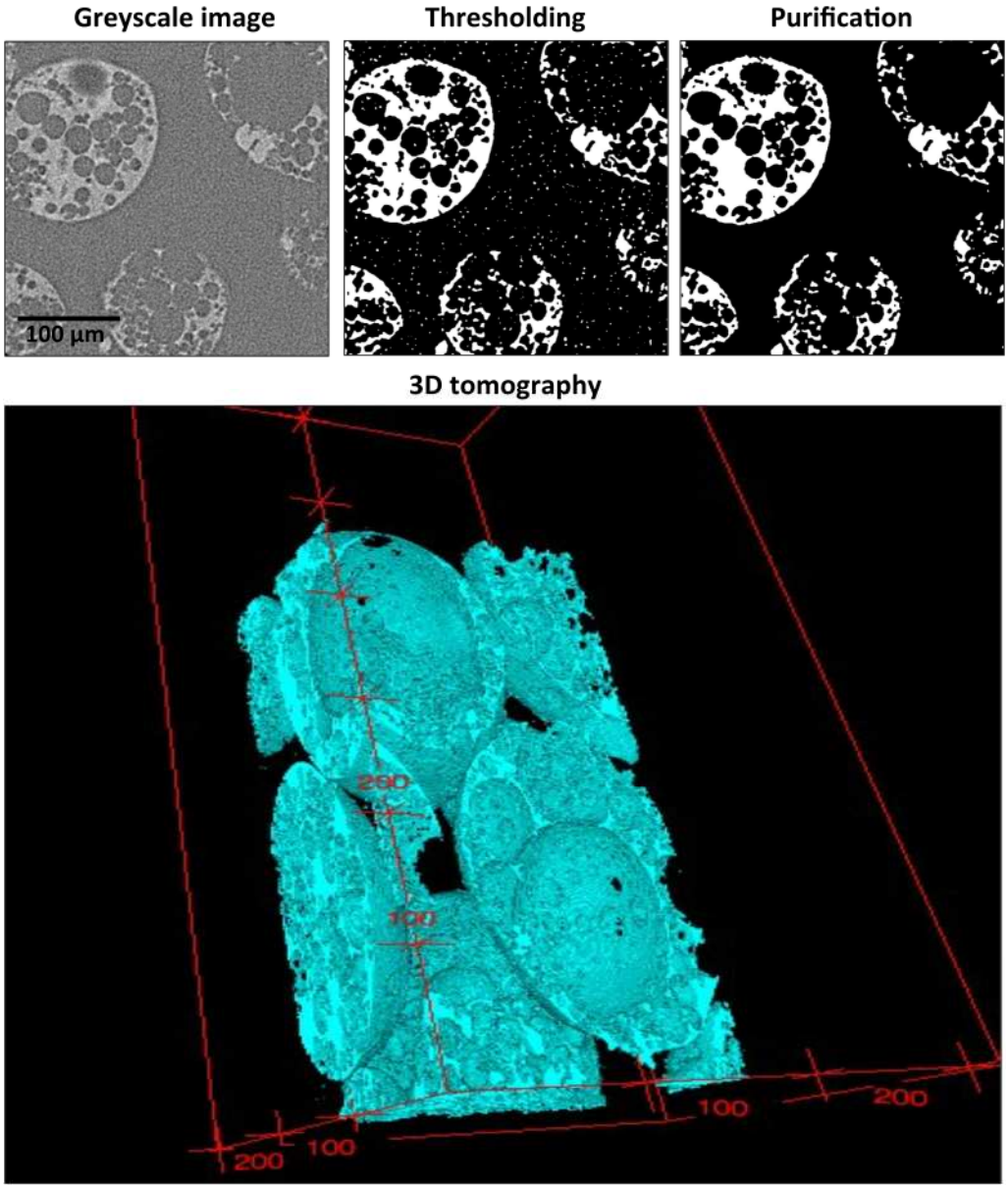

Figure 3-11: Micro CT analysis of AG1 P45 PGMS 200-300 µm. Greyscale images or raw images were generated after X-ray imaging, which were then threshold to separate the material from the background signal and further cleaned (purified) to remove noise. The purified images were then used to generate the 3D tomography (cyan colour represents material) and perform porosity measurements. The 3D reconstruction has a porosity of 82 ± 10% and the markings on red cubes indicate scale in µm.

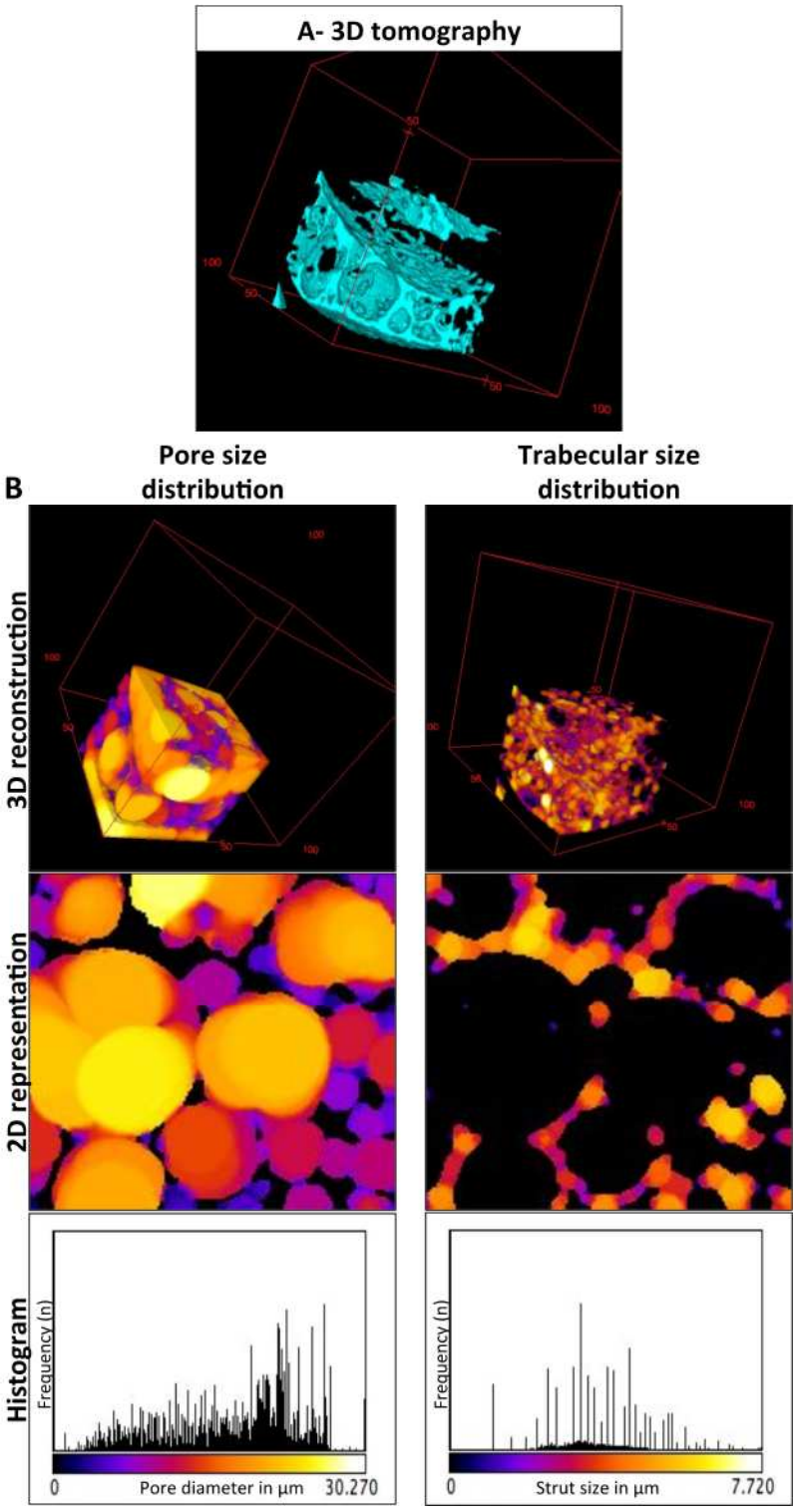

Figure 3-12: Structural analysis of AG1 P45 PGMS 200-300 µm using micro CT. (A) 3D tomography of the selected region showed presence of a number of pores in the internal structure of a porous MS. The markings on red cubes indicate scale in µm. (B) 3D constructions (top), 2D representations (middle) and histograms (bottom) of the pore size distributions and trabecular thickness (strut size) of same 3D tomography. Yellow regions are thicker than the blue regions. The pore diameter ranged from 1-30 µm and strut size ranged from 1-8 µm.

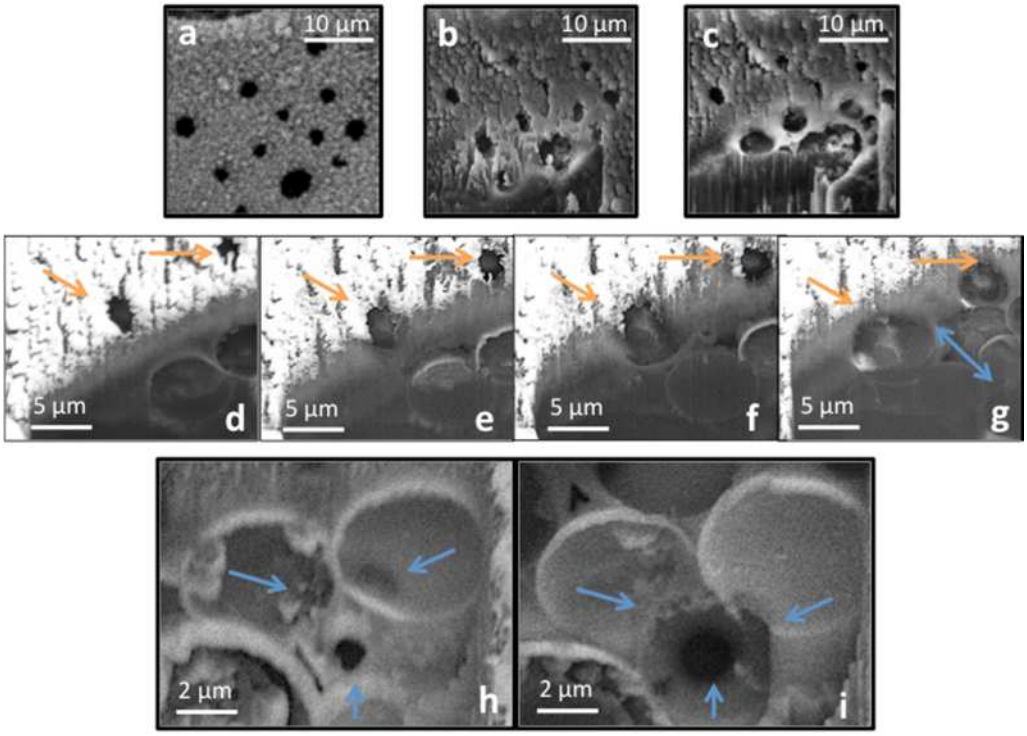

Figure 3-13: Internal pore structure of AG6 P40 PGMS AW using Cryo-FIB SEM. (a) Backscattered image showed the presence of pores on the surface of PGMS. These pores had pore windows of less than 5 µm and the surface of these MS shows rough topography. SEM (b-c) and BSE (d-f) images showed that after sectioning with ion beam, though the pore windows were small, the pore diameters of same pores were much bigger. (h, i) Higher mag BSE images also showed interconnectivity between three larger pores in the internal structure of PGMS. The pores had a diameter in the range of 5-6 µm and interconnecting tunnels with of 1-2 µm. Yellow arrows indicate open pores and blue arrows indicate interconnection between pores.

3.4.2 Pore window size distribution on PGMS

Pore window measurements were initially performed on AG1 P45 PGMS in the size ranges of 100-200 µm, 200-250 µm, 250-300 µm and 300-500 µm and the corresponding results have been shown in Figure 3-14. There was an increase in mean pore window MAL as the MS size increased. Moreover, there were larger pore windows (>25 µm) present on MS >250 µm in diameter.

Next, pore window measurements were also performed on AG5 P40 PGMS AW, AG6 P40 PGMS AW and AG6 P40 PGMS samples so as to investigate batch-to-batch variability and effect of acid washing on pore windows.

The results in Figure 3-15 A-B showed that the pore windows AG5 P40 PGMS AW and AG6 P40 PGMS AW had similar pore window MAL and pore window roundness distributions, with mean MAL at 4.2±0.1 µm and 3.8±0.1 µm, respectively and mean roundness at 0.58±0.01 for both.

The results in Figure 3-15 A-B also showed that before acid washing AG6 P40 PGMS had lower pore window MAL of 4.0±0.1 µm and higher pore window roundness of 0.60±0.01. The MAL distribution shifted towards the mean and there was higher proportion of pore windows at higher end of roundness, after acid washing. However, despite these effects, the mean MAL of pore windows remained below 5 µm.

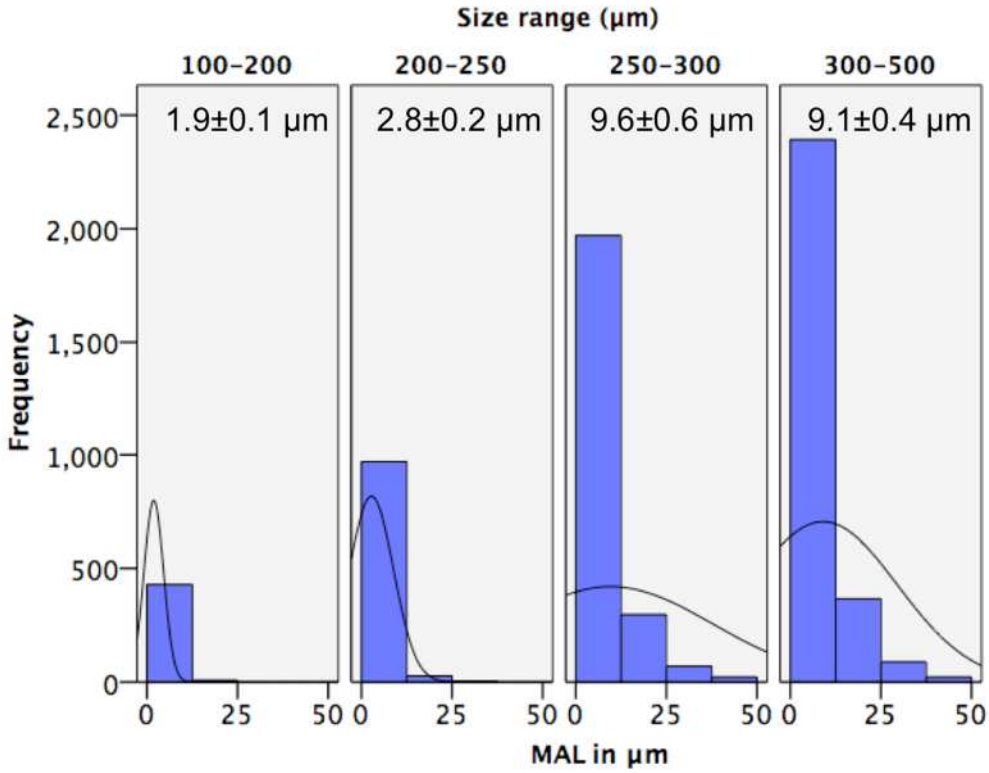

Figure 3-14: Major axis length (MAL) measurements of sieved fractions of AG1 P45 PGMS. Bars represent frequency and curve represents best-fit distribution curve. Mean ± S.E. is shown on top of distribution of each size range. Bigger pore windows (>25 µm and up to 50 µm) were observed only for MS in size range of 250—500 µm.

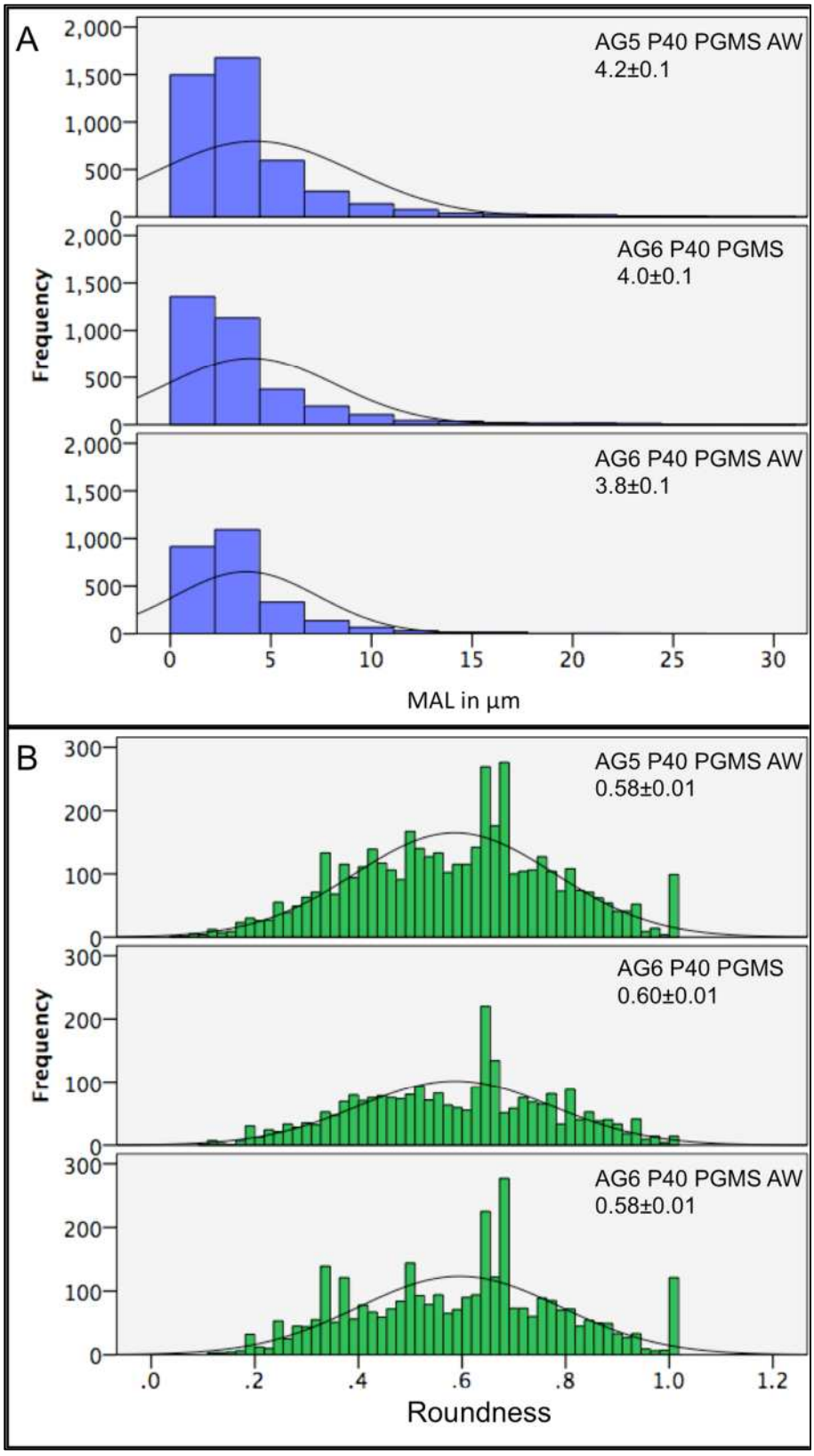

Figure 3-15: Major axis length (A) and sphericity (B) measurements of AG5 P40 PGMS AW, AG6 P40 PGMS and AG6 P40 PGMS AW. Bars represent frequency and curve represents best-fit distribution curve. Mean ± S.E. is shown on top of distribution of each batch.

3.5 Particle compositional analyses

3.5.1 Relative density measurements

The results in Figure 3-16 A showed that the relative density of AG1 P45 BGMP was 2.75±0.01 (mean ± S.D.), which was same as the density of previously reported P45 glass discs (Hasan et al. 2012). However, after flame spheroidisation, the density of AG1 P45 BGMS, AG1 P45 PGMS reduced to 2.68±0.01 and 1.96±0.04, respectively, which indicated closed porosity of 2% and 28%, respectively in them.

Comparison of relative densities of BSG Batch 1 and BSG Batch 2 (see Figure 3-16 B) showed that there was 3.5% higher relative density of BSG Batch 2 as compared to BSG Batch 1, with values of 2.16±0.01 and 2.23±0.01, respectively, suggesting some batch-to-batch variability. Also, separate comparisons of P45 BGMS batches or P40 BGMS batches showed significant differences among them, again suggesting batch-to-batch variability.

Borosilicate (SAMCO, UK), P45 and P40 (Hasan et al. 2012) in form of bulk glass, are known to have relative densities of 2.34, 2.75 and 2.73, respectively. Therefore, comparison of these values to the measured relative densities of different MS batches indicated closed porosity of up to 9% inside these bulk MS, see Table 3-3 for details. In case of P45 BGMS and P40 BGMS, closed porosity was also visible in backscattered electron images in Figure 3-26, shown in Section 3.5.3.

Comparison of AG5 P40 PGMS AW and AG6 P40 PGMS AW also showed some differences between the two batches, again indicative of batch-to-batch variability. Finally, comparison of all porous MS batches suggested that the acid wash significantly reduced closed porosity from 28% and 35%, in case of AG1 P45 PGMS and AG6 P40 PGMS, respectively, to 15% and 8%, in case of AG5 P40 PGMS AW

and AG6 P40 PGMS AW, respectively, which was at similar level as bulk MS.

3.5.2 Tapped density measurements

The results in Figure 3-17 A showed that the tapped density of AG1 P45 BGMP, AG1 P45 BGMS and AG1 P45 PGMS was 1.0 g cm^{-3}, 1.3 g cm^{-3} and 0.6 g cm^{-3}, respectively.

Comparison of BSG batches showed that BSG Batch 1 had 30% more tapped density as compared to BSG Batch 2 and likewise there were also significant differences among P45 BGMS batches, P40 BGMS batches and P40 PGMS AW batches see Figure 3-17 B.

When the tapped density was normalised to the closed porosity, AG1 P45 BGMS still had higher normalised tapped density as compared to AG1 P45 BGMP. Moreover, there was also batch-to-batch variability in BSG, P45 BGMS and P40 BGMS but not P40 PGMS AW. Finally, comparison of AG6 P40 PGMS and AG6 P40 PGMS AW suggested that there was a decrease in normalised density from 0.77±0.01 g cm^{-3} to 0.61±0.01 g cm^{-3}.

A summary of density measurements for all of particles used in this study has been provided in Table 3-3.

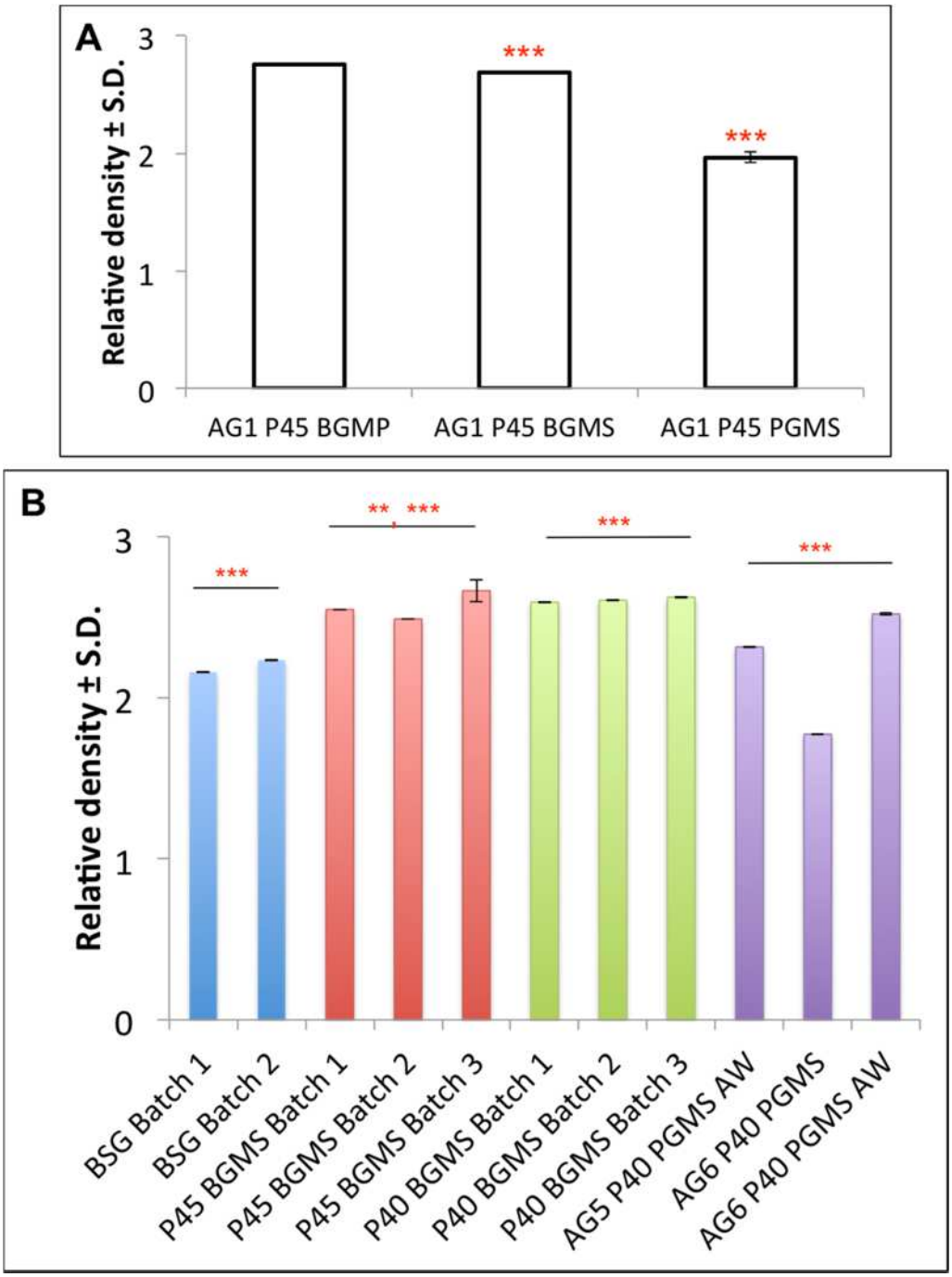

Figure 3-16: Relative density measurements. (A) Comparison of AG1 P45 BGMP, AG1 P45 BGMS and AG1 P45 PGMS (n=20). (B) Comparison of next generation MS batches (n=10). **p<0.01, ***p<0.001.

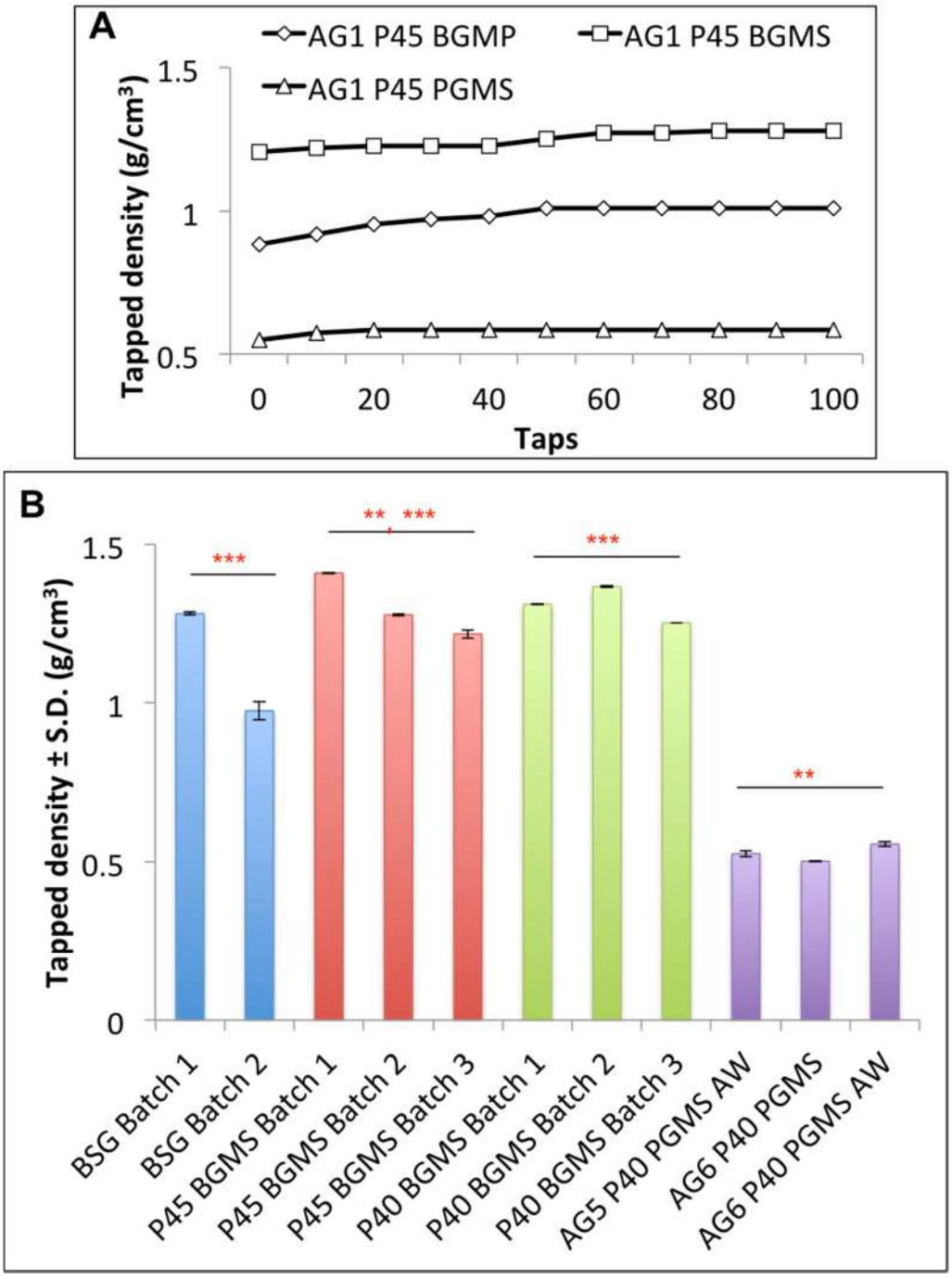

Figure 3-17: Tapped density measurements. (A) Comparison of AG1 P45 BGMP, AG1 P45 BGMS and AG1 P45 PGMS. (B) Comparison of next generation MS batches. n=3, **p<0.01, ***p<0.001.

Table 3-3: Summary of density and closed porosity measurements of particles.

Sample	Relative density ± S.D.	Closed porosity (%)*	Tapped density ±S.D. (g/cm^3)	Normalised density ±S.D. (g/cm^3)#
AG1 P45 BGMP	2.75±0.01	-	1.01	1.01±0.01
AG1 P45 BGMS	2.69±0.01	2	1.28	1.31±0.03
AG1 P45 PGMS	1.97±0.04	29	0.58	0.81±0.01
BSG Batch 1	2.16±0.01	8	1.28±0.01	1.39±0.01
BSG Batch 2	2.23±0.01	5	0.97±0.03	1.02±0.01
P45 BGMS Batch 1	2.55±0.01	7	1.41±0.01	1.52±0.01
P45 BGMS Batch 2	2.49±0.01	9	1.28±0.01	1.41±0.01
P45 BGMS Batch 3	2.67±0.07	3	1.22±0.01	1.26±0.01
P40 BGMS Batch 1	2.59±0.01	5	1.31±0.01	1.38±0.01
P40 BGMS Batch 2	2.61±0.01	5	1.37±0.01	1.44±0.01
P40 BGMS Batch 3	2.63±0.01	4	1.25±0.01	1.30±0.01
AG5 P40 PGMS AW	2.31±0.01	15	0.53±0.01	0.62±0.01
AG6 P40 PGMS	1.77±0.01	35	0.50±0.01	0.77±0.01
AG6 P40 PGMS AW	2.52±0.01	8	0.56±0.01	0.61±0.01

*Relative density of borosilicate (SAMCO, UK), P45 and P40 (Hasan et al. 2012) are known to be 2.34, 2.75 and 2.73, respectively. These values were used to calculate closed porosities in each batch. #Normalised density represents tapped density after normalisation to closed porosity.

3.5.3 Elemental compositional analyses

To investigate the composition of glass particles or MS under study, energy dispersive X-ray spectroscopy (EDS) was carried out as described in Section 2.2.10. Initial EDS compositional and mapping analyses were performed on AG1 P45 BGMP, AG1 P45 BGMS and un-sieved AG1 P40 PGMS.

In case of AG1 P45 BGMP, the oxide percentages of P_2O_5-CaO-MgO-Na_2O-Fe_2O_3 (mol%) were 48±1%, 15±1%, 23±1%, 11±1%, 4±1%, respectively (see Figure 3-18) and after spheroidisation, i.e., AG1 P45 BGMS, the oxide percentages were 43±1%, 17±1%, 26±1%, 9±1%, 4±1%, respectively, showing slight reduction in P and Na contents and slight increase in Ca and Mg contents, respectively. To identify the source of these changes, the elemental analysis results for AG1 P45 BGMS were plotted as a function of MS diameter. The results, see Figure 3-19, confirmed that MS <45 μm in diameter had

higher Ca, Mg and Fe contents and lower P and Na contents. However, this trend was not visible in MS with diameter >45 µm.

In case of AG1 P45 PGMS, the oxide percentages of P_2O_5-CaO-MgO-Na_2O-Fe_2O_3 (mol%) were 33±2%, 39±8%, 17±1%, 6±1%, 3±1%, respectively, which suggested that introduction of porosity led to higher Ca content but reduced P, Mg and Na contents in MS. At higher magnification, see Figure 3-20, the EDS analysis revealed that there was higher Ca and lower P present near the pore edges as compared to other regions of the same MS in AG1 P45 PGMS batch. This indicated retention of Ca-based porogen near the pore edges, together with the evaporation of lighter elements, such as P and Na, in the same region.

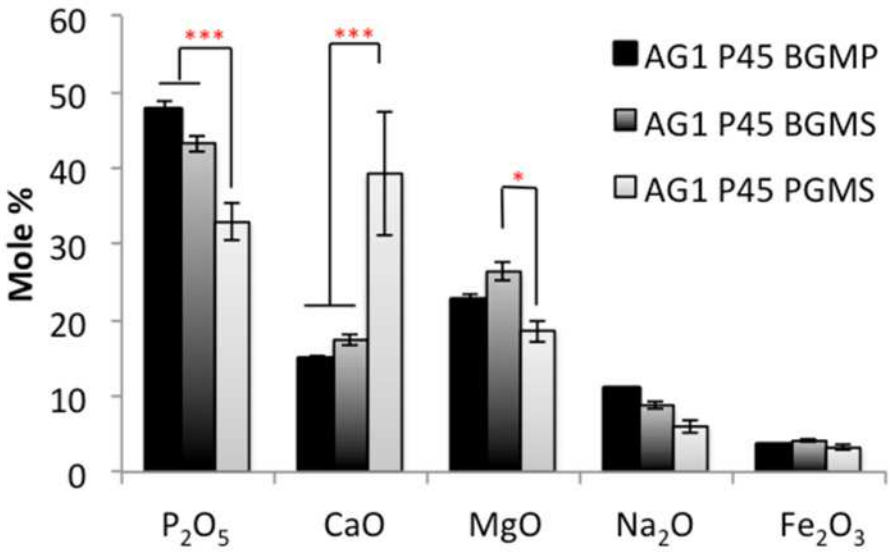

Figure 3-18: Elemental composition of AG1 P45 BGMP, AG1 P45 BGMS and AG1 P45 PGMS using EDS. *p<0.05, ***p<0.001. Error bars represent S.E.

Confirmatory EDS mapping analysis, see Figure 3-21, showed that in case of AG1 P45 BGMS and AG1 P45 PGMS, MS <45 µm in diameter had significantly reduced Na and P contents and increased Mg and Ca contents as compared to larger sized MS within the same sample, in line with results in Figure 3-19. Moreover, there were also some particles present in AG1 P45 BGMP with higher Ca content as compared to other particles.

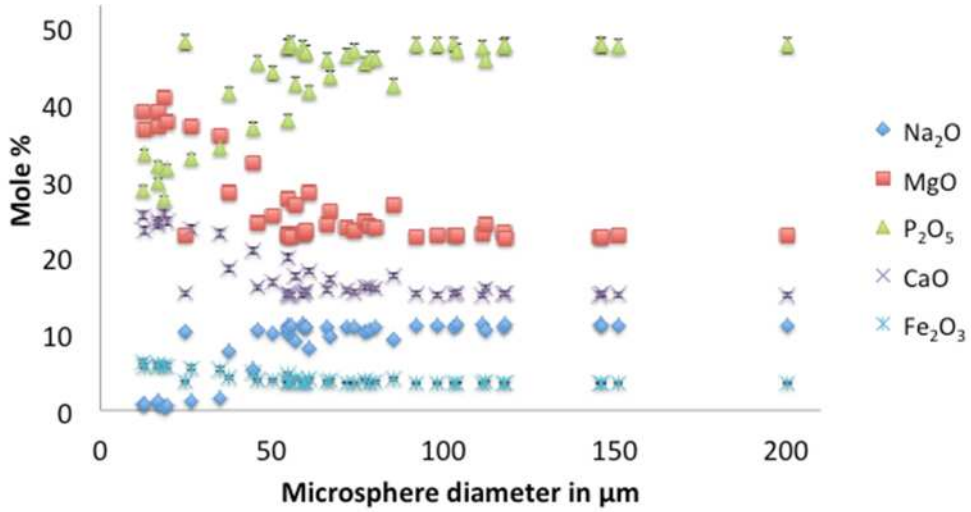

Figure 3-19: Compositional analysis for AG1 P45 BGMS as an effect of MS diameter. Notice the presence of higher Ca, Mg and Fe contents and lower P and Na contents in MS with diameters less than 45 µm. Error bars represent ±2% measurement error.

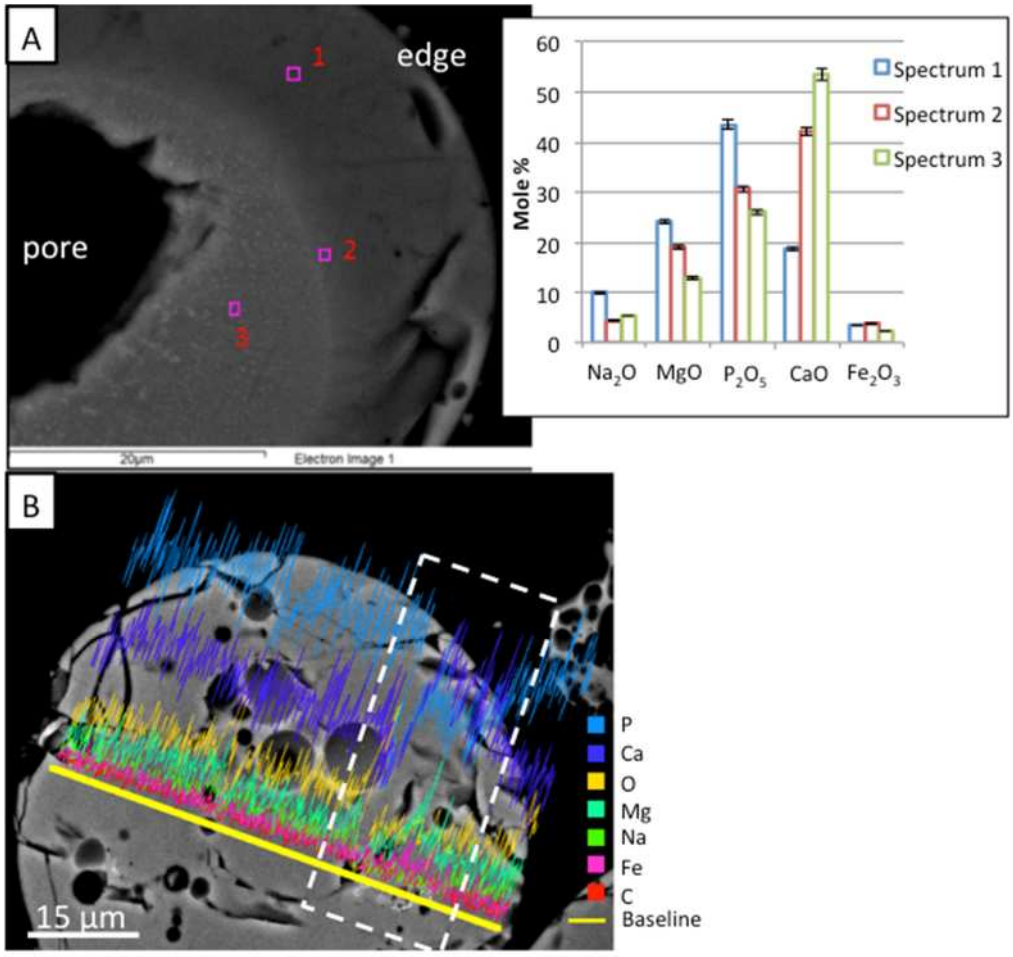

Figure 3-20: Retention of porogen in AG1 P45 PGMS. Scale bar- 20 µm. (A) Three elemental spectra from in porous MS were selected and analysed. The higher contrast regions near the pores showed more CaO and lesser Na_2O, MgO, P_2O_5 and Fe_2O_3 as compared to other regions. (B) Elemental

line scan in porous MS showed higher Ca content in some regions (white box) as compared to other regions. Error bars- 2% measurement error.

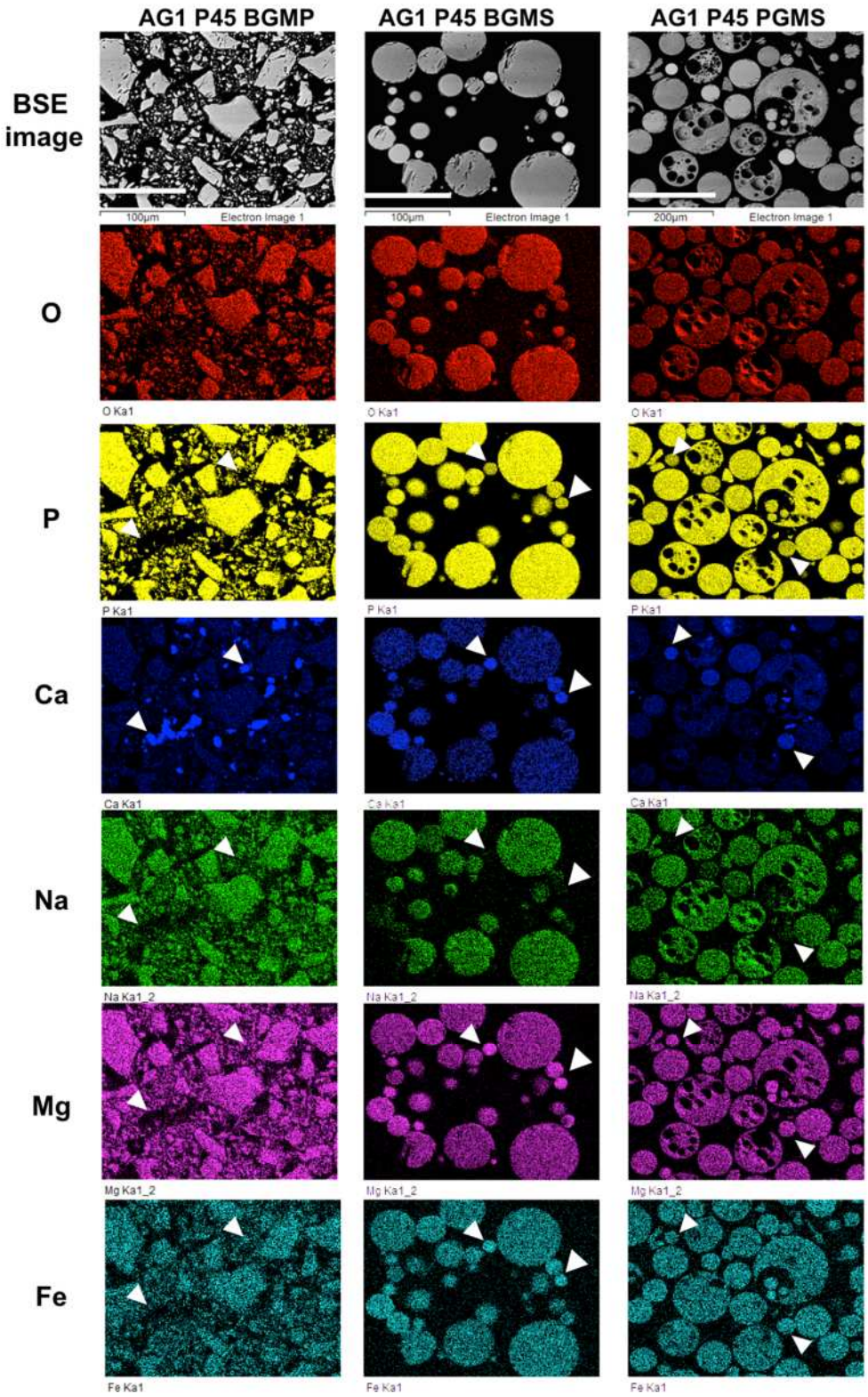

Figure 3-21: EDS mapping analysis of AG1 P45 BGMP, AG1 P45 BGMS and AG1 P45 PGMS. White arrow-heads indicate particles of with higher Ca, Mg and Fe contents and lower P and Na contents. Scale bars- 100 µm for AG1 P45 BGMP, AG1 P45 BGMS and 200 µm for AG1 P45 PGMS.

Next, the compositional analyses were performed for all other particles used in the present study to explore batch-to-batch variability.

In case of BSG, see Figure 3-22, at fixed boron oxide mole% of 9.5% (SAMCO, UK), the oxide percentages of SiO_2-Na_2O-Al_2O_3-CaO were 81±2%, 6±1%, 2±1% and 1±1%, respectively for BSG Batch 1 and 83±2%, 5±1%, 3±1% and 2±1%, respectively for BSG Batch 2, showing no differences between the two batches. In BSG Batch 1, there were also traces of K_2O and BaO, measured at 0.3±0.1% and 0.2±0.1%, respectively. Moreover, EDS mapping analysis, see Figure 3-23, suggested non-homogeneous elemental composition across MS in BSG Batch 1, where some MS had more Na and Al as compared to other MS. However, in BSG Batch 2, such variability was less common.

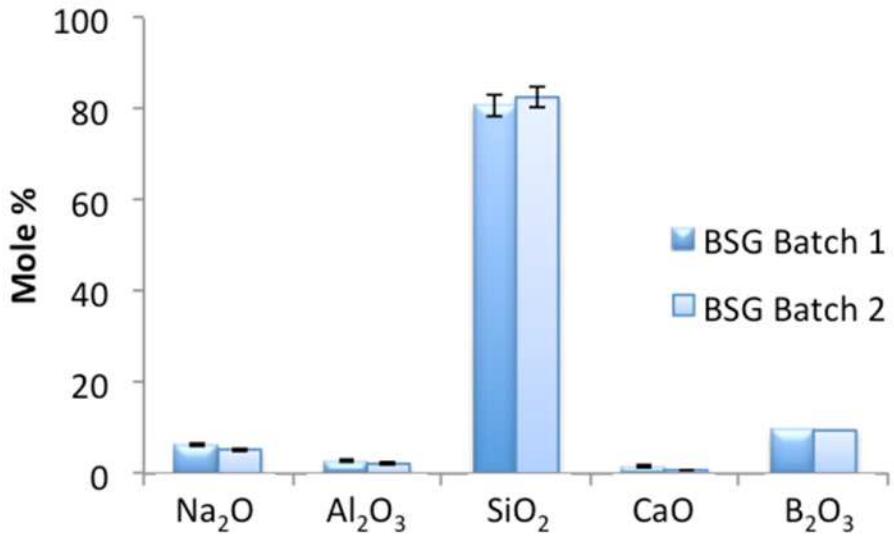

Figure 3-22: Elemental composition of BSG Batch 1 and BSG Batch 2 using EDS. Error bars represent S.E.

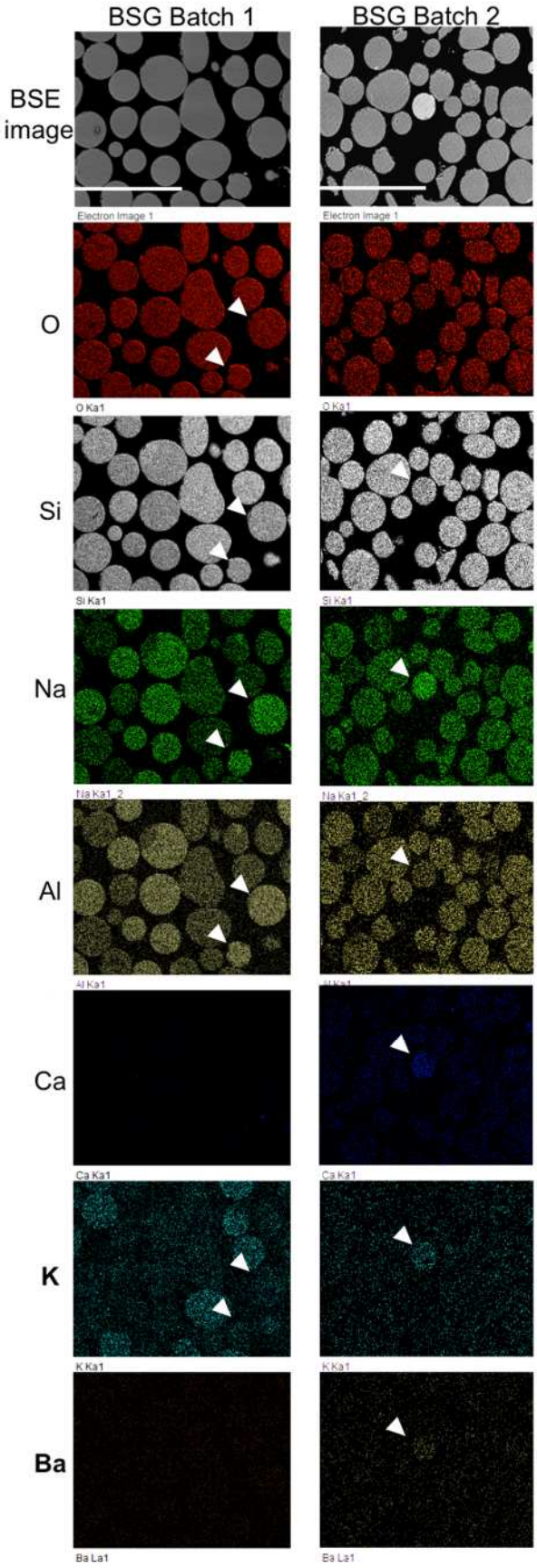

Figure 3-23: EDS mapping analysis of BSG Batch 1 and BSG Batch 2. White arrow-heads indicate MS with different elemental composition relative to other MS within the same sample. Scale bars- 300 µm.

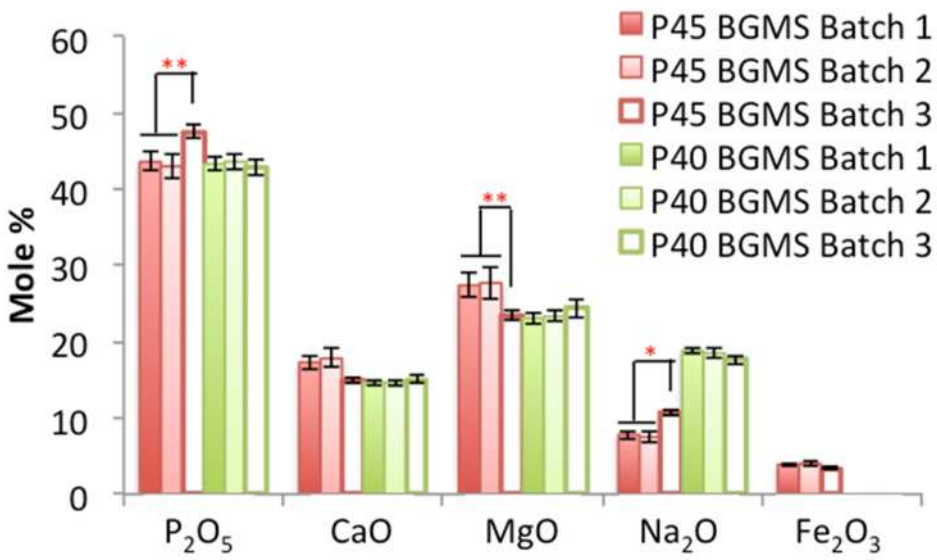

Figure 3-24: Elemental composition of P45 BGMS Batches 1, 2 and 3 and P40 BGMS Batches 1, 2 and 3 using EDS. *p<0.05, **p<0.01. Error bars represent S.E.

Elemental quantification (mol%) results for P45 and P40 BGMS batches, see Figure 3-24 and Table 3-4, showed that despite different nominal compositions of P45 and P40 glasses, the P_2O_5, CaO and MgO contents in P45 BGMS and P40 BGMS were in similar range of 43-48%, 15-18% and 23-27%, respectively. However, there was no Fe_2O_3 and 18-19% Na_2O in P40 BGMS batches in comparison to 3-4% Fe_2O_3 and 8-11% Na_2O in P45 BGMS batches.

Separate comparisons of three P40 BGMS batches showed no significant differences between their elemental compositions. However, there was 4-5% higher P_2O_5 and 2-3%, 3-4%, 3% and 1% lower CaO, MgO, Na_2O and Fe_2O_3, respectively, in P45 BGMS Batch 3 compared to P45 BGMS Batches 1 and 2, suggesting some batch-to-batch variability.

Again, the elemental mapping analysis, see Figure 3-25 and Figure 3-26, showed that P45 BGMS batches 1 and 2 had non-homogenous elemental composition, similar to as seen in AG1 P45 BGMS, AG1 P45 PGMS and BSG Batch 1. However, this was not observed in case of P45 BGMS Batch 3 or any of the P40 BGMS batches. Additionally, the BSE images in Figure 3-25 and Figure 3-26 also showed presence of closed porosity in all P45 or P40 BGMS batches.

Comparison of elemental composition of AG5 P40 PGMS AW, AG6 P40 PGMS and AG6 P40 PGMS AW, see Figure 3-27, showed that the acid wash was not leading to any significant change in chemical composition of AG6 batch. However, there was 9% lower CaO while 6%, 2% and 2% higher P_2O_5, MgO and Na_2O contents, respectively, in AG6 P40 PGMS AW compared to AG5 P40 PGMS AW, suggesting batch-to-batch variability. Further analysis, see Figure 3-28, also confirmed that the acid wash was unable to completely remove excess Ca from the edges of the pores. The retention of excess Ca across all three PGMS batches was also visible through elemental mapping analysis, shown in Figure 3-29.

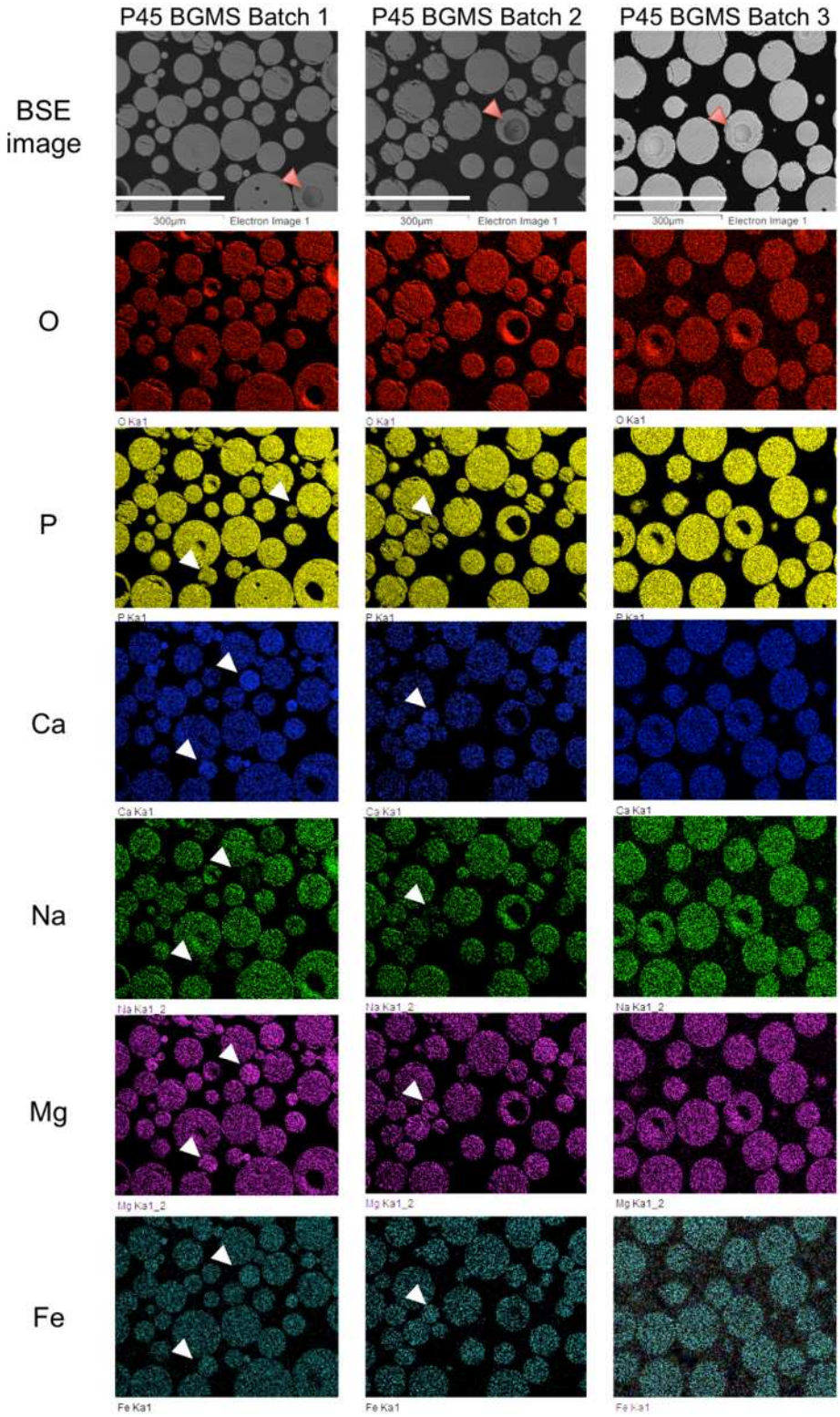

Figure 3-25: EDS mapping analysis of P45 BGMS Batches 1, 2 and 3. Within batch variability in P45 BGMS Batches 1 and 2 is indicated by white arrow-heads and closed porosity is indicated by red arrow-heads in BSE images. Scale bars- 300 µm.

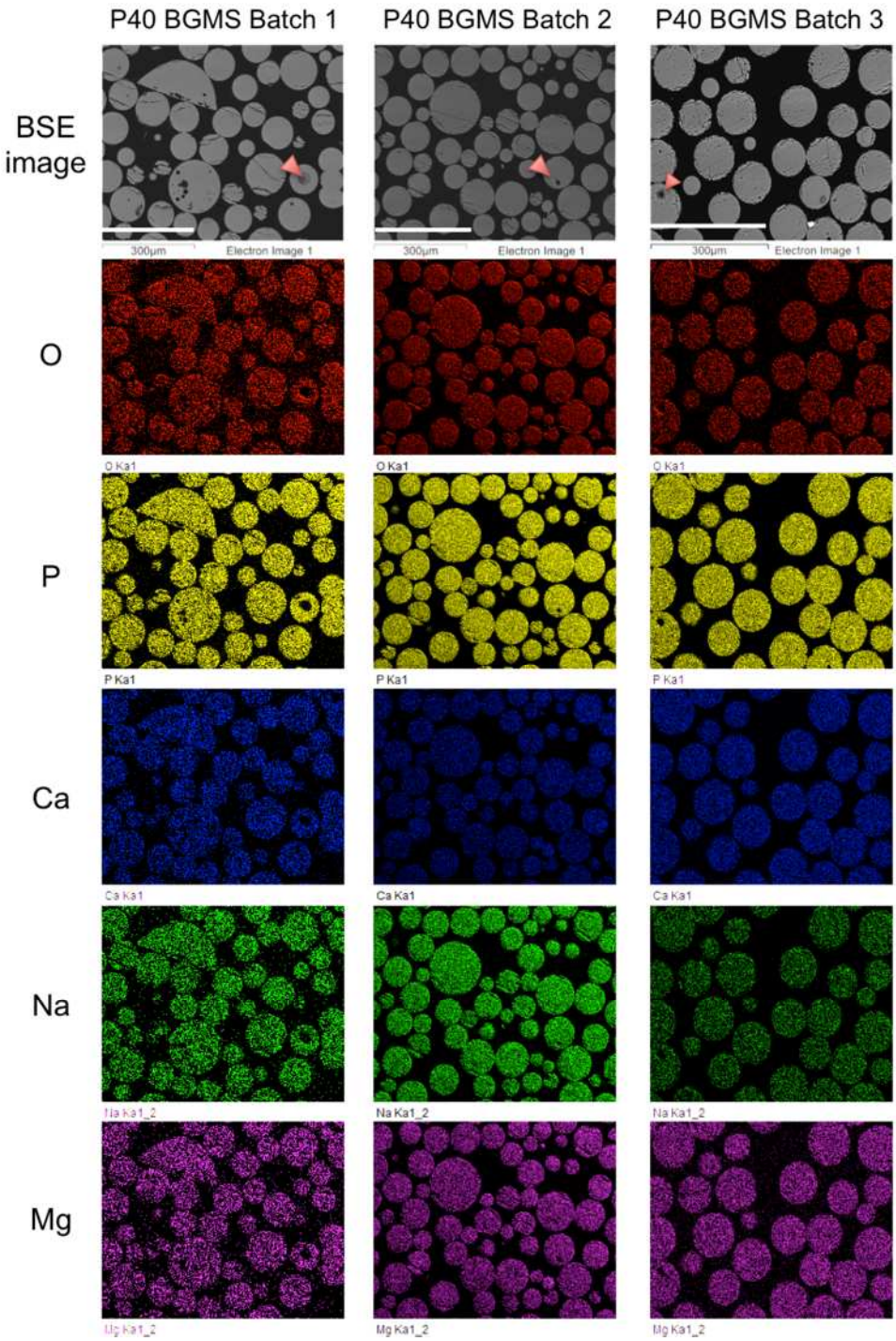

Figure 3-26: EDS mapping analysis of P40 BGMS Batches 1, 2 and 3. Closed porosity is indicated by red arrow-heads in BSE images. Scale bars- 300 µm.

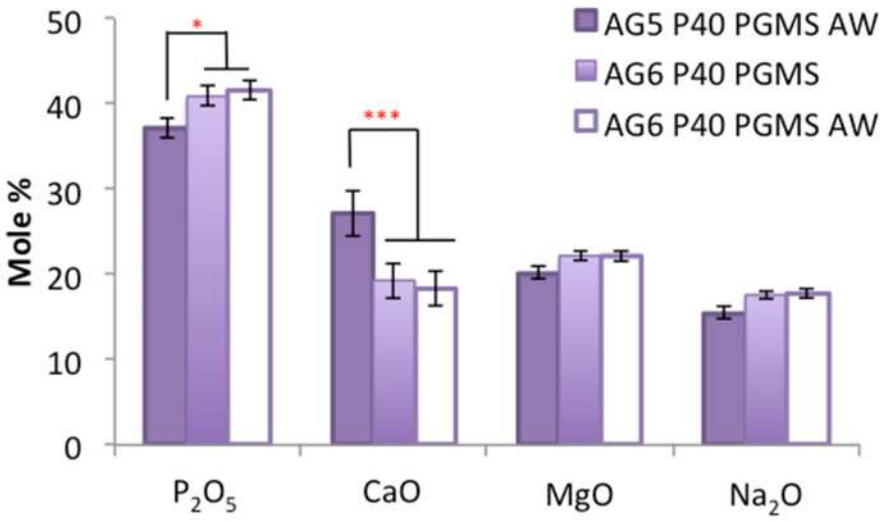

Figure 3-27: Elemental composition of AG5 P40 PGMS AW, AG6 P40 PGMS and AG6 P40 PGMS AW. *p<0.05, ***p<0.001. Error bars represent S.E.

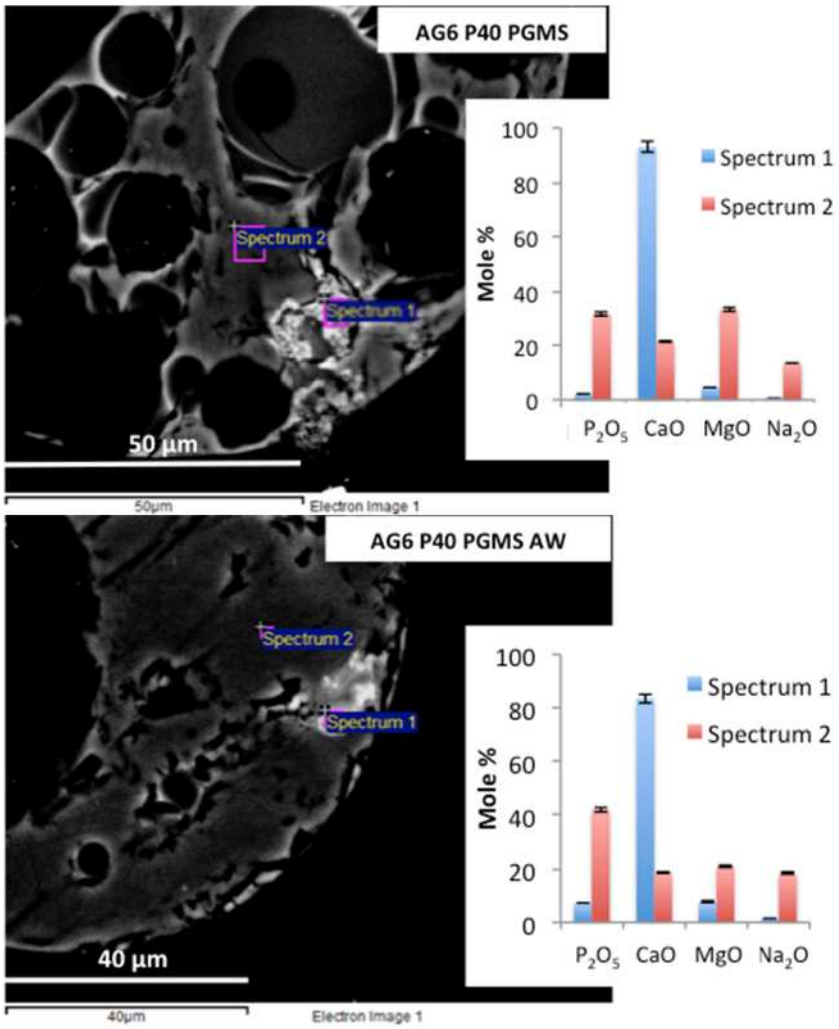

Figure 3-28: Retention of porogen in AG6 P40 PGMS and AG6 P40 PGMS AW. Two elemental spectra per sample were selected and analysed. The brighter patches in BSE images had higher CaO content and lower P_2O_5, MgO and Na_2O contents relative to other regions of MS. Error bars represent measurement error of 2%.

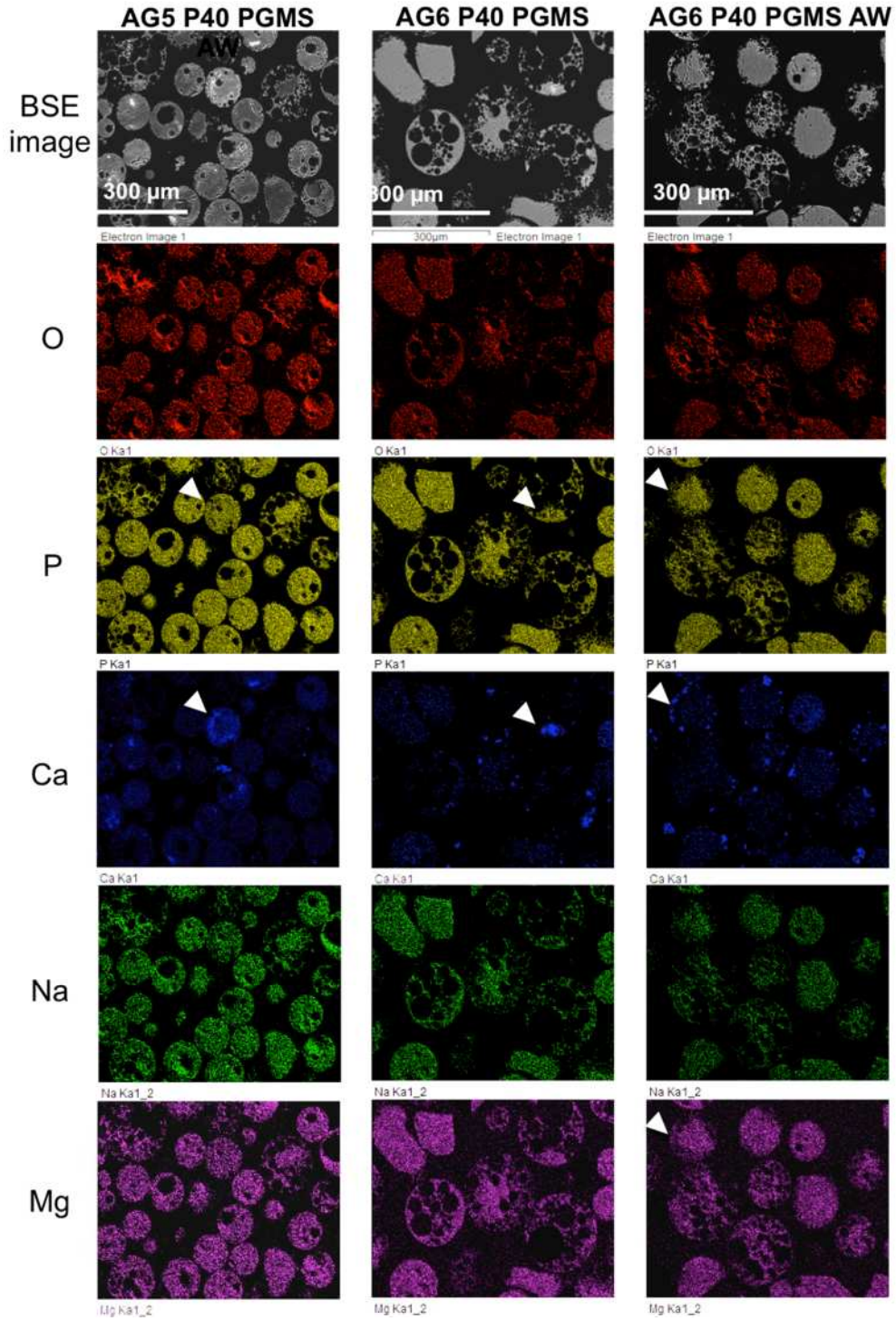

Figure 3-29: EDS mapping analysis of AG5 P40 PGMS AW, AG6 P40 PGMS and AG6 P40 PGMS AW. Regions of higher Ca content are indicated by white arrow-heads. Scale bars- 300 µm.

Table 3-4: Summary of elemental composition of particles using EDS analysis.

Borosilicate glass composition (mole % ± S.E.)							
Glass	B_2O_3	Si_2O	Al_2O_3	Na_2O	CaO	K_2O	BaO
BSG Batch 1	9.5	81±2	2±1	6±1	1±1	0.3±0.1	0.2±0.1
BSG Batch 2	9.5	83±2	3±1	5±1	2±1	-	-
Phosphate-based glass compositions (mole % ± S.E.)							
Glass	P_2O_5	CaO	MgO	Na_2O	Fe_2O_3		
AG1 P45 BGMP	48±1	15±1	23±1	11±1	4±1		
AG1 P45 BGMS	43±1	17±1	26±1	9±1	4±1		
AG1 P45 PGMS	33±2	39±8	17±1	6±1	3±1		
P45 BGMS Batch 1	44±1	17±1	27±2	8±1	4±1		
P45 BGMS Batch 2	43±2	18±1	28±2	8±1	4±1		
P45 BGMS Batch 3	48±1	15±1	24±1	11±1	3±1		
P40 BGMS Batch 1	43±1	15±1	23±1	19±1	-		
P40 BGMS Batch 2	44±1	15±1	23±1	19±1	-		
P40 BGMS Batch 3	43±1	15±1	24±1	18±1	-		
AG5 P40 PGMS AW	37±1	27±3	20±1	16±1	-		
AG6 P40 PGMS	41±1	19±3	22±1	18±1	-		
AG6 P40 PGMS AW	42±1	18±2	22±1	18±1	-		

3.5.4 Glass chemistry after acid washing

To investigate whether acid washing was leading to any chemical changes in different glass formulations; FTIR analysis was carried out as described in Section 2.2.11. The results, see Figure 3-30, showed that there were no peak shifts for different P-O bonds in PBGs or B-O, Si-O and B-O-Si bonds in BSG glass after the acid wash. These results suggested that acid washing was not leading to any significant changes in chemistry of BSG, P45 or P40 glasses.

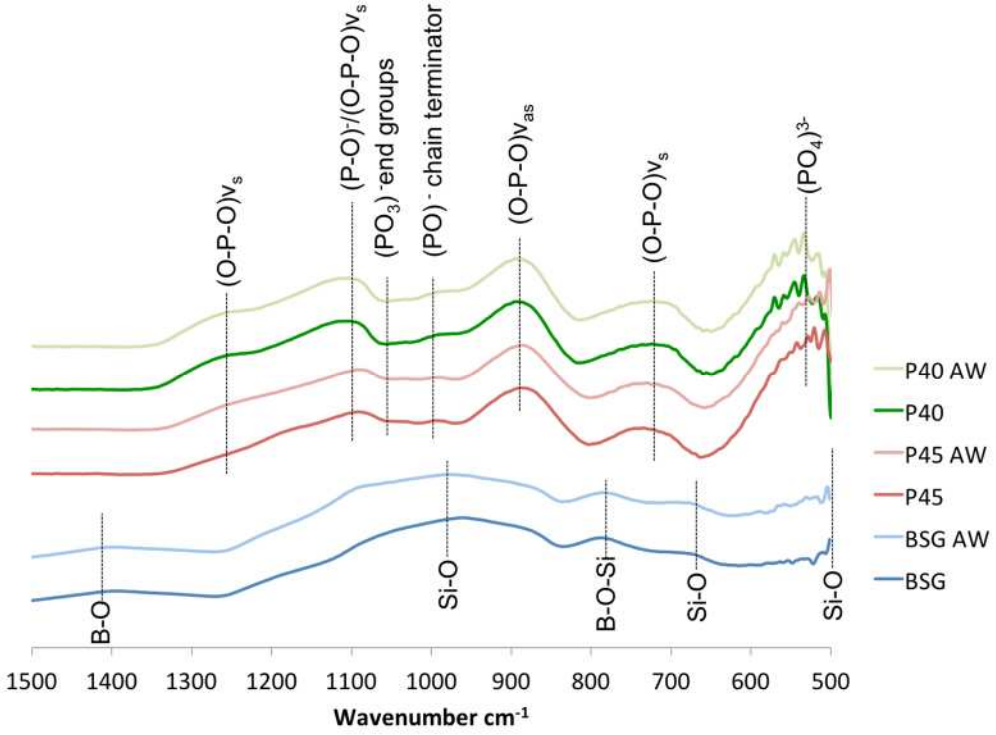

Figure 3-30: FTIR analysis of glasses before and after acid washing. There were no differences between the peaks before and after acid washing in either BSG, P45 or P45 glass discs. AW-acid washing.

3.6 Degradation of particles

Two degradation studies were performed- degradation in water and degradation in culture medium.

3.6.1 Degradation in water

To investigate the effect of hydration on PBG MS, degradation in water was carried out as explained in Section 2.2.12.1.

SEM examination before and after degradation, see Figure 3-31, showed that in case of BSG no surface changes occurred as a result of degradation. However, effect of hydration was clearly visible on PBG MS. After degradation, P45 BGMS and P40 BGMS had circular cracks with crater-like perforations on surface and P40 PGMS AW also had crater-like perforations with delaminating pore edges on their surface.

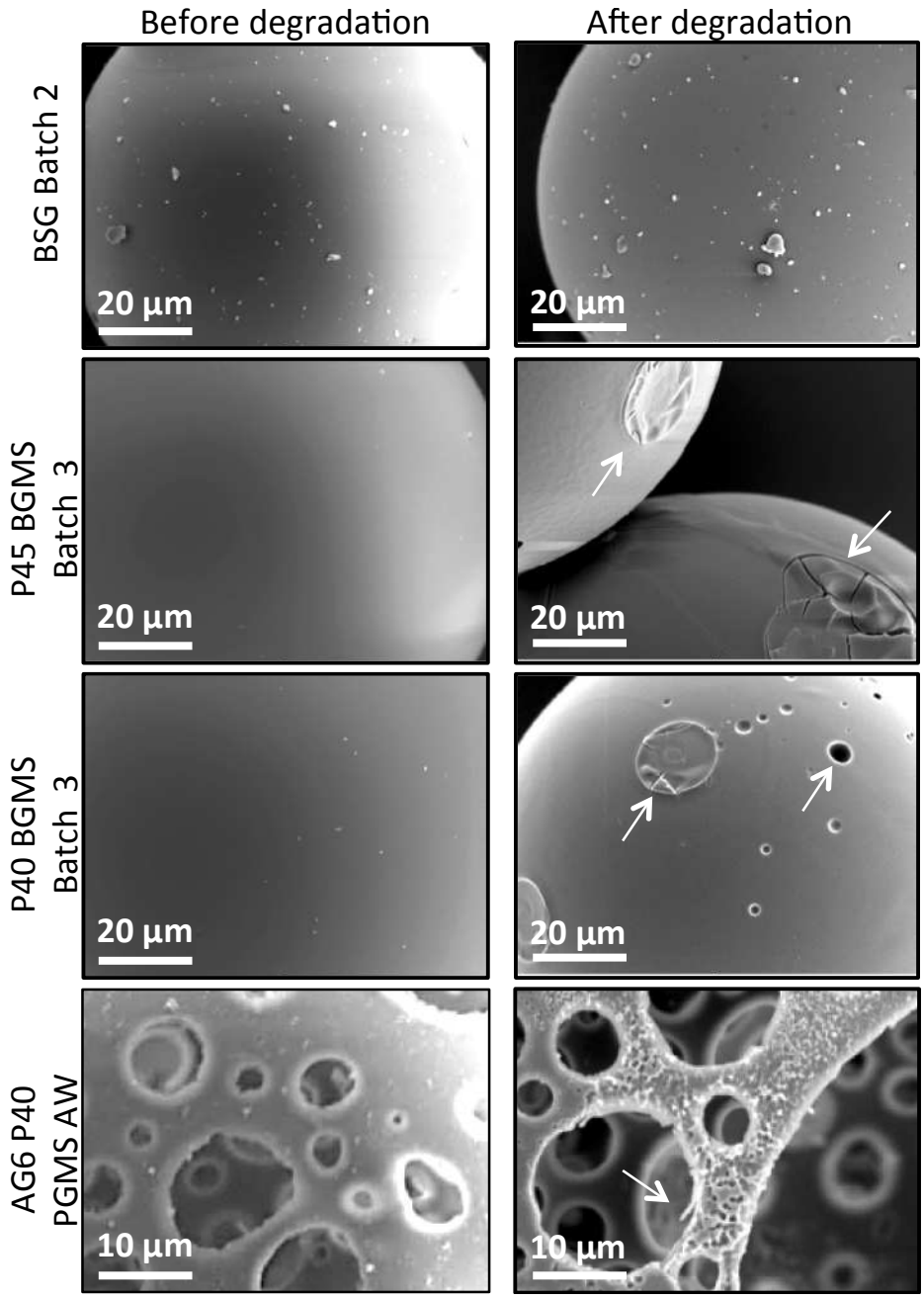

Figure 3-31: Degradation of MS in water. (A) SEM images showing the morphology of MS before degradation. (B) SEM images showing morphology of MS after 24h of degradation in water. There were no changes on the surface of BSG but P45 BGMS, P40 PGMS and P40 PGMS AW had visible crater-like perforations and surface delamination (arrow heads).

3.6.2 Degradation in culture medium for 42 days

Degradation of the MS was carried out in culture medium for 42 days, as described in Section 2.2.12.2.

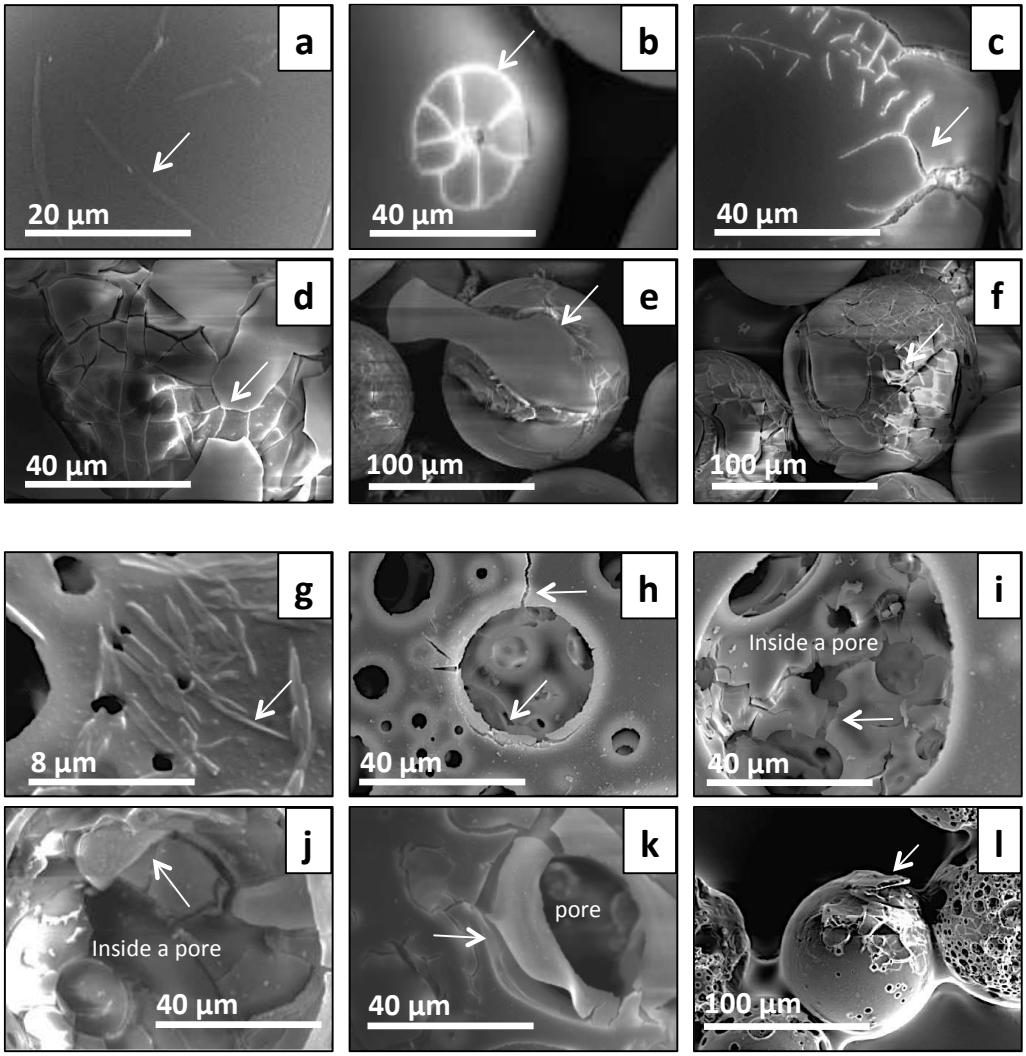

Figure 3-32: Progression of surface damage on bulk and porous MS as a result of degradation in culture medium over 42 days. In case of bulk PBG MS (a to f), cracks (arrows) developed on the surface and as these cracks progressed, it lead to delamination of the surface. In case of porous PBG MS (g-l), the cracks (arrows) developed around and inside pores and led to delamination of glass surface.

Qualitative assessment using SEM again showed that cracks and delamination occurred on the surfaces of both bulk and porous PBG MS and there were differences in progression of cracks developed on the two MS-types (see Figure 3-32). In case of P45 BGMS and P40 BGMS, small lined-features appeared on the surface of MS that propagated in the form of cracks, ultimately leading to delamination of glass surface. These cracks were not limited to the top surface of MS but cracks underneath the cracks also developed that led to total disintegration of MS surface. In case of acid washed P40 PGMS, the cracks were initially observed near the pore edges, which later

propagated on glass surface and also towards the internal pore cavities. The delamination always seemed to be in the vicinity of these cracks.

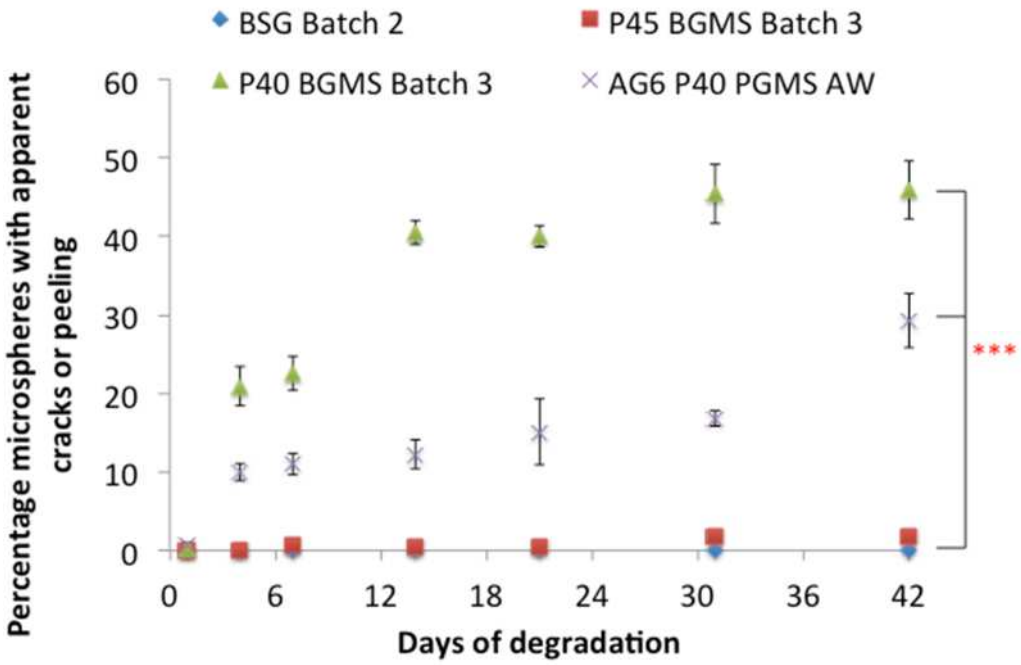

Figure 3-33: Quantification of degradation of MS in culture medium. There was highest surface damage on P40 BGMS (46%), then P40 PGMS (29%), followed by P45 BGMS (2%) and BSG (0%), after 42 days of degradation in medium. n=5 fields of view per MS-type per time point. ***p<0.001. Error bars represent S.E.

Upon quantification of degradation, it was observed that the cracks and delaminating surfaces appeared at a much faster rate on P40 bulk and porous MS compared to P45 BGMS (see Figure 3-33). By the end of 42 days of degradation, 2%, 29% and 46% of P45 BGMS, P40 PGMS AW and P40 BGMS, respectively, had cracks and/or peeling surfaces. For P40 BGMS, there was maximum damage occurring initially between day 1 and day 4 of degradation and then later between day 7 and day 14 of degradation. Moreover, the percentage P40 BGMS with apparent cracks or peeling did not seem to change significantly between day 14 and day 42 of degradation. In case of acid washed P40 PGMS, maximum surface damage occurred initially between day 1 and day 4 of degradation and then later between day 31 to day 42 of degradation.

3.7 Discussion

3.7.1 Effect of spheroidisation on particles

To understand the change in particle characteristics after the flame spheroidisation process, the results for AG1 P45 BGMP were compared to AG1 P45 BGMS, AG1 P45 PGMS and/or other MS-batches used in this study.

3.7.1.1 Particle shape and size

The AG1 P45 BGMP, AG1 P45 PGMS and other PGMS batches had a bimodal size distribution; however, in case of AG1 P45 BGMS and other bulk MS batches, a monomodal size distribution was observed. Similar size distribution for flame spheroidised glass-ceramic MS and non-spheroidised irregular glass particles has been reported before (Martinelli et al. 2010) and may be occurring due to the following reasons.

Firstly, BGMP and PGMS both had sharp edges on their surface, which may have caused high angle diffractions, also reported as "ghost" diffractions (Kaye et al. 1997), and this may have contributed to bimodal distribution. Secondly, the larger aspect particles (also present in BGMP or PGMS batches) may have had both minor and major axes measured by laser diffraction, also contributing to bimodal distribution (Kelly & Kazanjian 2006). Since both of these features were less common in bulk MS batches, a single peak for their size distribution was observed.

A study recently demonstrated that the spheroidisation of the particles depends upon their size and position of their entrance into the flame. If the thermal trajectory does not allow the particle to reach the temperature of vitreous transition, the particle does not melt or spheroidise (Bortot et al. 2012). This may explain presence of some angular shaped particles in MS-batches and may also be responsible for low sphericity and low tapped density in case of BSG batches compared to some commercially available borosilicate glass

MS from MO-SCI Corporation, USA (1-300 µm in diameter, sphericity of 0.95, tapped density of 1.2 g/ cm^{-3}) and Cospheric, USA (20-150 µm in diameter, sphericity of 0.9, tapped density of 1.2 g/ cm^{-3}). These differences also indicate that the current manufacturing process for BSG may need further optimisation to achieve a more uniform and higher mean sphericity for a commercially viable production.

Another observation from LD measurements was the forward shift in D[4.3] after spheroidisation. Similar results are also reported for glass-ceramic MS developed by flame spheroidisation (Martinelli et al. 2010); spherical Ti-6Al-4V alloy powder developed by radio frequency plasma (Sheng et al. 2012); and spherical alumina particles developed by radio frequency thermal plasma (Z. Károly & Szépvölgyi 2005). This indicated that this is a widely occurring phenomenon and may be a result of collision and coalescence of small melted glass particles with large melted glass particles to form larger MS (and sometimes agglomerates) under the hot flame (Sheng et al. 2012).

Finally, there was also batch-to-batch variation in sizes of MS (both for bulk and porous), which again may be due to variation in the sizes and aspect ratios of initially ground angular glass particles used for production of different batches (Bissett et al. 2015).

3.7.1.2 Particle surface area

The surface areas of bulk MS were found to be in similar range and comparable to some commercially available non-porous MS such as, Biosilon[a] (160-300 µm, 255 cm^2 g^{-1}), Hillex® (150-210 µm, 350 cm^2 g^{-1}), polystyrene MS (150-210 µm, 380 cm^2 g^{-1}) and glass MS (15-210 µm, 380 cm^2 g^{-1}) by SoloHill, USA. Moreover, the results showed variation in size and sphericity distributions in different MS batches, which may also have contributed to variation in surface areas of these batches. Generally, the larger sized MS-batches

seemed to have lower surface area (cm^2 g^{-1}) as compared to smaller sized MS-batches, which was expected.

In case of porous MS, AG5 P40 PGMS AW and AG6 P40 PGMS AW, both had very effective high surface areas at approximately 6,500 and 11,000 cm^2 g^{-1}, respectively. The difference between the two PGMS batches may be a result of the way the porogen was applied or influenced by the spheroidisation process or a consequence of higher levels of Ca-based porogen retained in AG5 batch compared to AG6 batch, which if removed, may enhance the surface area of the AG5 batch.

Comparison of these PGMS-batches with commercially available porous MS, including Cytopore™ (cellulose-based, 200-280 µm wide, 30 µm mean pore windows, 11,000 cm^2 g^{-1} surface area) by Amersham Biosciences, Sweden; confirmed that introduction of porosity led to at least 10-fold enhancement in surface area of PBG MS with good commercial viability.

3.7.1.3 Porosity

When pore window MAL measurements of AG1 P45 PGMS sieved fractions were performed, the results indicated that the mean MAL of pore windows increased with increase in porous MS size. Moreover, >25 µm pore windows were present only in porous MS >250 µm in diameter. These results were in line with the SEM images and surface area measurements of corresponding sieved fractions and suggested that if the MS size is increased from 100 to 500 µm, the total porosity, pore size and pore interconnections may also increase beyond 82%, 30 µm and 20 µm, respectively. However, pore and interconnection sizes may still remained below the favourable range for *in vivo* bone formation and vasculature formation, based on the literature review in Sections 1.8.2 and 1.8.3.

Porous glass structures are widely known to have poor mechanical properties. For example, Bioglass® 45S5 fibers have fracture

toughness of 0.7±0.1 MPa $m^{1/2}$ (Clupper et al. 2004a), tape cast and sintered bioactive ceramics sintered at 1000°C for 3h have fracture toughness in the range of 0.9-1.1 MPa $m^{1/2}$ (Clupper et al. 2004b) and 3D bioactive glass foam scaffolds sintered at 800°C for 2 h (with interconnected pore diameter of 98 μm and 82% porosity) have a compressive strength of 2.26 MPa (Jones et al. 2006). Hence, introduction of such porosity may prove detrimental for the mechanical strength of porous MS, not ideal for bone repair or reinforcement applications.

3.7.1.4 Particle composition

EDS mapping analysis revealed that there was compositional variability between MS within the batches of AG1 P45 BGMS, AG1 P45 PGMS, BSG Batch 1 and P45 BGMS Batches 1 and 2. This may have been due to variation in the compositions of initial raw materials or due to some variation introduced at the time of flame spheroidisation process.

The boiling points of Na, P, Mg, Ca, Fe, Si, Al and B are 882.8°C, 280.5°C, 1091°C, 1484°C, 2862°C, 3265°C, 2470°C and 3927°C (Luo 2007) and the temperature of oxygen/acetylene flame is 3480°C. Moreover, it easier to heat up the smaller particles as compared to the larger sized particles under the hot flame (Suzuki et al. 2011). Therefore, it is possible that the elements with high volatility such as P and Na, may have vaporised from the smaller sized particles, changing their composition and leading to heterogeneity within the sample. In support of this hypothesis, Bortot et al. (2012) developed yttrium aluminosilicate glass MS using propane-butane-oxygen flame and reported a slight increase of yttrium concentration from centre towards the surface of glass MS, indicating of a lower concentration of lighter elements towards the surface. Suzuki et al. (2011) draw attention towards the role of pressure of the combustion field and the heat quantity added to the particles under the flame. They suggested that the flame length and residence time of silica particles in the flame may be shortened by increasing the

pressure of the combustion field, which would ultimately inhibit the vaporization of silica from the surface of the particles under the flame.

Quantification of elemental composition revealed that despite different nominal compositions of P45 and P40 glasses, the measured P, Ca and Mg contents in P45 or P40 BGMS batches were in a similar range. This suggested that either these compositional similarities existed in the raw material (before spheroidisation) or these similarities were not present in the raw material and exposure of glass particles under the hot flame led to changes in chemical composition of particles through a similar process as described above (Bortot et al. 2012).

The BSE images in Figure 3-25 and Figure 3-26 also showed presence of closed pores inside some bulk MS, which were reflected in the relative density measurements and may have also contributed to batch-to-batch variability. Presence of these closed pores may be explained by the possible entrapment of gas bubbles inside some glass particles at the time of rapid spheroidisation process (Z. Károly & Szépvölgyi 2005; Bortot et al. 2012). Similar drop in relative density with entrapment of gas bubbles, has also been reported for yttrium aluminosilicate glass MS mentioned above (Bortot et al. 2012).

Following spheroidisation, both tapped density (ranging between ca. 1.2-1.4 g cm^{-3}) as well as normalised density (ranging from 1.3-1.5 g cm^{-3}) of AG1 P45 BGMS and other PBG bulk MS batches was higher than that of angular glass particles (AG1 P45 BGMP). Additionally, there was also visible batch-to-batch variability in tapped density. These may be explained by firstly, closer packing of spherical particles but jammed packing in case of angular-shaped particles (Torquato et al. 2000) and secondly, due to batch-to-batch variation in particle size distribution. Enhanced tapped density has also been reported for spherical Ti-6Al-4V alloy powder after

spheroidisation (Sheng et al. 2012) and for Ti-powder after spheroidisation (Bissett et al. 2015).

From a commercial standpoint, low batch-to-batch variability is a desired characteristic for a reliable manufacturing process. Though a number of studies have previously reported the development of bulk MS using flame spheroidisation for therapeutic purposes; for example, dysprosium lithium borate glass MS for radiation synovectomy (Conzone et al. 2002), hollow hydroxyapatite MS as delivery vehicles for proteins, drugs and growth factors (Wang et al. 2006; Fu et al. 2010; Fu et al. 2013), PBG MS for radiotherapy (Sene et al. 2008), glass-ceramic bulk MS for thermotherapy (Martinelli et al. 2010) PBG MS for cell expansion (Guedes et al. 2012; Lakhkar et al. 2012; Lakhkar 2014); none of these studies investigated batch-to-batch variability in their manufacturing process.

3.7.2 Effect of acid washing on PGMS

The EDS analysis showed significantly higher Ca and lower P, Mg and Na present on the edges of the pores of AG1 P45 PGMS as compared to the rest of the MS region. This suggested that excess Ca on pore edges may be due to retention of Ca-based porogen in those regions (patent WO 2016027110 A1) (Ahmed 2016).

Since, nano-sized calcium-based particles have been previously shown to cause cytotoxicity in Human intestinal epithelial (INT-407) cells (Kim et al. 2015) and higher doses (>4 mM) of calcium have also been shown to cause cytotoxicity in mouse primary osteoblasts (Maeno et al. 2005), it was decided to acid-wash PGMS in order to remove excess porogen and to avoid any possible cytotoxic effects on human mesenchymal stem cells due to higher concentration of calcium.

The characterisation results later indicated that acid washing was neither changing the chemical composition of these particles nor completely removing excess Ca from the edges of the pores. This

indicated that this Ca deposit was not easily dissolvable by acetic acid (in 2.5 min) and may need further investigation. On the other hand, there were also some measureable changes in the physicality of these MS such as, increase in relative density, sphericity and MAL of MS by 40%, 9% and 17%, respectively, and decrease in closed porosity, pore window MAL and pore window roundness by 23%, 5% and 3%, respectively; strongly suggesting an effect of acid washing on glass structure.

3.7.3 Particulates on glass surface: a source of cytotoxicity

On all particle-types, glass particulates (<10 µm in diameter) were found deposited on glass surface. Similar deposited particulates were also seen on PBG particles (Martinelli et al. 2010), on PBG MS after flame spheroidisation (Sene et al. 2008) and on bioactive glass foams developed by sol-gel method (Sepulveda & Hench 2002), which suggested that these particulates may be a consequence of glass processing during manufacturing process.

Suzuki et al. (2011) proposed that when particles such as made from silica, are melted during flame spheroidisation, smaller particles are vaporized from the surface of larger particles in the range of less than the saturated vapour pressure without the boiling. After that, the vaporized particles are condensed again with the decrease in the saturated vapour pressure and the ultra fine particles are formed on larger spheroidised particles. Similar phenomenon may also have occurred in case of BSG and PBG MS. Suzuki et al. (2011) also suggested that changing the pressure of the flame may reduce vaporisation of glass surface and deposition of ultra fine particles after spheroidisation. Therefore, future investigations may be performed to test the effect of flame pressure on PBG MS spheroidisation process.

Previous studies have shown that particulates <10 µm can be internalised by the cells and interact with different organelles based

on their chemistry, size and shape (Buzea et al. 2007; Labbaf et al. 2011). This interaction may lead to altered cell function and even cell death. For these reasons, cytotoxicity of PBG MS has been discussed in greater detail in Chapter 5.

3.7.4 Degradation of microspheres

Degradation of MS in water and culture medium indicated development of lined-features (swellings), circular cracks and crater-like perforations on the surface of PBG MS during early stages of degradation. There may be two or more contributing factors for the same. Firstly, the MS surface may have swelled up due to water retention causing ingress of water leading to perforations (Choueka et al. 1995); and secondly, the manufacturing of bulk and porous MS involves rapid cooling after flame spheroidisation step, which may also have led to development of stresses and strain in glass structure of these MS (Varshneya 2013).

In case of bulk glass MS, the core may have cooled at a faster rate as compared to the outer regions and when the core tried to freeze, it may have compressed the outer surface, leading to its cracking. On the other hand, in case of porous glass MS, the glass struts of varying thickness may have cooled at different rates, which may have strained the glass in certain regions, leading to formation of cracks.

SEM images showed significantly higher surface damage seen in case of P40 BGMS compared to P45 BGMS and these results are in line with a previous related study where P45 and P40 glass discs were found to be loosing 0.8% and 1.1% of mass, respectively, after 42 days of degradation in PBS (Hasan et al. 2012). This difference between the two glass formulations has been attributed to the formation of Fe–O–P bonds in P45 glass, which are more resistant to hydration than the P–O–P bonds (Yu et al. 1997).

The results also showed a drop in peeling effect in case of P40 PGMS AW compared to P40 BGMS. This may be due to presence of pores

in the crack path that may have affected the crack propagation in one direction by distributing the stresses in multiple directions (Kranz 1979), thereby reducing the chances of delamination of glass surface.

Surface damage on glass implant surfaces is a commonly occurring phenomenon and it has been associated with faster degrading glasses in all forms such as, fibres (Choueka et al. 1995; Haque et al. 2013; Sharmin et al. 2014), MS (Sene et al. 2008; Guedes et al. 2012; Lakhkar 2014) and discs (Skelton et al. 2007; Leonardi et al. 2010; Asif et al. 2014). From cytocompatibility stand point, appearance of cracks or delaminating surfaces on glasses is a detrimental phenomenon, offering potential small glass fragments that can be internalised by cells (Labbaf et al. 2011; Tsigkou et al. 2014) and at the same time, leading to detachment of cells or cell death (Skelton et al. 2007; Leonardi et al. 2010; Asif et al. 2014; Lakhkar 2014).

3.7.4.1 Annealing: a possible solution for reducing delamination

Annealing is a process where glass material is heated to specific temperature and then allowed to cool slowly so that the whole of glass structure cools down at the same rate, thereby minimising stress and toughening the glass (Varshneya 2013).

Annealing at higher temperature of 450^0C has been shown to delay degradation and peeling effect on surface of bioresorbabale glass fibres when compared to non-annealed fibres or fibers annealed at 250^0C (Choueka et al. 1995). Similar observations were also reported by Parsons et al. (2009) after annealing PBG fibers. Moreover, longer annealing durations (72 h at 34 ^{0}C) has been shown to increase the average pore size from 6±2 μm to 110±50 μm and average porosity from 19±4% to 59±3% as compared to non-annealed porous scaffolds made from 13-93 bioactive glass (Liu et al. 2011). Furthermore, annealing of boron oxide doped PBG

fibers at 60 min at 10 ^{0}C was found to decrease the dissolution rate, enhance the density and increase the tensile modulus of fibers (Sharmin et al. 2013).

These studies strongly suggest that if PBG bulk and porous MS are annealed, their mechanical strength and porosity may be enhanced, while cracking and delamination may be delayed or reduced.

3.8 Conclusions

In this chapter, material characterisations for PBG particles and spheres have been described. A number of investigations including, particle morphology, surface area, porosity, elemental composition and degradation behaviour, were performed.

In conclusion, particle morphology changed from irregular-shape to a more regular shape after flame spheroidisation and the spheroidised particles of all formulations had a similar size range of lying between 8-280 μm (as seen through major axis length measurements). Introduction of porosity led to more than 10-fold increase in surface area of PGMS as compared to BGMS, however, the pore size and interconnectivity in PGMS were significantly smaller than the desired ranges for efficient bone formation and vascularisation *in vivo*. The acid wash seemed to change the physicality of these particles, apparent through closed porosity and pore window MAL and roundness distributions but it did not chemically alter PGMS or increase the mean pore window MAL beyond 5 μm, EDS mapping analysis revealed that in case of some MS-batches, smaller MS had a different composition from larger sized MS. This was hypothesised to be a consequence of evaporation of elements with higher vapour pressure during the spheroidisation process under the hot oxygen/acetylene flame.

Furthermore, there were some clear differences in degradation behaviours of P45 and P40 bulk MS and between P40 bulk and porous MS, evaluated using a novel method for degradation

quantification. Significant surface damage occurred on faster degrading P40 glass MS and the introduction of porosity seemed to decrease the propagation of cracks and delamination of glass surface. Annealing was offered as a possible solution to reduce this damage and the subsequent release of glass fragments.

Finally, results revealed subtle batch-to-batch variability in bulk and/or porous MS-batches via size distributions, surface area and compositional analyses. Therefore, the effect of this variability on hMSC growth has been investigated in subsequent chapters.

Chapter 4 2D VS. 3D Culture System

4.1 Introduction

There is now a growing body of evidence suggesting that 2D may be as more like an artificially induced system rather than a reliable positive control which may not truly mimic the complex three dimensional (3D) system *in vivo* (Walters & Gentleman 2015). Studies have shown that in 2D, cells express integrin proteins only in one plane while in 3D, cells express integrins in multiple planes (Baker & Chen 2012) and this leads to changes in cell morphology, which may ultimately affect cellular fate.

Due to these differences and in order to decide for a suitable control culture system for future investigation on phosphate based glass microspheres, differences between human mesenchymal stem cell (hMSC) responses in monolayer culture system (2D) and borosilicate glass microspheres (MS) culture system (3D), have been explored in this chapter.

The chapter starts with Section 4.2, which discusses the batch-to-batch variability of BSG before comparing them to 2D and this is followed by more intensive cell health comparisons between 2D and 3D in following sub-section. In Section 4.3, osteogenic differentiation in 2D and 3D are explored and finally, in Section 4.4 and Section 4.5, all the results from this chapter are discussed and concluded, respectively.

4.2 Cell health analysis

In this section, hMSC attachment (Section 4.2.1), growth (Section 4.2.2) and viability (Section 4.2.3) have been explored in 2D and 3D. Preliminary to these tests, the batch-to-batch reproducibility of BSG in terms of the hMSC responses was explored in Experiments-BR01 and BR02 as described in Section 2.3.3.

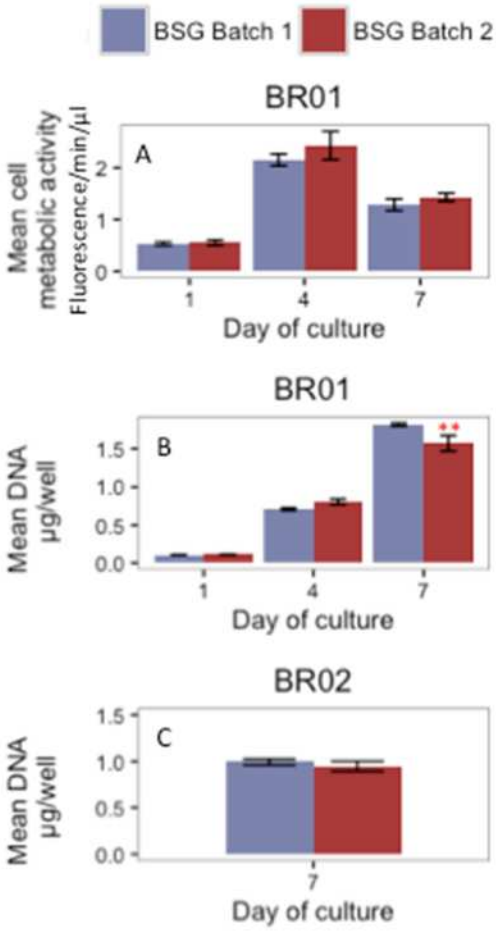

Figure 4-1: Batch-to-batch reproducibility of BSG. (A, B) Experiment-BR01 and (C) Experiment-BR02. Cells were seeded at 2,500 cells cm^{-2} in both experiments and DNA assay and cell metabolic activity assay were performed using PicoGreen® assay and PrestoBlue® assay, respectively. **$p<0.01$ between two batches at specific time point, n=3, error bars represent S.E.M. Scale bar- 250 µm. BSG- borosilicate.

In Experiment BR01, cell metabolic activity and DNA measurements were performed on days 1, 4 and 7 of culture and the results in Figure 4-1a showed no significant differences in the cell metabolic activities of the two batches of BSG on any time point. At the same time, there was a significant drop in cell metabolic activities in both batches from day 4 to day 7 of culture ($p<0.001$), which has been explored in greater detail in Section 4.2.2.

DNA measurement (see Figure 4-1 b) of same biological replicates also showed no significant difference between BSG Batch 1 and BSG Batch 2 on days 1 and 4 of culture. However, on day 7, there was significantly higher DNA content (15±4%) in BSG Batch 1 compared

to BSG Batch 2 ($p<0.01$). When the test was repeated in Experiment BR02, the results in Figure 4-1 c showed no significant differences between the DNA contents on two batches on day 7, indicative of batch-to-batch reproducibility.

4.2.1 Cell attachment

To compare the efficiency of hMSC attachment in 2D and 3D systems, Experiments CA01 and CA02 were performed as described in Section 2.3.3.

In Experiment CA01, the results showed that the metabolic activity (Figure 4-2 A) in 3D was 2, 2.3 and 1.7 times more than in 2D at higher cell seeding densities of 2,500, 5,000 and 10,000 cells cm^{-2}, respectively ($p<0.001$). However, no significant differences were observed at lower cell seeding densities of 625 and 1,250 cells cm^{-2}. On the other hand, the DNA assay results also showed 1.4 and 1.2 times more DNA content (Figure 4-2 B) in 3D compared to 2D at 5,000 and 10,000 cells cm^{-2} seeding densities ($p<0.001$). These results suggested a disproportional increase in DNA content with increasing cell metabolic activity in 3D system.

The repeat Experiment-CA02 (Figure 4-2 C) also showed 3.2, 3.5 and 2.4 times more cell metabolic activities in 3D compared to 2D at all cell seeding densities of 2,500, 5,000 and 10,000 cells cm^{-2}, respectively ($p<0.01$, 0.001), which strongly indicated differences in hMSC attachment mechanisms in 2D and 3D.

In addition to quantitative measurements, qualitative assessments for cell attachment were also performed using fluorescence imaging. For this, images of live hMSCs in 2D and 3D were captured after 24 h of cell seeding. The results shown in Figure 4-2 D indicated that there was aggregate-formation at higher densities of 2,500, 5,000 and 10,000 cells cm^{-2}, in 3D only and these aggregates seemed to have been formed as a result of cells present in inter-particulate regions, possibly trying to bridge across from one MS to another.

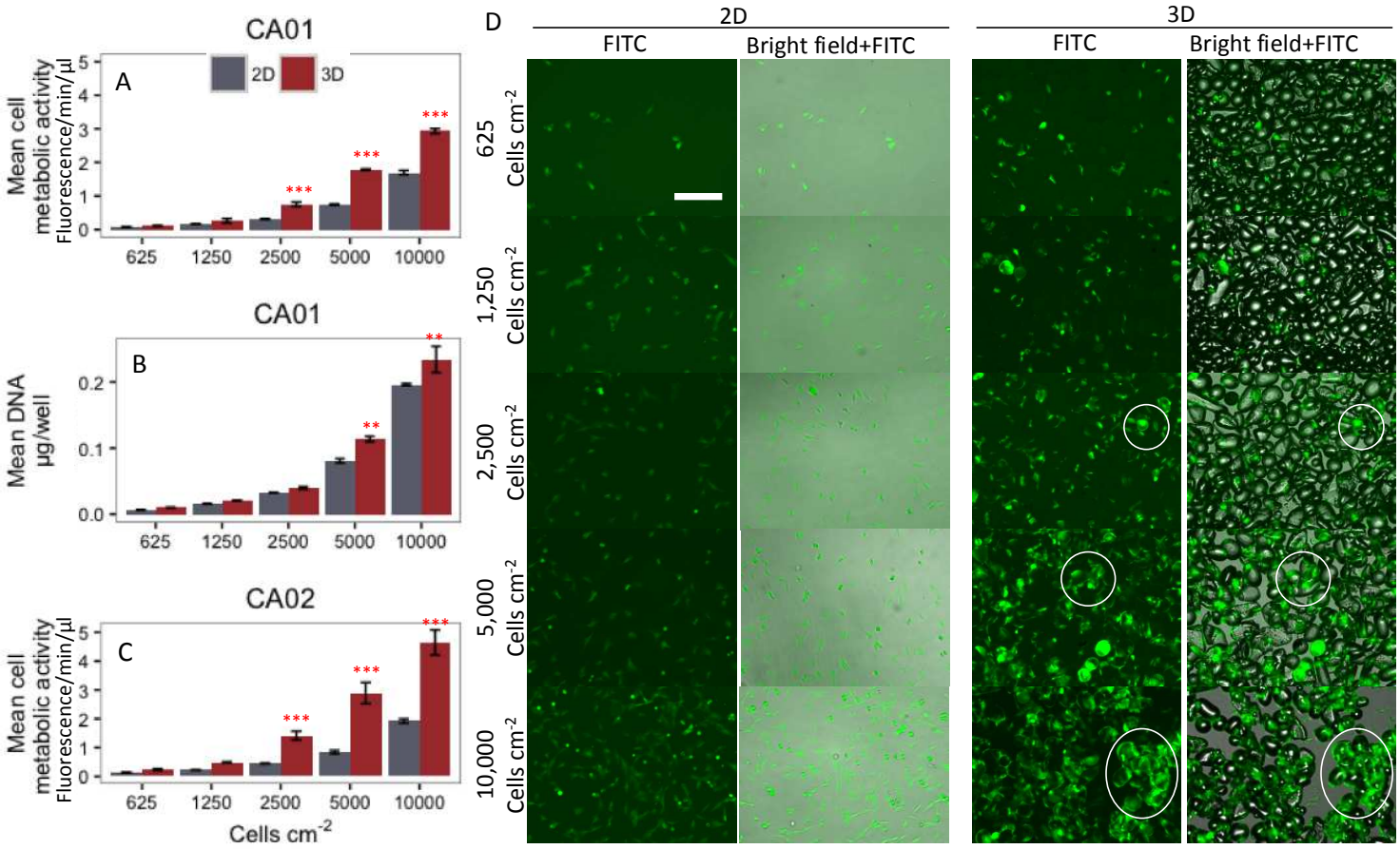

Figure 4-2: Cell attachment of hMSCs in 2D and 3D. (A, B) Experiment-CA01 and (C) Experiment-CA02. Cells were seeded at 625, 1,250, 2,500, 5,000 and 10,000 cells cm^{-2} in both experiments and DNA assay and cell metabolic activity assay were performed using PicoGreen® assay and PrestoBlue® assay, respectively. (D) Representative FITC channel and overlay (bright field+FITC) images taken on day 1 of culture. Aggregate formation is highlighted with white circles. **p<0.01, ***p<0.001 between 2D and 3D at that time point, n=3, error bars represent S.E.M, Scale bar- 250 µm.

4.2.2 Cell growth

To investigate the effects of 2D and 3D culture on cell proliferation, Experiment CP01 was performed, as described in Section 2.3.3. The results (see Figure 4-3 A-B) showed that there was significantly higher DNA content and metabolic activity in 2D compared to 3D after 4 days of culture and beyond, despite same surface area provided for growth in both conditions ($p<0.001$). At the same time, there was again higher metabolic activity in 3D compared to in 2D on day 1, similar to as seen in Experiments CA01 and CA02. Further, using the DNA content measurements on day 31 of culture, it was calculated that 3D contained only 23% of the cells as compared to in 2D, which indicated that cells in 3D occupied only 23% of the surface area provided for cell proliferation.

In case of 2D, the results, see Figure 4-3 A-B also showed an increase in DNA content and metabolic activity until day 14 and day 21 of culture, respectively ($p<0.001$), indicating a discrepancy in PicoGreen® and PrestoBlue® assays. More interestingly in 3D, the DNA content seemed to increase until day 31 but the metabolic activity increased until only day 4 ($p<0.001$), after which it remained unchanged until day 42. This again suggested no linear correlation between metabolic activity and DNA content in 3D, over extended culture periods.

Based on these results, it was hypothesised that cell metabolic assay was wrongly estimating the cell growth in 3D system and also in 2D system at later time points. To test this hypothesis, Experiment CP02 was performed. This experiment included 2D and 3D systems and a third condition, named 2D'. The 2D and 3D conditions offered 2 cm^2 surface area for 5,000 hMSCs to grow, while 2D' offered 6 times less surface area (0.33 cm^2) for same number of hMSCs to grow over a week's time. The cell count results, see Figure 4-3 C, showed nearly 4.5 times more cells in 2D compared to 2D' and 3D. On the other hand, cell metabolic activity results (Figure 4-3 D) showed highest cell metabolic activity in 2D',

followed by 2D and least in 3D over the same time period. It was also interesting to note that on day 3 and 5 of culture, when the cell counts in the three conditions were very similar, 2D' had significantly higher cell metabolic activity compared to 2D and 3D. These results again indicated no clear correlation between hMSC numbers and hMSC metabolic activity between the three culture conditions and strongly indicated that the hMSCs were at different metabolic states in these conditions.

4.2.2.1 Effect of seeding density on cell growth rate in 3D

To further investigate if initial cell-seeding density affects the hMSCs proliferation rate in 3D, Experiments CP03 and CP04 were performed as described in Section 2.3.3 with cell seeding densities of 10,000 and 167 cells cm^{-2}, respectively.

The results for Experiment CP03 in Figure 4-3 E, showed that again there were significantly more number of cells present on day 7, 14 and 21 of culture in 2D compared to 3D, similar to as seen in Experiment CP01. However, at this instance, there were only 2.5 times more cells in 2D relative to 3D, compared to 4.9 times more cells in Experiment CP01 on Day 21.

Finally, comparison of per day increase in DNA content between day 7 and day 21 of culture in Experiments CP01, CP03 and CD04 suggested a decrease in rate of cell growth in 2D and 3D with increasing cell-seeding density (see Table 4-1).

Table 4-1:Effect of cell seeding density on hMSC growth in 2D and 3D.

Experiment name	Initial cell seeding density (cells cm^{-2})	Increase in DNA content over 2 weeks* (µg)		Rate of cell growth (µg DNA/day)	
		2D	3D	2D	3D
CP04	167	nt	14.43	nt	1.03
CP01	2,500	7.31	1.47	0.52	0.11
CP03	10,000	1.24	0.93	0.09	0.07

*Increase in DNA content was calculated using day 7 and day 21 DNA measurements, nt-not tested.

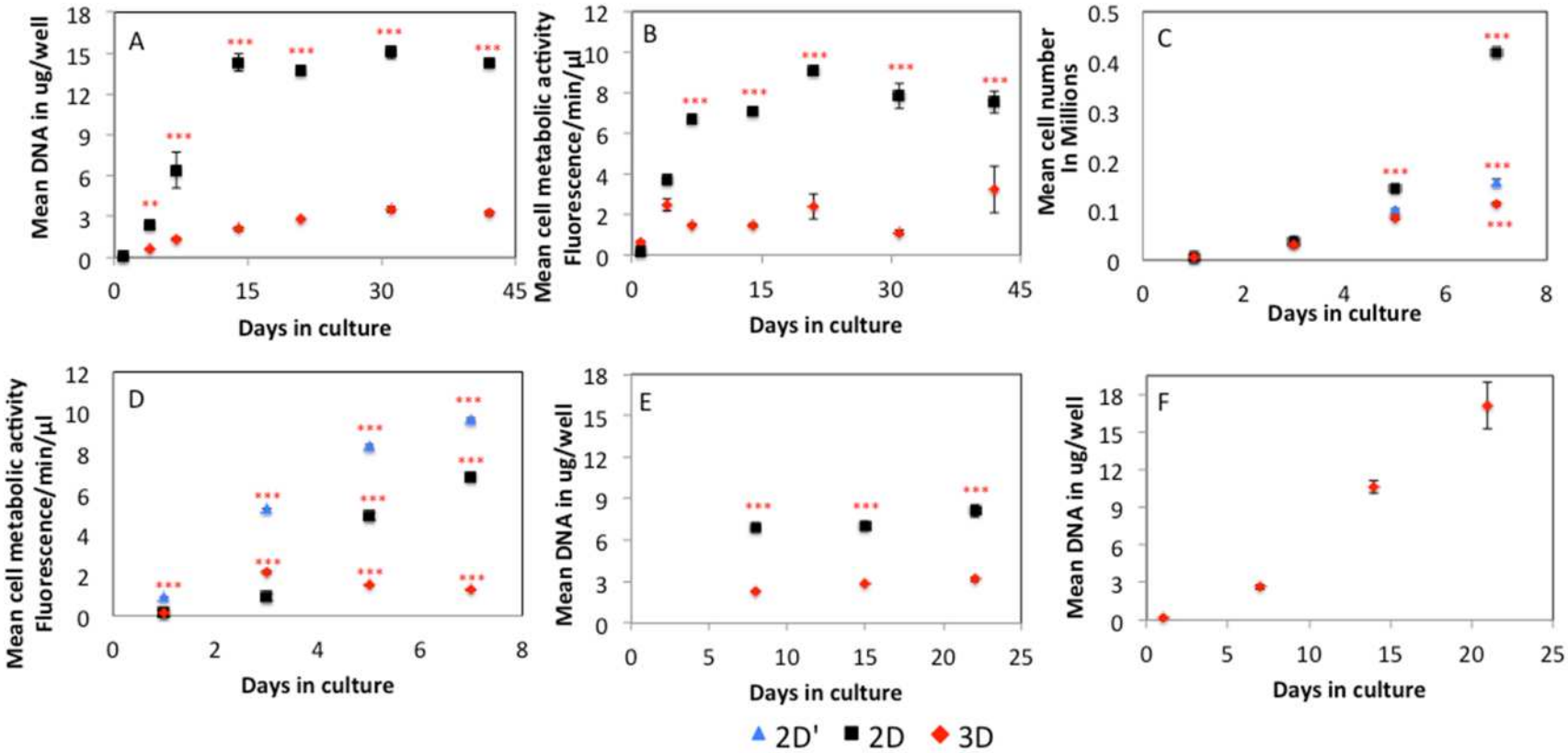

Figure 4-3: Growth of hMSCs in 2D and 3D. (A, B) Experiment-CP01 (cell seeding-2,500 cells cm^{-2} in 2D and 3D), (C, D) Experiment-CP02 (cell seeding at 2,500 cells cm^{-2} in 2D and 3D and 15,000 cells cm^{-2} in 2D'), (E) Experiment-CP03 (cell seeding at 10,000 cells cm^{-2} in 2D and 3D) and (F) Experiment-CP04 (2D not tested, 3D only with cells seeding of 167 cells cm^{-2}). DNA, cell metabolic activity and cell number measurements were performed using PicoGreen® assay, PrestoBlue® assay and manual cell counts, respectively. **p<0.01, ***p<0.001, compared to other condition on same time point, n=3, error bars represent S.E.M.

4.2.2.2 Heterogeneity in 3D system

To investigate reasons for slower cell growth of hMSCs in 3D compared to 2D, scanning electron microscopy was carried out for 3D samples, as described in Section 2.3.18, and images of typical 3D agglomerate have been shown in Figure 4-4 A-D. The images depict that there were thick cell layers (> 2 layers thick) outside the agglomerate. However, when this agglomerate was sectioned, there were more cells present near the edges as compared to the central (internal) regions of the agglomerate, which suggested heterogeneity in hMSC colonisation across a 3D sample.

Images also indicated presence of more cells in inter-particulate regions, where the cells acquired a more *in vivo*-like morphology. However, there were relatively fewer cells on the surfaces of these MS, where they acquired either a flat or a rounded morphology, see Figure 4-4 E-F. This again suggested heterogeneity in cell fate within the same 3D sample.

4.2.3 Cell viability

In order to investigate viability of hMSCs in 2D and 3D, Experiment CV01 was performed as described in Section 2.3.9. The results in

Figure 4-5 showed significantly higher proportion of dead cells in 3D compared to 2D on day 1 ($p<0.001$) and day 4 ($p<0.01$) of culture and the same was also observed qualitatively on day 7. However, by end of 21 days of culture, the cell viability seemed to have improved in 3D and very few dead cells were observed. It is important to note that the day 21 images are representative of the only the bottom face of 3D agglomerate.

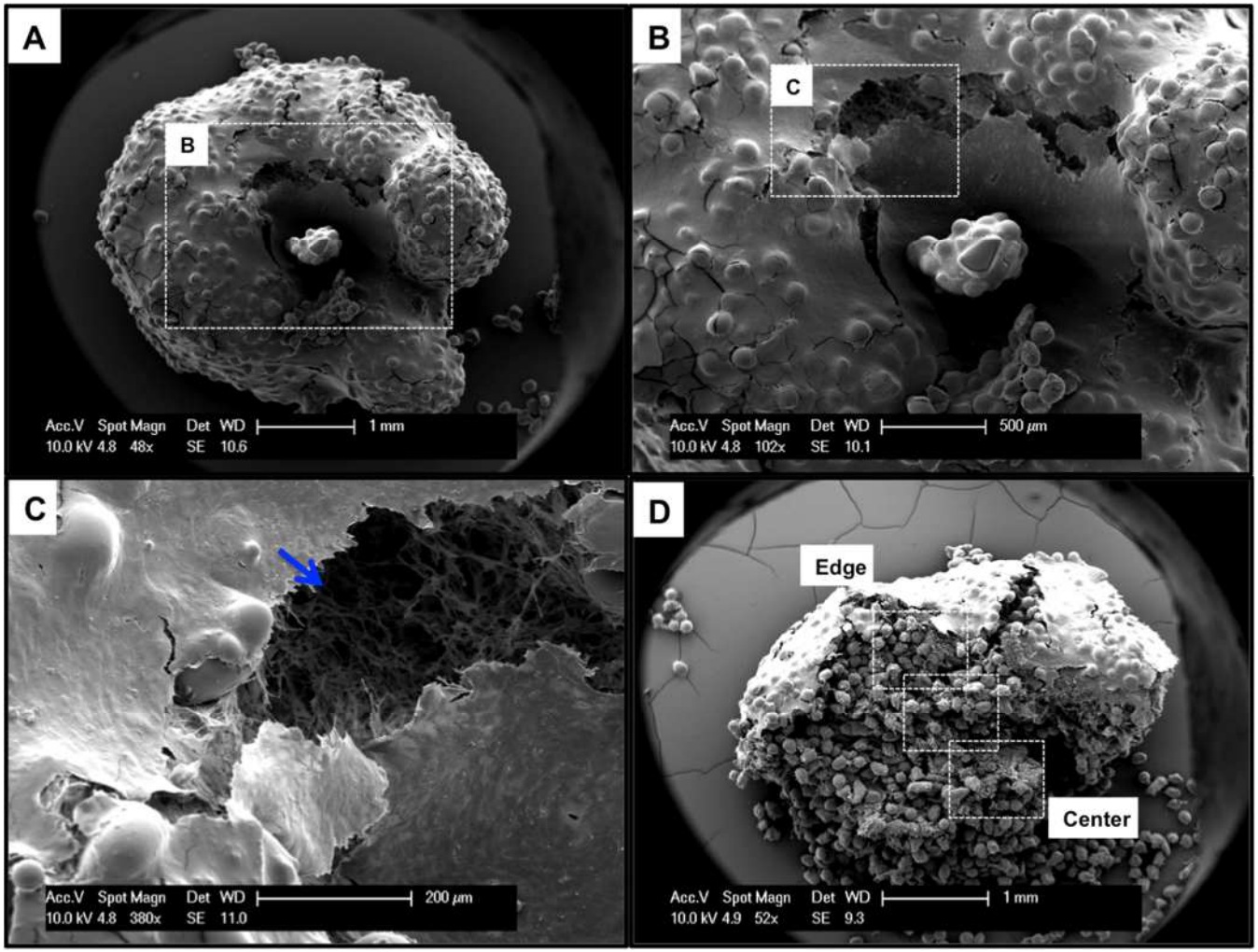

Figure 4-4: SEM images of 3D agglomerates. A sample was taken from Day 14 of Experiment-CP04 (cell seeding at 167 cells cm^{-2}) and visualised under SEM. Increasing magnification images (A to C) of intact 3D agglomerate showed that cells covered entire agglomerate in multiple layers (blue arrow). This agglomerate was sectioned (E) and images of cells were acquired from three internal regions (E). There seemed to be more cells near the edges of the agglomerate compared to central regions. Notice the presence of sheets of cells present near the edges of the agglomerate in comparison to the central regions (blue arrows in E). There was also presence of both rounded cells (red arrows) and flat cells (red arrow heads) (F) in the sample.

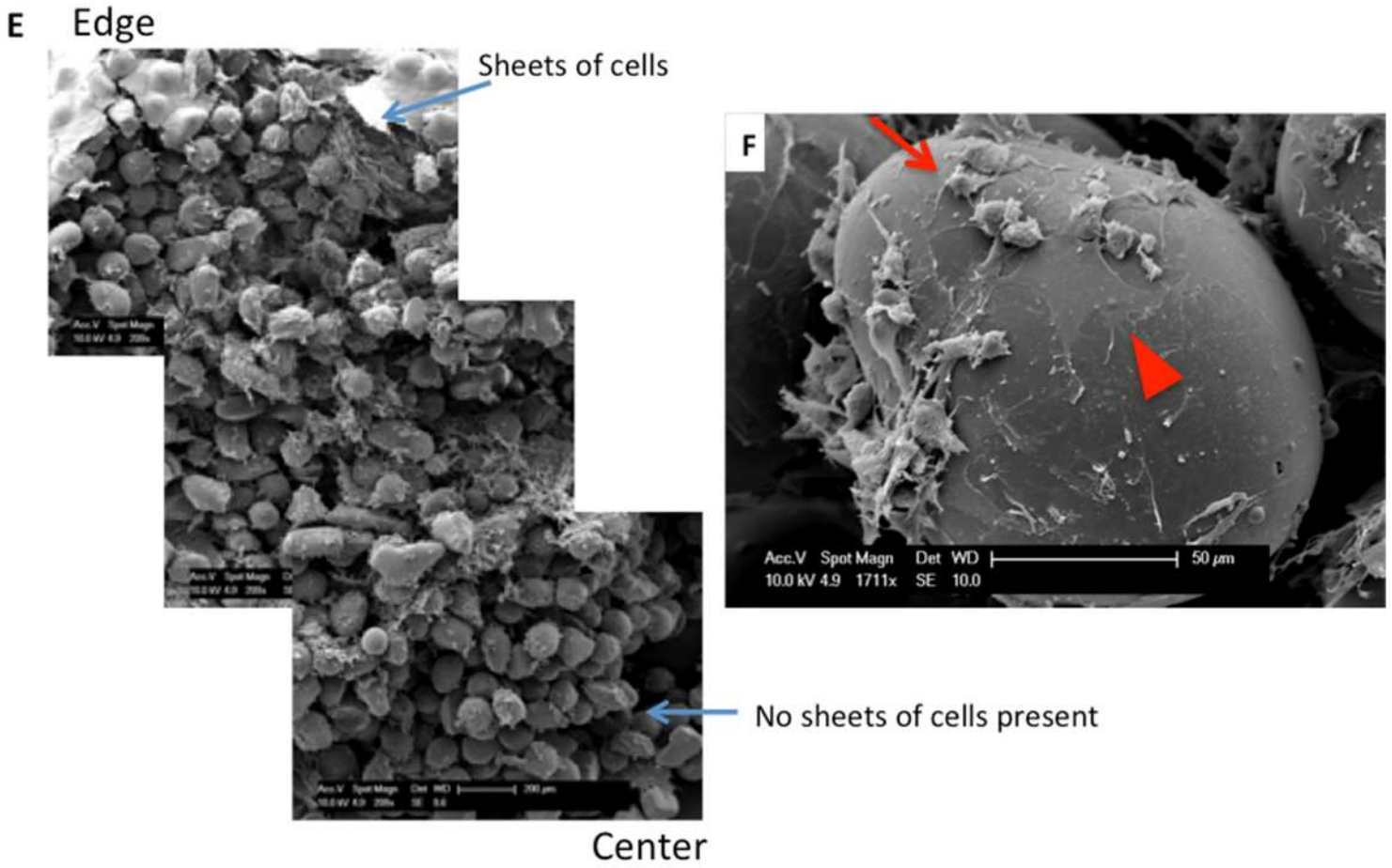

Figure 4-4 continued from previous page.

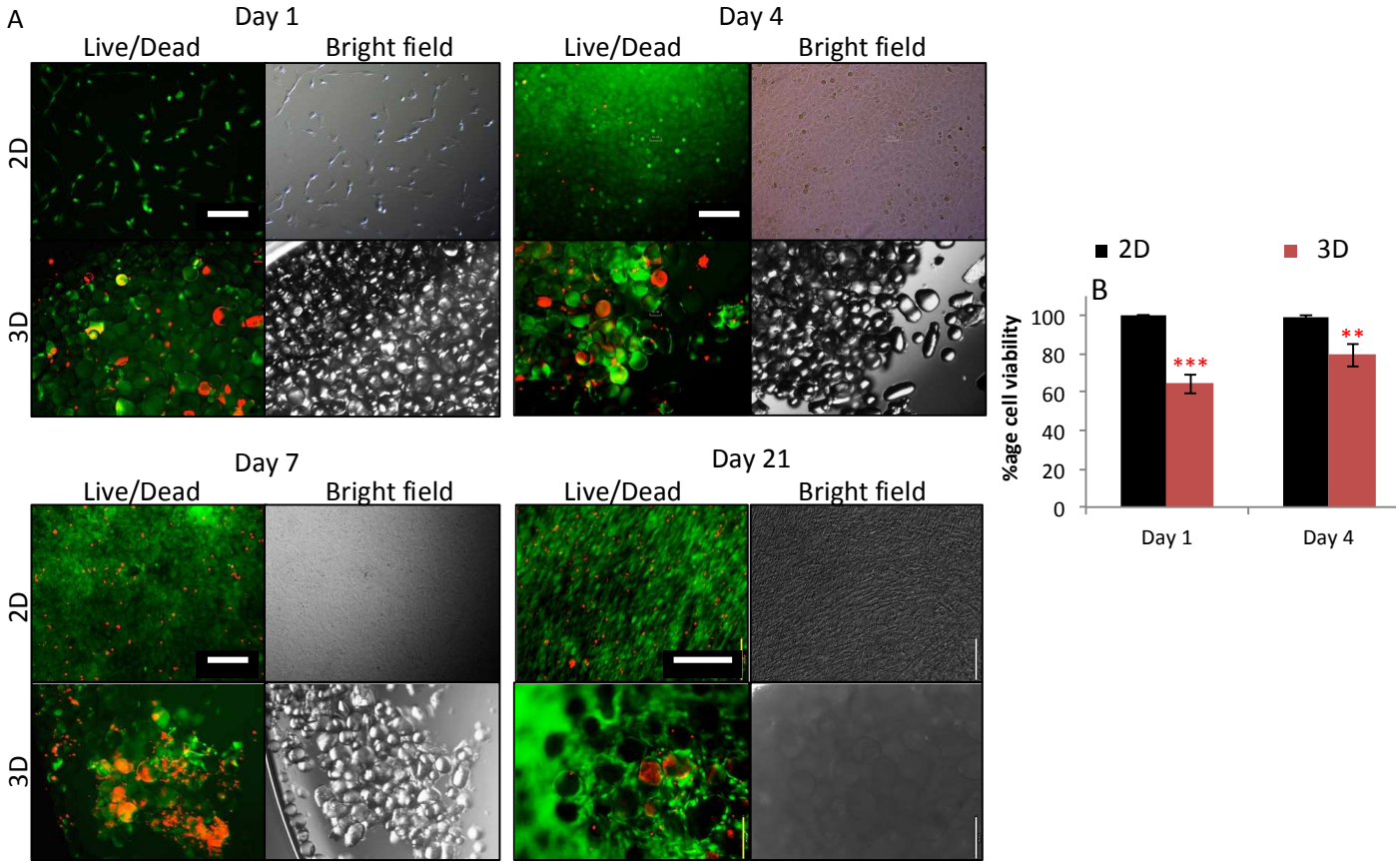

Figure 4-5: Viability of hMSCs in 2D and 3D. Green signal (Fluorescein diacetate stained) and red signal (Propidium iodide stained) represent live and dead cells, respectively. (A) Overlay of FITC/Texas Red channels and matching bright field images have been shown for days 1, 4, 7 and 21 of culture. (B) Percentage cell viability in 2D and 3D after 1 and 4 days of culture was calculated using image analysis by quantifying the pixels for green and red signal. **p<0.01 and ***p<0.001, n≥4. Error bars represent S.E.M.

4.3 Osteogenic differentiation

4.3.1 Alkaline Phosphatase activity

Early osteogenesis is marked by increased alkaline phosphatase (ALP) activity, reaching a peak and then a decline during late osteogenesis (Lorch 1949; Jaiswal et al. 1997). Hence, to assess the effect of culture platforms on ALP activity of hMSCs, Experiment CD01 was performed as described in Section 2.3.3 and Section 2.3.11. For this experiment, 10,000 cells cm^{-2} was chosen as cell seeding density because hMSCs have been previously shown to undergo osteogenic differentiation at this seeding rate (France et al. 2012).

The results in Figure 4-6 A showed that the hMSCs in 3D responded in the same manner to culture media in 2D, i.e., there was significantly higher ALP activity in 3D OS and 2D OS as compared to 3D SC and 2D SC, respectively ($p<0.001$). At the same time, there was also higher ALP activity in 3D compared to 2D on day 7 (both media, $p<0.05$), on day 14 (both media, $p<0.05$) and on day 21 (only OS medium, $p<0.01$) of differentiation.

To test the repeatability of these results, Experiment CD02 was conducted. The results in Figure 4-6 B again showed significantly higher ALP activity in 3D OS compared to 3D SC on day 7 and 21 ($p<0.001$) and significantly higher ALP activity in 3D compared to 2D in both media ($p<0.001$). This strongly suggested a positive effect of 3D environment on ALP activity of hMSCs.

Next, to investigate if the ALP activity followed a similar trend at a lower cell seeding rate of 2,500 cell cm^{-2}, Experiment-CD03 was set up. The results in Figure 4-6 C again showed significantly higher ALP activity in OS medium compared to SC medium ($p<0.001$) and higher ALP activity in 3D OS compared to 2D OS on day 7 and 21 of differentiation. On the other hand, in 3D SC condition higher ALP activity as compared to 2D SC condition was observed only on day

21 of differentiation ($p<0.01$). Finally, to test the repeatability of these results, Experment-CD04 was set up and the results, see Figure 4-6 D, showed that although there was higher ALP activity in 3D SC compared to 2D SC at all time points (day 7, 14 and 21 of differentiation), statistical significant difference was only seen at day 21 of differentiation ($p<0.05$). Thus, confirming the results in Experiment CD03.

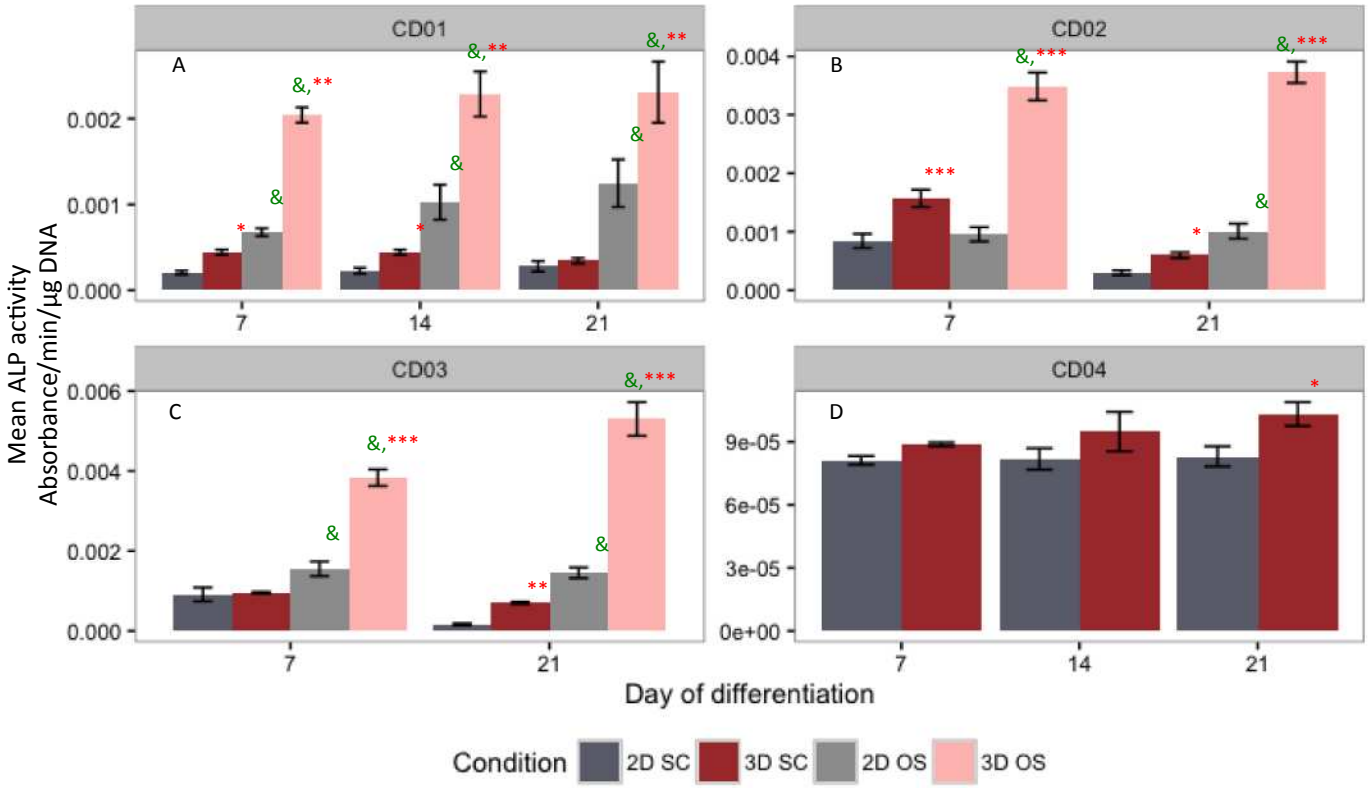

Figure 4-6: Alkaline phosphatase (ALP) activity measurements of hMSCs in 2D and 3D in standard culture (SC) medium and osteogenic (OS) medium. Measurements were acquired using SIGMAFAST™ p-Nitrophenyl phosphate tablets as substrates for ALP. (A) Experiment CD01 (cell seeding at 10,000 cells cm^{-2}), (B) Experiment CD02 (cell seeding at 10,000 cells cm^{-2}), (C) Experiment CD03 (cell seeding at 2,500 cells cm^{-2}) and (D) Experiment CD04 (cell seeding at 2,500 cells cm^{-2}).***p<0.001, **p<0.01 and *p<0.05 for comparisons between 2D and 3D in same culture medium on same time point, & p<0.001 for comparisons between SC and OS media for same culture platform on same time point, n=3, error bars represent S.E.M.

4.3.2 Collagen production

Formation of collagen fibrils in the ECM of the cells is considered as one of the osteogenesis markers (Weiner et al. 1999). Therefore, to study the effect of culture platform on collagen production potential of hMSCs, qualitative and quantitative assessments were performed as described in Section 2.3.13.

4.3.2.1 Qualitative assessment

For qualitative assessment, Experiment COL01 was performed. From Figure 4-7 it can be observed that the cells in 2D were responsive to OS treatment as there was more intense positive collagen staining in case of OS medium compared to SC medium. Moreover, the staining pattern increased significantly from day 7 to 21, suggesting that collagen deposition in 2D increased with time.

In case of 3D (Figure 4-8 A), low magnification images showed an increase in size of the 3D agglomerates in all conditions from day 7 to day 21 of differentiation. This observation is in line with results in Experiments CP01 and CP03.

To further assess the spread of collagen deposition in 3D, higher magnification imaging was performed and results in Figure 4-8 B illustrate that 3D agglomerates were difficult to focus on (as they were not flat samples like 2D) and individual cells were not identifiable under the microscope. Therefore, it was not possible to study collagen production on these intact 3D agglomerates.

To address this issue, the 3D samples from day 21 of differentiation were sectioned (as described in Section 2.3.12) before staining with Sirius Red and visualised under a microscope. The results in Figure 4-8 C showed that this time, it was possible to visualise individual cells in the 3D sectioned samples and also revealed presence of red-coloured spots (collagen) in both 3D OS and 3D SC conditions. These results validated that hMSCs in 3D were able to produce collagen.

4.3.2.2 Quantitative assessment

For quantitative assessment of collagen deposition, Experiment COL03 was performed with 10,000 cell cm^{-2} as cell seeding density. As expected, the results (Figure 4-9 A) showed significantly higher collagen in 2D OS than in 2D SC medium on day 7 ($p<0.01$) and day 21 ($p<0.001$) of differentiation. However, in case of 3D, there was no difference between OS and SC conditions on day 7 of differentiation. Moreover, there was also higher collagen in 3D SC compared to 3D OS by day 21 ($p<0.001$) due to significant drop in 3D OS collagen between day 7 and day 21 ($p<0.01$). This drop was not observed in case of 3D SC.

In the same experiment, comparison of 2D and 3D showed that on day 7 there were no significant differences between 2D OS and 3D OS conditions but there was significantly higher collagen in 3D SC compared to 2D SC ($p<0.01$). However, at the end of the experiment, there was 9 and 4 times more collagen in 2D OS and 2D SC conditions relative to 3D OS ($p<0.001$) and 3D SC conditions, respectively.

To investigate if the same trends were present at a lower cell seeding rate, Experiment COL04 was conducted with cell seeding at 2,500 cells cm^{-2}. The results (Figure 4-9 B) showed increased collagen production in 2D OS and 2D SC from day 7 to day 21 of differentiation ($p<0.001$). Moreover, there was also higher collagen in 2D OS and 2D SC conditions compared to 3D OS and 3D SC, respectively ($p<0.001$) by the end of 21 days of differentiation.

Interestingly, in case of 3D, two way ANOVA statistical analysis (inclusive of 2D and 3D data points) showed no significant change in collagen from day 7 to 21 in both OS and SC conditions. However, when the 2D conditions were removed from the statistical analysis, there were clear trends visible for 3D OS and 3D SC conditions (see Figure 4-9 C). Consistent with previous experiment, there was again

a significant drop in 3D OS collagen from day 7 to day 21 of differentiation ($p<0.001$) with no change in case of 3D SC.

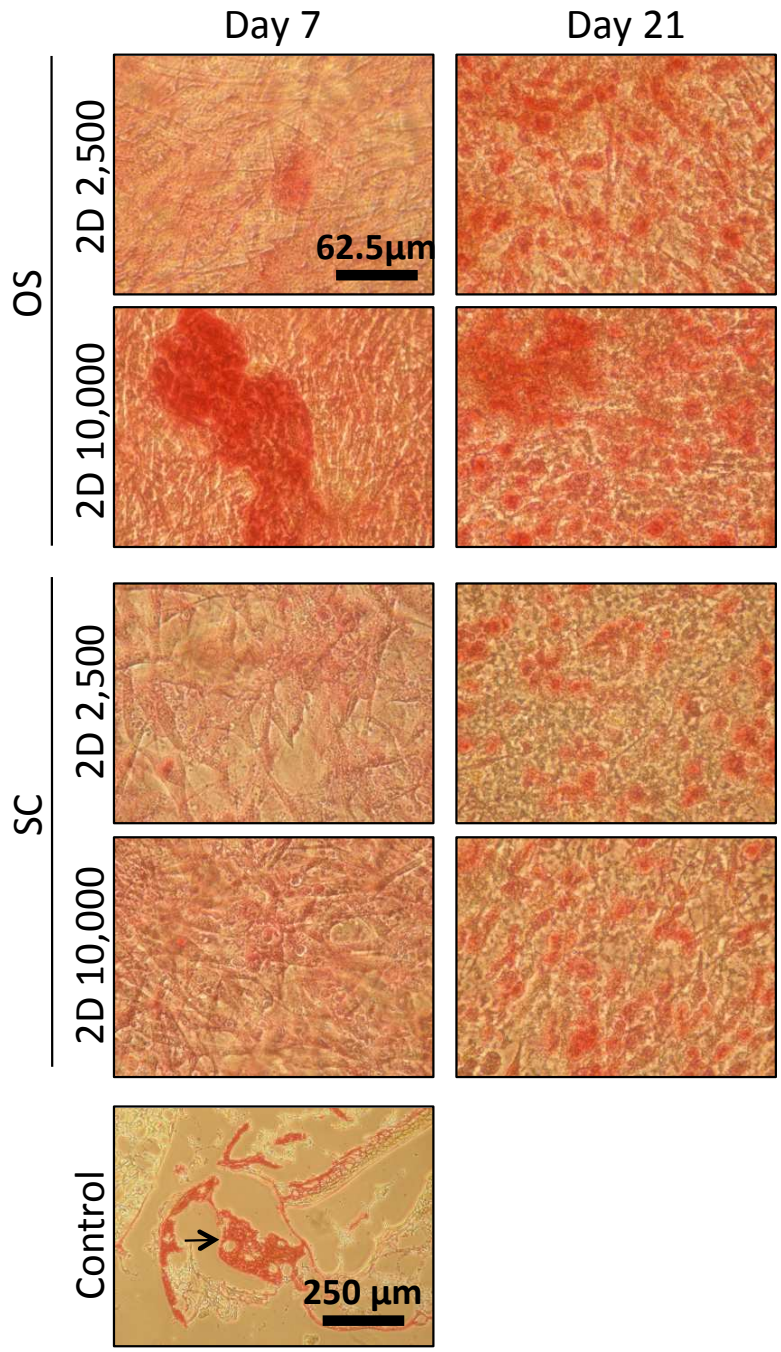

Figure 4-7: Qualitative assessment of collagen production by hMSCs in standard culture (SC) medium and osteogenic culture medium (OS) after 7 days and 21 days of differentiation in 2D. Cells were seeded at 2,500 and 10,000 cells cm^{-2} in Experiment COL01 and images were taken after staining with Sirius Red. There was an increase in collagen staining in all conditions from day 7 to 21. There were more collagen deposits in OS than in SC medium. Mouse calvarial tissue was used as a positive control for staining (arrow).

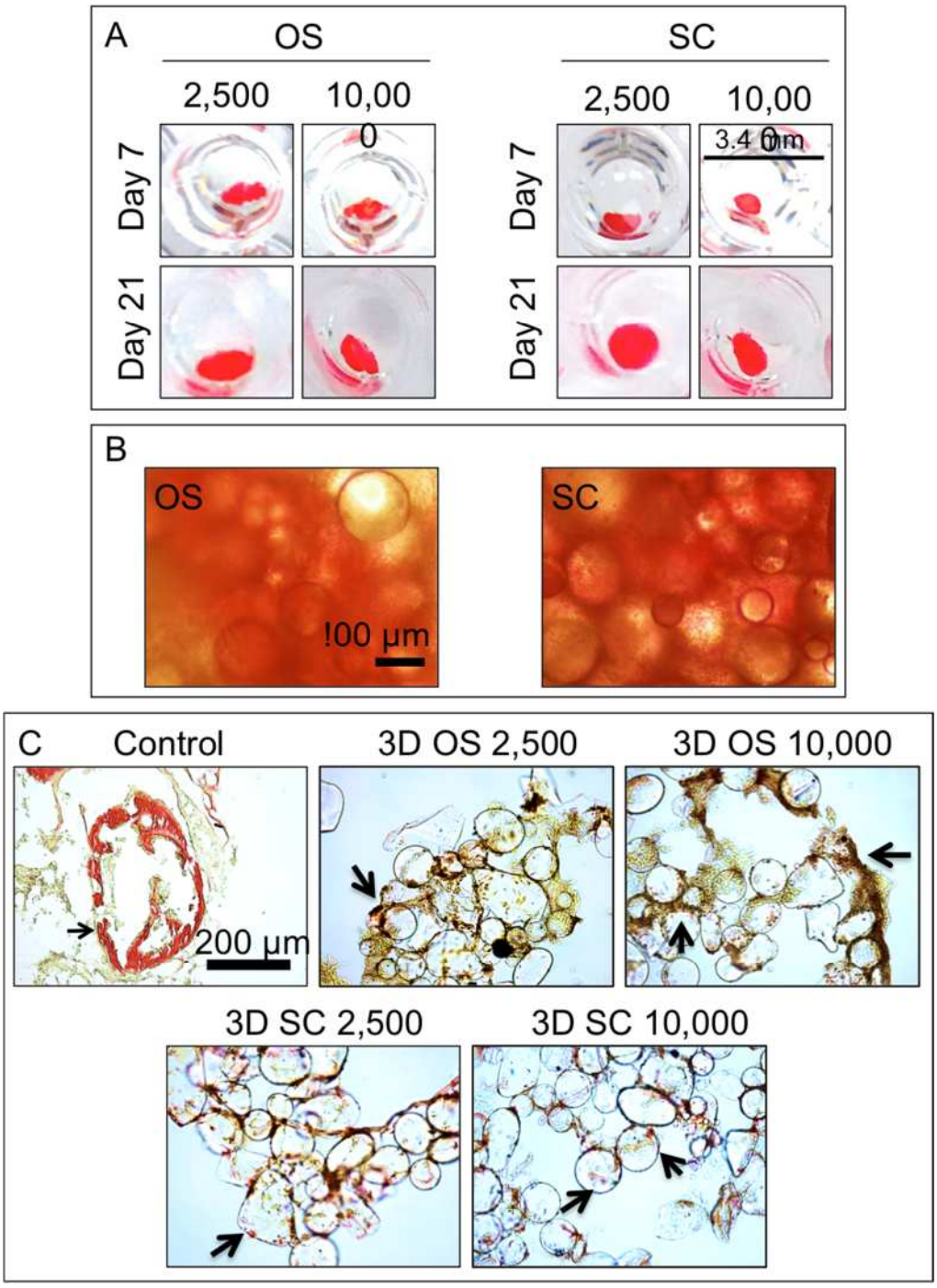

Figure 4-8: Qualitative assessment of collagen production by hMSCs grown in standard culture (SC) medium and osteogenic culture medium (OS) after 7 days and 21 days in 3D. Cells were seeded at 2,500 and 10,000 cells cm^{-2} in Experiment COL01 and Sirius Red staining was performed. (A) Stained intact 3D agglomerates on day 7 and 21 of differentiation. (B) Higher magnification images of 3D agglomerates. (C) Sirius Red staining for cryo-sectioned 3D agglomerates. Arrows indicate presence of collagen. Mouse calvarial tissue was used as a positive control for staining (arrow).

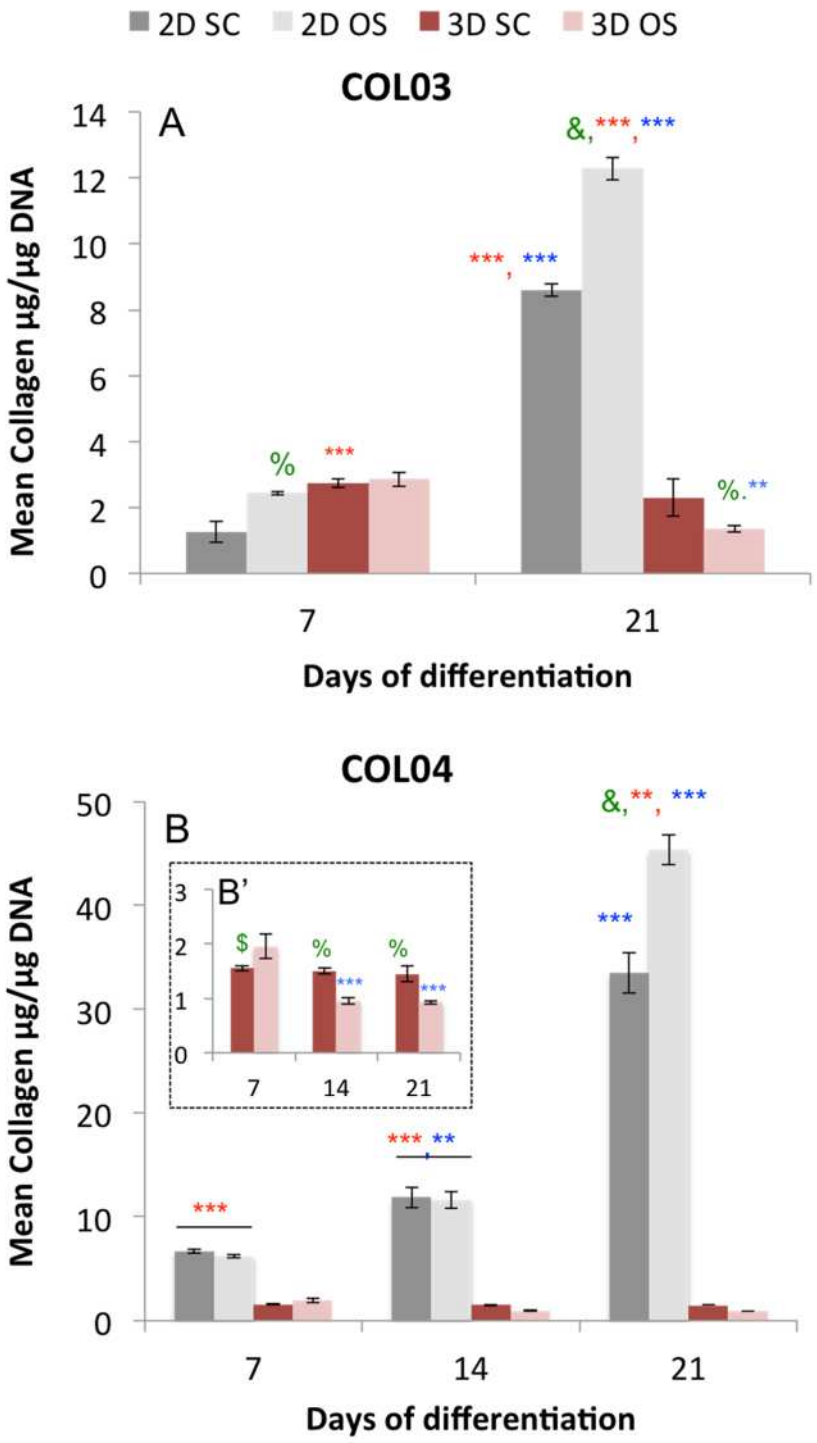

Figure 4-9: Quantification of collagen produced by hMSCs seeded in 2D and 3D in standard culture (SC) medium and osteogenic (OS) medium. (A) Experiment COL03, (B) Experiment COL04 and (B') Experiment-COL04 3D conditions only. Cells were seeded at 10,000 and 2,500 cells cm^{-2} in Experiments COL03 and COL04, respectively and Sirius Red assay was performed over 21 days of culture. ***p<0.001, **p<0.01 and *p<0.05 for comparisons between 2D and 3D in same medium on same time point. & p<0.001, % p<0.01, $ p<0.05 for comparisons between SC and OS on same time point of same culture condition. ***p<0.001, **p<0.01 for comparison between day 7 and specific time point, n=3. Error bars represent S.E.M.

4.3.3 Mineral deposition

Calcium is needed for formation of hydroxyapatite crystals in the extra cellular matrix of osteoblasts (Harada & Rodan 2003). Therefore, the extent of mineral production by hMSCs was also studied in 2D and 3D culture systems, as described in Section 2.3.3 and Section 2.3.14.

4.3.3.1 Qualitative assessment

In Experiment MIN01, qualitative assessment was performed. The Figure 4-10 shows Alizarin Red stained cells in two culture systems after 7 and 21 days of differentiation. On day 7, the cells in 2D condition did not show positive calcium staining but by day 21, there was presence of intense positive mineral staining in 2D OS. On the other hand, in case of 3D, there were patchy mineralised regions present in both 3D OS and 3D SC conditions on day 7 as well as day 21 of differentiation.

4.3.3.2 Quantitative assessment

For quantitative assessment, four experiments were performed. In Experiments-MIN02 and MIN03, cells were seeded at 10,000 cells cm^{-2} and mineral quantification was performed after 21 days of culture. The results in Figure 4-11 A-B showed significantly higher calcium in 2D compared to 3D in both media and as expected, 2D OS had significantly more calcium deposition as compared to 2D SC conditions. However, in the case of 3D, no significant differences were seen between 3D OS and 3D SC conditions after 21 days of differentiation.

Further, to investigate mineral deposition at lower cell seeding densities, Experiment MIN04 and MIN05 were performed with 2,500 cells cm^{-2} as cell seeding rate. The results again showed same trends on day 21 of differentiation for all culture conditions (Figure 4-11 C, D) as seen in Experiment MIN02.

Thus, these results strongly suggested that hMSCs in 3D were not responsive to the OS treatment over longer culture periods. At the same time, MS culture system was less supportive of calcium deposition relative to 2D.

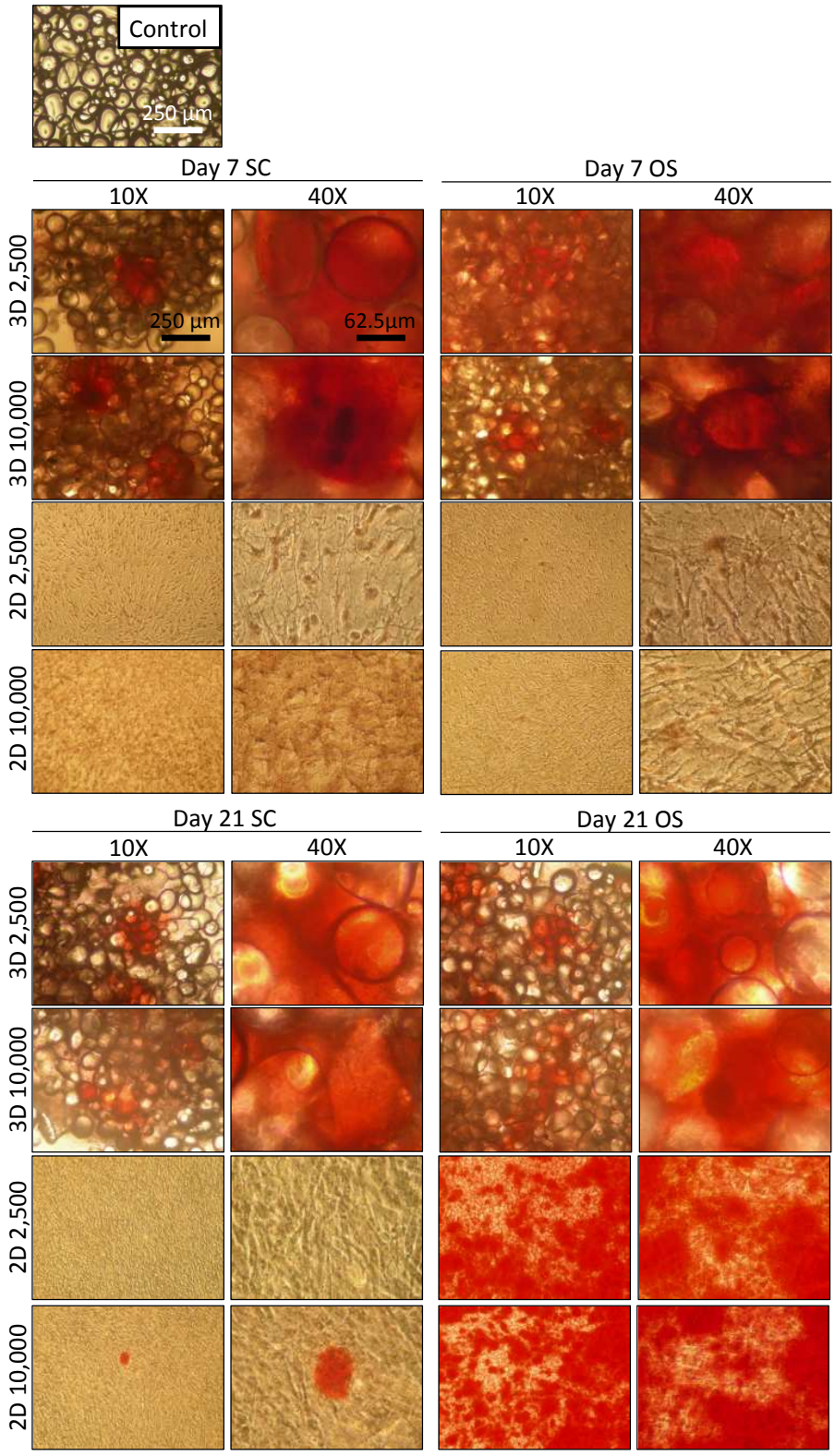

Figure 4-10: Qualitative assessment of calcium deposition by hMSCs in 2D and 3D systems in standard culture (SC) medium and osteogenic (OS) medium on Day 7 and 21 of differentiation. Cells were seeded at 2,500 and 10,000 cells cm^{-2} and images were taken in bright field at 10X and 40X. BSG without cells and stained with Alizarin Red were used as negative control. By Day 21, there was more calcium produced in 2D OS conditions than in 2D SC conditions. However, there were no visible differences between 3D OS ad 3D SC conditions.

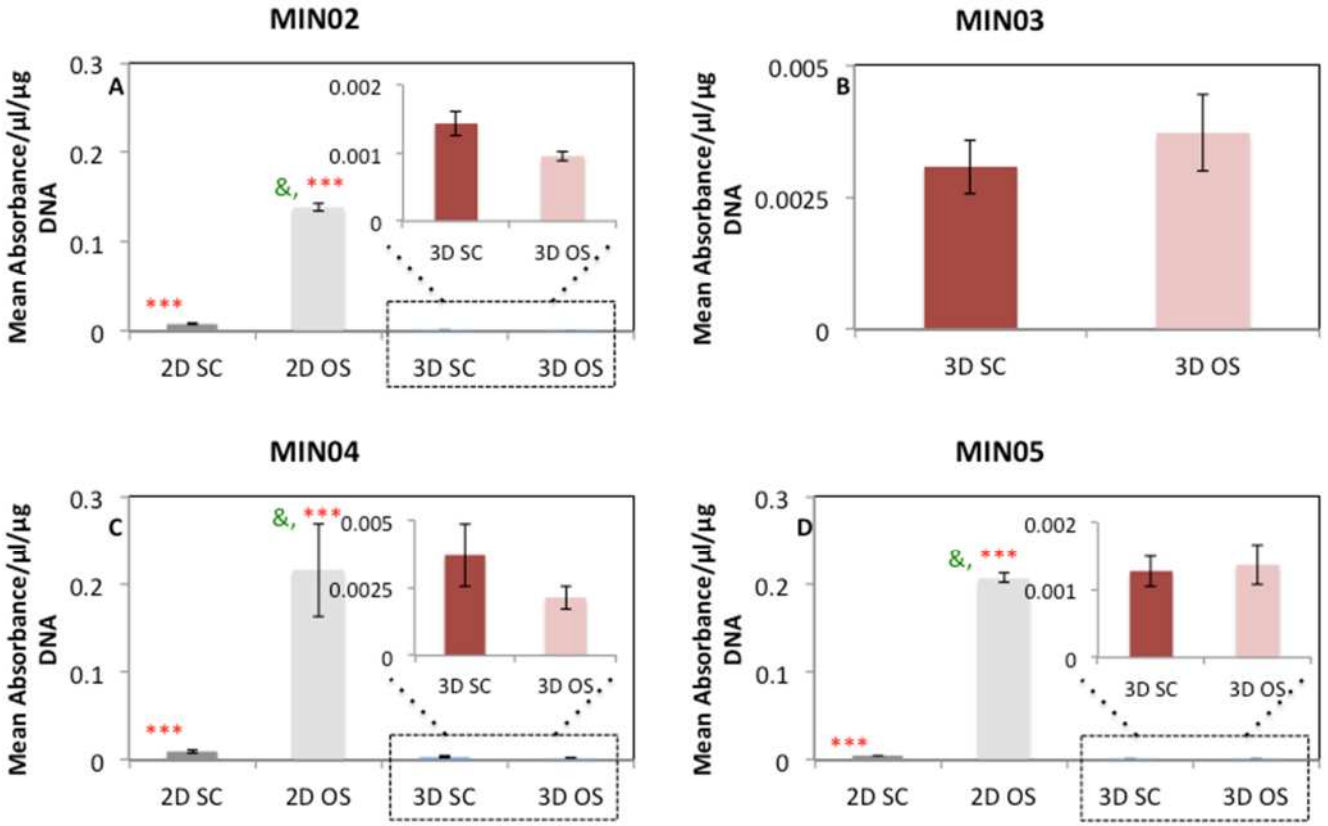

Figure 4-11: Quantification of calcium deposition by hMSCs in 2D and 3D systems in standard culture (SC) medium and osteogenic (OS) medium on Day 21 of differentiation. (A) Experiment MIN02, (B) Experiment MIN03, (C) Experiment MIN04 and (D) Experiment MIN05. Cells were seeded at 10,000 cells cm^{-2} in Experiments-MIN02 and MIN03 and at 2,500 cells cm^{-2} in Experiments-MIN04 and MIN05. Mineral deposition was quantified using Alizarin Red assay. ***$p<0.001$ for comparisons between 2D and 3D in same medium. & $p<0.001$ comparisons between SC and OS of same culture condition. n=3. Error bars represent S.E.M.

4.3.4 Osteocalcin Expression

Osteocalcin is one of the organic components of the extracellular matrix released by osteoblasts and is considered a late osteogenic marker (Hauschka et al. 1989). To assess the extent of bone formation in 2D and 3D, OCN immunostaining was performed in Experiment OCN01, as described in Sections 2.3.3 and 2.3.15.

The results in Figure 4-12 showed absence of OCN expression in negative control. Moreover, the hMSCs did not have any auto fluorescence (non-specific fluorescence from samples) in blank (2D or 3D) samples or non-specific primary and secondary antibody staining on both culture platforms.

The results in Figure 4-13 showed higher OCN expression in 2D OS as compared to 2D SC on day 21 of differentiation and again highlighted that hMSCs used were responsive to OS medium in 2D. In 3D, there did not seem to be any apparent differences between SC and OS conditions and these observations are in line with collagen and mineral quantitative analyses on same time point.

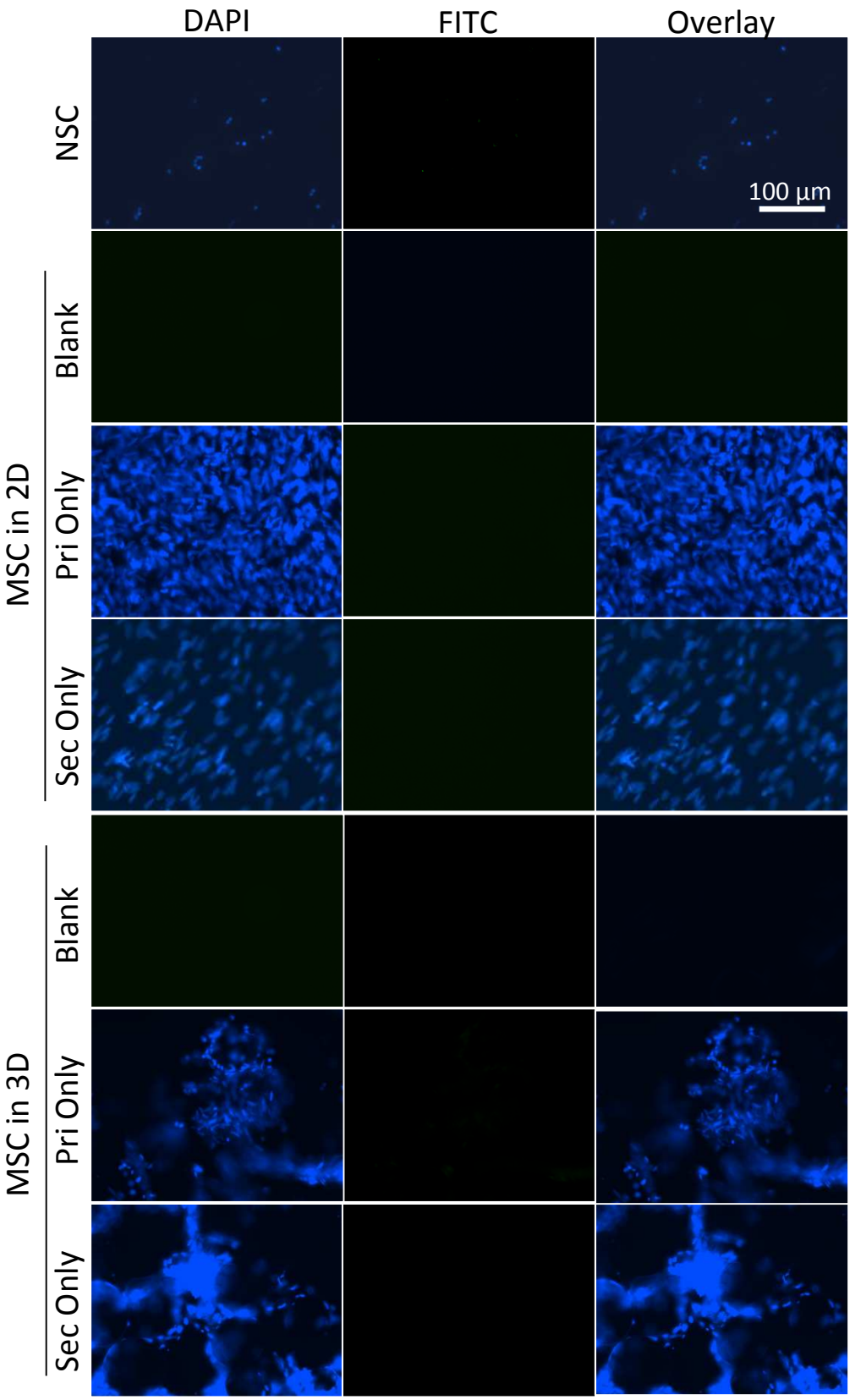

Figure 4-12: Controls for Osteocalcin staining in 2D and 3D. There was no auto-fluorescence (non-specific fluorescence from samples) or non-specific binding of Pri and Sec Abs in hMSCs seeded in 2D or 3D (BSG) and Neural Stem cells (NSC) were used as negative control.

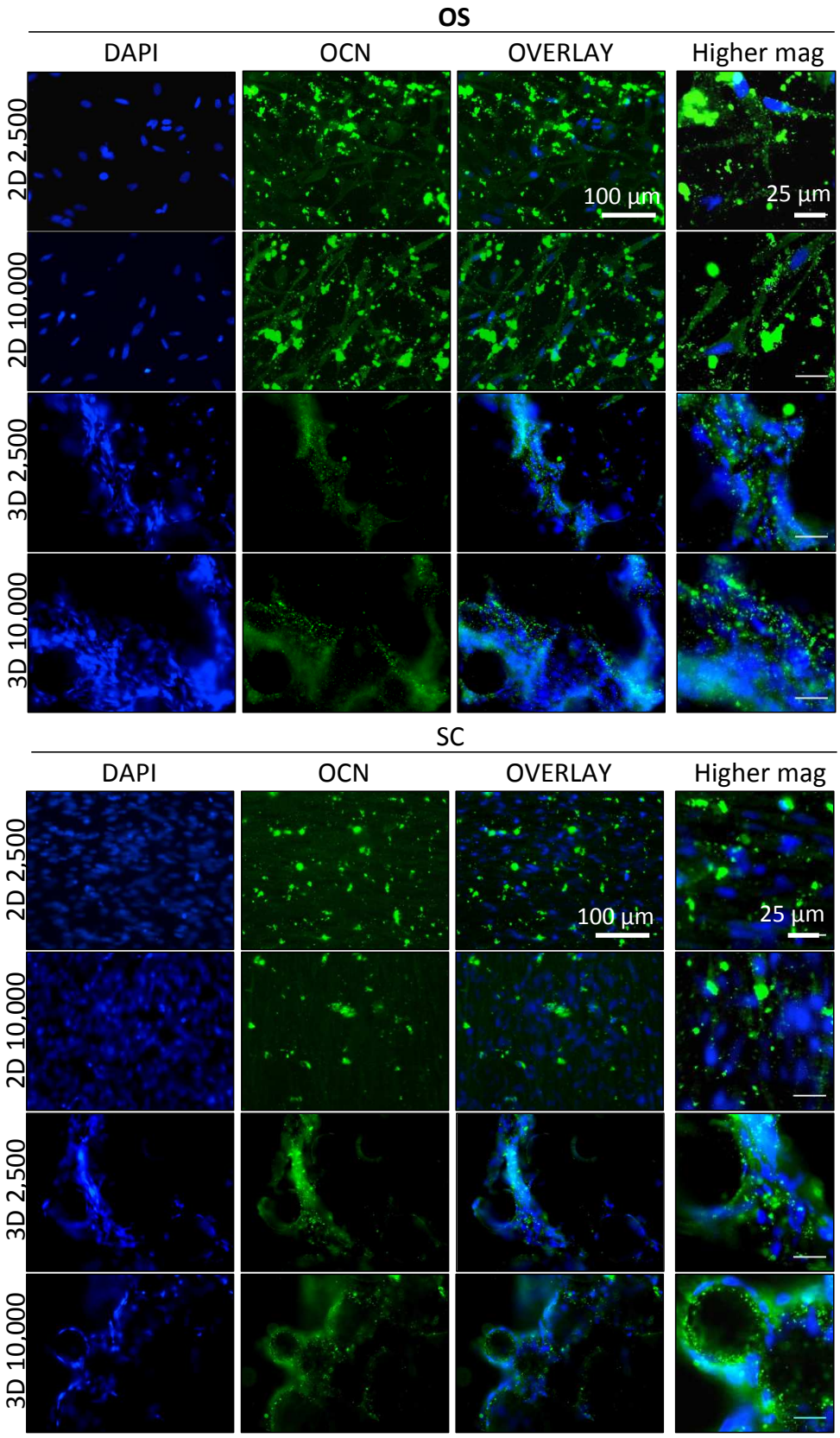

Figure 4-13: Osteocalcin (OCN) expression by hMSCs in 2D and 3D in Experiments OCN01, cells were seeded at 2,500 and 10,000 cells cm^{-2} and cultured for 21 days in osteogenic (OS) medium or standard (SC) medium. There was more OCN expressed in 2D OS than in 2D SC but there were no apparent differences between 3D OS and 3D SC.

4.3.5 Extracellular Matrix formation

To evaluate the ECM formation by hMSCs in 3D after 21 days of differentiation, Experiment-ECM01 was performed as described in Section 2.3.3 and 2.3.16.

Low magnification images (Figure 4-14 A) revealed that there was non-homogeneous distribution of cells across the 3D section with significantly more cells on the edges compared to the internal regions of the 3D sections, as seen in SEM images (Figure 4-4 E).

Higher magnification images (Figure 4-14 B) depict colonisation of cells in the inter-particulate regions and positive eosin staining was limited only to a few regions in the sample. Comparison of these images to positive control indicated poor ECM formation in 3D.

Since sectioning through individual glass MS was not possible, the resulting sections of 3D agglomerate were not flat and this may have affected the placement of cells in the section. However, two sections from multiple 3D agglomerates were stained and similar trends in ECM deposition were observed.

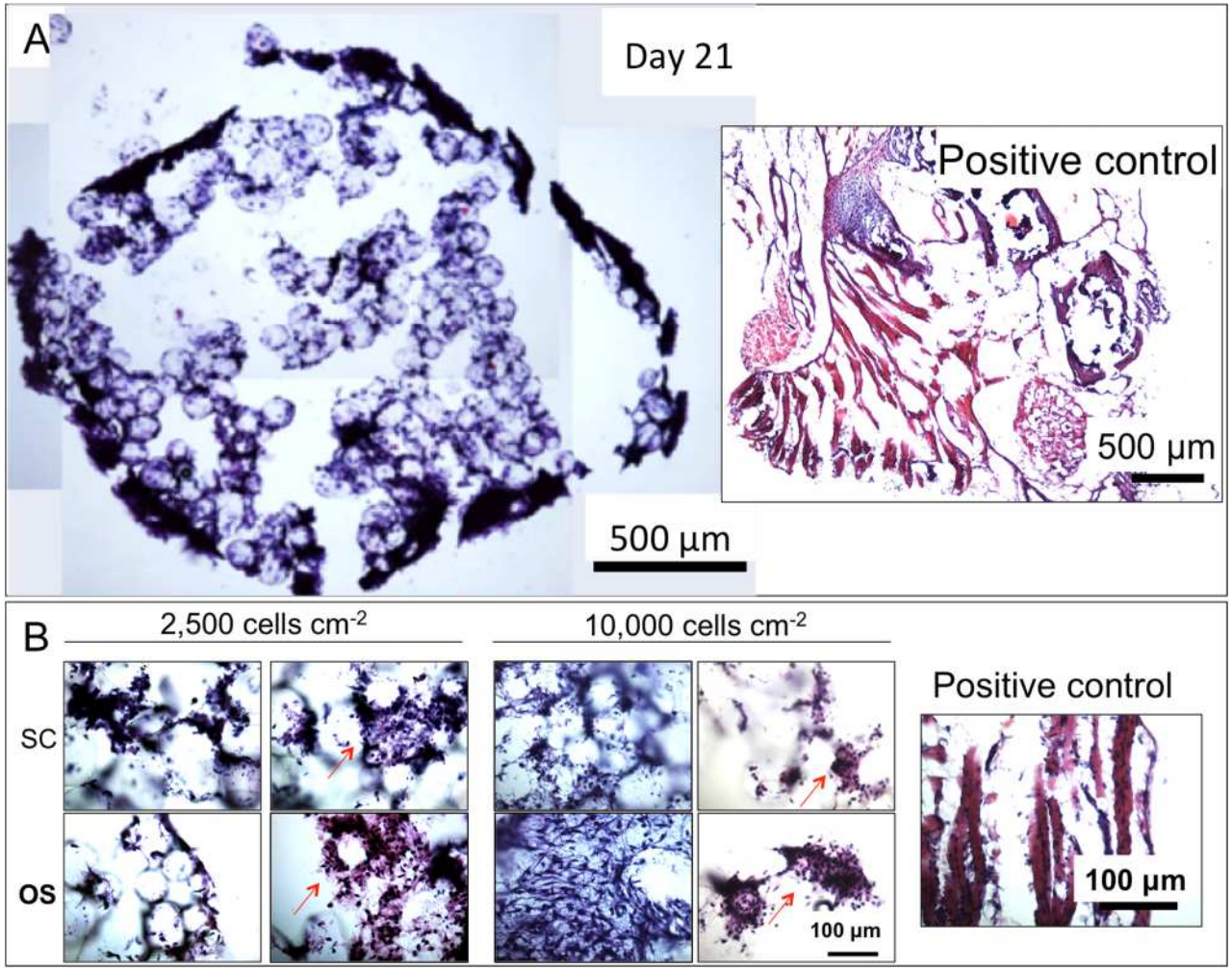

Figure 4-14: Extracellular matrix formation by hMSCs in 3D in Experiment ECM01. (A) A typical H&E stained 3D section. There were more cells on the edges as compared to the internal regions of the 3D agglomerate. (B) High magnification images of some regions inside 3D agglomerate. There was heterogeneity in cell colonisation within the agglomerates. Cells were mostly present in inter-particulate regions and only few regions (arrows) had positive eosin staining. Mouse calvarial tissue was used as a positive control.

4.4 Discussion

4.4.1 Batch-to-batch variability in BSG

There was subtle variability detected between BSG Batches 1 and 2, in terms of DNA content on day 7 of culture in one out of two experiments. This may be due to sampling error leading to Type 1 statistical error or affected samples on day 7 of Experiment BR01 (Banerjee et al. 2009) or due to variation in particle size distribution between the batches detected from laser diffraction as well as major axis length measurements in Chapter 3, Section 3.2.2. The Batch 2 had smaller mean size and may have presented hMSCs with higher mean convexities, which may have caused a negative effect on hMSC growth over the course of 7 days. The effect of surface curvatures is discussed in greater detail in Section 4.4.3.

Since the mean difference between the two batches was only 0.2 µg of DNA, which is not significant from *in vivo* perspective and also since there were similar DNA contents and mitochondrial activates in both batches, in six out of seven data points in Experiments BR01 and BR02; it was concluded that there was negligible batch-to-batch variability in BSG.

4.4.2 Metabolic differences exist in 2D and 3D

It was expected that with increase in hMSCs numbers or DNA content there would be a proportional increase in cell metabolic activity in 3D, similar as is seen is 2D. However, the results showed that though hMSCs had nearly twice as much metabolic activity in 3D as compared to 2D on day 1 of culture, the increase in DNA content was only 1.2-1.4 times. Additionally, there was no linear correlation between cell metabolic activity and DNA content in 3D in extended culture periods. The results also showed different cell metabolic activities in different 2D systems (cells seeded in 24 well plate and 96-well plate), despite same cell number.

Similar observations have also been reported for other cell lines. Ng et al. (2005) showed that Cell Titer 96, [^{3}H] thymidine and Alamar Blue assays provided an inaccurate measure of human dermal fibroblast numbers over 35 days culture period in 3D (PLGA-PCL fibrous scaffolds), in contrast to DNA assay and cell counts. This study is of particular importance because the 3D was a fibrous mesh scaffold containing 80 μm-wide PCL fibers and 20 μm-wide PLGA fibers, which provided similar curvature ranges as in the current study. Other than this, Quent et al. (2010) also showed Alamar Blue assay over-estimated the proliferative activity of OV-MZ-6 cells, BM-MSC, HUCPVC and SKOV-3 cells on 2D, by 21-64% in contrast to the Pico Green and CyQuant assays used for DNA quantification.

Other studies on cancerous cell lines have also suggested differences in metabolic state of cell in 2D and 3D. For example, almost 50-60% down regulation in mitochondrial enzymes (involved in oxidative phosphorylation) and iron metabolism proteins, and 50-60% upregulation in anaerobic glycolysis, nucleotide metabolism and cytoskeletal-related proteins, was observed in human liver cancer cells grown on collagen scaffolds (Lyostypt® from B. Braun, Germany and collagen type I as major constituent) as compared to monolayers (Pruksakorn et al. 2010). There was six times higher expression of human leukocyte antigen (associated with resistance of cancerous cells to Natural Killer cells *in vivo*) by glioma cells in 3D spheroids compared to monolayers (He et al. 2014). There was higher expression of paracrine factors including CXCL12, MMP14, HGF, COX2, and TGFβ1 (involved in invasive transition of breast cancer) by human mammary fibroblasts on collagen scaffolds compared to monolayers (Sung et al. 2013). Finally, there was also 77% and 7% decrease in lactate and alanine levels, respectively (involved in bioenergetics) in 3D spheroids of MG63 cells compared to monolayers (Santini et al. 2004).

These studies strongly suggest that there may be different metabolic states of hMSCs in 2D and 3D and due to this,

extrapolating cell numbers in 3D samples using 2D standard curves may provide an inaccurate measure of cell proliferation in 3D.

Additionally, these differences may not be limited to mitochondrial metabolism but may also be affecting other cellular processes such as osteogenic differentiation. For instance, Maeno et al. (2005) investigated the effect of calcium ion concentration (0 to 50 mM) on mouse primary osteoblasts proliferation and differentiation in 2D and 3D (type II collagen gels) in growth medium. After 60 days, 5mM and 20mM Ca^{2+} promoted better proliferation than 0mM in 2D while, 5mM and 0mM Ca^{2+} promoted more proliferation than 20mM Ca^{2+} in 3D. After 7 days, 6-15 mM Ca^{2+} was needed for 2-fold increased osteocalcin mRNA expression compared to 0mM in 2D but 2mM Ca^{2+} was enough to reach >2-fold increase in 3D. This expression level did not seem to change even if the concentration was increased up to 20mM Ca^{2+} in 3D. Mineral deposition was prominent at 10mM Ca^{2+} in 2D but 6mM Ca^{2+} was enough for the same in 3D. Comparison of Ca^{2+} deposition of cells over a time period of 17 days showed presence of mineral deposition in 3D after 3 days in culture but in 2D this was not observed until day 10 of culture. This clearly demonstrates that differentiation is differently regulated in 2D and 3D and may also explain the unexpected similar or higher levels of mineral, OCN or collagen levels in 3D SC compared to 3D OS at day 7 or 21 of differentiation.

4.4.3 Geometrical control of hMSCs-survival

Cell attachment experiments showed similar DNA contents in 3D and 2D after 24 h of hMSCs seeding at ≤2,500 cells cm^{-2}. However, as the culture period increased, the cells grew significantly slower on 3D with visible MS-cell aggregate formation, similar to as seen in case of commercially available MS, including Cytodex 1, Cytodex 3, Cultispher GL, and HyQsphere P102-L MC (Goh et al. 2013).

Some other studies have also reported slower cell growth in 3D compared to 2D. For example, Kim et al. (2007) seeded rat bone

marrow derived MSCs (3,000 cells ml^{-1}) on smooth collagen or collagen-apatite MS (mean diameter 166 μm, 10 mg per well on 24-well plate) and in plastic wells (2D) in normal growth medium, and found more cells in 2D on day 7 and 10 of culture, in addition to presence of particle aggregation over the culture period. Hong et al. (2009) seeded rat bone marrow derived MSC (1,000,000 cells ml^{-1}) on smooth poly(e-caprolactone) MS (261 μm, 30 mg per well) and in plastic wells (2D) in osteogenic medium and found higher cell numbers in wells on day 3, 7 and 10 of culture. Guedes et al. (2012) seeded mouse primary fibroblasts (300,000 cells ml^{-1}) on smooth Ti-doped PBG MS (63–106 μm wide, 15 mg per well in 96-well plate) and in TC-plastic in normal growth medium and found higher cell numbers in TC-plastic on days 1, 3, 5, 7, 10 and 14 of culture, in addition to particle aggregation in 3D.

Reduced survival during early growth periods on 3D was also observed in the present study. This has also been shown in other studies. For example, Liang et al. (2012) reported higher lactose dehydrogenase release by MSCs on PLGA smooth MS (50-80 μm diameter) compared to monolayers grown on polystyrene dishes over 7 days. Barrias et al. (2004) also reported reduced neutral red uptake by MG63 cells on HA porous MS (550 μm mean diameter, <5 μm pores) compared to cells in polystyrene wells over 7 days. One possible hypothesis is that the reduced viability on 3D may have contributed to slower cell growth on 3D and in order to decipher the possible reasons for this, it is important to understand the effect of surface curvatures on cellular mechanics.

Cells are able to sense the radii of curvature much larger than the size of the cells themselves (Zadpoor 2015). At molecular level, plasma membrane (PM), RhoA/ROCKII, focal adhesion proteins, Myosin IIa and actin fibers have been suggested to work in tandem in order to sense and adapt to local curvatures (McBeath et al. 2004; Ozdemir et al. 2013; Elliott et al. 2015). Once the curvature-sensing proteins and lipids of PM sense the local curvature of underlying surface, they accumulate themselves in the regions of

membrane that needs to be bended and therefore, induce a local membrane curvature (Graham & Kozlov 2010; Vogel & Sheetz 2006). This curved membrane region then integrates to the underlying matrix via integrin-focal adhesion proteins-actomyosin fibers-RhoA assembly (Ozdemir et al. 2013). Finally, as this assembly causes a physical tension on plasma membrane, it affects the signalling pathways involved in osteogenic differentiation and survival (McMahon & Gallop 2005; Ozdemir et al. 2013).

Hence, this suggests that though hMSCs can attach efficiently on MS surfaces, this may have also induced high cytoskeletal-mediated tension on the PM of these cells, leading to damage and ultimately cell death in some cases. In other cells, reduced cell membrane integrity may negatively affect cellular processes, such as cell division and cell migration and ultimately limit their growth (Binamé et al. 2010).

Recently, it has also been suggested that curvatures can even dictate cell colonisation. For example, Rumpler et al. (2008) grew MC3T3-E1 cells on HA plates (2mm thick) containing four channel shapes including, triangular, square, hexagonal and circular with negative curvatures (concavities) and showed thicker cell layers present only in corners of triangular, square and hexagonal channels (concave surfaces) and fewer cells present on flat regions or convex surfaces of the same channels. They also showed that in circular channels, the cells grew uniformly on the entire surface area of the 3D matrix. This is possibly because concavities have faster rate of tissue invasion as compared to convex and flat surfaces (Knychala et al. 2013) and this growth rate is inversely proportional to the width of concavity (Bidan et al. 2013).

In the present study, BSG batches had particles between 40-275 μm in diameter, they may have presented the cells with radii of curvatures from 20-136 μm. This may have affected the cells differently in different regions of same 3D sample and may have further induced different cell-fates. The regions with high

convexities (MS surfaces) may have allowed fewer cells to proliferate (see Figure 4-15 A). On the other hand, star-shaped concavities and flatter regions in the inter-particulate concavities inside the 3D agglomerate and the outer edges of the same agglomerate, respectively, may have allowed cells to grow more rapidly (see Figure 4-15 B, C). Moreover, each of these star-shaped concavities possibly had different patterns of cell colonisation (Kollmannsberger et al. 2011) and this may have further led to formation of heterogonous microenvironments within the 3D sample (see Figure 4-15 D). Some optimal-sized pores may have been more osteoinductive than others and led to the deposition of ECM and mineral by differentiated osteoblasts. Thus, giving it a patchy appearance. This hypothesis is also supported by other studies suggesting that concave surfaces induce osteogenic differentiation in osteogenic sites (Karageorgiou & Kaplan 2005) as well as ectopic sites (Ripamonti 2009) *in vivo*.

Recently, it has been shown that curvature sensing is not limited to single cells. Cells seem to be able to adapt to physical stresses in their environment by distributing proliferative activity and integrating the mechanical equilibrium through cell-cell adhesion and communication, spread across layers of cells (Nelson et al. 2005; Kollmannsberger et al. 2011; Bidan et al. 2013). This suggests that the cells may be able to develop a growth pattern so that they collectively overcome harsher convexities of particles in order to increase their survival rate. This may explain enhanced viability in 3D on day 21 of culture relative to day 1, 4 and 7 of culture. In support of this hypothesis, Boukhechba et al. (2009) showed 70% human osteocytes viability after 20h of cell seeding on biphasic calcium phosphate (BCP) angular particles (60% HA and 40% of β-TCP, 40-80 µm size) and 99% viability by days 7 and 28 of culture. Lei et al. (2011) also showed increasing hMSC viability on irregular-shaped and spherical-shaped bioactive glass MS (1-9 µm and 2-6 µm diameter, respectively) from 4h of seeding to day 7 of culture.

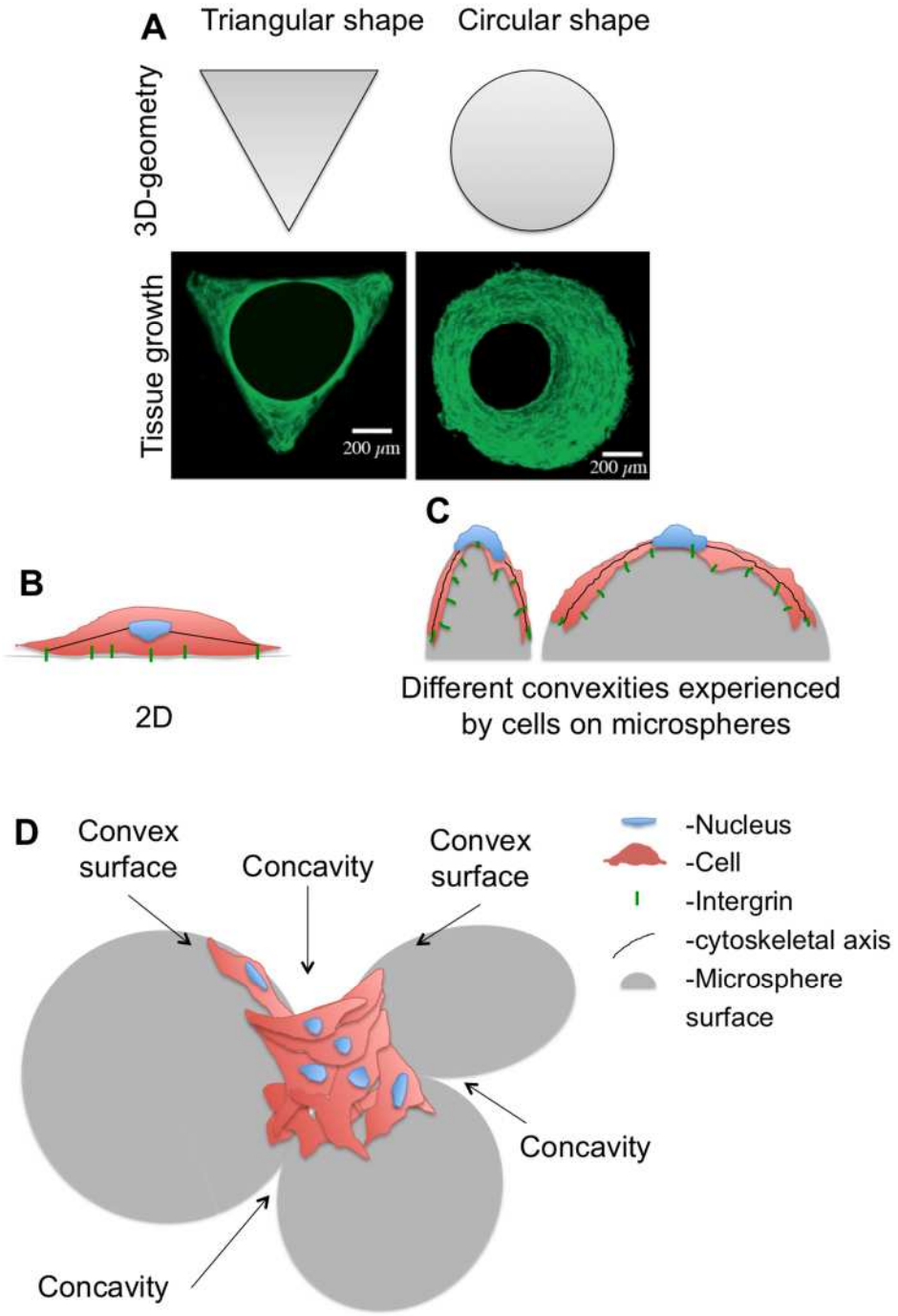

Figure 4-15: Cells sense surface curvature on 3D matrix. (A) New tissue formation in a triangular and circular 3D HA matrix has been shown. Actin stress fibers were stained with phalloidin-FITC and visualized under a confocal laser-scanning microscope. Taken from (Rumpler et al. 2008). (B) Cell morphology in 2D. (C) Different cell-morphologies on MS with different convexities. (D) Cell morphologies in concavities (inter-particulate porosity) created by MS aggregation.

4.4.4 Geometrical control of osteogenesis

The results also revealed higher ALP activity by hMSCs in 3D relative to 2D. This has also been observed for human embryonic stem cells cultured on porous PLGA scaffolds in osteogenic medium up to 21 days (Tian et al. 2008); for pre-osteoblast (MC3T3) cells cultured on CaP cement-alginate MS (150-300 μm wide, 5 μm pore size on surface) in osteogenic differentiation medium up to 14 days (Park et al. 2014); and for pre-osteoblast (MC3T3-E1) cells cultured on poly(methyl methacrylate) fibers (1.153±0.310 μm diameter) in osteogenic differentiation medium (Ozdemir et al. 2013).

This difference has been attributed to cytoskeletal tension-mediated osteogenic differentiation, involving induction of acto-myosin contractility in cells due to the curvatures, followed by enhancement in RhoA expression and ROCKII activation, thereby increasing Runx2 expression and ALP activity (Hansen et al. 2007; Seo et al. 2011; Ozdemir et al. 2013).

Additionally, hMSCs in 3D OS were also observed to have higher ALP activity as compared to 3D SC condition. This result verified that osteogenic supplements (β-glycerophosphate, ascorbic acid and dexamenthsone) in OS medium had an inductive effect on early osteogenesis of hMSCs in 3D, similar to as seen in 2D (Jaiswal et al. 1997; Sottile & Thomson 2003; France et al. 2012). But surprisingly, further investigations revealed significantly lower mineral and collagen production in 3D compared to 2D, irrespective of the culture medium or cells seeding density.

Similar results have also been reported for dental pulp stem cells, which had higher ALP activity on convex surfaces, made from HA chips, compared to concave and flat surfaces, made from PLGA and Ti, respectively, after 48 h of culture. However, after 30 days of culture, there was scarce cell proliferation and lower osteocalcin, osteonectin and BSP production on convex surfaces compared concave and flat surfaces (Graziano et al. 2008). In addition to this,

a study recently showed 2-fold and 1.5-fold drop in Ca^{2+} release by human fetal MSCs (hfMSCs) expanded on Cytodex 3 compared to unexpanded hfMSCs and 2D expanded hfMSCs, respectively, over the course of 28 days in osteogenic medium (Goh et al. 2013). Together, these studies indicate that the cytoskeletal changes induced by convex MS-surfaces may enhance early osteogenesis but they were not suitable for mineralisation/collagen deposition/ECM formation in the present case. This may be because the MSCs are adapted to the bone formation process inside the resorption pits which offers them with concave surfaces and not convex surfaces (Teitelbaum & Ross 2003; Florencio-Silva et al. 2015).

It was interesting to note that despite evidence of weak mineralised matrix and ECM in 3D after 21 days of differentiation, there was presence of OCN expression in not only 3D OS but also at 3D SC at both cell seeding densities. Higher OCN expression in hMSCs cultured on convex spherical structures (350 µm diameter) compared to flat and concave spherical structures (350 µm diameter) has been reported by (Werner et al. 2017) and they further showed that as the radii of curvature (of convex or concave structures) increases, the OCN expression also increases. OCN is characteristic of mature osteoblasts, actively depositing mineralised tissue (Hauschka et al. 1989), it is also known to inhibit apatite crystal growth both *in vivo* (Ducy et al. 1996) and *in vitro* (Romberg et al. 1986). This indicates that OCN expression in 3D is possibly a function of cytoskeletal changes induced as a result of membrane curvatures and may have also affected the formation of mineralised bone matrix by hMSCs. To test this hypothesis, future work is needed.

OCN expression has also been reported for human osteoblasts cultured on PLAGA smooth MS (600-710 µm) after 16 days in culture (Borden et al. 2003); for bone marrow stromal cells cultured on polystyrene (205 µm) or HA (607 µm) MS after 14 and 21 days of culture (Barrias et al. 2005); for rat MSCs cultured on collagen and collagen-apatite MS (166 µm) after 7 days of culture (Kim et al.

2007). However, all of these studies used osteogenic induction medium and none of these reported OCN expression in growth medium without osteogenic supplements, as seen in this study.

Some other studies have suggested that rather than chemical composition of medium, the 3D geometry may sometimes play a more dominant role in determining the cell fate. For example, micro-contact printing studies of individual hMSCs grown in medium containing 1:1 ratio of osteogenic and adipogenic factors, have shown that increasing the cell spread leads to an osteogenic fate in hMSCs. However, rounded morphology, with radius of curvature as 6 μm, induces adipogeneisis (McBeath et al. 2004). Moreover, it has also been demonstrated that in addition to cell spread, the geometric features (membrane curvatures) that increase acto-myosin contractility in MSCs, similar to *in vivo* environment, promote osteogenesis over adipogenesis. This is attributed to c-Jun N-terminal kinase (JNK) and extracellular related kinase (ERK1/2) activation in conjunction with elevated Wnt signalling, a RhoA-independent mechanism for osteogenesis (Kilian et al. 2010). These studies support the hypothesis that rather than the osteogenic supplements, the 3D geometry of hMSCs may have predominantly affected cell fate in the present study and may explain similar levels of mineral, ECM and possibly OCN production in 3D OS and 3D SC conditions on day 21 of differentiation.

Another interesting aspect of this study was the decrease in collagen production from day 7 to 21 of differentiation in 3D OS condition. Likewise, Liang et al. (2012) also showed a 75% drop in collagen mRNA production by rat MSCs cultured on Dex and bFGF loaded- or unloaded-PLGA MS from week 1 to week 4 of culture, despite Dex and bFGF being osteogenic factors. This again is in support of the hypothesis that differentiation may be regulated differently in 3D and the combinational effect of convex surfaces with well-known osteogenic factors needs to be further investigated.

There is currently a good understanding of RANKL signalling pathways and cross talk between osteoclasts, osteoblasts, osteocytes and bone lining cells during bone remodelling *in vivo* (Teitelbaum & Ross 2003; Florencio-Silva et al. 2015). However, the control of osteogenic fate by via geometrical cues is poorly understood. Therefore, based on this study and related literature (Graziano et al. 2008; Hansen et al. 2007; Seo et al. 2011; Ozdemir et al. 2013; Bidan et al. 2016), the following a model for geometrical control of osteogenesis is proposed, see Figure 4-16.

Stage 1: MSCs are recruited for bone formation on relatively flat bone surface where they attach and migrate towards the resorption pit created by osteoclast.

Stage 2: during migration, they initially encounter the convex edges of concavity, which causes cytoskeleton-tension and induces early osteogenesis through RhoA-ROCKII-Runx2/ALP pathway.

Stage 3: as these cells enter the concavity, they experience a concave topography, which may also induce cytoskeletal changes and subsequent molecular signalling causing the osteoblasts to form collagen fibers and mineralised bone matrix.

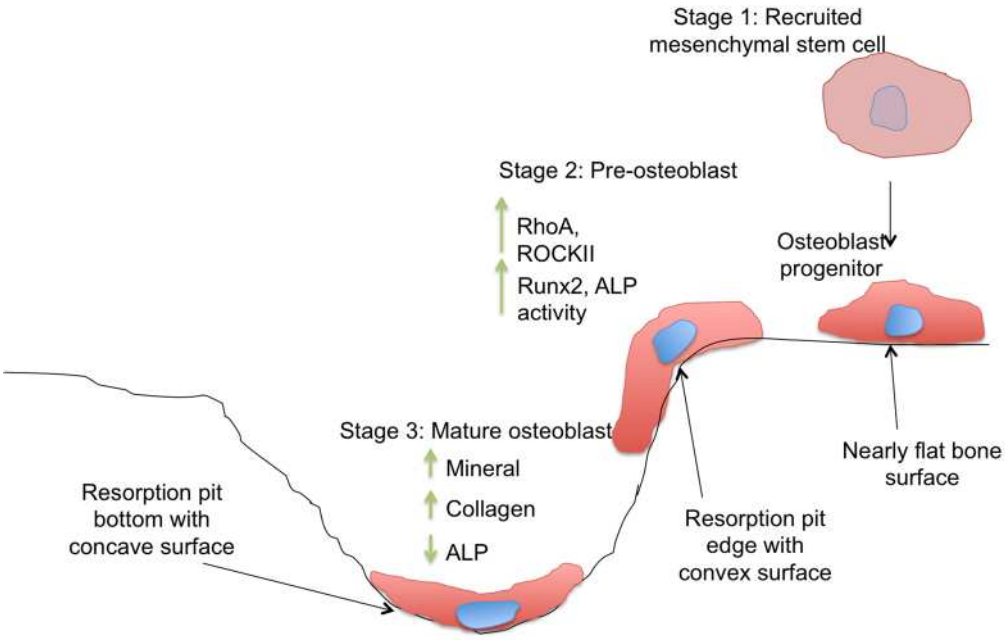

Figure 4-16: Proposed model for geometrical regulation of *in vivo* bone formation, based on contributions also from (Graziano et al. 2008; Hansen et al. 2007; Seo et al. 2011; Ozdemir et al. 2013; Bidan et al. 2016).

4.5 Conclusions

In this chapter, a number of experiments were carried out to understand hMSCs response to 2D and MS culture system and the results presented an array of differences between the two systems, ranging from metabolism, survival, proliferation and differentiation, some of which may need further investigation.

These observations also suggest that cells in 2D do not truly mimic the *in vivo* environment and therefore, due to this borosilicate glass MS culture system was used as a control to study the effect of phosphate based glass microspheres formulation and effect of introduction of porosity on hMSC-fate in Chapter 5.

Lastly, there is clearly a role of cytoskeletal-tension in the osteogenic differentiation. However, questions of how cell mechanics modulate cell contractility and how this tension transduces into biomechanical signals, are yet to be answered.

Chapter 5 Phosphate-Based Glass Microspheres

5.1 Introduction

In this chapter, different phosphate based glass (PBG) degradable microspheres (MS) have been explored, in terms of human mesenchymal stem cell (hMSC) growth and osteogenic differentiation. Both direct and indirect cell-material experiments were performed in order to study the effect of geometry, surface chemistry and degradation products on hMSC-fate.

The cytocompatibility of angular and spherical shaped P45 particles is compared in Section 5.2, followed by effect of acid washing on porous MS in Section 5.3 and batch-to-batch variability of different MS-types in Section 5.4. This leads on to assessments of hMSC attachment, aggregation, viability, growth and morphology in Sections 5.5, 5.6, 5.7, 5.8, 5.9, respectively. In the following sections, osteogenic differentiation of hMSCs on different MS is explored, which includes alkaline phosphatase activity, collagen production, Ca and P release, osteocalcin expression and extracellular matrix formation in Sections 5.10, 5.11, 5.12, 5.13, 5.14, respectively. Cytotoxicity of MS is also investigated in Section 5.15 and lastly, all the results have been discussed and concluded in Sections 5.16 and 5.17, respectively.

5.2 Angular vs. spherical particles

To study the effect of different glass geometries on hMSC growth, Experiments-PRE01 was performed as described in Section 2.3.3.

The results in Figure 5-1 showed that there was more cell metabolic activity in AG1 P45 BGMS and AG1 P45 PGMS relative to AG1 P45 BGMP, at all time points with statistically significant differences ($p<0.05$, $p<0.01$, $p<0.001$). It was also interesting to observe that

despite higher surface area of AG1 P45 PGMS, the metabolic activity of cells was not significantly different between AG1 P45 BGMS and AG1 P45 PGMS.

ESEM images from day 7 of culture, see Figure 5-2, illustrated fewer hMSCs present on AG1 P45 BGMP compared to spherical particles. Moreover, the hMSCs on AG1 P45 BGMP showed poorer cell spread and growth. In case of AG1 P45 BGMS, hMSCs grew more efficiently in inter-particulate porosity, forming cellular networks made from dense sheets of continuous cell material, together with visible cytoplasmic interconnections bridging across one MS to another.

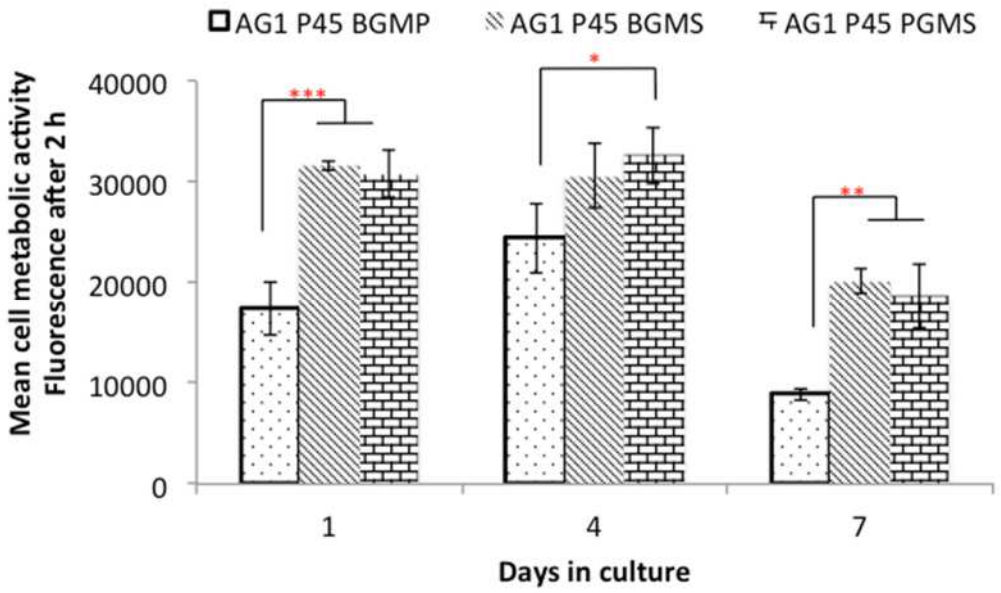

Figure 5-1: Effect of particle shape on hMSC metabolic activity. Cells were seeded at 5,000 cells well^{-1} on AG1 P45 BGMP, AG1 P45 BGMS and AG1 P45 PGMS and cell metabolic activity was measured after 1, 4 and 7 days of culture, using AlamarBlue® assay. n=6. *, **, *** indicate $p<0.05$, $p< 0.01$, $p<0.001$, respectively.

In case of AG1 P45 PGMS, ESEM images, see Figure 5-3, showed that most of the cells either grew over the pore windows or around the pore window edges, without penetrating them. Only the pore windows >25 μm in size, allowed penetration of cells and if the pores were interconnected, the cells were also able to proliferate and grow in the interconnecting pores. Based on these results, only spherical shaped particles (BGMS and PGMS) were selected for further investigations.

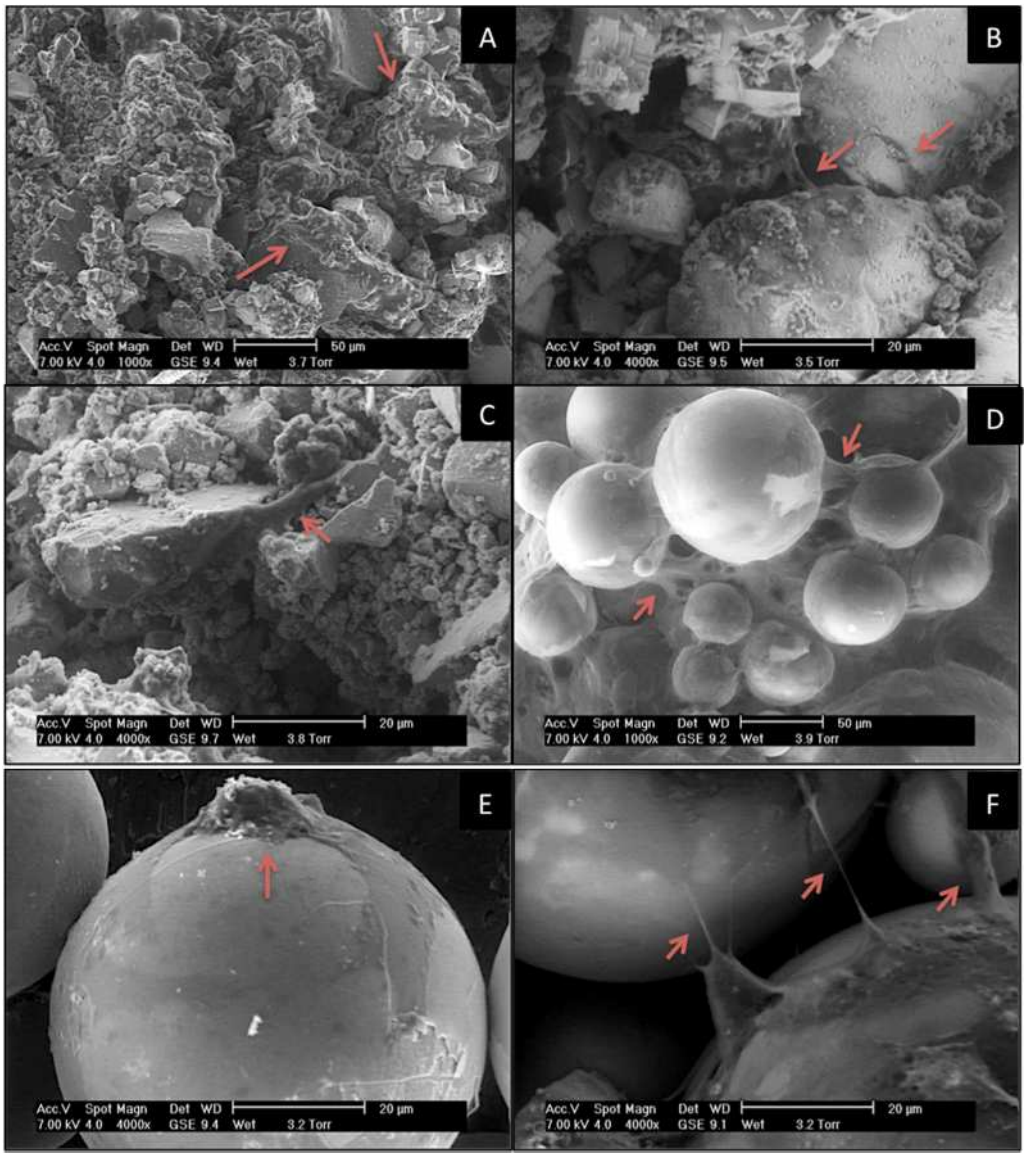

Figure 5-2: ESEM images of hMSCs AG1 P45 BGMP (A-C) and AG1 P45 BGMS (D-F) after 7 days of culture in Experiment-PRE01. Scale bars A, D-50 µm and B, C, E, F-25 µm. Arrows indicate cells.

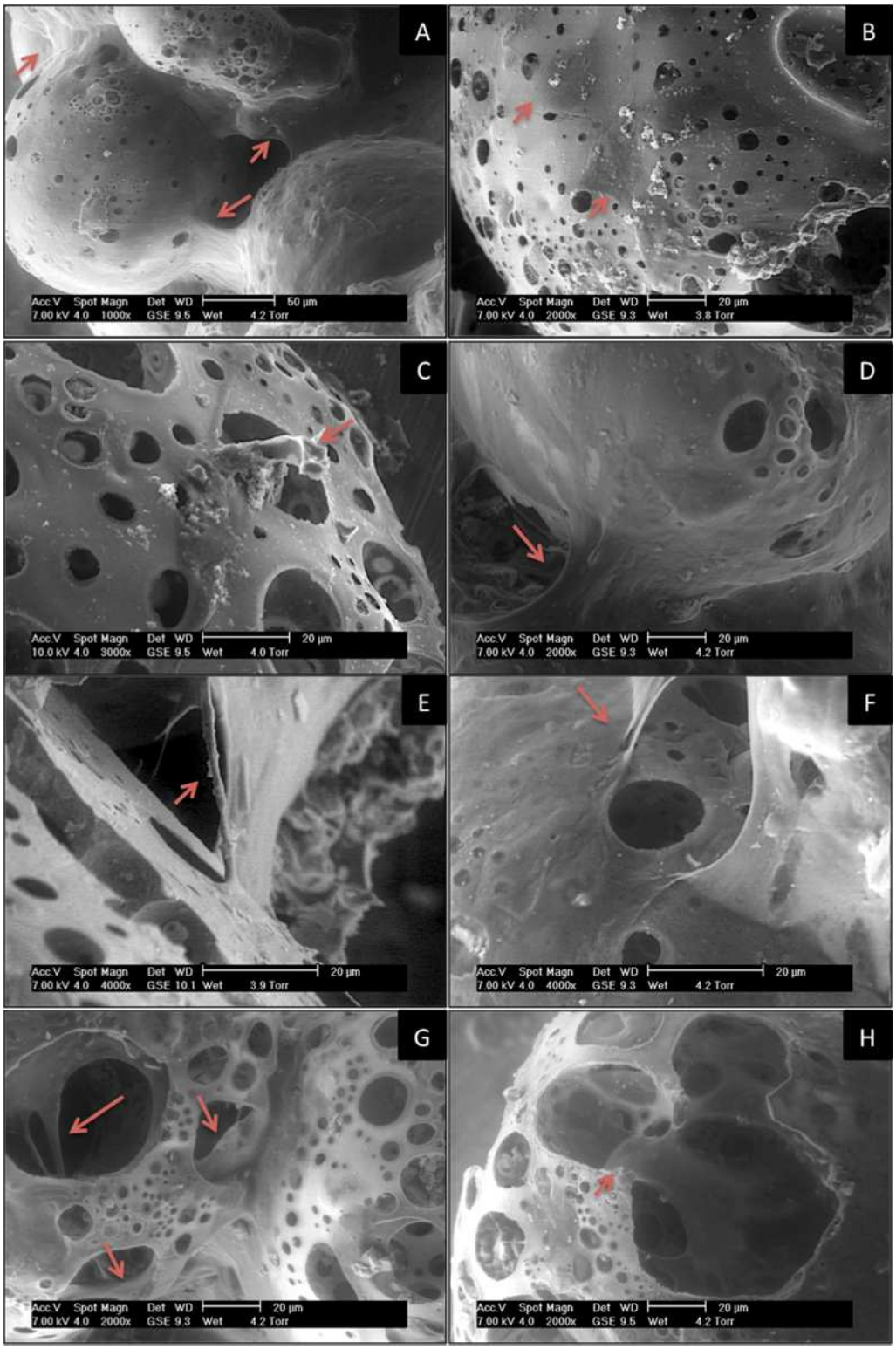

Figure 5-3: ESEM images of hMSCs on AG1 P45 PGMS after 7 days of culture in Experiment-PRE01. Scale bars A-50 µm and B to H- 25 µm. Notice the presence of cells over and around the edges of pore windows <25 µm in B, C, D, E and F and presence of cells inside the pores >25 µm in G and H. Arrows indicate cells.

5.3 Acid washed vs. non-washed PGMS

The acid washing step, as detailed in Section 2.1, was performed on PGMS in order to remove excess porogen as well as to reduce the closed porosity (see Chapter 3, Section 3.7.2 for discussion on physical changes in PGMS after the acid wash). To study the effect of acid washing on hMSCs, Experiment-AW01 was performed as described in Section 2.3.3.

The results in Figure 5-4 A showed no significant difference in cell metabolic activity on days 1 and 7 of culture but higher metabolic activity on acid washed P40 PGMS relative to non-washed PGMS ($p<0.05$) on day 4. DNA measurements of same biological replicates also showed higher DNA content in acid washed P40 PGMS on day 4 and day 7 of culture, see Figure 5-4 B, with statistical significance on day 7 ($p<0.001$). To test the repeatability of these results, Experiment-AW02 was performed and results in Figure 5-4 C again showed higher DNA content in acid washed P40 PGMS ($p<0.001$) on day 7.

To investigate if the chemical nature of glass surface after acid washing was affecting hMSC growth, Experiments AW03 and AW04 were performed. In both experiments, only bulk MS (acid washed or non-acid washed from same batch) were compared to avoid the effect of porosity.

In Experiment-AW03, hMSCs were seeded at 500, 1,000, 2,000 and 3,000 cells cm^{-2} and a DNA assay was performed after 1 day. The results in Figure 5-5 A indicated no effect of acid washing on hMSC attachment as there were no significant differences between non-washed or acid washed BSG, P45 BGMS or P40 BGMS for all the cell seeding densities.

In Experiment-AW04, hMSCs were seeded at 2,500 cells cm^{-2} on acid washed or non-acid washed P40 BGMS and cultured for 7 days. The results in Figure 5-5 B and C showed no significant differences

in hMSC metabolic activity and DNA content on day 1 and day 7 of culture. However, both parameters were higher in non-acid washed P40 BGMS ($p<0.05$), opposite to as seen in Experiment-AW01.

These results together suggested that the enhancement in hMSC growth seen in case of P40 PGMS AW in Experiments-AW01 and AW02, was not due to any possible change in chemical nature of P40 glass, as a result of acid washing.

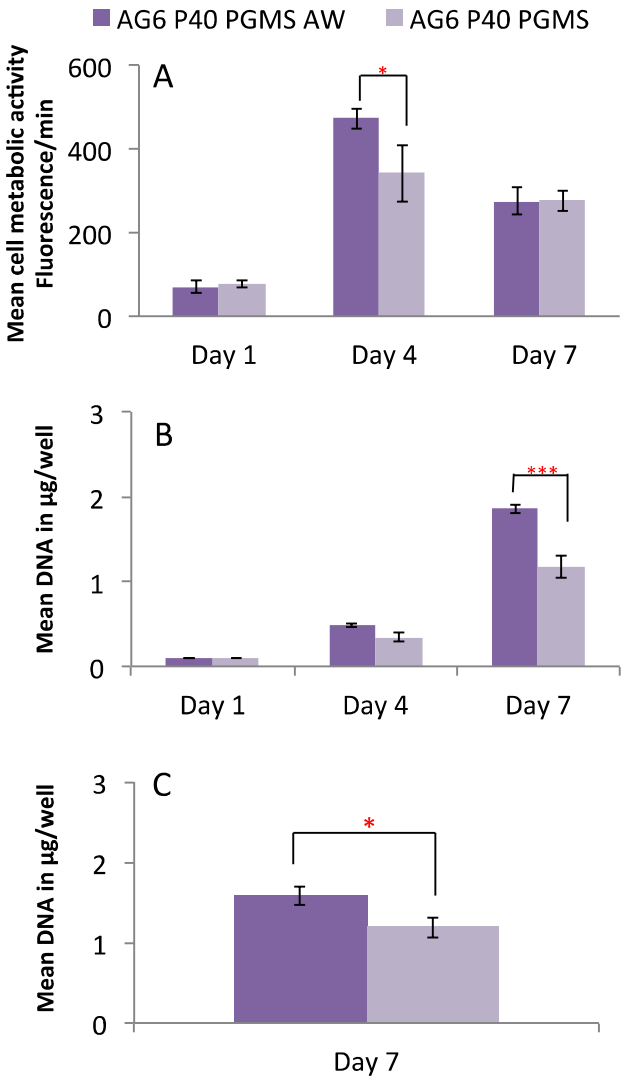

Figure 5-4: Effect of acid washing of PGMS on hMSC growth. (A, B) Experiment-AW01 and (C) Experiment-AW02. Cells were seeded at 2,500 cells cm^{-2} in both experiments and DNA assay and cell metabolic activity assay were performed using PicoGreen® assay and PrestoBlue® assay, respectively. n=3. *, *** indicate $p<0.05$ and $p<0.001$, respectively. Error bars represent S.E.M.

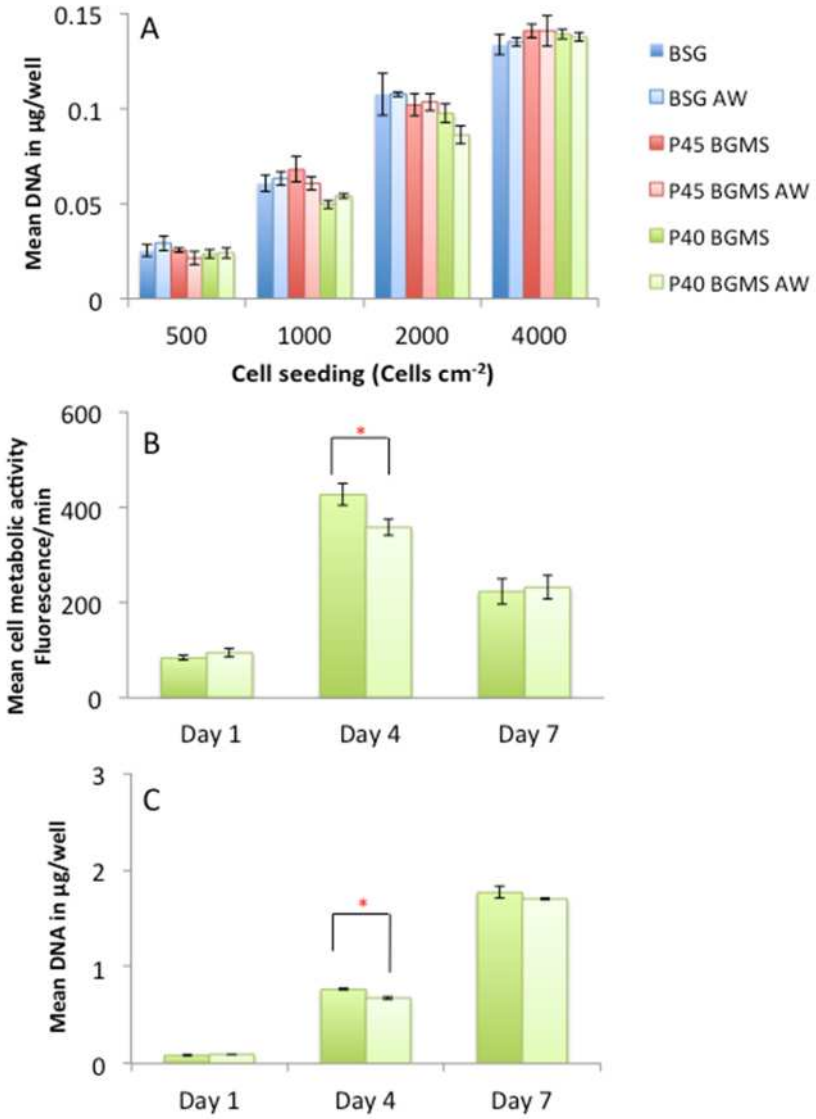

Figure 5-5: Effect of acid washing of bulk glass microspheres on hMSC attachment and growth. (A) Experiment-AW03 (Day 1), (B, C) Experiment-AW04. Cells were seeded at 500, 1,000, 2,000 and 4,000 cells cm^{-2} in Experiment-AW03 and at 2,500 cells cm^{-2} in Experiment-AW04. DNA assay and cell metabolic activity assay were performed using PicoGreen® assay and PrestoBlue® assay, respectively. n=3. * indicates $p<0.05$. Error bars represent S.E.M.

5.4 Batch-to-batch variability

To study the batch-to-batch reproducibility of each MS-type, in terms of the cellular responses and also to draw comparisons across different experiments, hMSC proliferation was compared on two batches of BGMS and PGMS separately as described in Section 2.3.3.

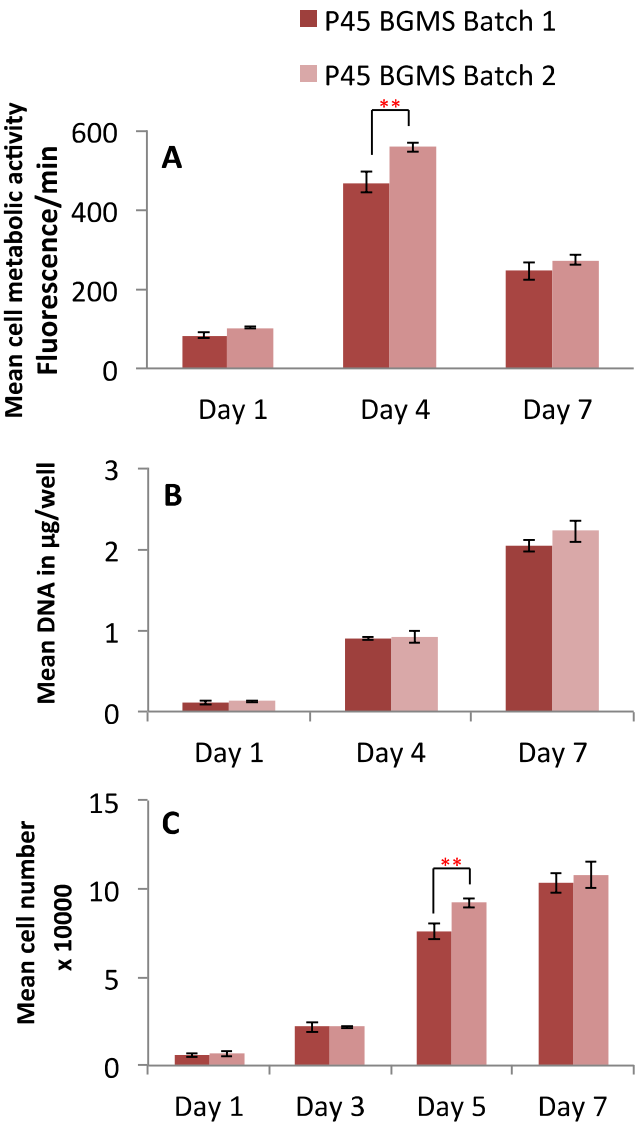

Figure 5-6: Batch-to-batch variability in P45 BGMS in terms of hMSC growth. (A, B) Experiment-BR03 and (C) Experiment-BR04. Cells were seeded at 2,500 cells cm^{-2} in both experiments. DNA, cell metabolic activity and cell number measurements were performed using PicoGreen® assay, PrestoBlue® assay and manual cell counts, respectively. n=3, *,**,*** indicate $p<0.05$, $p<0.01$ and $p<0.001$, respectively. Error bars represent S.E.M.

In Experiments-BR03 and BR04, P45 BGMS Batch 1 and P45 BGMS Batch 2 were compared. The results showed no significant differences in cell metabolic activity on day 1 and 7 of culture. However, on day 4, there was higher metabolic activity in Batch 2 compared to Batch 1 ($p<0.01$) (Figure 5-6 A). Additionally, DNA measurements of same biological replicates showed no significant differences on any time points (Figure 5-6 B). Cell count measurements further confirmed no significant differences between

the two batches on days 1, 3 and 7 of culture, with some differences only on day 5 ($p<0.01$) (Figure 5-6 C). These results collectively suggested good batch reproducibility for P45 BGMS after 7 days.

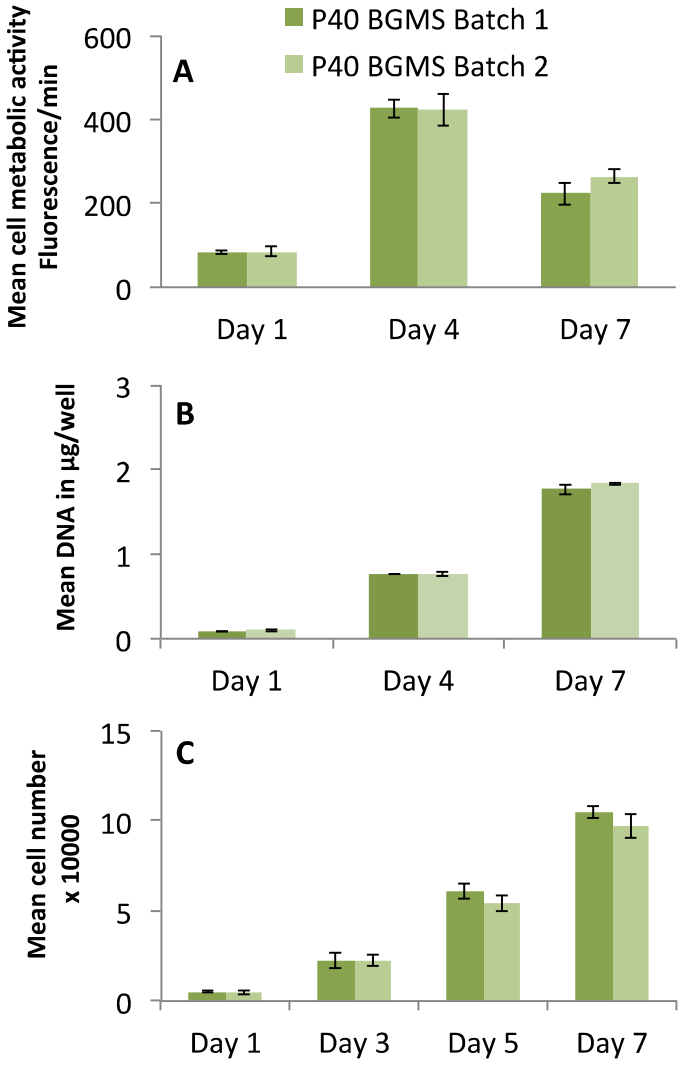

Figure 5-7: Batch-to-batch variability in P40 BGMS in terms of hMSC growth. (A, B) Experiment-BR05 and (C) Experiment-BR06. Cells were seeded at 2,500 cells cm^{-2} in both experiments. DNA, cell metabolic activity and cell number measurements were performed using PicoGreen® assay, PrestoBlue® assay and manual cell counts, respectively. n=3, error bars represent S.E.M.

In Experiments-BR05 and BR06, P40 BGMS Batch 1 and P40 BGMS Batch 2 were compared. The results in Figure 5-7 A, B and C showed no significant differences in metabolic activity, DNA content or cell counts over 7 days of culture and this suggested high batch-to-batch reproducibility for P40 BGMS.

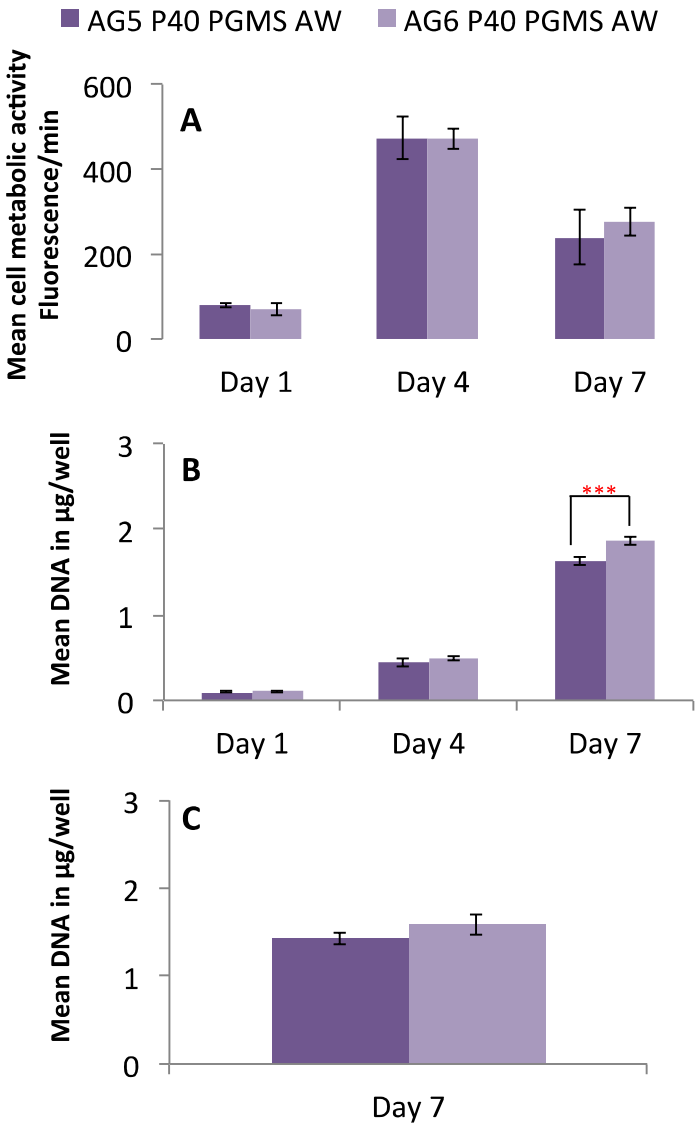

Figure 5-8: Batch-to-batch variability in P40 PGMS AW in terms of hMSC growth. (A, B) Experiment-BR07, (C) Experiment-BR08. Cells were seeded at 2,500 cells cm^{-2} in both experiments. DNA and cell metabolic activity measurements were performed using PicoGreen® assay and PrestoBlue® assay, respectively. n=3, *** indicate $p<0.001$. Error bars represent S.E.M.

Finally, in Experiment-BR07, AG5 P40 PGMS AW and AG6 P40 PGMS AW were compared. The results in Figure 5-8 A, B showed no significant differences in cell metabolic activity and DNA content between the two batches on days 1 and 4 of culture. However, on day 7, though there was no difference in metabolic activity, there was a mean difference of 0.24 µg in DNA content present on AG5 P40 PGMS AW and AG6 P40 PGMS AW ($p<0.001$). When the repeatability of day 7 DNA measurements was tested in Experiment-

BR08, the results in Figure 5-8 C again indicated similar trend with mean difference of 0.16 µg in DNA content. However, there was no statistical significance. These results suggested subtle batch-to-batch variability in P40 PGMS AW.

5.5 Human MSC attachment on microspheres

To explore the effects of MS glass formulation and introduction of porosity on hMSC attachment in a 3D system, Experiments-CA03 and CA04 were performed as described in Section 2.3.3.

In Experiment-CA03, results in Figure 5-9 A showed a general decreasing trend in cell metabolic activities, where BSG>P45 BGMS>P40 BGMS>P40 PGMS AW, at lower cell seeding densities up to 5,000 cells cm^{-2}. At higher cell seeding density of 10,000 cells cm^{-2}, this trend was visible only for bulk MS and P40 PGMS AW had similar cell metabolic activity as BSG (Figure 5-9 A).

The DNA measurements (Figure 5-9 B) for same biological replicates showed no significant differences between the DNA content in different MS conditions at cell seeding densities of ≤2,500 cells cm^{-2}. However, at 5,000 cells cm^{-2} there was significantly lower DNA content in P40 PGMS AW compared to P45 BGMS and P40 BGMS ($p<0.01$) and at 10,000 cells cm^{-2} there was significantly lower DNA content in BSG compared to P45 BGMS ($p<0.001$), P40 BGMS ($p<0.001$) and P40 PGMS AW ($p<0.05$).

Comparison of DNA and metabolic activity assessments indicated that although there were similar number of hMSCs attaching to different MS conditions at 2500 cells cm^{-2}, their metabolic activities were different. This suggested that PBG MS, especially P40 BGMS and P40 PGMS, may be having a negative effect on hMSC metabolic activity after one day of culture.

In Experiment-CA04 (Figure 5-9 C), only the cell metabolic activity measurements were performed and the results again showed a general decreasing trend in cell metabolic activities, where

BSG>P45 BGMS>P40 BGMS>P40 PGMS AW samples at cell seeding densities of 625, 2,500 and 5,000 cells cm^{-2}, without statistical significance (based on two-way ANOVA), possibly due to larger error bars for measurements at cell seeding densities of 5,000 and 10,000 cells cm^{-2}.

5.6 Particle aggregation

To investigate the extent of particle aggregation in different MS at different cell seeding densities in the Experiment-CA03, then live cell imaging was performed 24 h after cell seeding. The results in Figure 5-10 showed that all MS-types formed aggregates at higher cell densities of 5,000 and 10,000 cells cm^{-2} but it was more prevalent in bulk MS conditions relative to porous MS.

In Experiment-AG01, hMSCs were seeded at 2,500 cells cm^{-2} and live cell images, see Figure 5-11 A, indicated that P40 BGMS aggregated faster than P45 BGMS, and both BSG and P40 PGMS AW did not show significant aggregation.

In Experiment-AG02, the cell seeding density was increased to 10,000 cells cm^{-2}, in order to enhance the aggregation process over 24 h culture period. The images in Figure 5-11 B again showed that the fastest aggregation was in the case of P40 BGMS, followed by P45 BGMS and BSG with least aggregation in case of P40 PGMS AW.

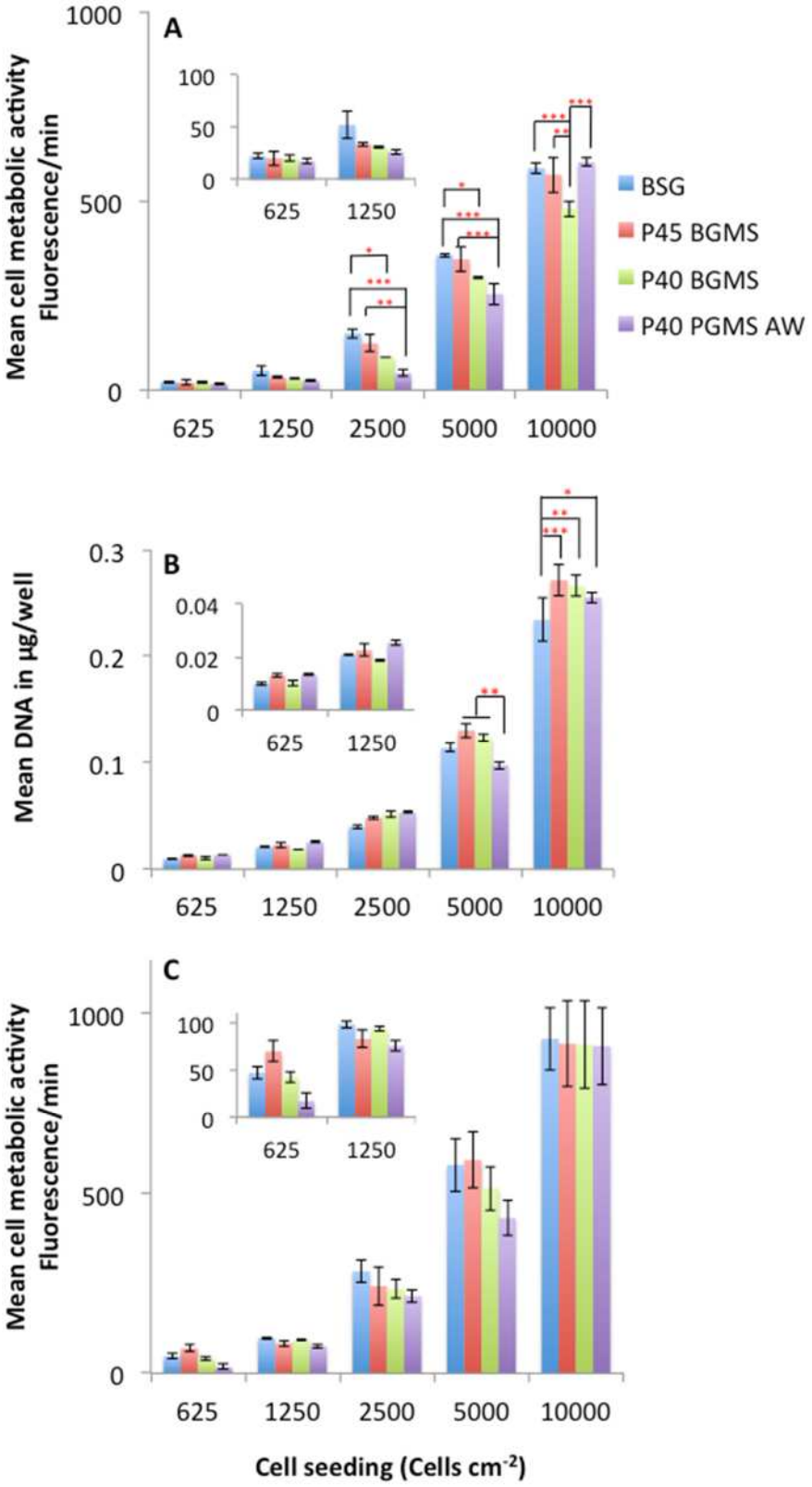

Figure 5-9: Human MSC attachment on different glass microspheres. Cells were seeded at increasing cell seeding densities of 625, 1,200, 2,500, 5,000 and 10,000 cells cm^{-2} and assessed after 1 day of culture. (A, B) Experiment-CA03 and (C) Experiment-CA04. DNA and cell metabolic activity measurements were performed using PicoGreen® assay and PrestoBlue® assay, respectively. n=3. *, **, *** indicate $p<0.05$, $p<0.01$ and $p<0.001$, respectively. Error bars represent S.E.M.

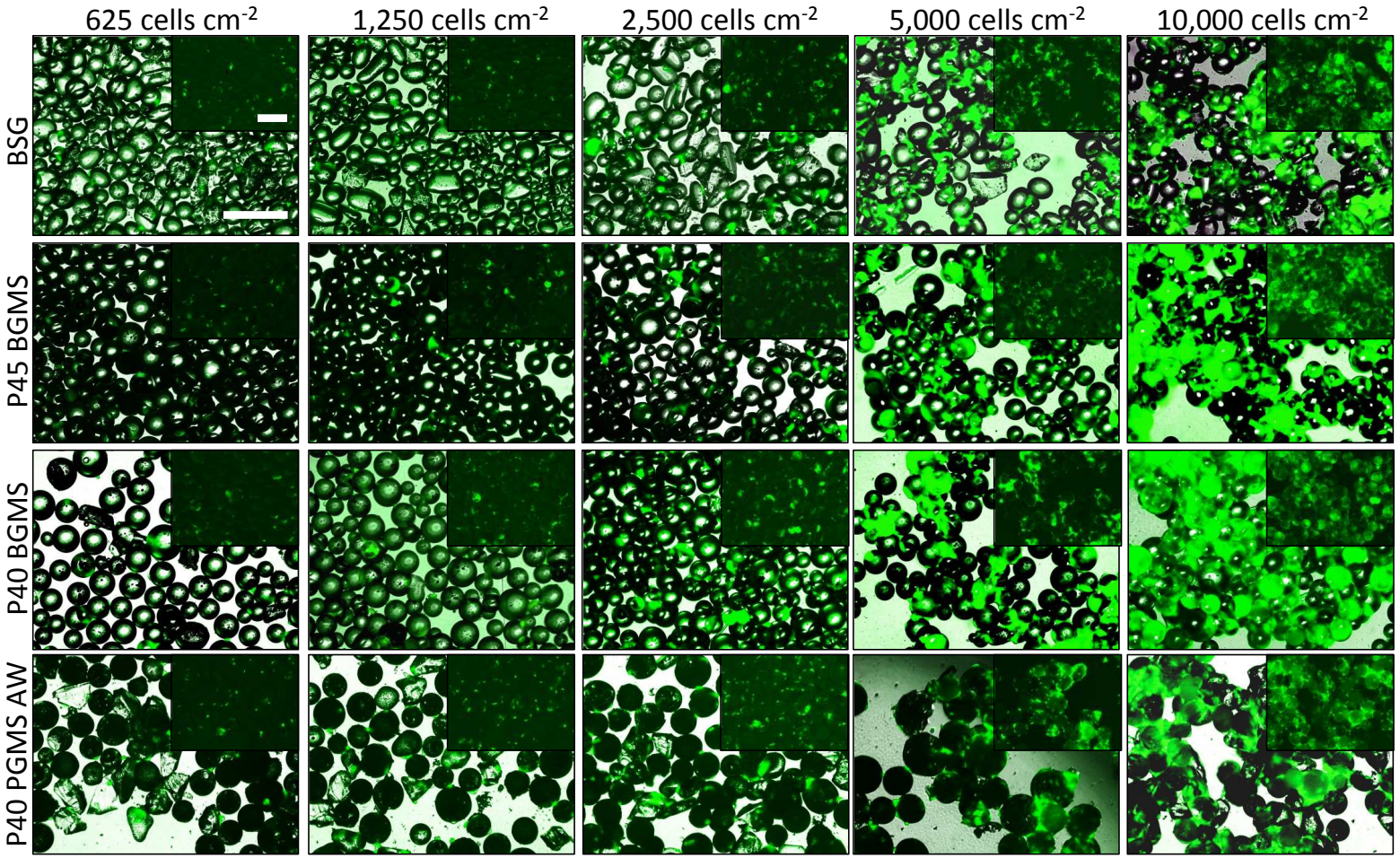

Figure 5-10: FITC channel and overlay (FITC + Bright field) images of live hMSCs on different microsphere conditions after 1 days of culture. Cells and particles formed agglomerates in all MS types at higher cell seeding densities of 2,500, 5,000 and 10,000 cells cm^{-2}. Scale bars- 250 μm.

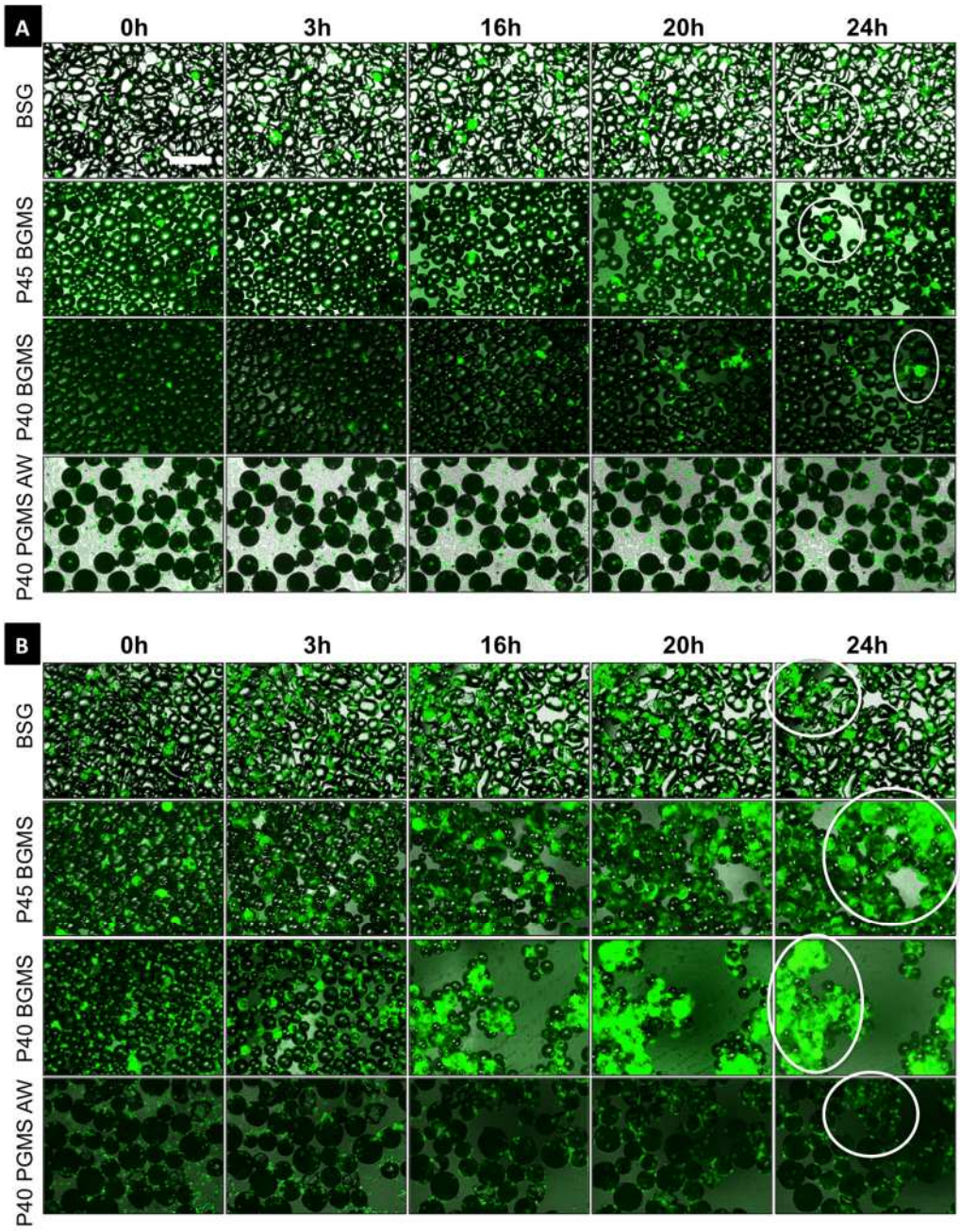

Figure 5-11: Human MSC spread and microsphere agglomeration during initial 24 h of culture. (A) 2,500 cm^{-2} cell density (B) 10,000 cm^{-2} cell density. Aggregation was fastest in case of P40 BGMS and least in case of P40 PGMS AW. White circles show areas of aggregation. Scale bar – 250 µm.

5.7 Human MSC viability on microspheres

To explore the viability on hMSCs on different MS-types, Experiment-CV02 was performed as explained in Section 2.3.9.

The results, see Figure 5-12, showed significantly lower cell viability on P40 PGMS AW compared to all other bulk MS conditions on day 1

of culture ($p<0.05$). However by day 4 of culture, the viability on porous MS behaved similarly as the other types with no significant differences observed.

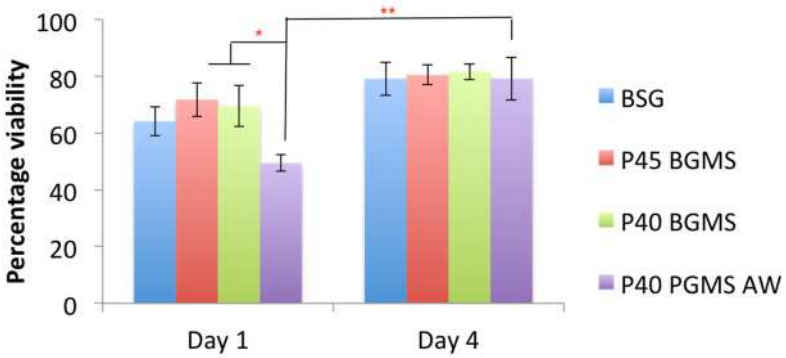

Figure 5-12: Percentage hMSC viability in fields of view (normalised to cells in 2D) on day 1 and day 4 of culture on different glass microspheres measured using Fluorescein diacetate/Propidium iodide staining and image analysis. Cells were seeded at 2,500 cells cm^{-2}. $n \geq 4$, *$p<0.05$, **$p<0.01$.

Quantification could not be carried on day 7 and day 21 of culture due to excessive agglomeration of MS in all conditions. However, qualitative assessment on day 7 showed a number of dead cells present in all MS conditions (Figure 5-13).

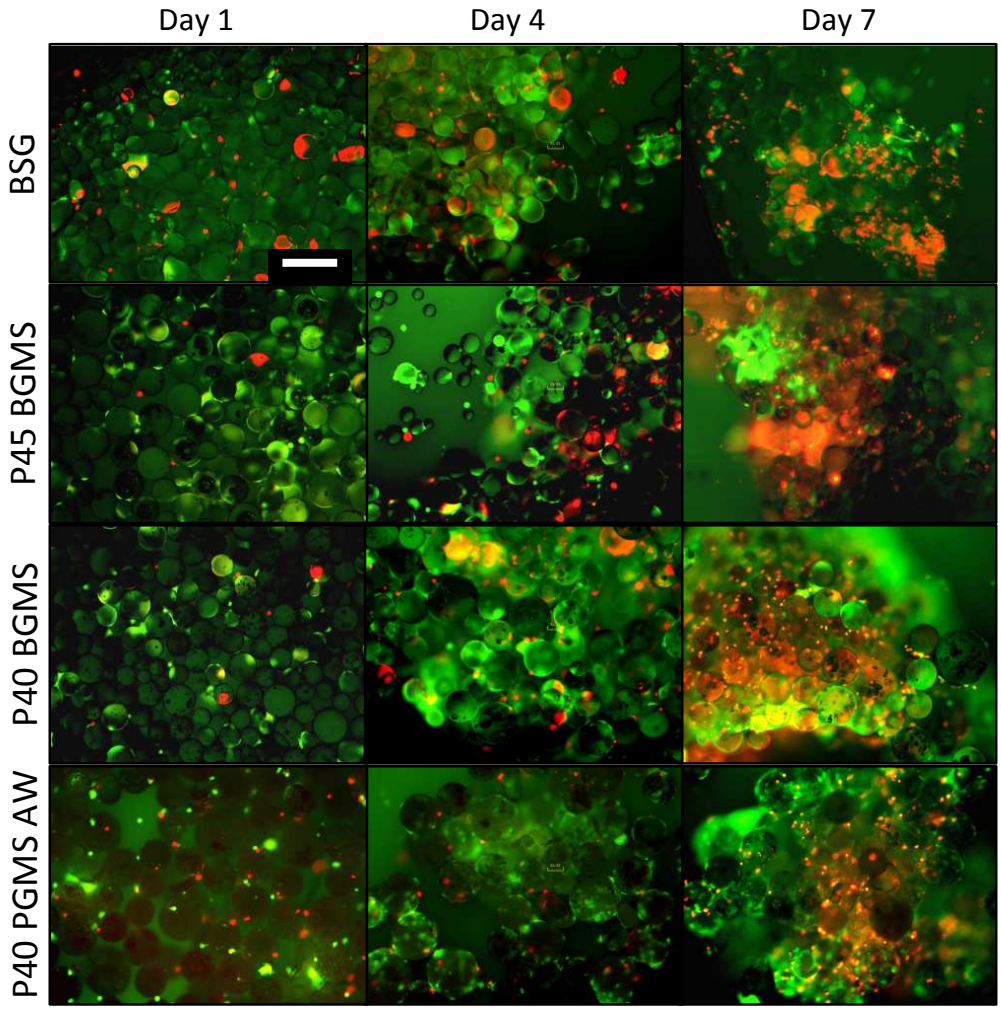

Figure 5-13: Representative images of live (green, Fluorescein diacetate stained) and dead (red, Propidium iodide stained) hMSCs on day 1, 4 and 7 of culture. Cells were seeded at 2,500 cells cm^{-2}. Scale bar- 200 µm.

On day 21 of culture, viability of cells was assessed from three regions of 3D agglomerates formed from different MS-types, top (region of agglomerate facing the well plate lid), bottom (region of agglomerate facing the bottom of the well) and cross-section (internal region of the 3D agglomerate observed after cryo-sectioning). The results, see Figure 5-14, showed more cell death in P45 BGMS as compared to all other MS conditions from all three views.

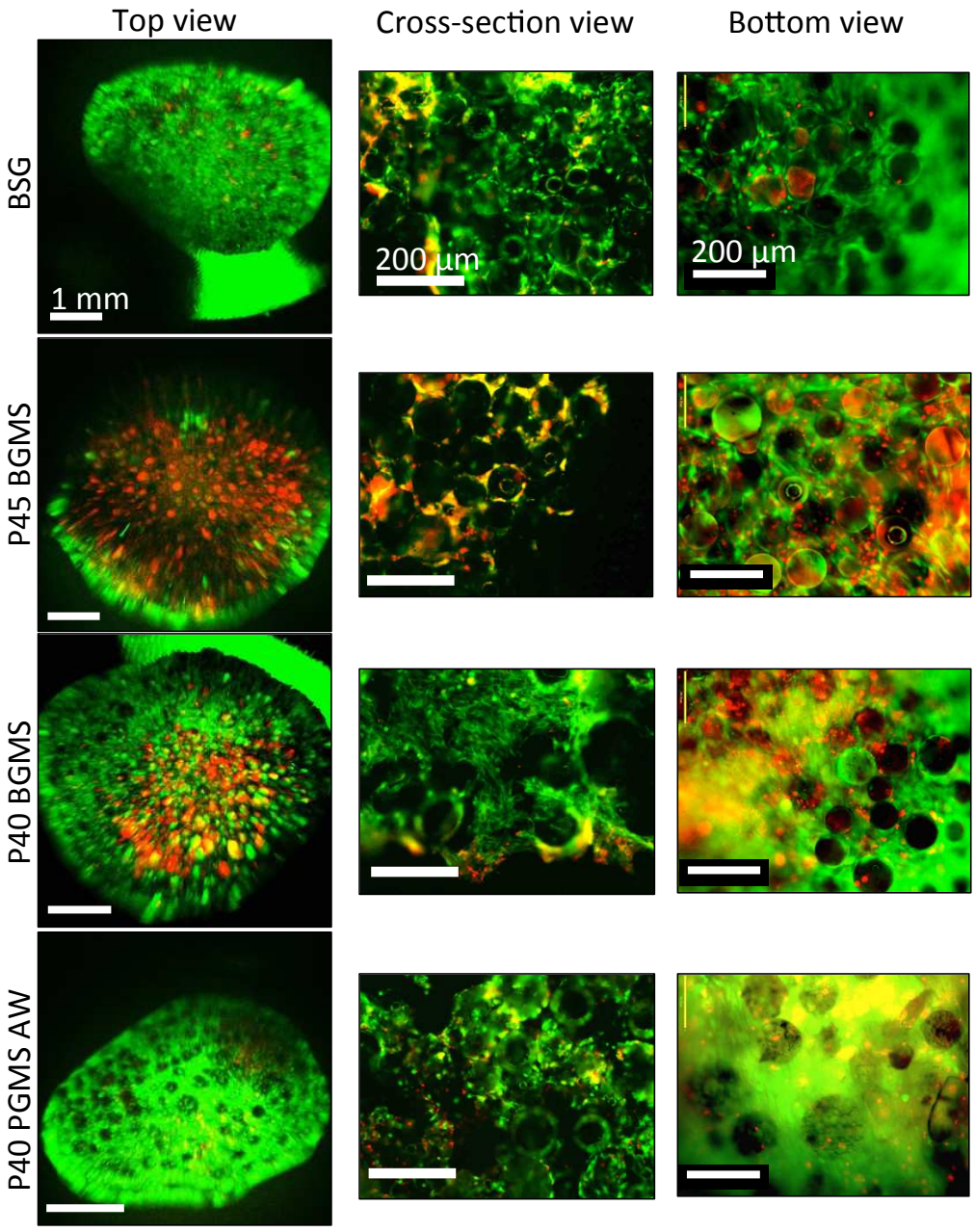

Figure 5-14: Representative images of live (green, Fluorescein diacetate stained) and dead (red, Propidium iodide stained) hMSCs on day 21 of culture from top, bottom and cross-sectional views of different 3D agglomerates. Cells were seeded at 2,500 cells cm^{-2}.

5.8 Human MSC growth on microspheres

To explore the effect of MS formulation and porosity on early growth of hMSCs in 3D system, Experiment-CP05 and CP06 were performed using different batches of BSG, P45 BGMS, P40 BGMS and P40 PGMS AW, as detailed in Section 2.3.3, Table 2-4.

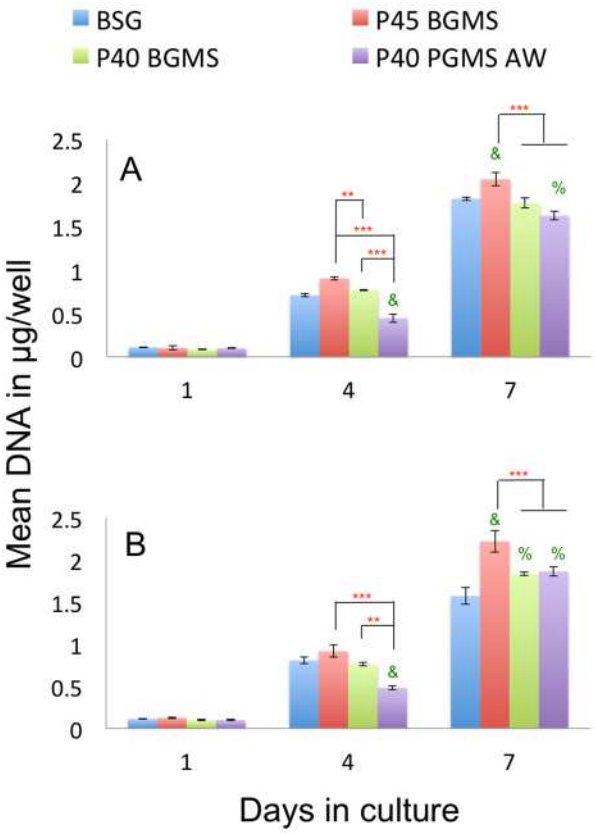

Figure 5-15: Human MSC growth on microspheres over shorter culture periods. (A) Experiment-CP05 (B) Experiment-CP06. Cells were seeded at 2,500 cells cm^{-2}. DNA measurements were performed using PicoGreen® assay. *, **, *** indicate $p<0.05$, $p<0.01$, $p<0.001$, respectively. $, %, & indicate $p<0.05$, $p<0.01$, $p<0.001$, respectively compared to BSG of same time point, n=3, Error bars represent S.E.M.

In both experiments there were no significant differences among DNA contents of different MS conditions on day 1 (see Figure 5-15). However, on day 4, there was a decreasing trend observed in DNA content for PBG MS, suggesting P45 BGMS> P40 BGMS> P40 PGMS AW ($p<0.01$, $p<0.001$). On day 7 as well this trend was repeated either completely in CP05 or partially in CP06. Moreover, BSG on all time points had similar levels of DNA content as P40 BGMS in both experiments, except on day 7 of Experiment-CP06.

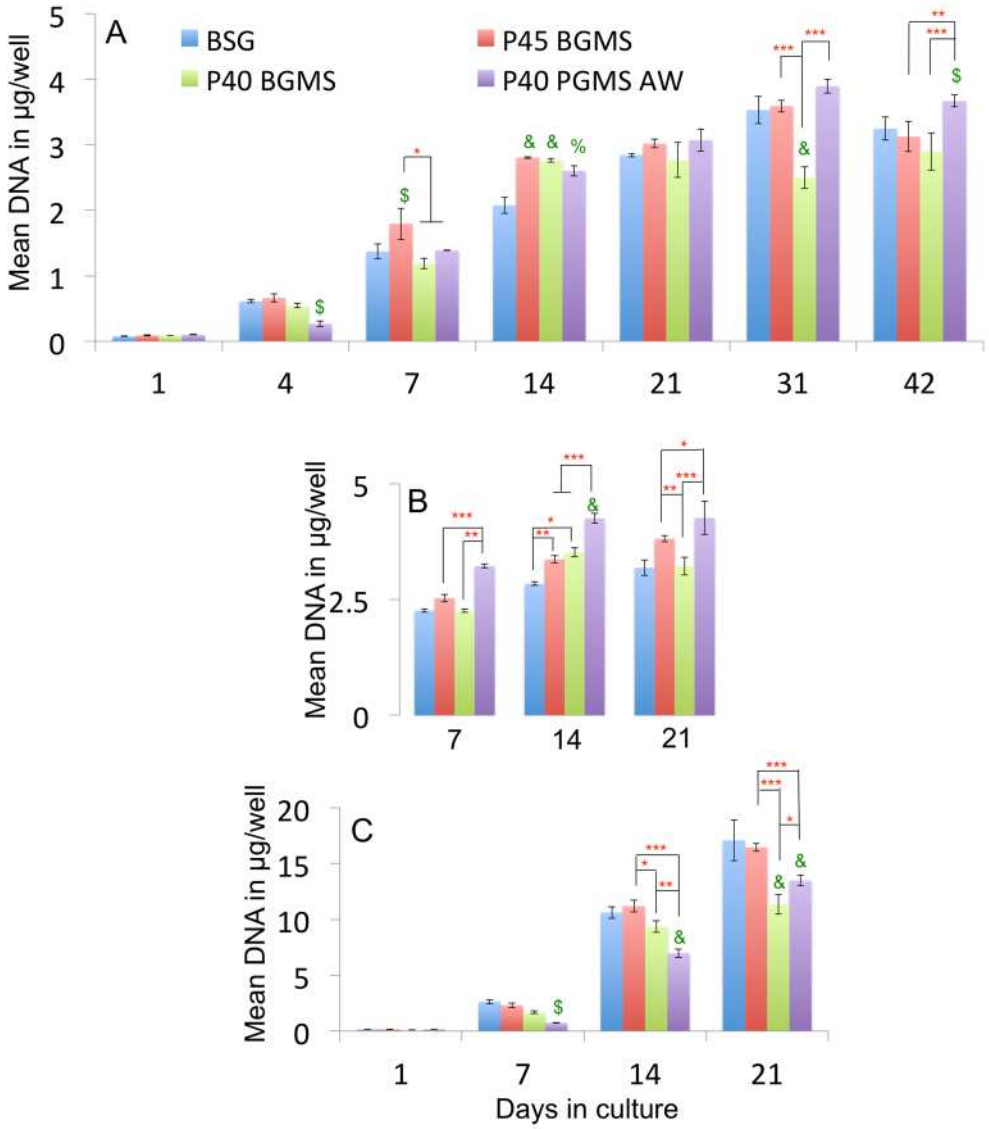

Figure 5-16: Human MSC growth on MS over longer culture periods. (A) Experiment-CP07 (cells seeded at 2,500 cells cm^{-2}), (B) Experiment CP08 (cells seeded at 10,000 cells cm^{-2}) and (C) Experiment-CP09 (cells seeded at 167 cells cm^{-2}). DNA measurements were performed using PicoGreen® assay. *, **, *** indicate $p<0.05$, $p<0.01$, $p<0.001$, respectively. $, %, & indicate $p<0.05$, $p<0.01$, $p<0.001$, respectively compared to BSG of same time point, n=3, Error bars represent S.E.M.

In order to investigate hMSC growth on different MS in extended culture periods, Experiments-CP07, CP08 and CP09 with cell seeding densities of 2,500, 10,000 and 167 cells cm^{-2}, respectively, were performed as described in Section 2.3.3.

The results, see Figure 5-16, showed that irrespective the cell seeding density used, the DNA content did not increase significantly in P40 BGMS after 2 weeks of culture and by the end of all three

experiments, there were higher DNA contents in P45 BGMS and BSG relative to P40 BGMS ($p<0.01$, $p<0.001$).

The second observation from these experiments was the difference in cell growth pattern in P40 PGMS AW at different cell seeding densities. The negative effect of porosity on hMSC growth was visible until day 14 and day 4 at 167 and 2,500 cell cm^{-2} seeding rates, respectively. However, no such effect was observed at 10,000 cell cm^{-2}. Additionally, there was significantly more DNA content in porous MS relative to all other MS conditions by day 31 and day 7 of culture at 2,500 and 10,000 cell cm^{-2} seeding rates, respectively ($p<0.01$, $p<0.001$).

5.8.1 Effect of degradation products on cell growth

To investigate the effect of degradation products of different MS on hMSC growth, Experiments CON01 and CON02 were performed as described in Section 2.3.3.

In both experiments, hMSC metabolic activity measurements showed no significant differences between control (no MS in medium) and other test conditions after 25 days of culture (see Figure 5-17). However, there was significantly higher metabolic activity in case of P45 BGMS-and P40 BGMS-conditioned medium, compared to BSG-conditioned medium and control on day 10 ($p<0.001$) and day 16 ($p<0.05$) in Experiment-CON02. Additionally, there was also significantly higher metabolic activity in P40 PGMS AW-conditioned medium relative to BSG- conditioned medium and control ($p<0.05$) on day 16 ($p<0.05$) in the same experiment.

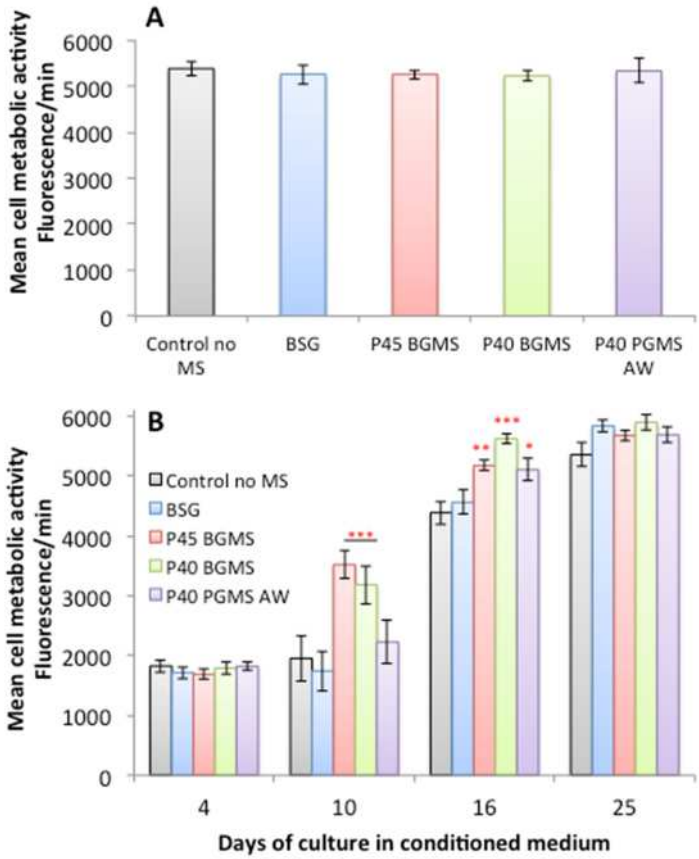

Figure 5-17: Effect of degradation products of glass microspheres on hMSC metabolic activity measured using PrestoBlue® assay. Cells were seeded at 5,000 cells well^{-1} and cultured in different microspheres-conditioned media for 25 days. (A) Experiments-CON01, (B) Experiment-CON02. *p<0.05, **p<0.01 and ***p<0.001 compared to control (no MS) of same time point. Error bars represent S.E.M.

The results in Figure 5-18 also showed no significant differences between DNA contents of any test conditions and control on day 4 and day 16 of culture in both experiments. However, there was significantly higher DNA content in medium conditioned with PBG MS relative to control ($p<0.001$, $p<0.01$) on day 10 and significantly lower DNA content in P40 PGMS AW-conditioned medium relative to control ($p<0.05$, $p<0.01$) on day 25, in Experiments-CON01.

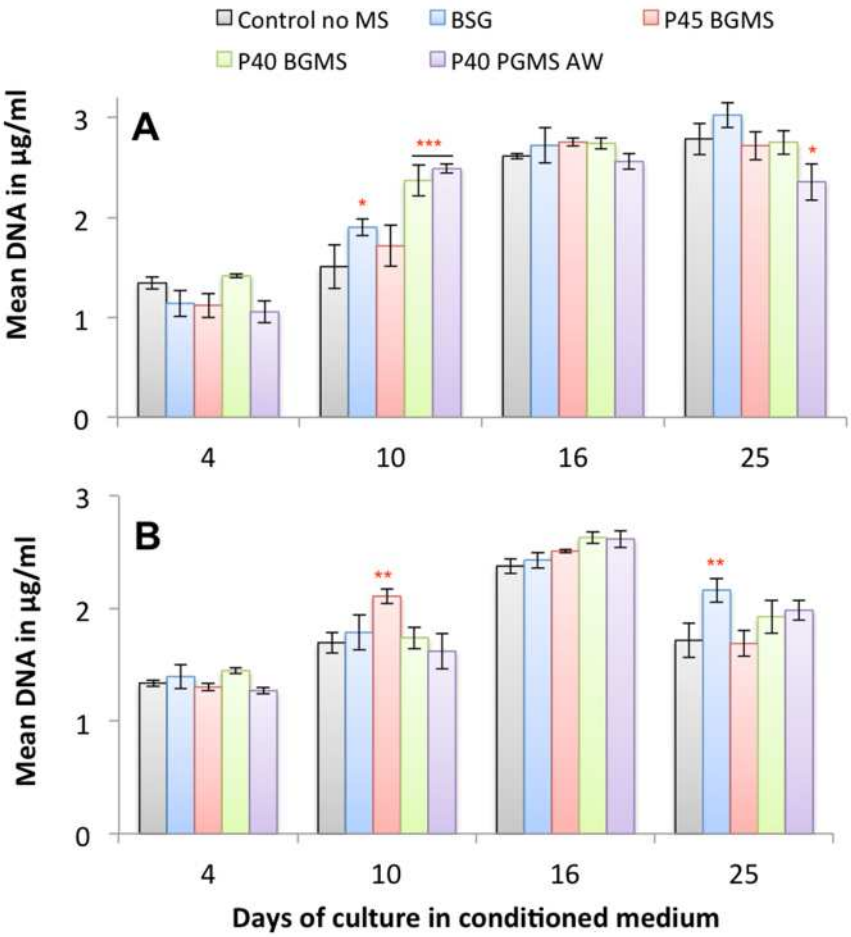

Figure 5-18: Effect of degradation products of glass microspheres on hMSC proliferation in Experiments-CON01 (A) and CON02 (B). Cells were seeded at 5,000 cells well^{-1} and cultured in different microspheres-conditioned media for 25 days. DNA measurements were performed using PicoGreen® assay. *p<0.05, **p<0.01 and ***p<0.001 compared to control (no MS) of same time point. Error bars represent S.E.M.

5.9 Human MSC morphology on microspheres

To explore hMSC morphology on different MS, scanning electron microscopy (SEM) was carried out as described in Section 2.3.18, on day 1, 4, 14 and 21 of culture in Experiment-CP07.

The images in Figure 5-19 A-D depicted that on bulk MS cells had a flat morphology on day 1 and day 4 but on P40 PGMS AW, they seemed to have a round morphology, indicative of poorer attachment.

During extended culture periods, more rounded cells started to appear primarily on P45 BGMS and less so on BSG. However, in case of P40 BGMS and P40 PGMS AW the cells seemed to be interacting with cracks and delaminating glass surfaces from day 4 onwards, see Figure 5-19 E-P.

To assess the growth of cells inside the 3D agglomerate of porous MS, Micro CT scans were performed as detailed in Section 2.3.20. The images in Figure 5-20 show the 3D reconstructions of porous 3D agglomerate after 7 days of culture from different perspectives. These reconstructions show more cells on the surface that faced the top of well plate than the surface facing the bottom of well plate and the cells were more evenly spread out on the four lateral edges. Additionally, cross- sectional views showed more cells present on the outer edges of the agglomerate relative to the internal regions of same agglomerate.

Higher resolution scan images, see Figure 5-21, further confirmed that cells were present on the outer region as well as internal region of same porous MS. However, it was also interesting to note that the MS with more porosity, contained more cells and MS with less porosity contained lesser cells.

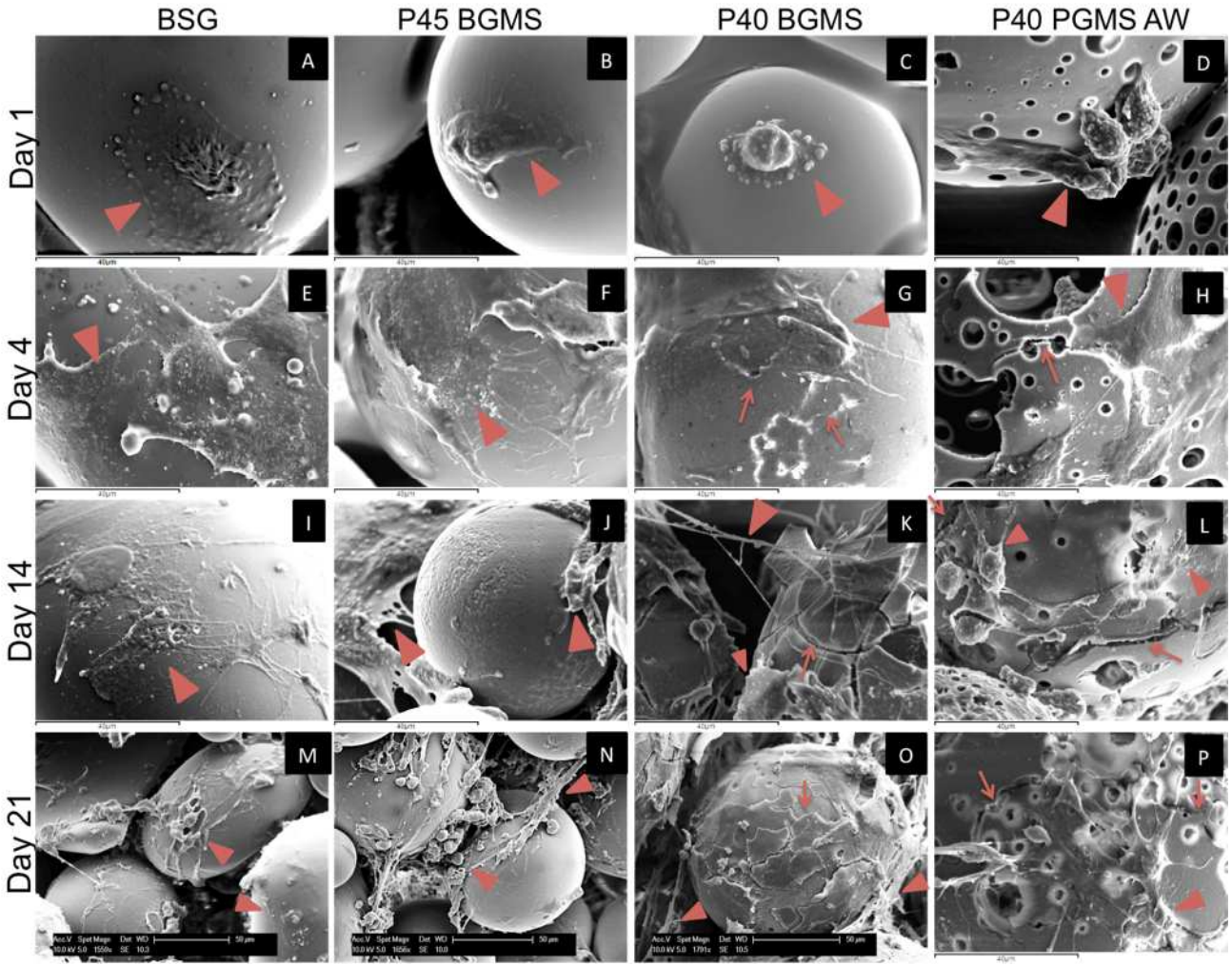

Figure 5-19: SEM images of cells growing on different glass MS in Experiment-CP07 (cell seeding at 2,500 cells cm^{-2}). Cells and surface damage on microspheres are highlighted as red arrow-heads and arrows, respectively. Scale bars- 40 µm in A-L and P, 50 µm in M-O.

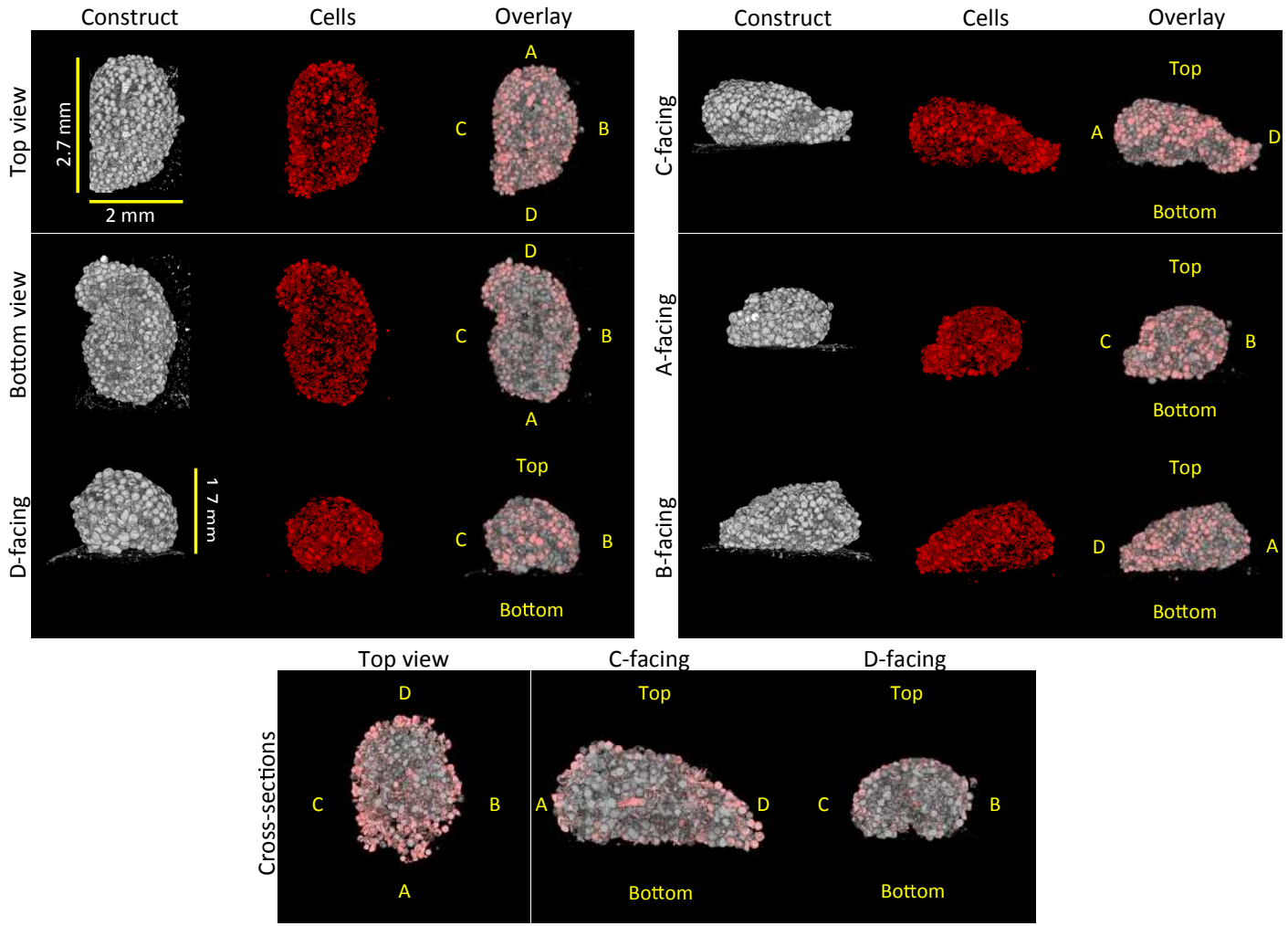

Figure 5-20: Micro CT of cell-PGMS agglomerate after 7 days in culture (hMSCs seeded at 10,000 cells cm^{-2}). 3D tomographies of the construct (acid washed PGMS), cells (red) and overlay (Construct+cells) from all the faces of the agglomerate have been shown. The 'top' faces the top of the well plate and 'bottom' faces the bottom of the well. A, B, C and D are the four lateral faces of the agglomerate. There were more cells present in the top face than the bottom face while the lateral faces showed similar cell distribution. Cross-sectional views from the top, C and D faces showed more cells on the outer edges than on the inside of agglomerate.

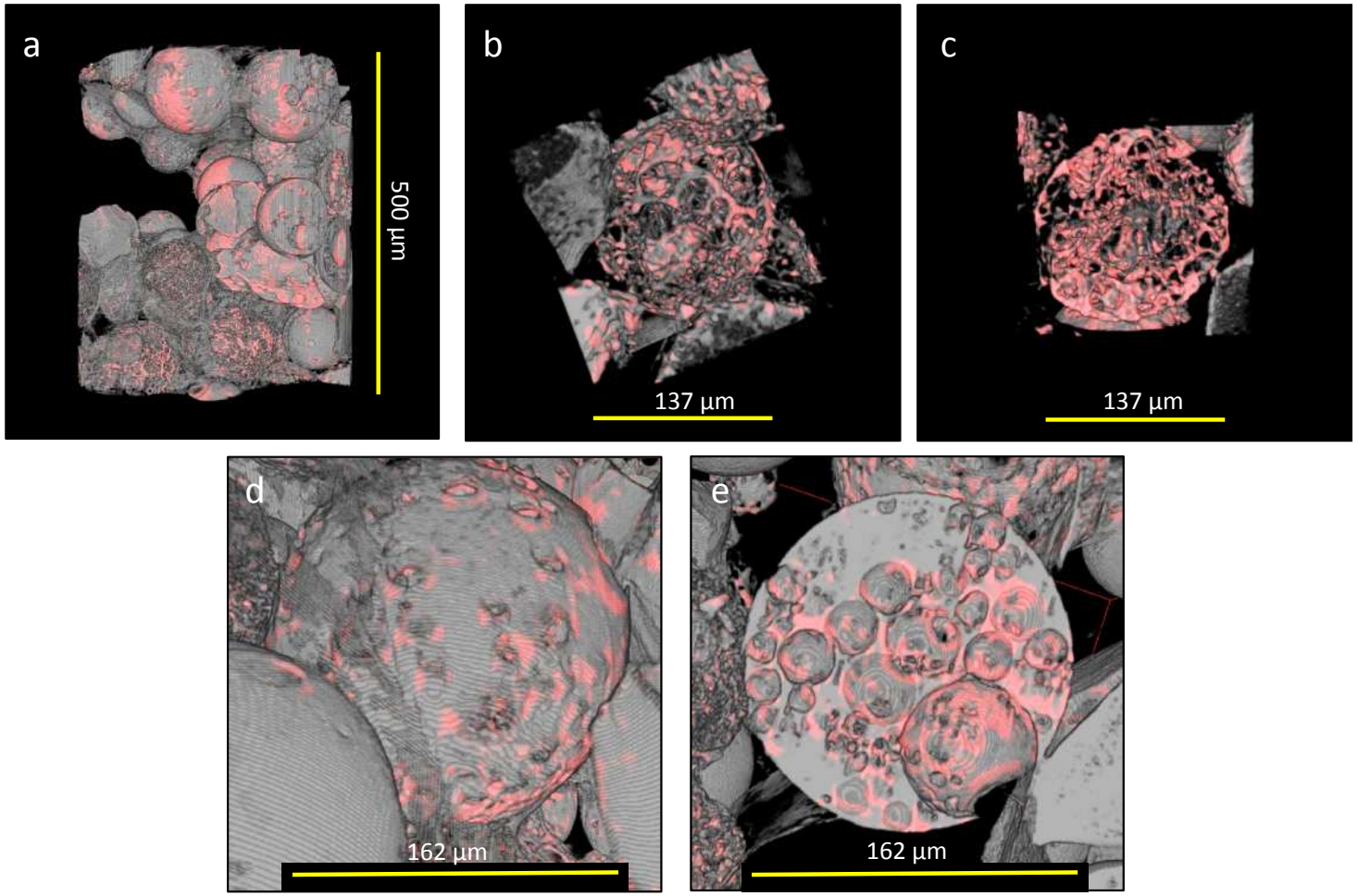

Figure 5-21: Cell colonisation inside PGMS. (a) Higher resolution scan of the cells-PGMS agglomerate shown in Figure 5-20. The cells seem to be unevenly distributed on PGMS. (b) Highly porous glass microsphere (MS) with cells present on the outer surface of the MS and (c) cross-sectional view of the same MS showing cells present also on the inside of the MS. (d) Relative less porous glass MS with cells present on the outer surface and (e) cross-sectional view of the same MS showing cells present also on the inside of the MS.

5.10 Alkaline Phosphatase activity on microspheres

To investigate the alkaline phosphatase (ALP) activity of hMSCs seeded on different MS-types, Experiments-CD05, CD06, CD07 and CD08 were measured as described in Section 2.3.3 and 2.3.11.

In Experiment-CD05, cells were seeded at 2,500 cells cm^{-2} and results in Figure 5-22 A showed higher ALP activity in P40 PGMS AW compared to all other conditions on all time points ($p<0.001$). Moreover, there was also higher ALP activity in P40 BGMS compared to P45 BGMS and BSG ($p<0.05$) on day 7. By day 14, the ALP activity dropped significantly ($p<0.05$) in case of P40 BGMS, which resulted in no significant differences between bulk MS on day 14 and beyond. This drop in ALP activity was also seen in case of P40 PGMS AW from day 7 to 14 of culture ($p<0.001$).

To test the repeatability of these results, Experiment-CD06 was performed and results in Figure 5-22 B confirmed highest ALP activity in P40 PGMS AW on day 7 and 21 of culture ($p<0.001$) and higher ALP activity in P40 BGMS compared to P45 BGMS and BSG on days 7 and 21 of culture ($p<0.01$). There was also a significant decline in ALP activity in case of P40 PGMS AW ($p<0.001$), P40 BGMS ($p<0.001$), P45 BGMS ($p<0.001$) and BSG ($p<0.05$) from day 7 to 21 of culture.

In Experiment-CD07, cells were seeded at 10,000 cells cm^{-2} and results in Figure 5-22 C again indicated higher ALP activity in P40 PGMS AW compared to all other conditions on days 7, 14 and 21 of culture ($p<0.001$). In addition to this, there was again a significantly higher ALP activity in P40 BGMS compared to BSG ($p<0.05$) and P45 BGMS ($p<0.001$) on day 7 of culture, with a significant drop in ALP activity in P40 PGMS AW ($p<0.001$) and P40 BGMS ($p<0.01$) from day 7 to 14.

Finally, in Experiment-CD08, cells were seeded at 167 cells cm^{-2} and the results (Figure 5-22 D) again showed significantly higher ALP activity in P40 PGMS AW relative to all other conditions on day 14 and 21 of culture ($p<0.001$). Moreover, there is also higher ALP activity in P40 BGMS compared to P45 BGMS and BSG on day 7 but it was not statistically significant ($p=0.063$) based on two-way ANOVA analysis.

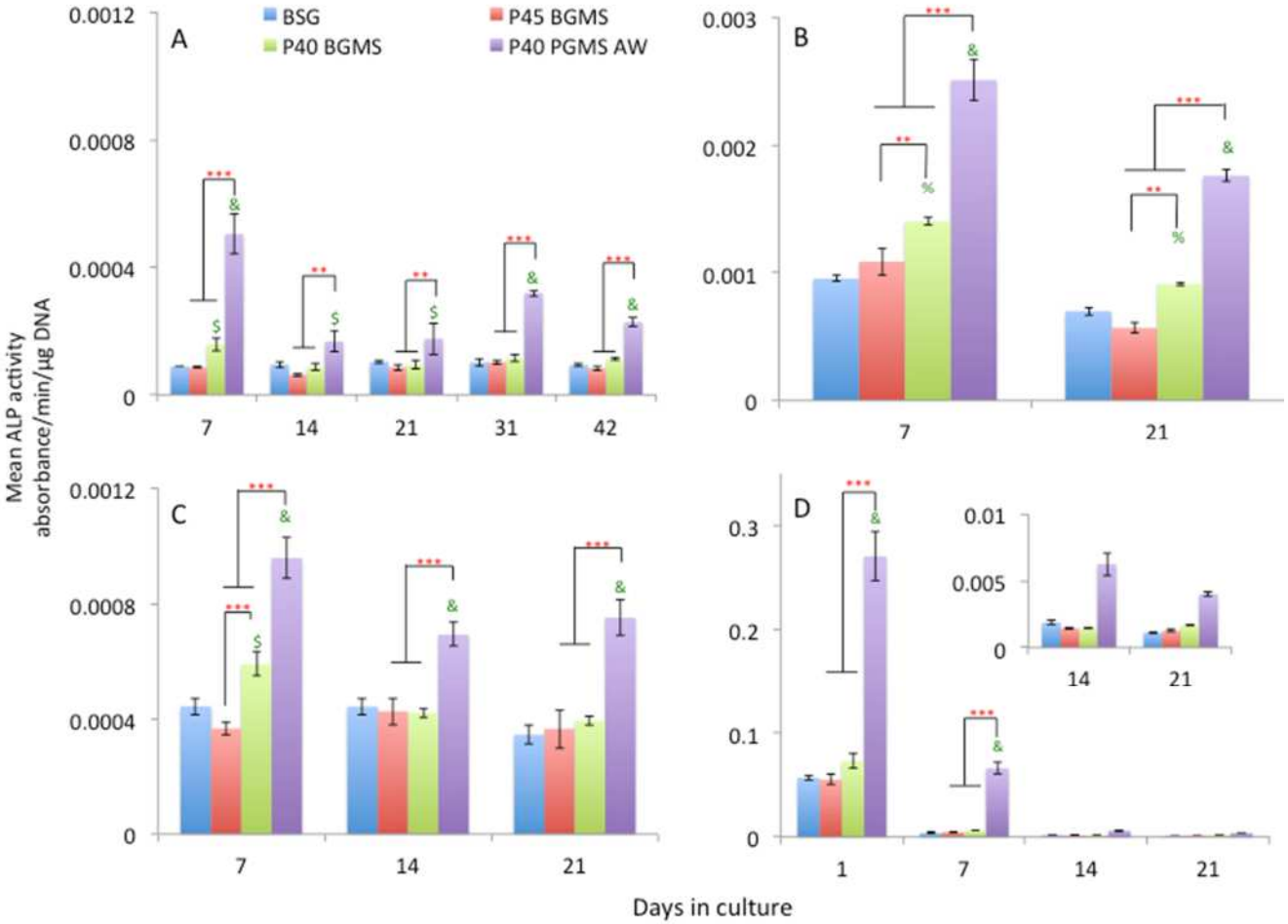

Figure 5-22: Alkaline phosphatase activity (ALP) activity of hMSCs on different microspheres. Cells were seeded at 2,500 cells cm^{-2} in Experiments-CD05 (A) and CD06 (B), at 10,000 cells cm^{-2} in Experiment-CD07 (C) and at 167 cells cm^{-2} in Experiment-CD08 (D). Measurements were acquired using SIGMAFAST™ p-Nitrophenyl phosphate tablets as substrates for ALP. *, **, *** indicate $p<0.05$, $p<0.01$, $p<0.001$, respectively. $, %, & indicate $p<0.05$, $p<0.01$, $p<0.001$, respectively compared to BSG of same time point, n=3, Error bars represent S.E.M.

5.10.1 Effect of degradation products on ALP activity

To investigate the effect of degradation products of different MS on ALP activity of hMSCs, ALP activity was performed in Experiments CON01 and CON02, as described in Section 2.3.11.

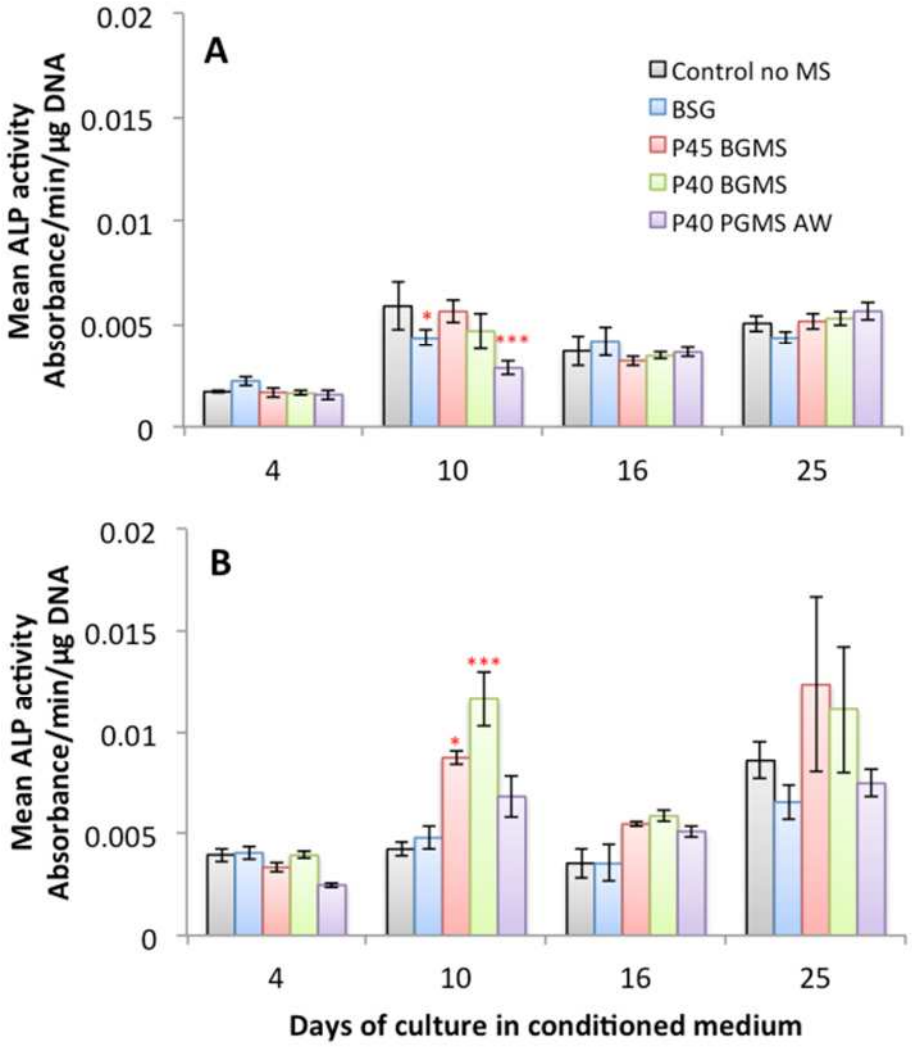

Figure 5-23: Effect of degradation products of glass microspheres on hMSC Alkaline phosphatase (ALP) activity in (A) Experiments-CON01 and (B) Experiment-CON02. Cells were seeded at 5,000 cells well^{-1} and cultured in different microspheres-conditioned media for 25 days. Measurements were acquired using SIGMAFAST^{TM} p-Nitrophenyl phosphate tablets as substrates for ALP. *p<0.05, **p<0.01 and ***p<0.001 compared to control (no MS) of same time point. Error bars represent S.E.M.

In both experiments, there were no statistically significant differences between control and test conditions on day 4, day 16 and day 25 of culture (see Figure 5-23). However, on day 10, there was significantly lower ALP activity in P40 PGMS AW-conditioned

medium in Experiment-CON01 ($p<0.001$) and also higher ALP activity in PBG bulk MS-conditioned media in Experiment-CON02 ($p<0.05$ and $p<0.001$, respectively), as compared to control.

5.11 Collagen production

5.11.1 Qualitative assessment

In Experiment-COL02, Sirius Red staining was used to assess collagen production by hMSCs after 21 days of culture in different MS-types with mouse calvarial tissue as positive control (see Section 2.3.13 for method). The images in Figure 5-24 illustrated that irrespective of cell seeding density, there was more collagen deposited in P40 MS conditions relative to BSG and least collagen was deposited in case of P45 BGMS.

5.11.2 Quantitative assessment

A number of experiments were conducted to measure the amount of collagen deposited by cells after 21 days of culture in different MS conditions, as described in Section 2.3.3 and Section 2.3.13. In Experiments-COL05, COL06 and COL07, hMSCs were seeded at 2,500 cells cm^{-2} and in Experiments-COL08, COL09, COL10, hMSCs were seeded at 10,000 cells cm^{-2}.

The results (Figure 5-25 and Figure 5-26) indicated that there was lowest collagen deposited in P45 BGMS by day 21 of culture relative to BSG or P40 MS ($p<0.05$) in four out of six experiments. Moreover, there was also more collagen deposited in P40 PGMS AW as compared to P40 BGMS ($p<0.05$) in four out of six experiments.

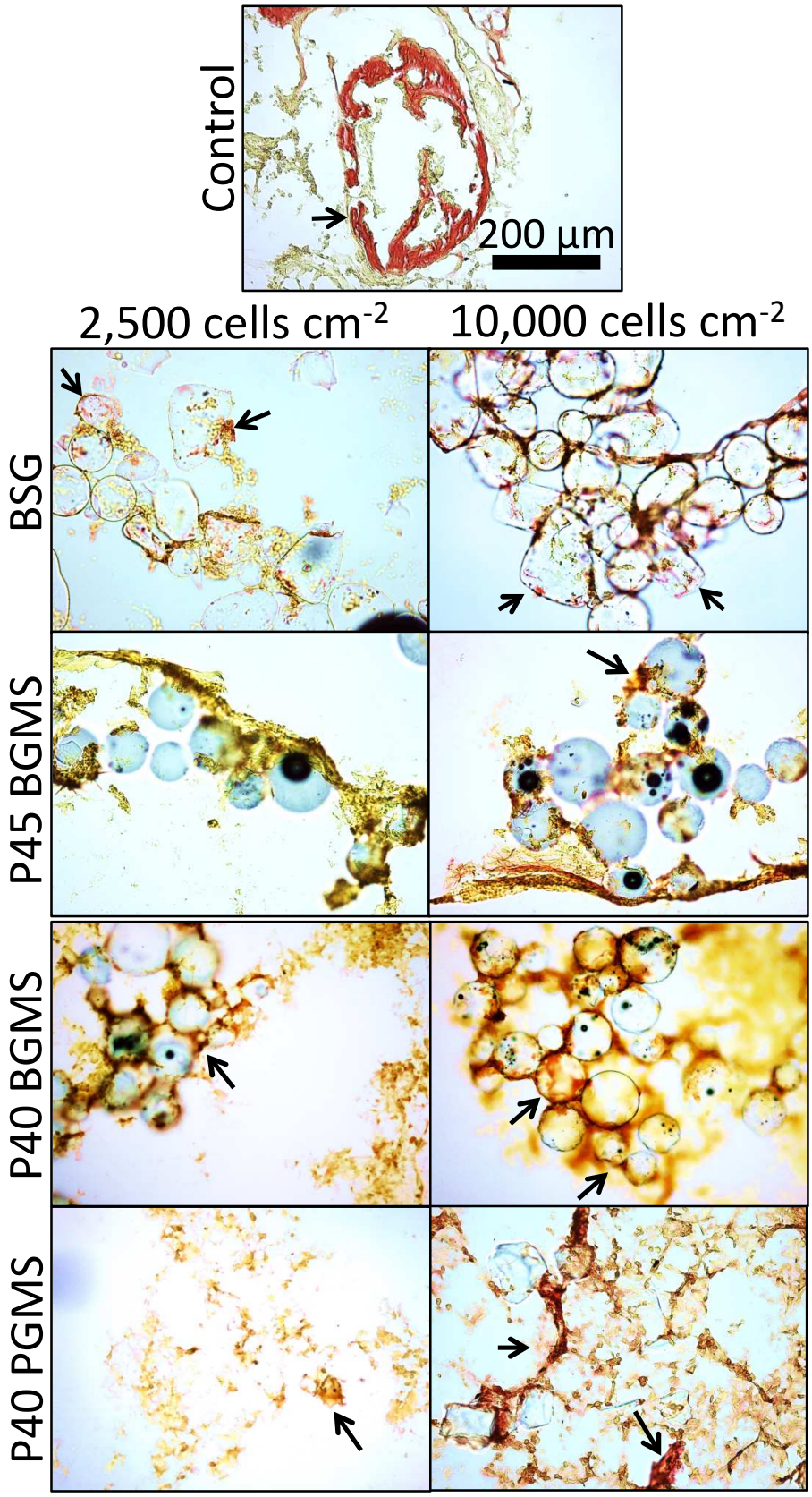

Figure 5-24: Qualitative analysis of collagen deposition by hMSC on different glass microspheres using Sirius Red staining, after 21 of culture. Yellow regions represent cell cytoplasm and red regions represent collagenous proteins (arrows). Mouse calvarial tissue was used as a positive control for staining.

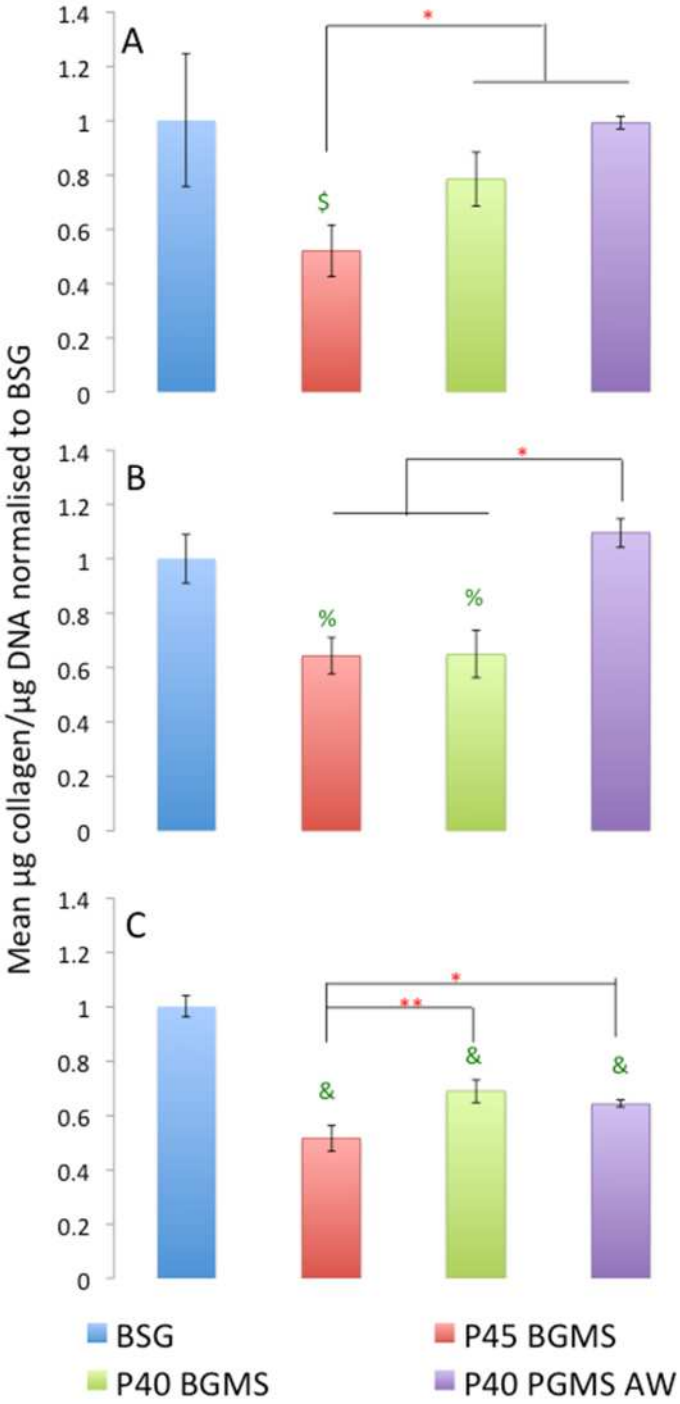

Figure 5-25: Collagen production by hMSCs on different glass microspheres on Day 21 of culture after cell seeding at 2,500 cells cm^{-2}. Measurements were performed using Sirius Red assay. (A) Experiment-COL05, (B) Experiemnt-COL06 and (C) Experiemnt-COL07. *, ** indicate $p<0.05$, $p<0.01$, respectively. $, %, & indicate $p<0.05$, $p<0.01$, $p<0.001$, respectively compared to BSG of same time point, n=3, Error bars represent S.E.M.

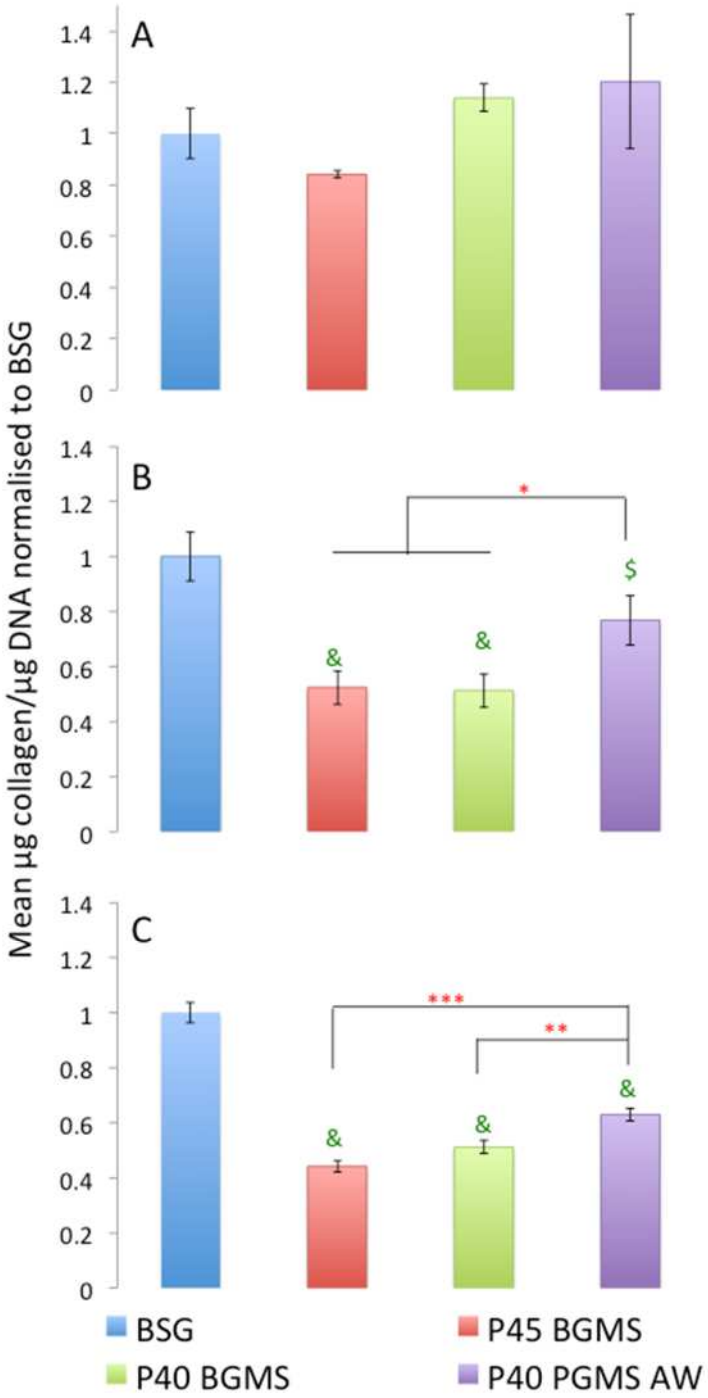

Figure 5-26: Collagen production by hMSCs on different glass microspheres on Day 21 of culture after cell seeding at 10,000 cells cm^{-2}. Measurements were performed using Sirius Red assay. (A) Experiment-COL08, (B) Experiemnt-COL09 and (C) Experiemnt-COL10. *, **, *** indicate $p<0.05$, $p<0.01$, $p<0.001$, respectively. $, %, & indicate $p<0.05$, $p<0.01$, $p<0.001$, respectively compared to BSG of same time point, n=3, Error bars represent S.E.M.

5.11.3 Effect of degradation products on collagen production

To investigate the effect of degradation products of different MS on collagen production by hMSCs, Sirius Red assay was performed in Experiments CON01 and CON02, as described in Section 2.3.13. In both experiments (see Figure 5-27), there was an increasing trend in collagen deposition with increasing degradation rate of bulk MS ($p<0.05$), i.e., P40 BGMS>P45 BGMS>BSG. Additionally, across the two experiments, in three out of four time points there was lower collagen in P40 PGMS AW-conditioned medium relative to P40 BGMS-conditioned medium ($p<0.05$ for Experiment-CON02).

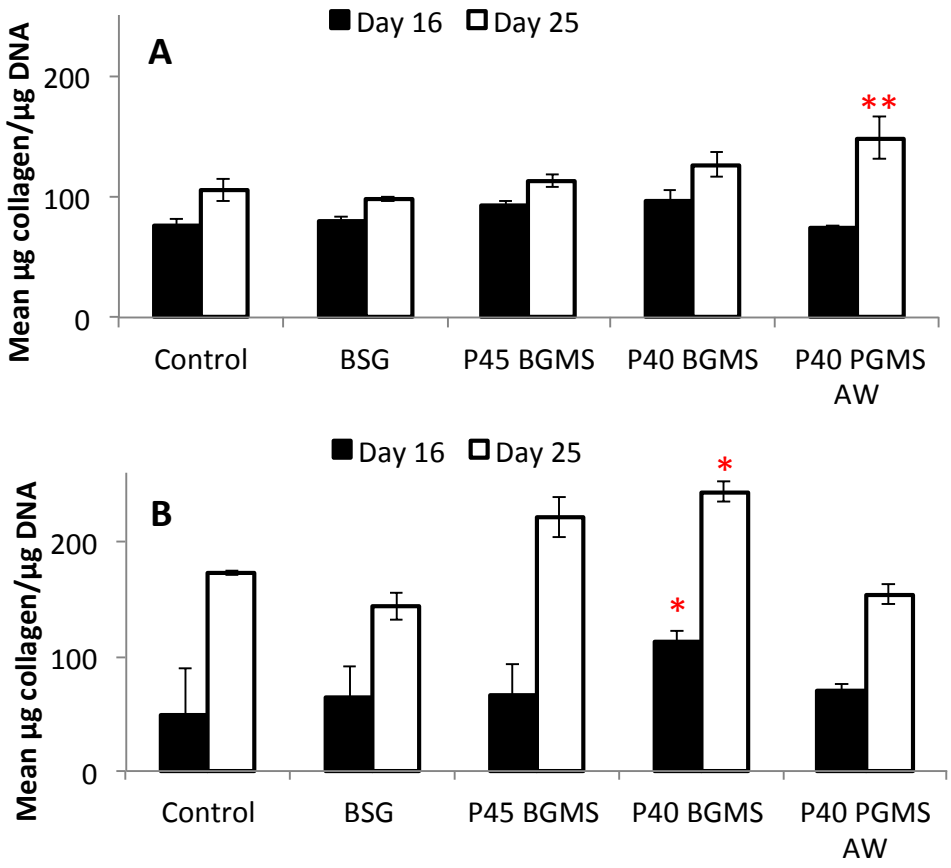

Figure 5-27: Effect of degradation products of glass microspheres on collagen deposition by hMSCs in Experiments-CON01 (A) and CON02 (B). Cells were seeded at 5,000 cells well^{-1} and cultured in different microspheres-conditioned media for 25 days. Measurements were performed using Sirius Red assay. *$p<0.05$ and **$p<0.01$ compared to control (no MS) of same time point. Error bars represent S.E.M.

5.12 Ca and P deposition on microspheres

To study the calcium and phosphorous present in the extracellular matrix (ECM) of hMSCs lying on the top face of different 3D agglomerates, Experiments-MIN06 and MIN07 were performed as described in Section 2.3.3 and 2.3.17.

In Experiment-MIN06, only bulk MS were tested and measurements were taken on Day 21 of culture. The results in Figure 5-28 A-B indicated significantly higher P/N and Ca/N in case of cells on P40 BGMS relative to BSG and P45 BGMS. Moreover, there was also highest Ca/P ratio in P40 BGMS.

In Experiment-MIN07 measurements were taken on days 7, 14 and 21 of culture. The results, see Figure 5-29 A-C, again indicated higher Ca/N, P/N and Ca/P in P40 BGMS relative to P45 BGMS on all time points with a significant drop in Ca/N and P/N from day 7 to 21 of culture ($p<0.001$) in case of PBG bulk MS. Additionally, the results also showed lower Ca/N on day 7 ($p<0.001$) and lower P/N on days 7 and 14 ($p<0.001$, $p<0.05$) on P40 PGMS AW relative to P40 BGMS, which was again accompanied by decreasing Ca/N, P/N and Ca/P in porous MS from day 7 to 21 of culture ($p<0.01$).

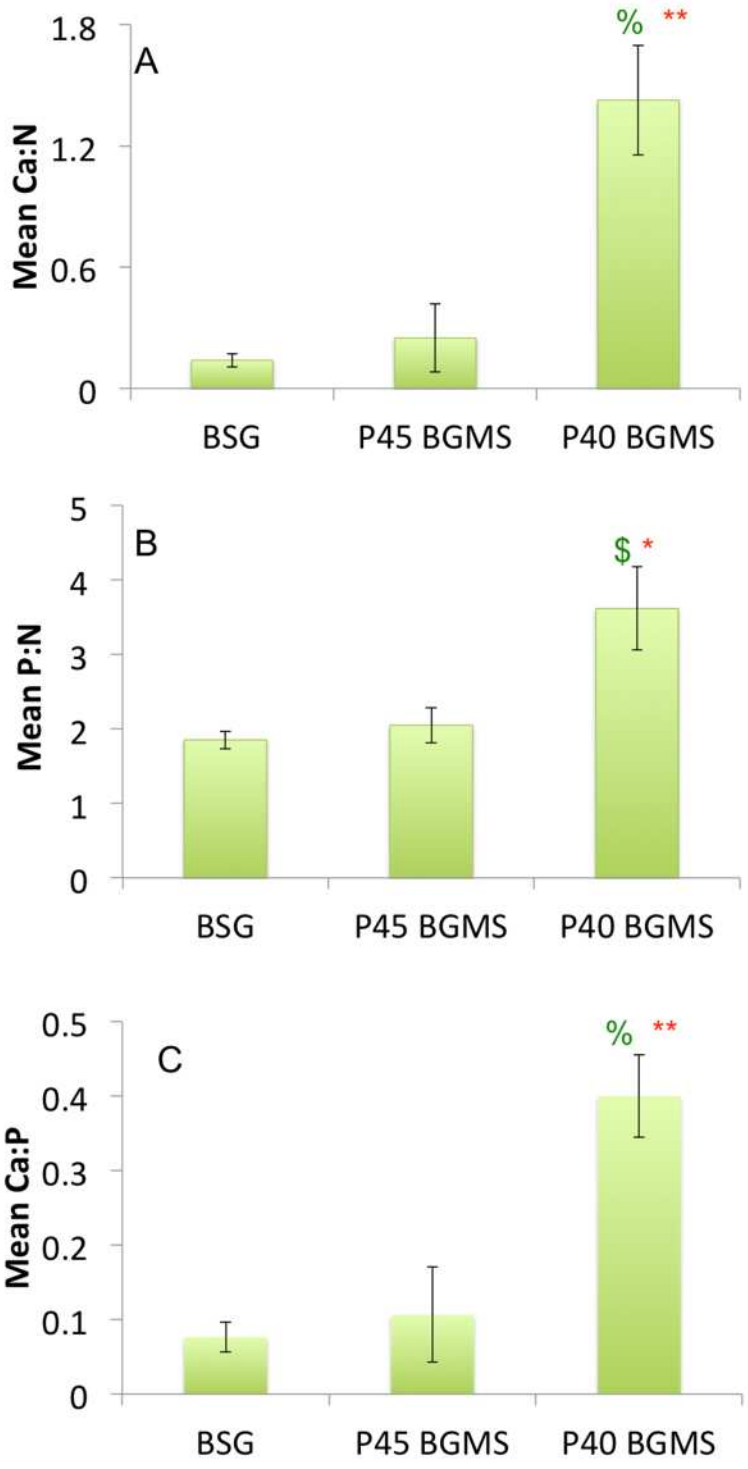

Figure 5-28: Ca and P deposition by hMSCs on different microspheres on Day 21 in Experiment-MIN06, where cells were seeded at 2,500 cells cm^{-2}. Ca 2p, P 2p, N 1s peaks in XPS spectra were measured and Ca:N (A), P:N (B) and Ca:P (C) have been reported. *, ** indicate $p<0.05$, $p<0.01$, respectively relative to P45 BGMS, $, % indicate $p<0.05$, $p<0.01$, respectively relative to BSG. n=3, Error bars represent S.E.M.

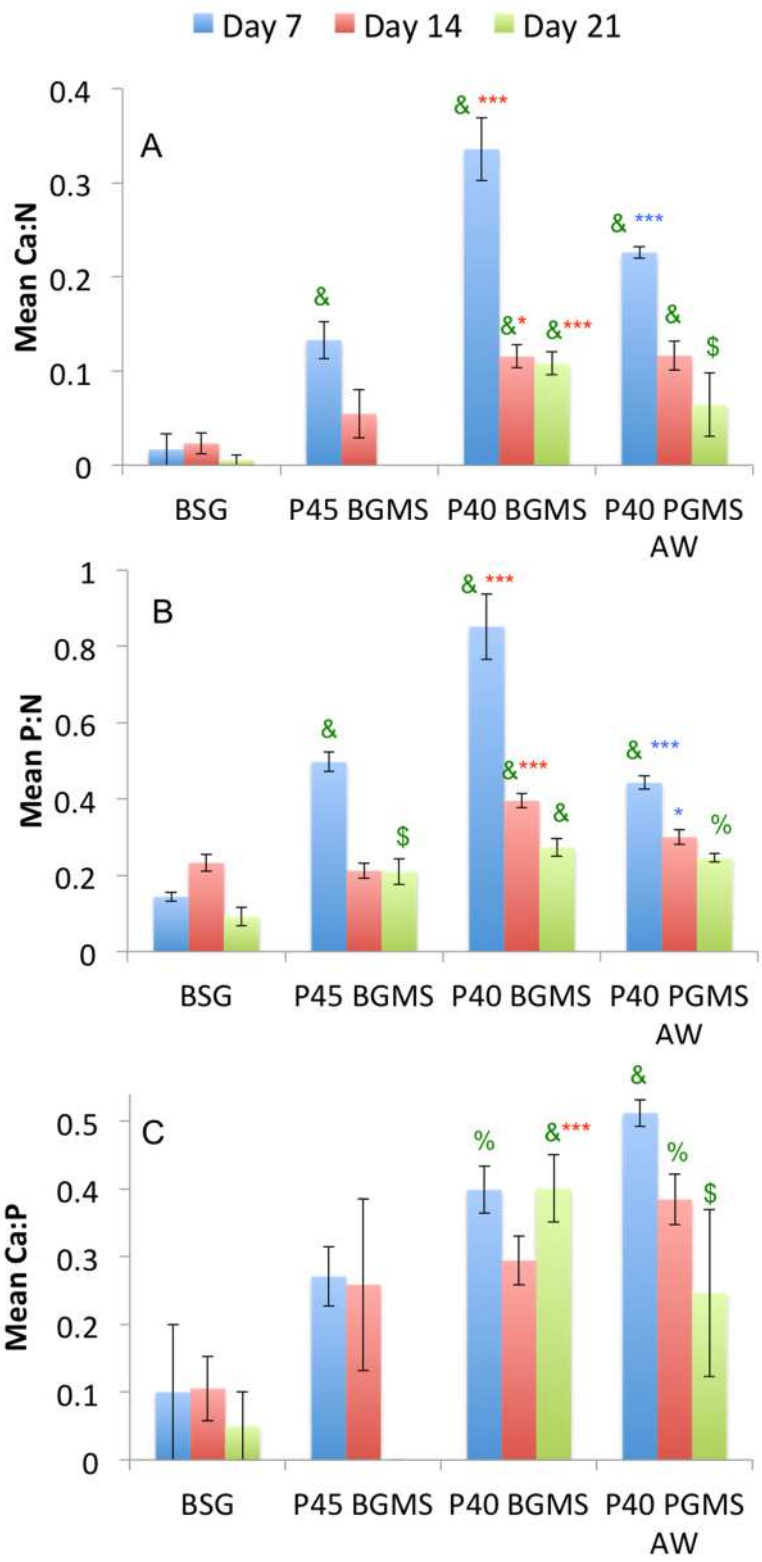

Figure 5-29: Ca and P deposition by hMSCs on different microspheres on Day 7, 14 and 21 of culture in Experiment-MIN07, where cells were seeded at 2,500 cells cm^{-2}. Ca 2p, P 2p, N 1s peaks in XPS spectra were measured and Ca:N (A), P:N (B) and Ca:P (C) have been reported. *, *** indicate $p<0.05$, $p<0.001$, respectively relative to P45 BGMS of same time point. $, %, & indicate $p<0.05$, $p<0.01$, $p<0.001$, respectively relative to BSG of same time point. *** indicate $p<0.001$ relative to P40 BGMS of same time point, n=3, Error bars represent S.E.M.

5.12.1 Effect of degradation products on Ca production

To investigate the effect of degradation products of different MS on mineral deposition by hMSCs, Alizarin Red assay was performed in Experiments CON01 and CON02, as described in Section 2.3.14.

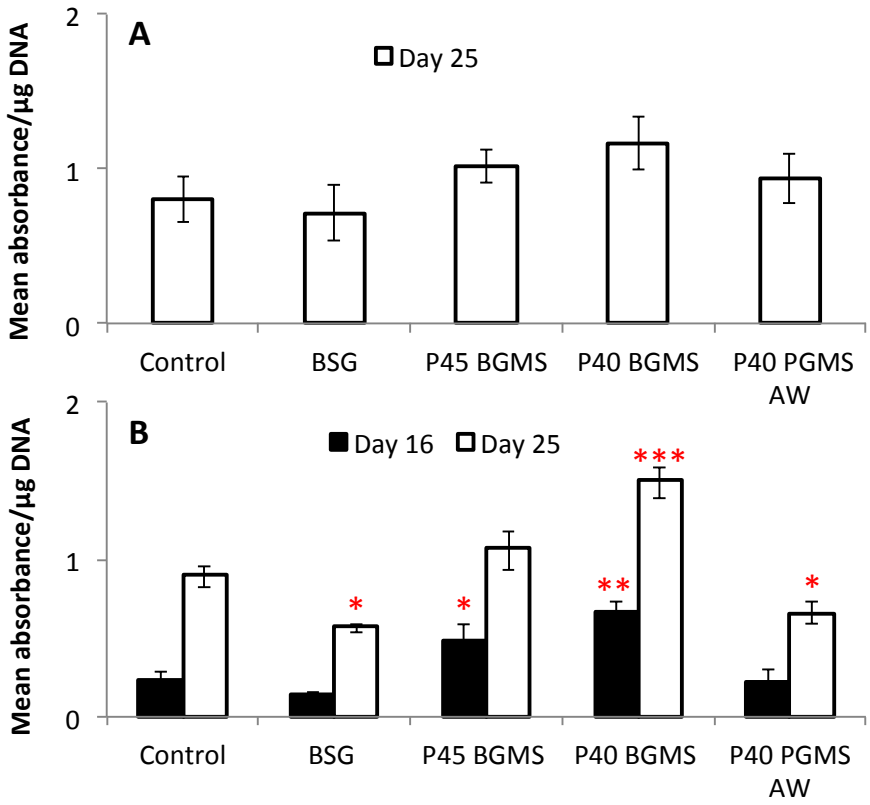

Figure 5-30: Effect of degradation products of glass microspheres on Ca deposition by hMSCs in Experiments-CON01 (A) and CON02 (B). Cells were seeded at 5,000 cells well^{-1} and cultured in different microspheres-conditioned media for 25 days. Measurements were performed using Alizarin Red assay. *p<0.05, **p<0.01 and ***p<0.001 compared to control (no MS) of same time point. Error bars represent S.E.M.

In Experiment-CON01 (see Figure 5-30 A), there was highest amount of mean mineral deposited in PBG bulk MS-conditioned media compared to all other conditions on Day 25. However, these differences did not show statistical significance based on one-way ANOVA analysis.

In Experiment-CON02 the results, see Figure 5-30 B, showed increasing trend in mineral deposition with increasing degradation rate of bulk MS ($p<0.05$), i.e., P40 BGMS>P45 BGMS>BSG on day

16 and 25 of culture. Additionally, there was lower mineral deposited in P40 PGMS AW-conditioned medium relative to P40 BGMS-conditioned medium on both time points.

5.13 Osteocalcin production on microspheres

To assess the extent osteocalcin (OCN) production in different MS conditions, Experiment-OCN02 was performed as explained in Section 2.3.3 and Section 2.3.15. The results in Figure 5-31 showed absence of any auto-fluorescence (non-specific fluorescence from samples) or non-specific antibody staining in all MS conditions.

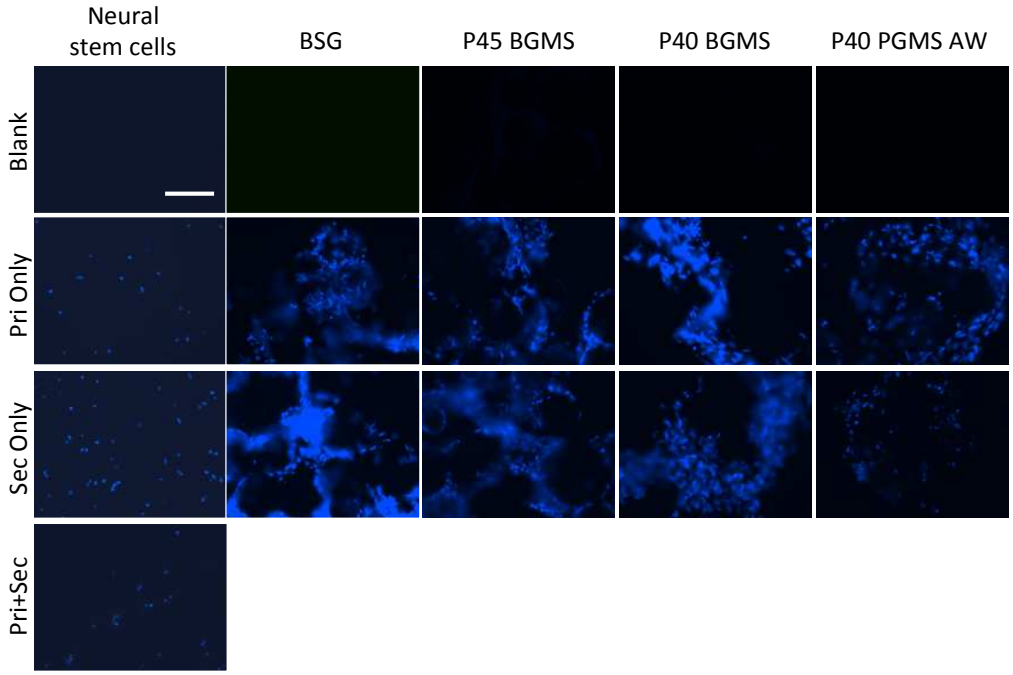

Figure 5-31: Osteocalcin staining on neural stem cells and detection of auto fluorescence (non-specific fluorescence from samples) and non-specific primary or secondary antibody staining in different microsphere conditions. The shown images are overlays of DAPI and FITC channels. Scale bar-100 µm.

The results in Figure 5-32 and Figure 5-33 showed positive OCN expression on BSG, P40 BGMS and P40 PGMS and absence of same on P45 BGMS, irrespective of the cell seeding density or culture medium used.

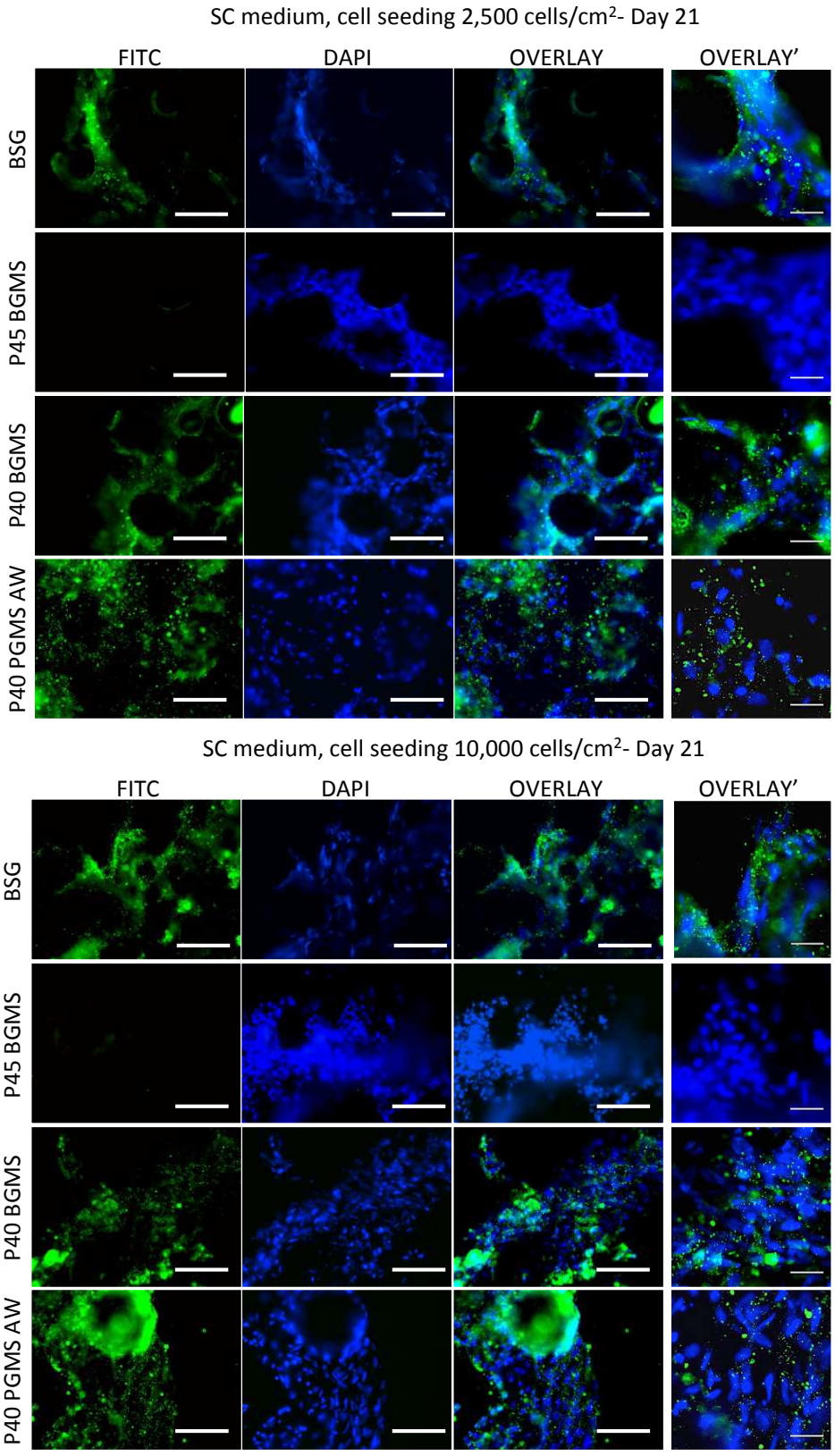

Figure 5-32: Osteocalcin (OCN) expression (FITC) by hMSC on different microspheres after 21 of culture in SC (Standard culture) medium. Cells were seeded at 2,500 and 10,000 cells cm^{-2}. Blue signal represents cell nuclei (DAPI). There was presence of OCN on BSG, P40 BGMS and P40 PGMS AW but not on P45 BGMS. Scale bars on FITC, DAPI and OVERLAY- 100 µm and OVERLAY'- 25 µm.

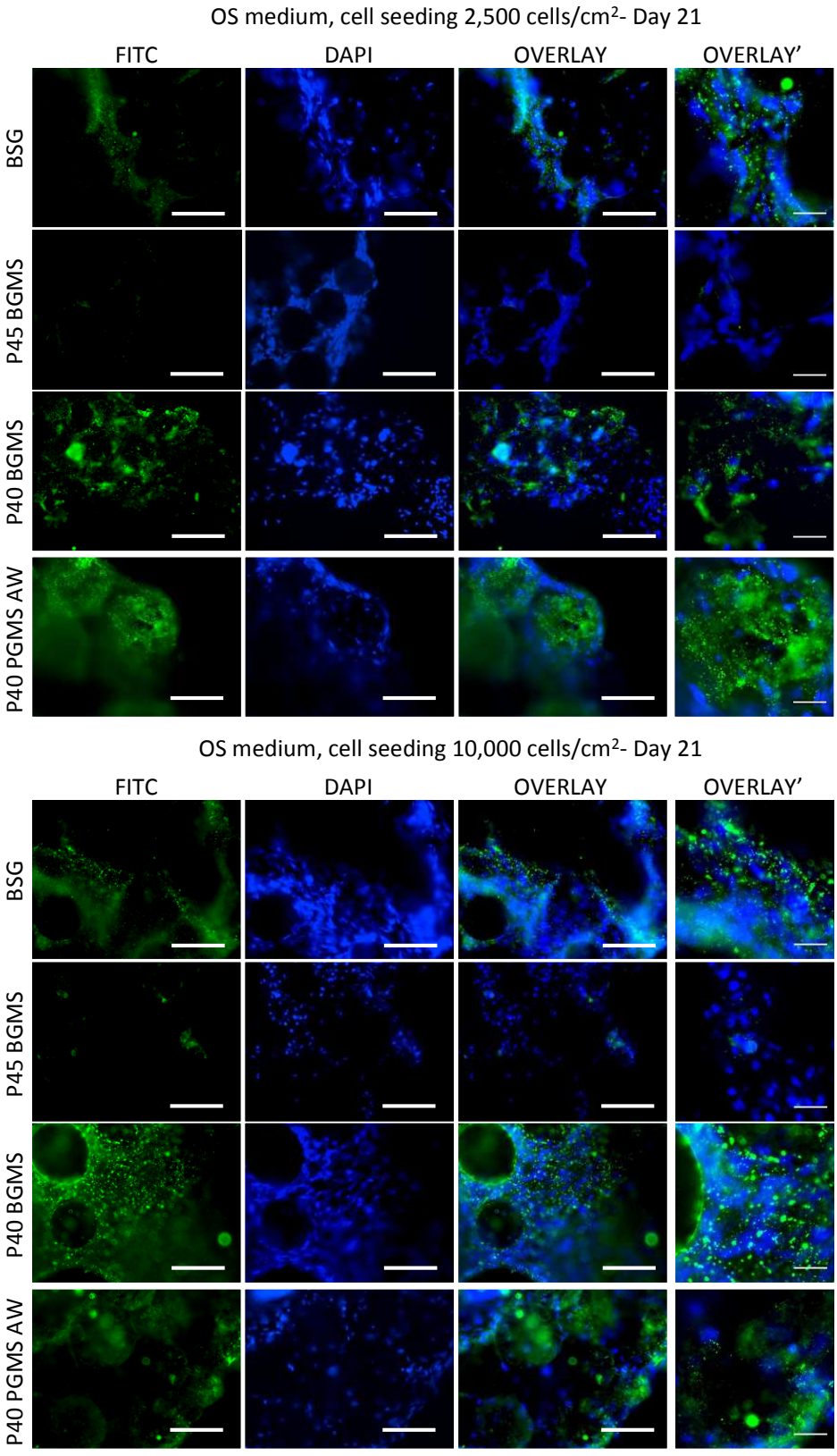

Figure 5-33: Osteocalcin (OCN) expression (FITC) by hMSC on different microsphere after 21 of culture in OS (osteogenic stimulation) medium. Cells were seeded at 2,500 and 10,000 cells cm^{-2}. Blue signal represents cell nuclei (DAPI). There was presence of OCN on BSG, P40 BGMS and P40 PGMS AW but not on P45 BGMS. Scale bars on FITC, DAPI and OVERLAY- 100 µm and OVERLAY'- 25 µm.

5.14 Extracellular matrix formation (ECM) on microspheres

The Figure 5-34 represents the H&E stained cross-sections (through the centre) of MS-cells agglomerates on day 21 of culture. Mouse tissue has been used as a control for staining.

In case of BSG and P45 BGMS, there were poor signs of ECM formation by cells. However, in case of P40 BGMS and P40 PGMS, there was extensive positive eosin staining, indicative of ECM formation by cells. These observations were made at both cell-seeding densities of 2,500 cells cm^{-2} and 10,000 cells cm^{-2}.

The Figure 5-35 shows low magnification view of a typical H&E stained section of cell loaded P40 PGMS AW after 21 days of culture. The image showed preferential positive eosin staining in the regions in and around porous MS. Moreover, there was also presence of some MS with positive H&E staining limited to their outer edges only.

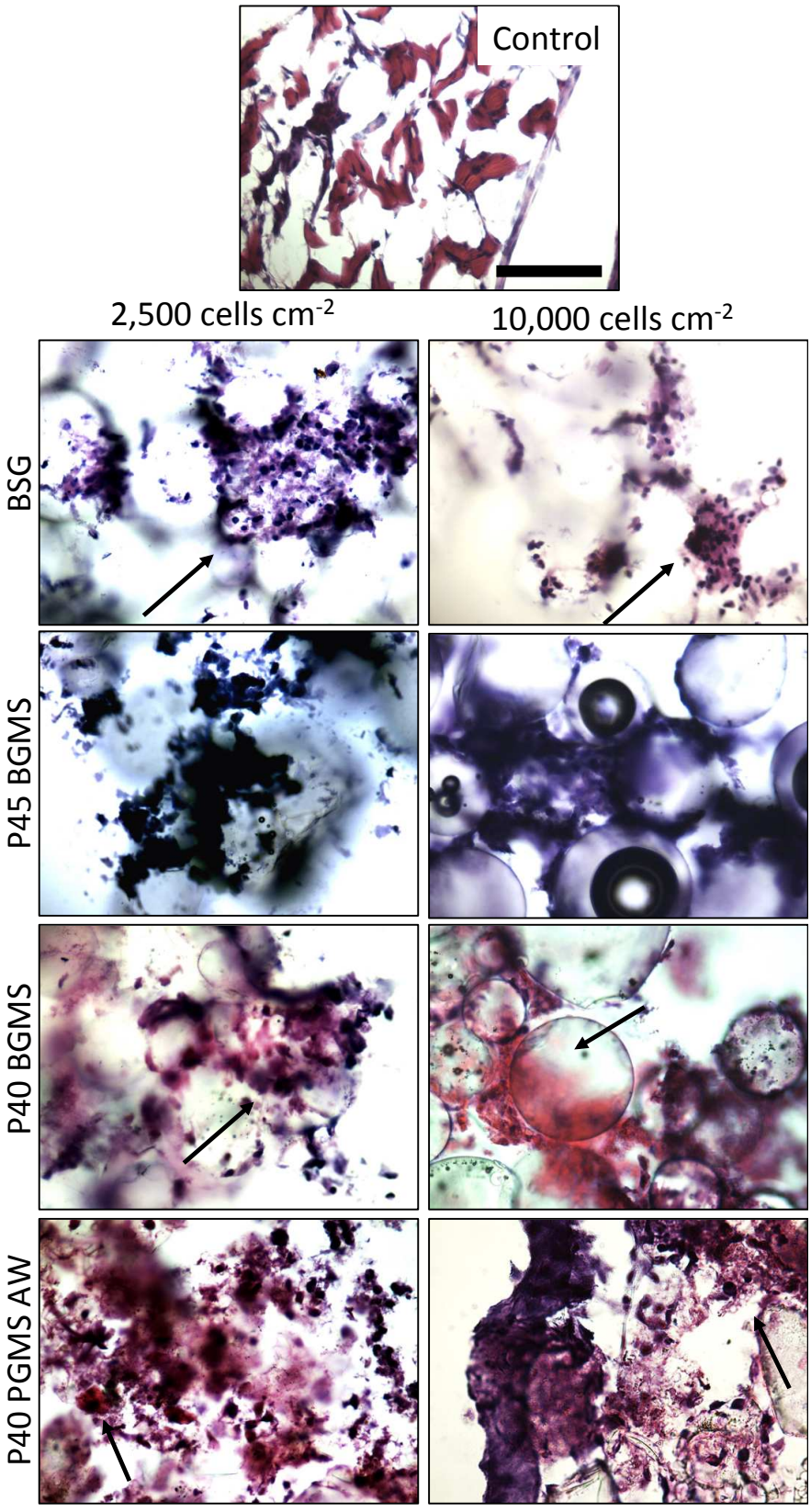

Figure 5-34: Extracellular matrix (ECM) formation by hMSCs on different glass microspheres after 21 of culture. Cells were seeded at 2,500 and 10,000 cells cm^{-2}. Blue and violet regions represent cell nuclei (acidic components) and pink regions represent proteins (basic components, arrows). Mouse calvarial tissue was used as a positive control for staining. Scale bar- 100 μm.

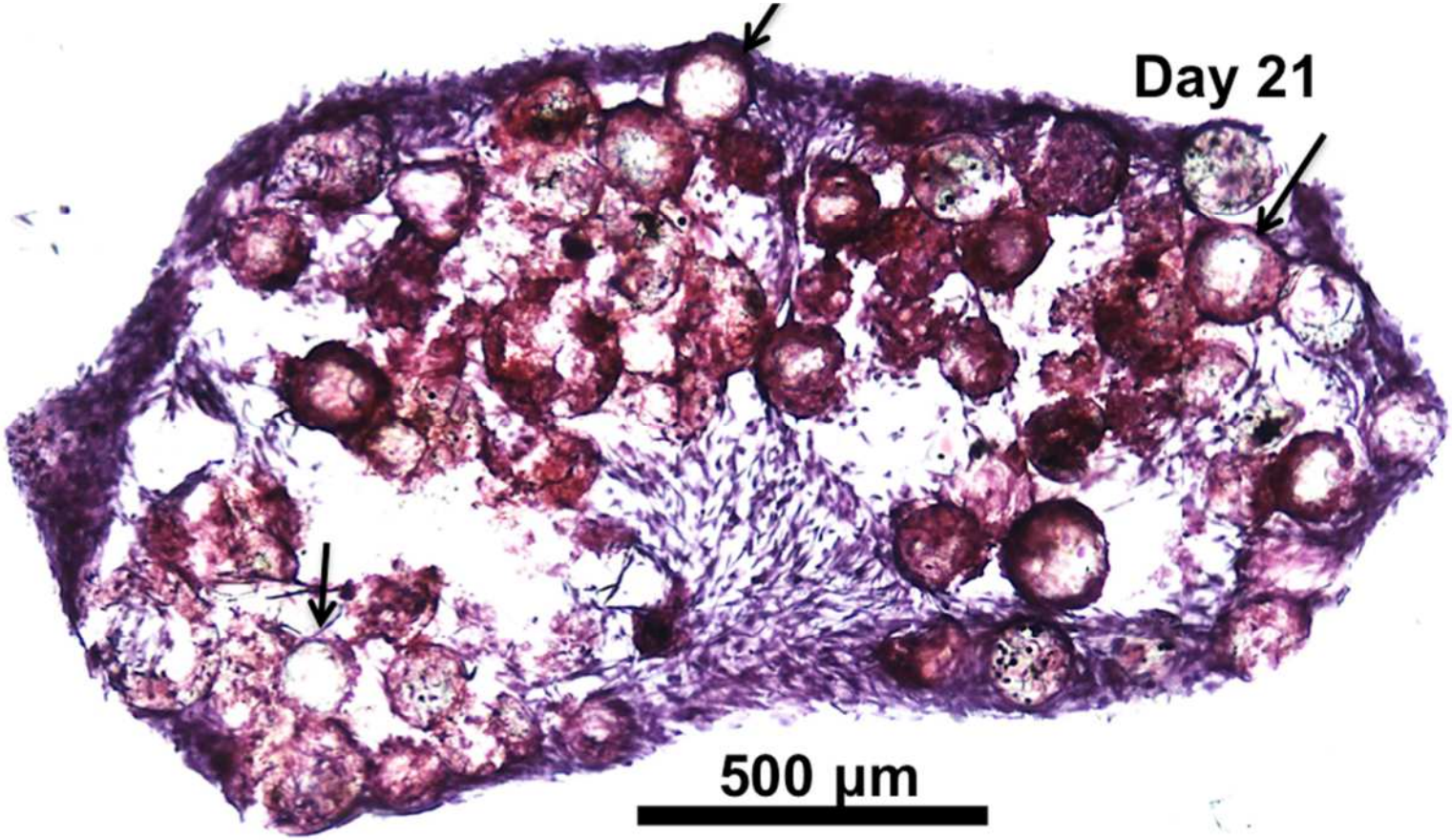

Figure 5-35: Typical H&E stained 3D cryo-section of P40 PGMS AW cultured with hMSCs for 21 days. Notice the preferential eosin staining in and around microspheres. Arrows indicate limited penetration of cells inside some of the microspheres. PGMS- porous glass microspheres, AW- acid washed.

5.15 Cytotoxicity of microspheres

As an essential requirement of BS EN ISO 10993-5:2009, cytotoxicity of MS was assessed using the indirect contact test and extract test.

5.15.1 Indirect contact test

Cytotoxicity via indirect contact test was measured using filter diffusion in Experiments TOX01 and TOX02, as described in Section 2.3.4.2.

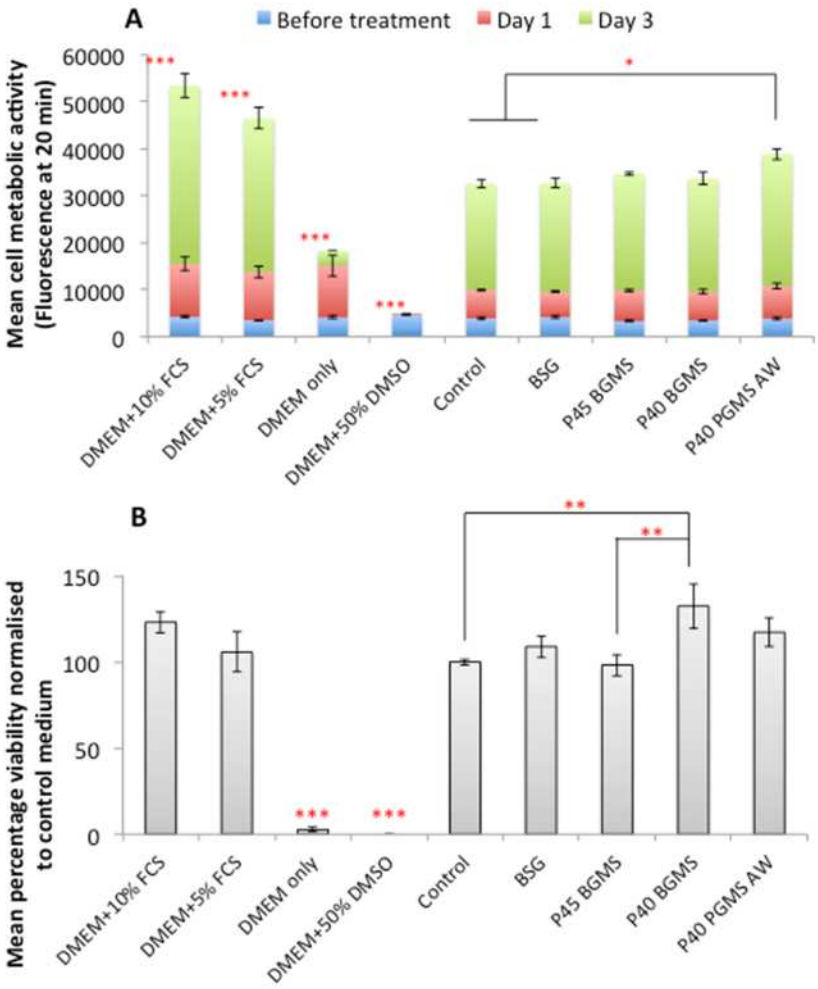

Figure 5-36: Indirect contact cytotoxicity evaluation for glass microspheres (MS) using a transwell in Experiment-TOX01. (A) Human MSC metabolic activity (PrestoBlue® assay) over 3 days of exposure to MS-eluted media. (B) Neutral Red uptake by hMSCs after 3 days of exposure to MS-eluted media. n=3 *, **, *** indicate $p<0.05$, $p<0.01$, $p<0.001$. Error bars represent S.E.M. Control condition represents cells in culture medium only.

In both experiments, cell metabolic activity was initially measured 24 h after hMSC seeding (before treatment) and as expected, the activity was similar in all wells (see Figure 5-36 and Figure 5-37).

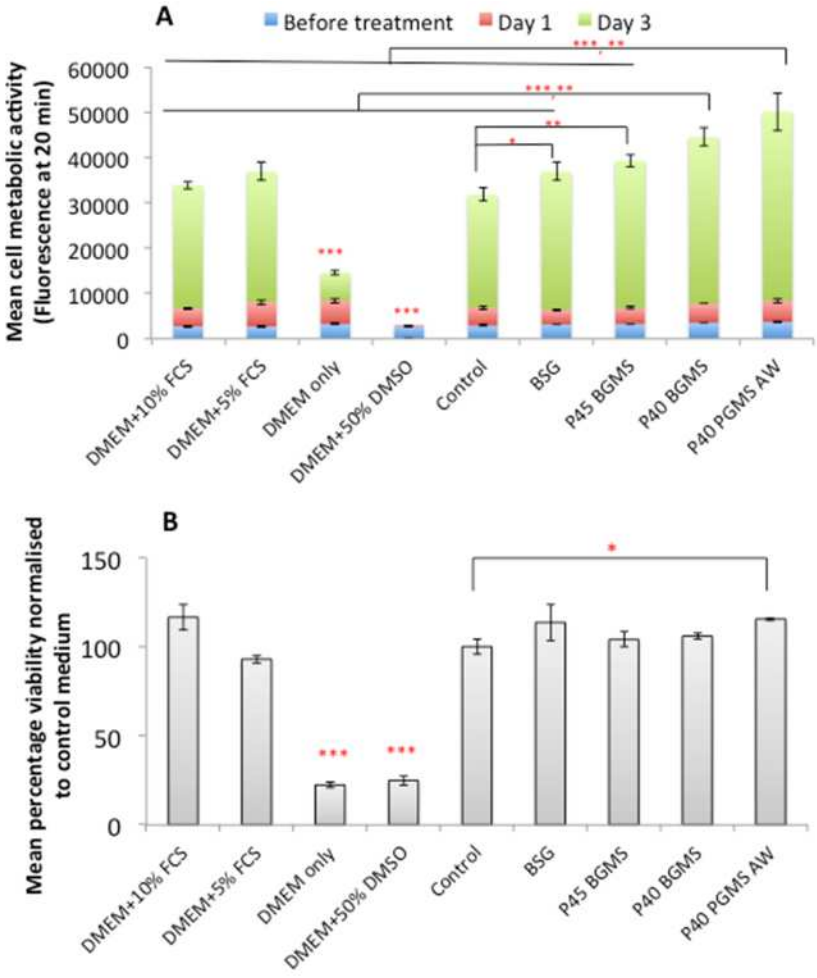

Figure 5-37: Indirect contact cytotoxicity evaluation for glass microspheres (MS) using a transwell in Experiment-TOX02. (A) Human MSC metabolic activity (PrestoBlue® assay) over 3 days of exposure to MS-eluted media. (B) Neutral Red uptake by hMSCs after 3 days of exposure to MS-eluted media. n=3 *, **, *** indicate $p<0.05$, $p<0.01$, $p<0.001$. Error bars represent S.E.M. Control condition represents cells in culture medium only.

However, after 3 days of indirect exposure, there was significantly higher cell metabolic activity in P40 PGMS AW condition compared to Control (no MS) and BSG Batch 1 in Experiment-TOX01 ($p<0.05$) and TOX02 ($p<0.001$). These results indicated a positive effect of P40 PGMS AW degradation products (<0.4 µm in size) on hMSC metabolic activity. It was interesting to note that this effect was not visible via neutral red assay on same biological replicates on same time point. This further suggested that the degradation products of

P40 PGMS AW (<0.4 μm in size) did not affect the hMSC membrane integrity and more likely interfered with mitochondrial metabolism without being cytotoxic.

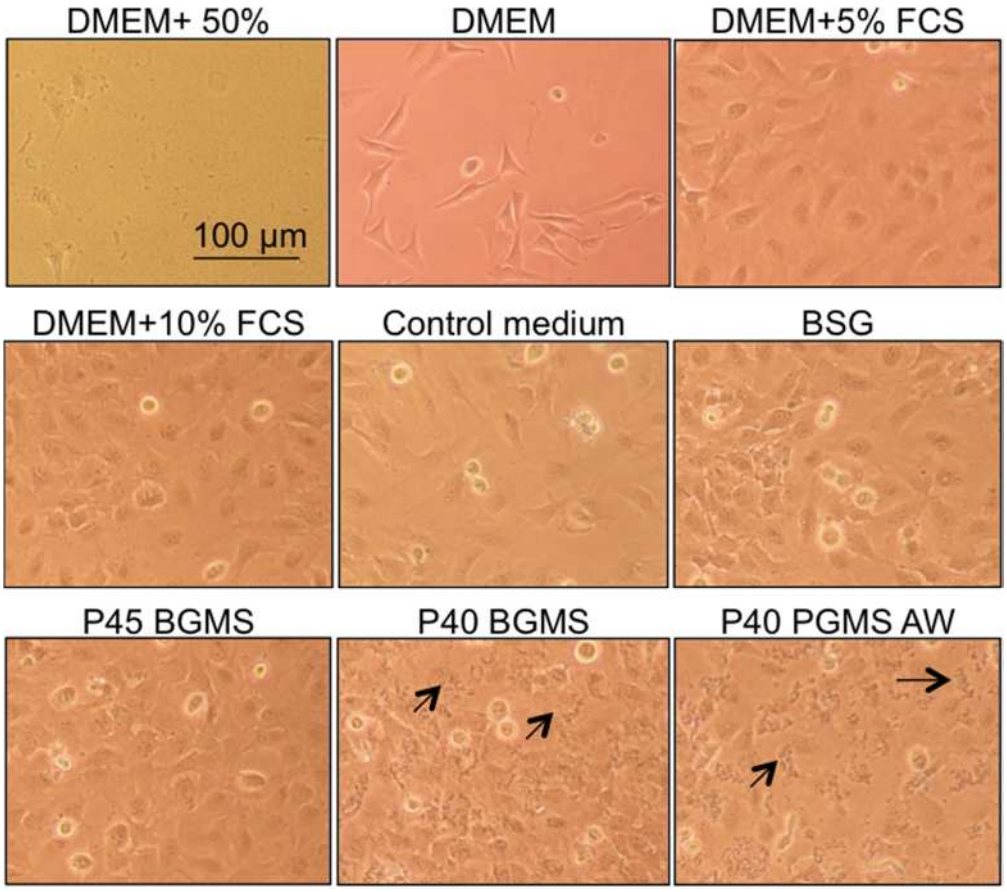

Figure 5-38: Images taken on day 3 of Experment-TOX02. ➔indicates particulates floating in medium in P40 BGMS and P40 PGMS AW conditions.

Comparison of PBG bulk MS with control showed that after 3 days of indirect exposure there were no significant differences between hMSC metabolic activity in P40 or P45 BGMS relative to control (no MS) or among themselves in Experiment-TOX01 but there was higher hMSC metabolic activity in both P40 BGMS ($p<0.001$) and P45 BGMS ($p<0.05$) relative to control in Experiment-TOX02. From neutral red assay, higher neutral red uptake in P40 BGMS relative to control and P45 BGMS was observed in Experiment-TOX01 but this was absent in Experiment-TOX02.

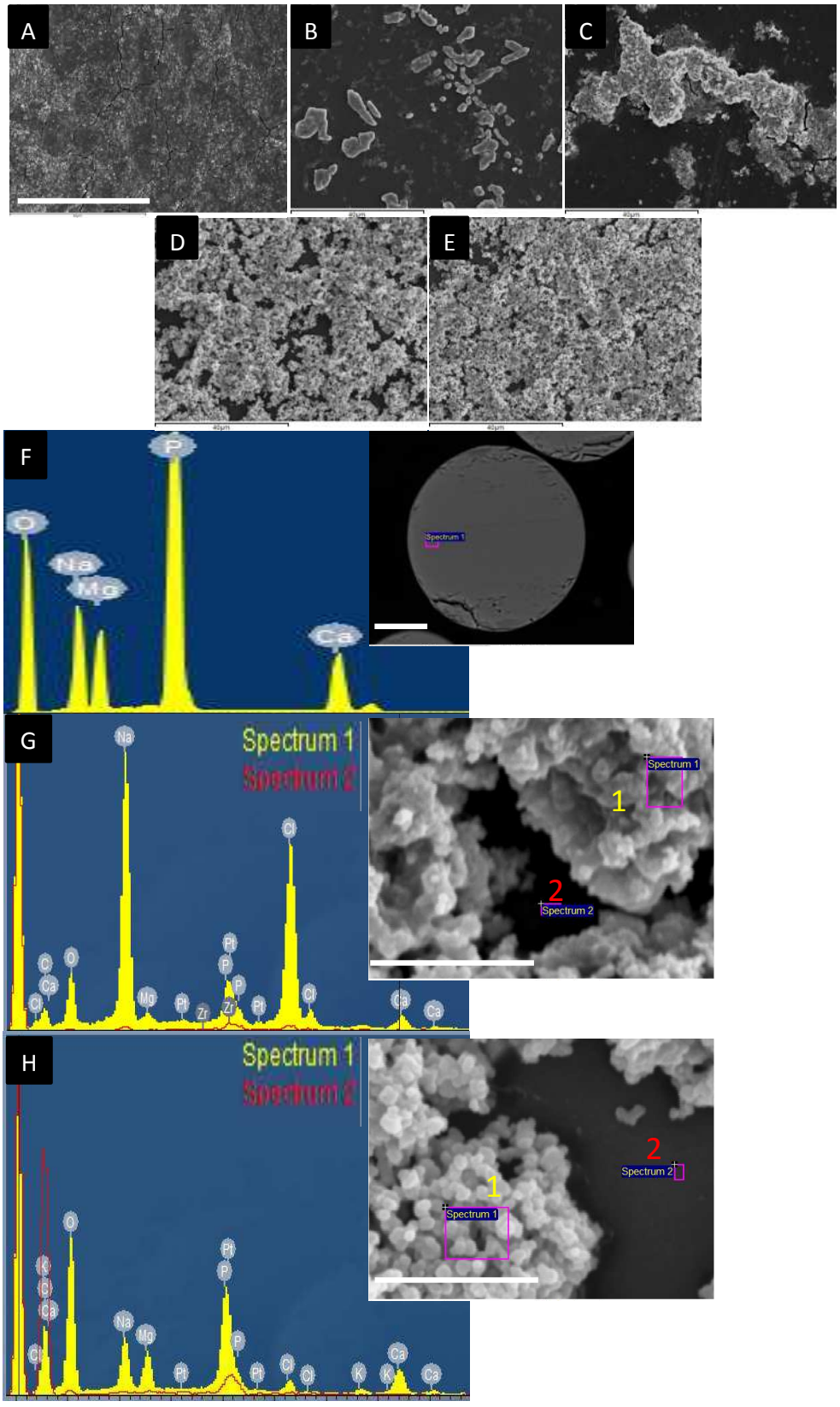

Figure 5-39: Characterisation of floating particulates collected in Experiment-TOX02. SEM images for control (no MS) (A), BSG (B), P45 BGMS (C), P40 BGMS (D) and P40 PGMS AW (E) conditions. Typical EDS spectrum of a P40 glass (F) is compared to EDS spectra for particulates collected from P40 BGMS extract (G) and P40 PGMS AW extract (H). Scale bars- 40 µm in A-F, 5 µm in G, H.

Additionally, on day 3 of both experiment, particulates (<0.4 µm in size) were seen floating in P40 BGMS and P40 PGMS AW medium and were absent in all other conditions, see Figure 5-38. These particulates were collected from medium after centrifugation and analysed for elemental composition using EDS analysis. The results, see Figure 5-39, showed that particulates in P40 BGMS and P40 PGMS AW extracts had similar elemental composition as P40 glass and in case of P40 BGMS there was also presence of NaCl, which may have been derived from culture medium.

5.15.2 Elution for 1 day

For initial extract tests, Experiment-TOX03 was performed three times as described in Section 2.3.4.2 and all the results have been combined for statistical analysis and shown in Figure 5-40.

Based on Neutral Red uptake (NRU), cell metabolic activity and DNA content assessments, none of the MS conditions were cytotoxic.

Moreover, the results also showed that there was significantly lower cell metabolic activity in P40 BGMS eluted medium as compared to control ($p<0.05$), which suggested a negative effect of P40 BGMS dissolution products on hMSC mitochondrial metabolism.

The Figure 5-41 shows neutral red uptake by hMSCs in different conditions. There was presence of glass fragments in P40 MS conditions, significantly more in case of P40 PGMS. The images also showed that these fragments were internalised by hMSCs and were present in the cytoplasm, see Figure 5-41, arrows.

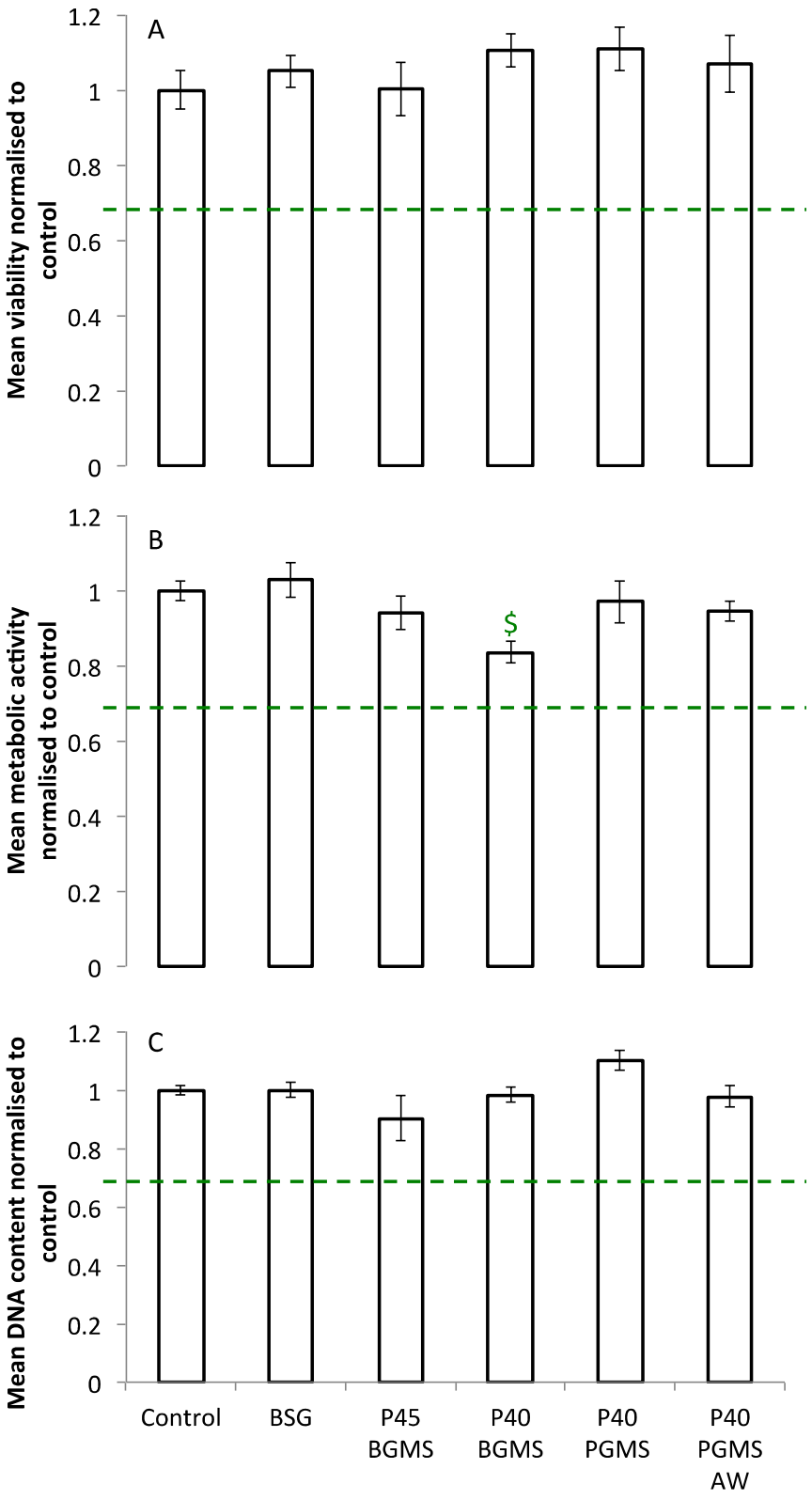

Figure 5-40: Extract tests of MS after 1 day of elution in medium in Experiment-TOX03. (A) hMSC viability via neutral red uptake. (B) hMSC metabolic activity via PrestoBlue® assay. (C) hMSC DNA content via PicoGreen® assay. All measurements were normalised to control (no MS). $ indicates $p<0.05$ relative to control. --- indicates 70% relative to control. n=9. Error bars represent S.E.M.

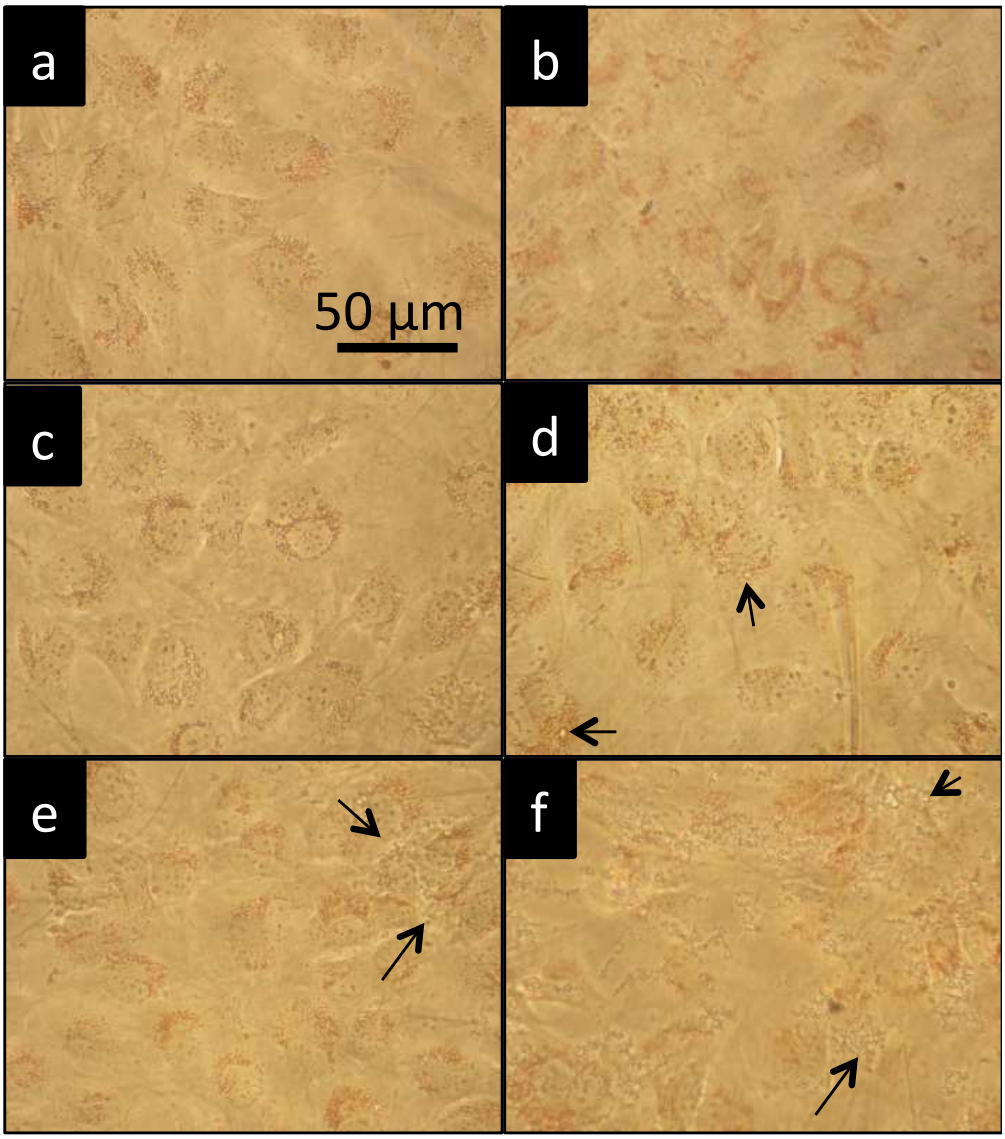

Figure 5-41: Neutral Red uptake by hMSCs in Experiment-TOX03. (a) Control- medium only, (b) BSG, (c) P45 BGMS, (d) P40 BGMS, (e) P40 PGMS, (f) P40 PGMS AW.➔indicates glass particulates inside hMSCs.

5.15.3 Elution for 7 days

In Experiment-TOX04, elution period was increased to 7 days without medium changes in static condition as described in Section 5.15.3. The results, see Figure 5-42, showed that P45 BGMS and P40 BGMS were cytotoxic based on NRU, cell metabolic activity and DNA assays, with measurements <40% compared to control. In addition, there was 28%, 25% and 27% more hMSC viability, metabolic activity and proliferation in P40 PGMS relative to P40 BGMS. However, all three parameters were still in cytotoxic range.

The hMSC viability and metabolic activity were further enhanced to 98% and 79% relative to control, after acid washing of PGMS. However, hMSC proliferation remained unaffected the same.

In Experiment-TOX05, elution medium was exchanged on day 1 and 4 of incubation and the day 7 medium was either used as neat or filter via a 0.4 µm filter, before evaluating for cytotoxicity. This experiment was performed twice and all the results have been combined for statistical analysis and shown in Figure 5-43.

The results indicated that none of the MS conditions were cytotoxic based on NRU, cell metabolic activity and DNA assays. However, there was lower hMSC proliferation and metabolic activity in P40 PGMS relative to control ($p<0.001$) and P40 PGMS AW ($p<0.05$), respectively. On filtering, there was significantly enhanced hMSC viability in P40 BGMS relative to control ($p<0.05$), similar to as seen in Experiment-TOX01, and significantly enhanced hMSC proliferation in both PGMS conditions relative to control or neat extracts ($p<0.001$).

The Figure 5-44 shows representative images of neutral red uptake by hMSCs in different MS-eluted medium from Experiments-TOX04 and TOX05. The images showed significantly less hMSCs with circular/swollen morphology, in medium eluted with P45 BGMS and P40 BGMS without medium changes, which suggested that there may have been reduction in osmolality of the BGMS-eluted medium, which led to cell death. However, this cell death was not observed when medium changes were performed during elution, suggesting a positive effect of medium replenishment on hMSC health.

Further, the images in Figure 5-44 also showed presence of glass fragments/particulates internalised by hMSCs in P40 PGMS- and P40 PGMS AW-eluted medium and these particulates were not visible after filtering.

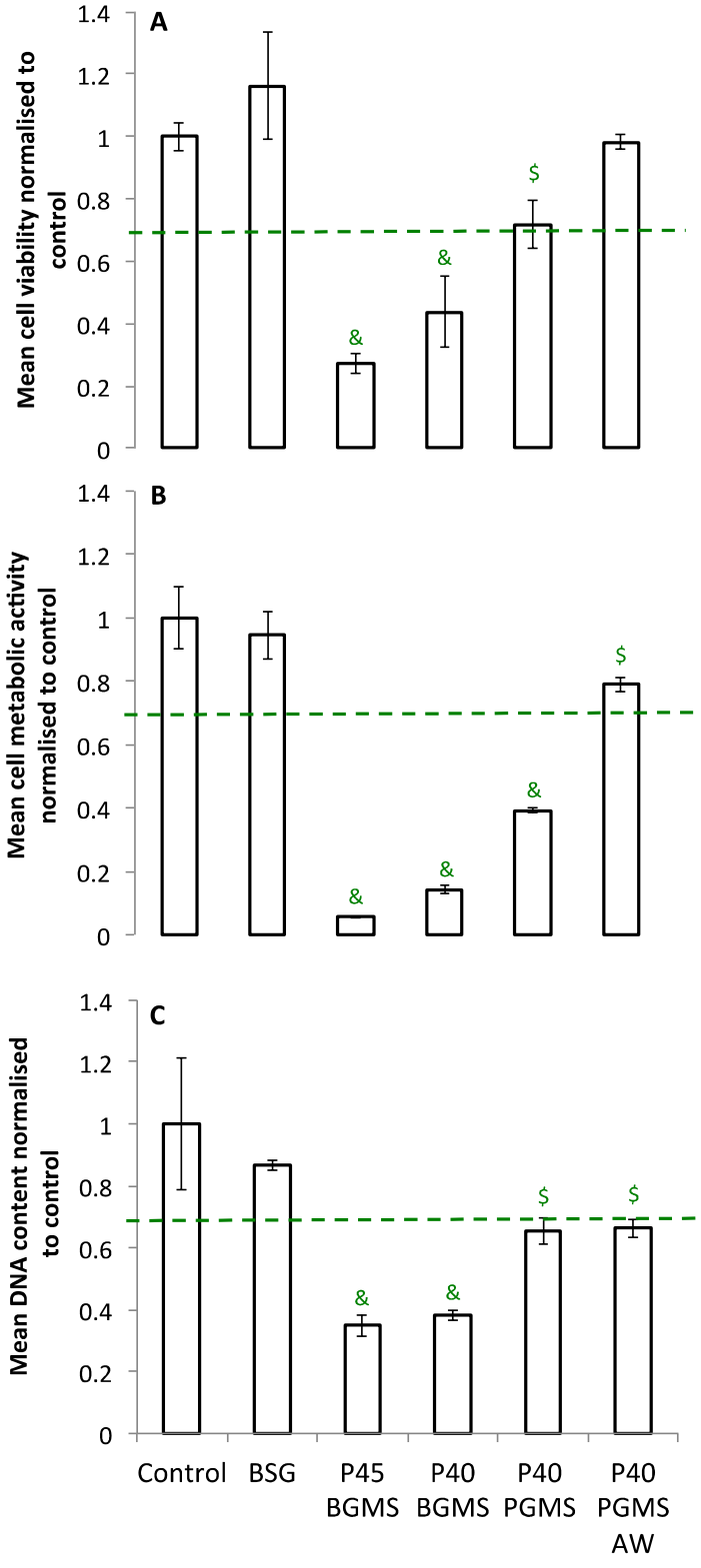

Figure 5-42: Extract tests of MS after 7 day of elution in medium without medium changes in Experiment-TOX04. (A) hMSC viability via neutral red uptake. (B) hMSC metabolic activity via PrestoBlue® assay. (C) hMSC DNA content via PicoGreen® assay. All measurements were normalised to control (no MS). $, & indicate $p<0.05$, $p<0.001$ relative to control. --- indicates 70% relative to control. n=3. Error bars represent S.E.M.

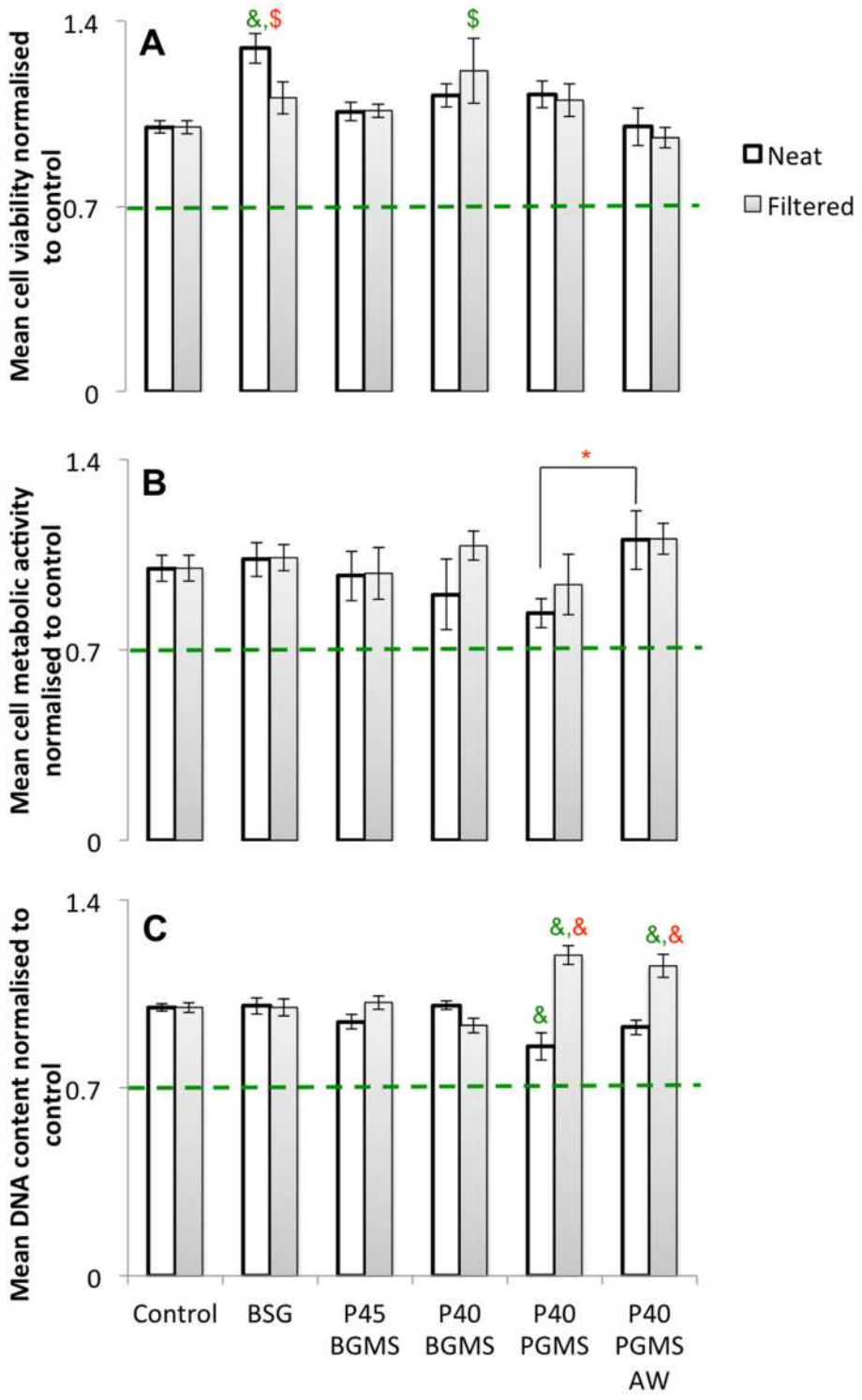

Figure 5-43: Extract tests of MS after 7 day of elution in medium with medium changes in Experiment-TOX05. The day 7 eluted medium was either used as neat or filtered using 0.4 µm filter. (A) hMSC viability via neutral red uptake. (B) hMSC metabolic activity via PrestoBlue® assay. (C) hMSC DNA content via PicoGreen® assay. All measurements were normalised to respective control (no MS). $, & indicate $p<0.05$, $p<0.001$ relative to respective control. $, & indicate $p<0.05$, $p<0.001$ relative to other medium condition of same MS type --- indicates 70% relative to control. n=6. Error bars represent S.E.M.

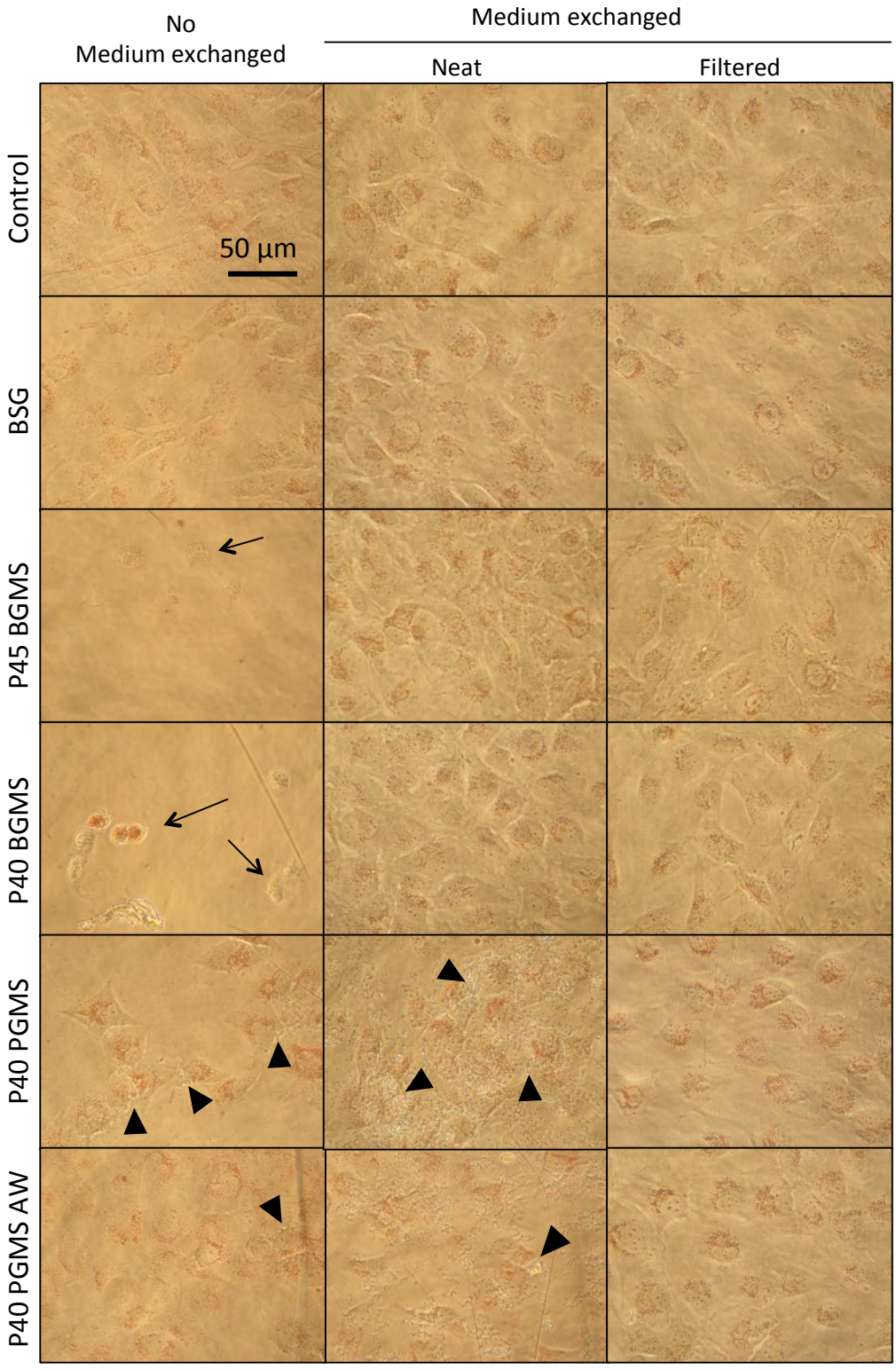

Figure 5-44: Neutral red uptake by hMSCs in Experiment-TOX05. Arrows indicate rounded cells and arrow-heads indicate glass particulates internalised by cells.

5.15.4 Cytotoxicity of spent culture medium

As the intended application of the developed PBG MS is for human MSCs delivery at the bone repair site, the final set of cytotoxicity experiments, Experiments-TOX06 and TOX07 were performed as described in Section 2.3.4.3. Briefly, hMSCs were loaded onto MS at 2,500 and 10,000 cells cm^{-2}, respectively and grown for 21 days in SC medium. The medium was exchanged every 2-3 days of culture and the spent media collected on day 7, 14 and 21, were evaluated for cytotoxicity via NRU assay. Cell-loaded BSG were used as control for each time point.

Initially, two-way ANOVA statistical analysis was performed for each experiment separately and the results showed very similar trends in both experiments (see Figure 5-45 A, B). On day 7 and day 21 of culture, there was significantly reduced viability in P40 PGMS AW spent medium compared to P40 BGMS or P45 BGMS spent medium. On the other hand, on day 14 of culture, there were no significant differences between the three conditions. By the end of 21 days, P40 PGMS AW spent medium was found to be cytotoxic.

DNA assay results in Experiments-CP07 and CP08 demonstrated that there can be different hMSC numbers on different MS-conditions on day 7, 14 and 21 of culture and this may have affected the amount of nutrients present in the spent media collected from each time point. Therefore, to address this issue, the results from Experiments-TOX06 and TOX07 were combined and statistical analysis was again performed using a Generalised Linear Mixed Model (GLMM) keeping DNA content on each time point as a random factor.

The results for GLMM, see Figure 5-45 C, showed no significant variation between the two experiments and despite adding DNA content as random factor, there was still least cell viability detected in P40 PGMS AW spent medium. These results strongly indicated a cytotoxic effect of PGMS-dissolution products on hMSCs.

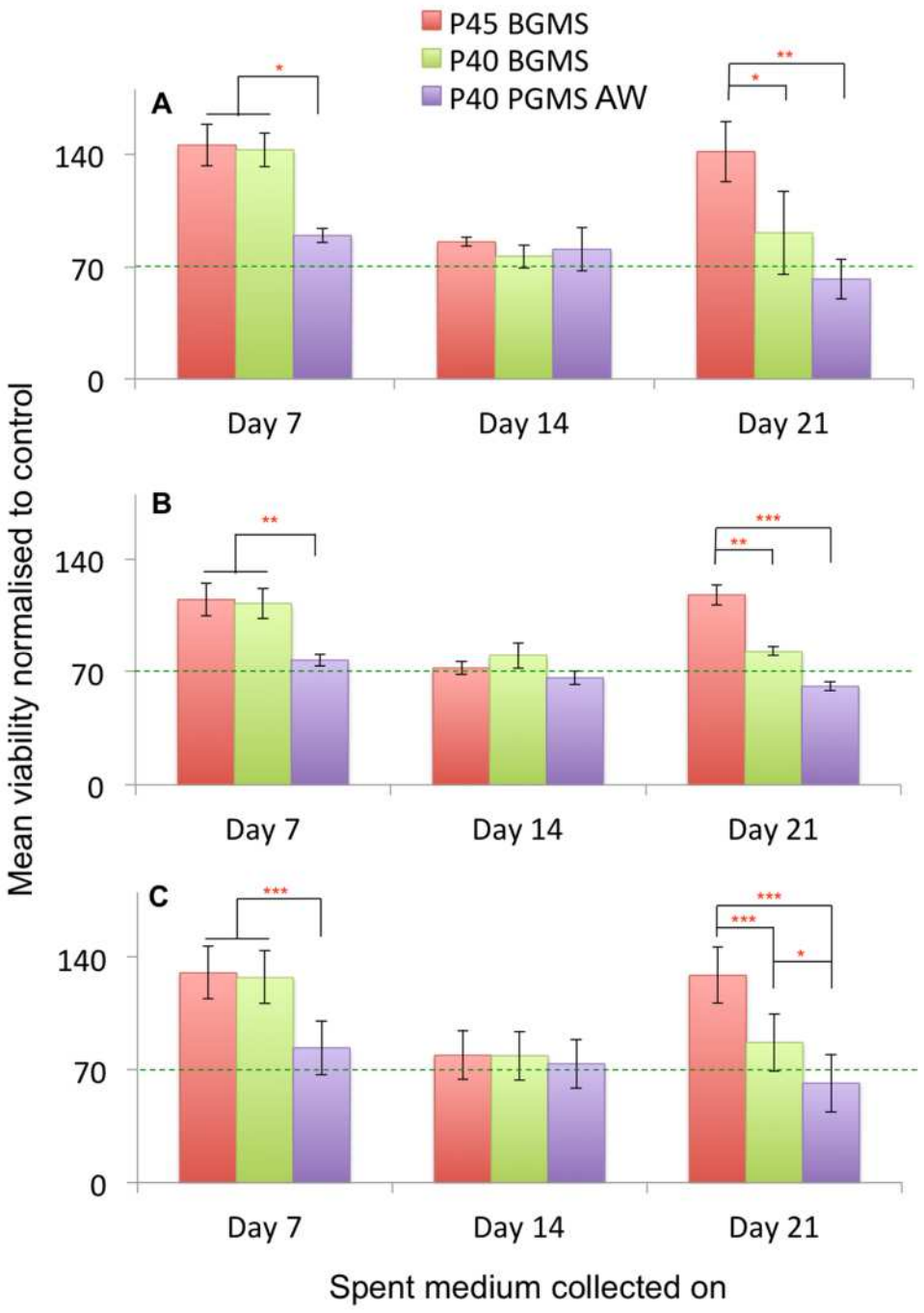

Figure 5-45: Cytotoxicity of spent medium removed from hMSC-loaded MS on day 7, 14 and 21 of culture. (A) Experiments-TOX06 (n=3) and (B) Experiment-TOX07 (n=3) both analysed via Two way ANOVA. (C) Combined Experiments-TOX06 and TOX07 (n=6) analysed by Generalised Linear Mixed Model. Cell viability measured via neutral red uptake. ***p<0.001, ** p<0.01 and * p<0.05. ----- indicates 70% viability compared to BSG. Error bars represent S.E.M.

The images in Figure 5-46 represent hMSC grown in spent medium collected from P40 BGMS and P40 PGMS AW conditions from Experiments-CP07 and CP08. There were a number of floating glass particulates seen in both conditions at all time points.

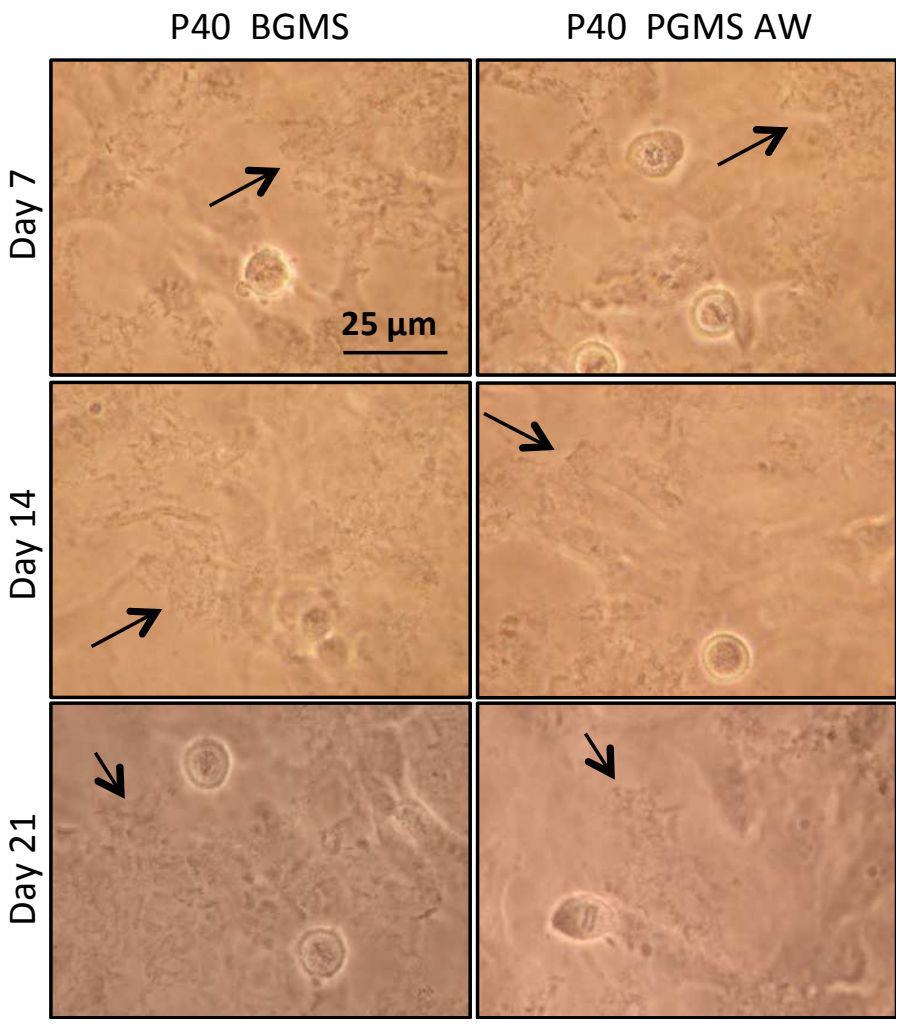

Figure 5-46: Floating glass particulates (arrows) in P40 BGMS and P40 PGMS AW-spent medium in Experiment-TOX06 and TOX07.

5.16 Discussion

5.16.1 Angular shaped vs. regular shaped particles

The preliminary experiment PR01 indicated significantly lower cell metabolic activity in AG1 P45 BGMP, relative to both AG1 P45 BGMS and AG1 P45 PGMS, which may be due to sharp edges (harsh convexities) provided by BGMP (Park et al. 2009). These convexities may have stressed the plasma membrane and cytoskeleton to a limit where the cells were unable to perform normal metabolic processes and this may have affected their survival and subsequently proliferation (Binamé et al. 2010). Mechanism behind this is also discussed in Chapter 4, Section 4.4.3.

Another reason for poor cell health on AG1 P45 BGMP may be due to presence of higher proportion of finer particulates (<10 µm) in AG1 P45 BGMP, as compared to AG1 P45 BGMS and AG1 P45 PGMS. Phagocytic uptake can lead to localization of particulates inside the vesicles but non-phagocytic uptake also can lead to localization in outer-cell membrane, cytoplasm, mitochondria, lipid vesicles, along the nuclear membrane or within the nucleus (Buzea et al. 2007; Labbaf et al. 2011). Depending upon their localization, they can damage organelles, possibly via excessive release of calcium ions into the cytosol, or even DNA via oxidative stress leading to death (Juin et al. 1998; Geiser et al. 2005; Xia et al. 2006). Transmission electron microscopy may be carried out in future to ascertain the actual mechanism for this potential debris-based cytotoxicity.

5.16.2 Batch-to-batch variability

The results in Experiments-BR03, BR04, BR05 and BR06, suggested no batch-to-batch variability after 7 days of culture in case of P45 BGMS and P40 BGMS. This may due to similar range of sphericity (ca. 0.9) and elemental composition offered by MS in of P45 BGMS Batches 1 and 2 or P40 BGMS Batches 1 and 2. These results also suggest that the subtle batch-to-batch variation in particle size distribution in these batches (see Section 3.2.3) did not affect hMSC growth.

In Experiments-BR07 and BR08, there was higher mean DNA content in AG6 P40 PGMS AW relative to AG5 P40 PGMS AW on day 7 of culture, which statistical significance only in Experiment-BR07. This may be due to two or more reasons. Firstly, there was 1.7 times more surface area and 7% less closed porosity in AG6 batch relative to AG5 batch, which may have allowed more penetration of hMSCs inside the AG6 porous MS (Karageorgiou & Kaplan 2005). Secondly, there was higher Ca content (see Section 3.5.3), and possibly more Ca-based porogen retained in AG5 batch relative to AG6 batch. This may have negatively affected hMSC growth by inducing more cytotoxicity (Maeno et al. 2005). Thirdly, it may be

due to a sampling error, leading to a Type 1 statistical error (Banerjee et al. 2009).

It is important to note that the difference between DNA content on AG6 P40 PGMS AW and AG5 P40 PGMS AW was only 0.16-0.24 µg of DNA on day 7 of culture and this difference may be considered negligible from an *in vivo* perspective. Based on this, it was concluded that there was no significant batch-to-batch variability in P40 PGMS AW batches.

5.16.3 Effect of acid washing on hMSC response

The results showed that closed porosity was reduced by 27% and median and mode pore window sizes increased from 2.63 µm to 2.73 µm and from 1.15 µm to 1.53 µm, respectively, in AG6 batch after acid washing. This suggests that washing with acetic acid may have opened up some closed or new pores and also increased the size of existing pores, thereby enhancing the porosity and possibly interconnectivity of PGMS and ultimately enhancing hMSC growth. Previous studies have shown that at constant pore sizes, if the interconnectivity of pores in increased, the bone formation is also increased *in vivo* (Lu et al. 1999; Flautre et al. 2001). This may explain more hMSCs in AG6 P40 PGMS AW as compared to AG6 P40 PGMS in Experiments-AW01 and AW02.

In Experiment-TOX04, there was marked improvement in hMSC membrane integrity and metabolic activity in PGMS-extracts after acid washing. Moreover, in Experiment-TOX05, there was more hMSC metabolic activity and proliferation in PGMS-extracts after acid washing. These results strongly indicated a cytotoxic effect of non-washed PGMS, possibly due to excessive release of calcium ions (Maeno et al. 2005) and glass fragments/particulates into the medium, leading to apoptosis (Juin et al. 1998; Gough et al. 2004) and structural damage (Geiser et al. 2005; Xia et al. 2006), respectively; and also suggested that acid washing not only changed

the physicality of PGMS, but may also have reduced excess release of calcium ions and the glass fragments/particulates from PGMS.

5.16.4 Cytocompatibility of P45 BGMS

The results indicated that P45 BGMS provided suitable surfaces for hMSCs attachment and there were more cells on these MS compared to any other bulk-MS condition, over extended culture periods. However, cell viability results indicated significant cell death in P45 BGMS by 21 days of culture and this may be responsible for absence of ECM formation and osteogenic markers on the same.

A possible explanation for these observations may be more hydrophobic surfaces provided by Fe containing PBG glasses relative to P40. A study has shown that with increasing iron content from 0 to 5% mole% in PBGs (P_2O_5-CaO-Na_2O glass system), the contact angle measurements (using water) increase from 13^0 to 26^0 (Abou Neel et al. 2005). Despite the increase, the contact angle values are relatively still low; however, this contact measurement was performed for flat surface on conventional melt cooled glass. It would be difficult to perform conventional contact angle measurement on microspheres due to their curved surfaces and it is also possible that the rapid cooling rate of the processing of the microspheres may have led to an enhancement of this effect of Fe resulting in a sufficiently lower wettability and protein adsorption on P45 BGMS relative P40 BGMS, ultimately contributing to poor cell migration and survival on P45 BGMS (Anselme 2000; Lotfi et al. 2013). This postulate is also supported results Experiments-AG01 and AG02, where there was less agglomerate formation in P45 BGMS relative to P40 BGMS.

Another contributing factor for poor biological performance of P45 BGMS may be the cytotoxicity induced by iron. Studies have shown that iron overloading in body is associated with increased risk of osteoporosis (Weinberg 2006; Diamond et al. 1991); ≥400 µmol/L of Fe in culture medium has been shown to diminish osteoblast cell

proliferation and function (Diamond et al. 1991); >1.5 mmol/L Fe(II) in medium has been shown to reduce membrane stability of Caco-2 cells (He et al. 2008); and ferric ammonium citrate (0.1-10μg/ml) has been shown to inhibit MC3T3-E1 proliferation, ALP activity, total protein content, mineral deposit and type 1 collagen deposit, in a dose-dependent manner (Yamasaki & Hagiwara 2009). Therefore, it is also possible that the resulting iron concentration experienced by hMSCs at glass-cell interface, may have led to a cytotoxic effect.

However, when degraded products of P45 BGMS were investigated for cellular responses, there was no apparent decrease in cell proliferation but rather there was a positive effect on collagen and mineral deposition after 16 and 25 days of culture relative to BSG and/or control. Therefore, it is likely that iron cytotoxicity may not have been the main reason for cell death on P45 BGMS but hydrophobic glass surfaces may have played a more dominant role in the same.

Finally, the OCN immunostaining showed that even after culturing hMSCs in OS medium for 21 days, they were unable to secrete OCN on P45 BGMS. This observation again strengthens the argument that hydrophilic glass surfaces are essential for hMSC survival and function and in absence of polar cell-material interactions dexamethasone, beta-glycerophosphate and ascorbic acid do not enhance the osteogenic fate. Contact angle measurements on P45 BGMS or discs may be carried out in future to investigate the surface hydrophobicity of these MS.

5.16.5 Cell growth on P40 BGMS

The cell attachment experiments indicated a subtle decrease in hMSC metabolic activity after one day of culture and the cell proliferation experiments indicated lower number of cells on P40 BGMS relative to P45 BGMS during short or extended culture periods. Additionally, there was also reduced cell metabolic activity

in neat medium extracts of P40 BGMS in Experiment-TOX03. These results may be due to one or more factors:

(1) Degradation studies, presented in Chapter 1, Section 3.6, showed P40 BGMS were more prone to hydration as compared to BSG or P45 BGMS and this led to appearance of cracks and peeling surfaces by as early as day 1 and 4 of culture. These cracks may have affected cell viability and structural integrity of cells present on them (Skelton et al. 2007; Leonardi et al. 2010; Lakhkar 2014). This postulate is supported by SEM images that clearly demonstrate significant structural damage to cells present on P40 BGMS, see Figure 5-19. However, the resulting cell morphology visible on in these images may also be an artefact of dehydration steps using increasing concentrations of ethanol in the sample preparation process for SEM.

(2) Bioactive glasses are known to release bioactive ions faster during initial 24 h of degradation as compared to later time point (Abou Neel et al. 2005; Penttinen 2011). Moreover, the degradation study results in Section 3.6, indicated significant surface damage occurring on P40 BGMS and P40 PGMS AW between day 1 and 4 of incubation in culture medium, indicative of faster degradation as compared to P45 BGMS or BSG. This may have led to a high extracellular Ca^{2+} ion concentration and excessive uptake of these ions by hMSCs, leading to cytotoxicity (Maeno et al. 2005).

(3) Cytotoxicity experiments revealed that degradation products may not only be in the form of ions but also in the form of glass fragments and particulates. These particulates may have induced cytotoxicity as described in Section 5.16.3.

In the conditioning experiments (where medium to material ratio was 10 mg per ml) an inconsistent positive effect of P40 BGMS–degraded products on cell proliferation was observed. Moreover, in cytotoxicity experiments, where medium to material ratio was 100 mg per ml, neat P40 BGMS extracts were unable to enhance any of

the cellular parameters. These results strongly suggest that the degradation products were able to induce a positive effect only at lower concentrations and at higher concentrations, the cells were under the influence of both positive and negative effect of calcium ions and glass fragments/particulates, respectively, which may have cancelled out each other. This postulate is supported by the evidence from Experiments- TOX01, TOX02 and TOX05, where higher cell viability and cell metabolic activity relative to control was observed after removal of glass fragments >0.4 μm in size.

In line with these observations, some studies have shown that bioactive nanoparticles enhance cell viability more effectively as compared to bioactive microparticles. For example, de Oliveira et al. (2013) showed significantly more osteoblast viability and ALP activity when cultured with 0.1 mg mL^{-1} of bioglass nanoparticles as compared to control or 0.1 mg mL^{-1} of bioglass microparticles. MačKović et al. (2012) also showed that MG-63 cells had more proliferation when cultured with 0.1–100 μg ml^{-1} of bioglass nanoparticles as compared to bioglass microparticles at same concentration. At the same time, there was higher ALP activity for MG63 cells when cultured with 200 μg ml^{-1} of bioglass nanoparticles as compared to bioglass microparticles.

The results also showed that irrespective of cell seeding density used, the cells never seemed to grow beyond day 14 time point on P40 BGMS, which is also the same time point beyond which no significant change in apparent surface changes occur on these MS, see Figure 3-33 in Section 3.6.2. This comparison suggests a direct correlation between degradation pattern and hMSC growth on P40 BGMS.

Some studies have shown that presence of grooves and pits on 2D surfaces can affect cellular responses, such as adhesion, migration and osteogenic differentiation (Dalby, McCloy, Robertson, Wilkinson, et al. 2006; Dalby et al. 2006; McMurray et al. 2011). Hence, it is

also likely that the resulting changes on P40 BGMS surfaces, may have affected hMSC fate, while reducing their growth.

Altogether, the findings from the current study suggest a combined effect of surface topography and degradation products on hMSC growth in P40 BGMS culture condition.

5.16.6 Differentiation on P40 BGMS

Experiments-CD05, CD06 CD07 and CD08 consistently showed significantly higher ALP activity for hMSCs cultured on P40 BGMS relative to BSG or P45 BGMS on earlier time points. These studies are in line with a previous study investigating MG63 cells seeded on P45 and P40 glass discs, where significantly higher ALP activity was reported in the case of P40 discs relative to P45 discs and TC-plastic (Hasan et al. 2012). This suggests a similarity in hMSC response to PBG formulations in both 2D and 3D cultivations.

Following investigations in Experiments-ECM02, COL05-COL10, OCN02 and MIN06-MIN07 also showed significantly more ECM formation together with collagen, OCN as well as Ca and P deposition by hMSCs in P40 BGMS as compared to other bulk MS-conditions, even in the absence of osteogenic supplements. This clearly demonstrated an osteoinductive effect of these MS on hMSCs, which was also validated via Experiements-CON01 and CON02, where hMSCs produced more collagen and mineral in P40 BGMS conditioned-culture medium, relative to all other conditions. This may be a result of increased intracellular Ca^{2+} ions in P40-conditioned medium that may have enhanced glutamate secretion by hMSCs, inducing an osteogenic fate (Taylor 2002; Valério et al. 2007; Valerio et al. 2009).

Finally, the results also showed that hMSCs were able form agglomerates on P40 BGMS relatively faster than any other MS conditions. This evidence supports the argument that P40 BGMS offered more hydrophilic surfaces for cell attachment and migration, which enabled cell proliferation and osteogenic differentiation.

However, at the same time, this hydrophilic nature also led to complete disintegration of P40 BGMS surfaces over extended culture periods (shown in Section 3.6.2) and therefore, some of the cellular material may have been lost into the culture medium with the delaminating glass surfaces. Hence, the peeling effect (Choueka et al. 1995) may have been responsible for lower or similar collagen measured on P40 BGMS relative to BSG in Experiments-COL05 to COL10, despite higher collagen and ECM formation detected in qualitative assessments (Experiments-COL02 and ECM02, respectively).

One of the methodologies suggested to reduce the peeling effect of the PBG surfaces is through annealing (see Section 3.7.4.1) which can reduce any stresses in the glass spheres during rapid cooling from the melt. The process not only improves cell growth by delaying the peeling of the surfaces but may also enhance the mechanical properties of the material (Choueka et al. 1995; Ahmed et al. 2009; Sharmin et al. 2014; Parsons et al. 2009). However, the subsequent loss of topography (cracks) on the glass surface and slower release of ions may also affect the osteogenic potential of hMSC seeded on annealed P40 BGMS.

Hence, based on current work, P40 BGMS are potential candidates for bone repair applications but due to peeling effect, they may delay the regeneration *in vivo* by excessive loss of ECM at least up to day 21 of culture. Future investigations may be performed in order to enhance surface integrity and to limit the release of toxic glass fragments/particulates from P40 BGMS.

5.16.7 Cell growth on porous microspheres

There was significantly lower cell metabolic activity and viability on porous MS on day 1 of culture. Additionally, there was reduced hMSC growth in P40 PGMS AW relative to P40 BGMS, up to day 14 and day 4 of culture, at cell seeding densities of 167 and 2,500 cells

cm^{-2}, respectively. These results may be explained as a combination of four factors:

(1) Previously, Gough et al. (2004), showed that 50% of human osteoblasts cultured in neat extracts of porous bioactive glass scaffolds (60mol% SiO_2, 36mol% CaO, 4mol% P_2O_5) underwent apoptosis after 24 h of culture, possible due to excessive release of calcium and silica ions. Thus, it is possible that increase in surface area of porous MS due to introduction of porosity (see Section 3.3) may have significantly enhanced the ionic calcium release from P40 PGMS AW. This may have enhanced extracellular and intracellular calcium concentration beyond the tolerance limit of cells (Eklou-Kalonji et al. 1997; Maeno et al. 2005; Kim et al. 2015), which ultimately interfered with mitochondrial metabolism (Gibson 1998; Szabadkai & Duchen 2008) and induced apoptosis (Juin et al. 1998; Gough et al. 2004; Szabadkai & Duchen 2008).

(2) Increase in surface area also increased the release rate of glass particulates/fragments, which were internalised by hMSCs in excessive amounts. Intracellularly, these particulates may have caused structural damage to various organelles and released excessive amount of calcium ions in the cytosol via degradation (Labbaf et al. 2011), leading to cell death. This postulate is again supported by cytotoxicity experiments (TOX01, TOX02 and TOX05), where removal of glass fragments >0.4 μm in size, significantly enhanced cell viability, metabolic activity or proliferation.

(3) At molecular level, Rho/ROCK-stimulated myosin II contractility controls cell-scale branching orientation by recognizing and minimizing local cell-surface curvature. This is brought about by myosin II mini-filaments that form stiff 300 nm rods, with bouquets of heads that extend an additional 40-50 nm on either side of each rod. These rods orient themselves along the axis of least curvature for full heads engagement with underlying surface, which translates into cell attachment (Even-Ram et al. 2007; Elliott et al. 2015). In case of high curvature regions such as concave surfaces of pores

and sharp edges provided by pore edges, the engagement of rod-heads with the underlying surface may be limited and this may have resulted in reduced hMSC attachment and survival on earlier time points (Binamé et al. 2010).

(4) A study reported that hMSCs actively "escaped" from concave surfaces (200-300 μm wide and 50-150 μm deep) made from poly(dimethylsiloxane) over 3 day culture period (Park et al. 2009). Reduced cell proliferation on microporous HA MS (212-300 μm diameter) was also seen on day 4 and 7 of culture as compared to non-porous MS (Fischer et al. 2003). Furthermore, reduced fibroblast migration on 2D pitted areas (35, 75, and 120 nm wide pits with pitch of 100, 200, and 300 nm, respectively) relative to 2D planar surface and reduced osteoprogenitor adhesion and spread on pitted 2D surfaces (120 nm in diameter and 100 nm deep pits) relative to planar 2D controls, have also been reported (Curtis et al. 2004; Dalby 2007; Biggs et al. 2007; Dalby et al. 2008). These studies strongly indicate that 0.39-70 μm wide pore windows on P40 PGMS AW surface may have negatively affected hMSC migration and contributed to reduced cell survival.

The results also showed similar cell metabolic activity in P40 PGMS AW relative to BSG after 1 day of culture at high cell seeding density of 10,000 cells cm^{-2}; and higher DNA content in P40 PGMS AW on day 21 in Experiment-CP09, on day 31 and 42 in Experiment-CP07 and on day 7, 14 and 21 in Experiment-CP08, relative to other bulk MS conditions. In addition to this, the cell viability in P40 PGMS AW was improved after day 21 of culture. Similar results have also been reported for microporous HA MS that showed similar cell number on day 12 and 21 of culture as compared to non-porous MS (Fischer et al. 2003). These results indicate that despite sharp convexities of pore edges and release of cytotoxic degradation products offered by porous MS, the cells were able to survive on these particles.

This may be explained as a consequence of increased cell-cell interaction at higher cells seeding densitites. The mechanical tension

generated by curvatures on single cells may easily induce cell death. However, when cells are present in larger numbers, mechanical equilibrium may be achieved via cell-cell adhesion and communication that spreads the tension across layers of cells, thereby reducing the tension per cell, ultimately enabling them to survive and differentiate (Nelson et al. 2005; Kollmannsberger et al. 2011; Bidan et al. 2013; Bidan et al. 2016). This mechanism is also discussed in Chapter 4, Section 4.4.3.

5.16.8 Differentiation on porous microspheres

Experiments-CD05, CD06, CD07 and CD08 consistently showed higher ALP activity of hMSCs in P40 PGMS AW relative to other MS conditions at all time points. Similarly, higher ALP activity was reported for hydroxyapatite porous MS (607±30 μm diameter, <5 μm pores) compared to smooth plastic MS (205±120 μm diameter) in osteogenic medium on day 4, 7, 14 and 21 (Barrias et al. 2005).

A previous study and the results in Chapter 4, Section 4.4.4 suggested that convex surfaces may induce higher ALP activity possibly via the RhoA-ROCKII-Runx2-ALP pathway (Graziano et al. 2007; Hansen et al. 2007; Seo et al. 2011; Ozdemir et al. 2013). Hence, it is possible that the sharp pore edges offered by PGMS (more convex than BGMS surfaces) led to enhanced ALP expression in hMSCs.

A number of *in vivo* studies have suggested that bone formation occurs preferentially in concavities of 3D scaffolds. For example, Ripamonti and co-workers showed extensive bone formation in concavities of highly crystalline porous hydroxyapatite implanted in adult baboon muscles for 1, 3, 6 and 9 months period (Ripamonti 1996; Calori et al. 2011; Ripamonti 2009). Coathup and co-workers investigated the effect of SiCaP particles with varying strut porosity, silica substitution and granular size on bone formation and also showed preferential bone formation in the concavities (macropores >100 μm wide) after 8, 12 and 24 weeks of implantation in ovine

muscles (Chan et al. 2012; Coathup et al. 2011; Coathup et al. 2012; Coathup et al. 2013). More recently, Gao et al. (2016) reported preferential bone formation in porous regions of β-tricalcium phosphate granules scaffolds after 4, 8 and 12 weeks of implantation in rabbit femurs.

Similar observations have also been reported *in vitro*. For example, micro-pits of 20, 30 or 40 μm diameter on 2D surfaces led to significantly more nodule formation relative to 2D planar surfaces after 21 days of culture without osteogenic factors (Wilkinson et al. 2011). Random nano-pit (120 nm diameter) arrangement also led to osteogenic fate (increased BMP2, BMPR1a, RUNX2, OSX, ALP, osteocalcin, osteopontin, nodule formation relative to flat 2D surfaces) over 8 weeks of culture without osteogenic factors (McMurray et al. 2011; Tsimbouri et al. 2013; Wang et al. 2014; Yang et al. 2014). More recently, collagen deposition was shown to occur preferentially in the tissue-pore interface of the concavities after sufficient cell growth and sequential expression of actin and fibronectin towards tissue-medium interface (Bidan et al. 2016).

These studies strongly indicate that the growth on the porous regions of PGMS may have induced osteogenic differentiation of hMSC and this explains presence of ECM, collagen, OCN and Ca and P deposition by cells in P40 PGMS AW by day 21 of culture, despite their possible cytotoxic effects.

5.16.9 Limited penetration of hMSCs in PGMS

The results in Section 5.8.1 showed that despite more than 10-fold higher in surface area of P40 PGMS AW relative to bulk MS after introduction of porosity, there was only 1.6 times more DNA content in P40 PGMS AW relative to P40 BGMS. This may be because although PGMS had internal pores up to 30 μm wide, majority of these pores may have been inaccessible to cells due to extremely small pore windows, <5 μm wide, present on the outer surface of these MS, even after the acid wash.

This argument is supported by the SEM images showing hMSCs growing over the pores, around the pores and not entering the pores, which had pore windows <25 μm wide, irrespective of the PGMS size or batch used. Similar observations were also reported by Berry et al. (2004) who grew that fibroblasts on 2D pitted surfaces and found that cells migrated in pits with 25 μm diameters but not in with 7 or 15 μm diameters. In case of the smallest sized pits, cells grew completely over the pits, without penetrating them, similar to present scenario.

Other studies have shown that the interconnections less than 10 μm diameter obstruct the ingrowth of soft tissue including blood vessels and prevent bone formation (Kokubun et al. 1994). In the present study, Cryo-FIB/SEM examination showed that interconnectivity tunnels in PGMS were <10 μm wide. Therefore, poor pore interconnectivity of PGMS may also have contributed to limited penetration of hMSCs inside these MS. In support of this postulate, Micro CT analysis clearly demonstrated that a porous MS with closed porosity and smaller pore windows contained significantly less cells compared to a porous MS with more open porosity and wider pore windows.

A review of literature (see Sections 1.8.2 and 1.8.3) also suggests that for *in vivo* bone infiltration, vascularisation and ultimately efficient bone repair requires optimal pore size range and minimum interconnection size of 100-750 μm and 50 μm, respectively (Bobyn et al. 1980; Lu et al. 1999; Hing et al. 1999; Flautre et al. 2001; Kasten et al. 2008; Wang et al. 2010; Feng et al. 2011; Lew et al. 2012; Zhao et al. 2016). Additionally, pore window measurements in Chapter 3, Section 3.4.2 indicated that if the size of PGMS is increased to >250 μm, some of pore window sizes may be increased to >25 μm.

Altogether, these finding suggest that it may be possible to further enhance the *in vivo* osteoinductive nature of PGMS by increasing their average size from 140 μm to >250 μm, which would not only

enhance hMSC penetration but may also allow some vasculature formation, which may not be feasible with current architecture of porous MS.

5.16.10 Cytotoxicity of porous microspheres

A comparison of Ca and P deposited by hMSCs on P40 BGMS and P40 PGMS AW indicates that porosity did not enhance mineral deposition in ECM. This pattern was repeated in collagen and mineral deposition measurements in conditioning experiments, which strongly suggested a negative effect of degradation products of PGMS on hMSC differentiation.

This finding is also substantiated by the cell viability results in Experiments-TOX06 and TOX07, which clearly showed that the glass particulates/fragments were being released form P40 MS even on day 21 of culture. Moreover, since PGMS had at least 10 times more surface area than BGMS, these fragments/particulates may also have been released significantly more in case of PGMS. Thereby, inducing more cytotoxicity via calcium signalling pathways and/or structural damage.

In support of this postulate, Eklou-Kalonji et al. (1997) reported a dose dependent decrease in DNA content, ALP activity and collagen synthesis for porcine osteoblasts after giving a pulse treatment for 1 or 3 days with medium containing 5, 7 and 10 mM of calcium concentration. The authors also reported that even after replacing the Ca-containing medium with normal medium, the ALP activity was still inhibited. Thus, excess calcium is not only detrimental for cell growth but also for osteogenesis.

Furthermore, increase in calcium containing nanoparticle concentration from 0 to 1 mg/ml can enhance apoptosis rate in melanoma cells up to 12-23% by affecting A375 cell proliferation, disrupting cytoskeleton (Huang et al. 2010). Also, 24 h pulse exposure to bioactive nanoparticles (250±75 nm, 85 mol% SiO_2 and 15 mol% CaO, at concentration of 0-200 µg/ml in culture medium)

can decrease hMSC metabolic activity after 7 days of culture in dose-dependent manner (Labbaf et al. 2011). Therefore, this suggests that even higher doses of PBG nanoparticles may induce cytotoxicity in hMSCs.

5.16.11 Re-precipitation of ions on bulk microspheres

Reichert et al. (2013) incubated NanoBone® (nanocrystalline HA embedded in a silica gel matrix, ArtOss, Rostock, Germany) in culture medium for up to 14 days and observed a sharp drop in calcium concentration in medium from 45.67 mg/l to 8.41 mg/l on day 1 and further to 2.09 mg/l by day 14 of incubation. The authors failed to explain the possible mechanism behind the same.

In a recent study, HA material extracts were prepared by incubating 0.1 g of pure HAp granulates (38 nm as particle size and high surface area of 50 m^2g^{-1}) in 1 ml of medium for 1 day, based on ISO 10993-5 standard. When this extract was fed on human foetal osteoblasts, there was only 52.4% and 70% cell viability (relative to control) after 24 h exposure based on MTT and NRU assays, respectively. The authors pointed out that based on these results, some of the HA matrices can be regarded as cytotoxic and also rejected for further evaluation as a potential biomaterial (Klimek et al. 2016). However, they continue to argue that pure HA should not release any toxic substances due to its high chemical purity and stability (Damien & Parsons 1991; Klimek et al. 2016) and have used for a wide range of HA-based implants in forms of powders, granules and scaffolds, which have not been reported cytotoxic *in vivo* (Gundle et al. 1995; Mankani et al. 2001; Patel et al. 2002; Patel et al. 2002a; Patel et al. 2002b; Fischer et al. 2003; Patel et al. 2005; Hsu et al. 2005; Habibovic et al. 2008; Soriano-Souza et al. 2015).

Klimek et al. (2016) further demonstrated that the concentrations of Ca^{2+}, Mg^{2+} and HPO_4^{2-} ions in HA extract were only 48%, 12.5% and 13.7%, respectively, relative to control and when these ions

were replenished to reach similar level to control, the cell viability was resumed to 76% and 97% based on MTT and NRU assay, respectively. These results confirmed that earlier cytotoxicity assessment based on ISO 10993-5 exhibited false cytotoxicity and this method is not suitable for cytotoxic evaluations for biomaterials with high ion-adsorption potential and bioactivity.

Considering that PBGs are also bioactive (Knowles 2003) and precipitation of ions on PBG fibers has already been reported (Abou Neel et al. 2005), it is possible that when PBG MS are eluted in culture medium in static conditions for 1 or 7 days, some of the vital ions such as Ca^{2+}, Mg^{2+} and HPO_4^{2-}, may precipitate onto MS-surfaces. This would render the extracted medium deficient of nutrients/ions and reduce its osmolality. This may explain significantly reduced hMSC viability, metabolic activity and proliferation and also the presence of circular/swollen cells in case of P45 BGMS and P40 BGMS in Experiment-TOX04. To test this hypothesis, the concentration Ca^{2+}, Mg^{2+} and HPO_4^{2-} ions in eluted medium extracts of same experiment may be measured as described in Klimek et al. (2016).

This hypothesis is also supported by the cytotoxic evaluations for PBGs developed for radiotherapy. Sene et al. (2008) tested medium extracts of PBG bulk monoliths made from P_2O_5-Al_2O_3-SiO_2-MgO glass system and reported <40% viability for CHO cells in undiluted extracts of glasses with faster dissolution, based on IS0 10993-5, 1992. It was suggested that cytotoxicity was induced due to higher silicon and phosphorus concentration in their extracts but no ion release measurements were reported in support of this hypothesis. Thus, it is also possible that the toxic effect of these glasses may also have been due to precipitation of vital ions for cell growth on MS surfaces.

5.17 Conclusions

In the present study biological performance of bulk and porous PBG MS was assessed through both direct-contact and indirect-contact experiments. The results demonstrated that slowly degrading P45 BGMS had poor cytocompatibility for osteogenic differentiation possibly due to their hydrophobic surfaces. On the other hand, faster degrading P40 BGMS were better potential candidates for bone repair application due to presence of ECM matrix enriched with collagen, osteocalcin and possibly mineral, deposited by cells. However, due to peeling effect on these particles, the bone regeneration process *in vivo* may be delayed and therefore, annealing process for these MS may be investigated in future in order to improve their surface integrity while limiting the excessive release of toxic glass fragments form them.

In case of PGMS, again there was indication of enhanced ALP activity and collagen production, possibly due to porosity of the surface that might have a beneficial effect in terms of topography and/or due to internal pore cavities that provided concave surfaces, which induced osteogenesis. However, the calcium and phosphorous released in the ECM was found to be in lower amounts than expected. This was correlated to possible cytotoxic effect of porous MS on hMSCs induced via constant exposure to high calcium ion concentration in culture medium and also glass fragments/particulates interacting both extracellularly and intracellularly. Additionally, based on current porous architecture, although these MS had significantly enhanced surface area (more than 10 times as compared to BGMS), this was not translated in hMSC proliferation and in turn contributed to cytotoxicity. Therefore, based on overall current findings, P40 PGMS AW are less suitable than P40 BGMS for osteoporotic bone repair and reinforcement applications.

Finally, the current results also validate that both cell-material direct interactions via surface chemistry and geometry, and cell-material

indirect interactions via ionic release and glass particles release, together influence the fate hMSCs in a 3D system.

Final Discussion and Other Applications

The overall aim of this work was to evaluate the biological performance of degradable bulk and porous phosphate based glass microspheres, developed at University of Nottingham, UK, for osteoporotic bone repair and reinforcement.

The results showed that both the physicality and chemical nature of particles influenced human mesenchymal stem cell (hMSC) behaviour. When the particle morphology changed from irregular shape to a more regular shape, after flame spheroidisation, the cell spreading and proliferation was enhanced. When the chemical formulation and degradation rate of bulk phosphate based glass microspheres was altered, the cell fate was also affected due to combined effects of cell-material direct and indirect interactions. If phosphate based glass microspheres were slow degrading, they may have provided a hydrophobic glass surface for cell proliferation, which was not ideal for cell survival or differentiation. But if the phosphate based glass microspheres were faster degrading, their glass surface may have been more hydrophilic and their dissolution products may be osteoinductive. However, excessive delamination of glass surface from these microspheres, as a result of their degradation, may have lead to loss of cellular material and extracellular matrix.

Based on a literature review, this is the first study that reports the biological evaluation of porous phosphate based glass microspheres for bone repair applications. These microspheres were found to be cytocompatible for hMSCs but allowed limited penetration of cells into their porous structures due to small pore and interconnection sizes, despite the acid wash. There was also evidence of early and late osteogenesis in the form of alkaline phosphatase activity, collagen deposition, osteocalcin deposition and possibly mineralisation, possibly due to the porous topography offered by

these microspheres. However, there was also evidence of cytotoxicity induced by these microspheres via excessive release of glass particulates and calcium ions, as a result of enhanced surface area.

This study reports a novel method for degradation quantification for glass microspheres via measurement of cracks and peeling off effect on degrading microspheres, which was found to be in line with the previously reported degradation studies using mass loss.

As one of the requirements of commercial success of biomaterial, batch reproducibility in these microspheres was also investigated. It was found that even though there was subtle batch-to-batch variability in size, shape, surface area and physicochemical properties of these microspheres, it did not significant impact hMSC proliferation, suggesting good commercial viability.

The application of phosphate based glass microspheres, both bulk and porous, may not only be limited to bone repair and reinforcement in fractured sites or fracture prone areas such as spine, hip, wrist, etc; but may also be used as bone grafting materials in fusion surgeries of spine. During such surgeries, a section from affected vertebral disc is removed and replaced with a bone autograft/allograft material, which is usually derived through an additional surgery from the iliac crest of patient or donor. This increases the cost of surgery and causes additional discomfort to the patient or donor. However, if the glass microspheres are used as grafting materials instead of autografts/allografts, an additional surgery may be avoided because microspheres can be easily injected *in situ* via minimal invasive procedure. Moreover, they will also provide timely release of bioactive ions into the repair site that may enhance bone regeneration process.

Since porous phosphate based glass microspheres provided a suitable surface topography for cells to undergo osteogenesis, these microspheres may be used in combination with metallic load-bearing

implants such as made from stainless steel or Titanium alloy, to fill the interstitial space between the implant and surrounding tissue. This may enable proper osseointegration (bond formation between surrounding bone and implant surface) and delay or avoid fibrous encapsulation, which often leads to implant failure.

Bulk and porous phosphate based glass microspheres may also be applicable as a standalone material or as composites in dentistry. They may be used as filling material to treat a cavity, to repair a cracked/broken tooth or to repair the tooth worn out from habits such as nail biting or tooth grinding. They may also be used as fillers into fresh extraction socket to avoid tooth shrinkage after tooth extraction.

Since, these microspheres made from degradable material and changing in their chemistry can alter their chemical modification, they may also be used as targeted drug delivery vehicles *in vivo* for controlled and predictable release of therapeutic drugs over a period of time. The microspheres may be loaded with biological agents such as nucleic acids, hormones, growth factors, cytokines, to cure genetic defects, target and kill cancer cells, viral infections, bacterial infections, or to elicit an immune response for rapid *in situ* wound healing. Other than this, these microspheres may be loaded with immunosuppressant drugs and used as adjuvants with transplanted organs or implant devices to avoid immune rejection.

Finally, in another aspect of this study, comparison of 2D and 3D culture system revealed variation in human mesenchymal stem cell responses due to different geometrical cues offered by both systems. The microsphere system provided a range of convexities and concavities, which may have played a dominant role in determining hMSC-fate and this system may better mimic the *in vivo* cell environment. There seemed to be a role of cytoskeletal-tension in the osteogenic differentiation. However, questions of how cell mechanics modulate cell contractility and how this tension transduces into biomechanical signals, are yet to be answered.

Future directions

Based on the results from this thesis and some studies in literature following recommendations are made:

In order to test the hypothesis for higher ionic release in porous phosphate-based glass microspheres and its possible cytotoxic effects on human mesenchymal stem cells (hMSCs), Inductively Coupled Plasma Mass Spectrometry analysis of MS-eluted medium, combined with degradation studies via mass loss (Lakhkar 2014), may be performed.

To study the fate of glass fragments and particulates released by degrading glass microspheres (MS) inside hMSCs and other cells such as in lungs, kidney, heart, etc., transmission electron microscopy studies are highly recommended. Such studies can provide valuable information on mechanism of action of these glass particles at nanoscale. Cytotoxicity studies may be performed to study apoptotic and stress markers such as Caspase 3 and heat shock proteins, etc. Additionally, gene and protein expression techniques such as flow cytometry, Real-time polymerase chain reaction, western blot analysis, microarrays and immunocytochemistry may also be used to perform epigenetic, genomic, proteomic and metabolomics studies in future to better understand hMSC-fate on MS. These studies may not be restricted to hMSCs from bone marrow but may also be investigated for other cell types such as MSCs from dentine (dental pulp stem cells) and adipose tissue or osteoblasts.

Further, cytocompatibility studies may also be performed using osteoclasts (with or without co-culturing with hMSCs or osteoblasts), in order to assess the response of these osteoclasts to these glass MS. Such investigation may also help fully understand the other potential orthopaedic applications of BGMS and PGMS, for example, dentine cavity fillers or fillers after tooth extraction, as adjuvants in

the form of interstitial space fillers between tissue and implant devices for enhanced tissue integration of implants, etc.

It was hypothesized that there may be loss of cellular material and ECM due to delamination of glass surfaces in case of P40 glass MS. One of the ways to test this hypothesis may be to measure the soluble collagen present in spent medium, collected during medium exchanges over 21 days of differentiation. If the results from such experiments show higher collagen levels in spent medium collected from P40 BGMS-cell seeded condition compared to BSG-cell seeded condition, then the hypothesis may stand true and will validate the collagen quantification results in the present study. Annealed P40 glass microspheres may also be tested for their cytocompatibility and osteogenic performance *in vitro*. Annealing may not only reduce delamination of glass surface but may also enhance the mechanical strength of the MS, which is currently unknown.

Since, aggregate formation was observed to be an effect of migration and bridging of cells from one microsphere to another, this aggregation process may be an indicator or migratory ability of hMSCs on different MS-types. On this basis, hMSCs were hypothesised to be most motile on P40 BGMS, followed by P45 BGMS and BSG and least in case of P40 PGMS AW. Therefore, to test this hypothesis, 3D cell motility studies may be performed as part of future investigations.

Finally, *in vivo* performance of the bone implant material is not only affected by hMSC differentiation but is also a function of implant's abilities to generate immune responses and inflammation, and withstand the mechanical stresses and strains in the implanted site. Hence, future *in vitro* investigations must also incorporate immunological testing of PBG MS using macrophage culturing and characterisation studies should also incorporate mechanical testing of these materials, before performing *in vivo* testing on animal models, in order to fully assess the potential of these materials.

References

Abbott, A., 2003. Biology' s new dimension. *Nature*, 424, pp.870–872.

Abou Neel, E.A. et al., 2009. Bioactive functional materials: a perspective on phosphate-based glasses. *Journal of Materials Chemistry*, 19(6), pp.690–701.

Abou Neel, E.A. et al., 2005. Effect of iron on the surface, degradation and ion release properties of phosphate-based glass fibres. *Acta Biomaterialia*, 1(5), pp.553–563.

Ahmadi, R. et al., 2011. Enhanced attachment, growth and migration of smooth muscle cells on microcarriers produced using thermally induced phase separation. *Acta Biomaterialia*, 7(4), pp.1542–1549.

Ahmed, I., Lewis, M., et al., 2004a. Phosphate glasses for tissue engineering: Part 1. Processing and characterisation of a ternary-based P2O5-CaO-Na2O glass system. *Biomaterials*, 25(3), pp.491–499.

Ahmed, I., Lewis, M., et al., 2004b. Phosphate glasses for tissue engineering: Part 2. Processing and characterisation of a ternary-based P2O5-CaO-Na2O glass system. *Biomaterials*, 25(3), pp.491–499.

Ahmed, I., 2016. POROUS AND NON-POROUS BODIES.

Ahmed, I., Collins, C.A., et al., 2004. Processing, characterisation and biocompatibility of iron-phosphate glass fibres for tissue engineering. *Biomaterials*, 25(16), pp.3223–3232.

Ahmed, I. et al., 2009. Retention of mechanical properties and cytocompatibility of a phosphate-based glass fiber/polylactic acid composite. *Journal of Biomedical Materials Research - Part*

B Applied Biomaterials, 89(1), pp.18–27.

Anderson, S.I., 2001. *The Effect of Silicon , Silica and Silicates on the Osteoblast*.

Anselme, K., 2000. Osteoblast adhesion on biomaterials. *Biomaterials*, 21(7), pp.667–681.

Aronson, J., 1997. Current Concepts Review - Limb-Lengthening, Skeletal Reconstruction, and Bone Transport with the Ilizarov Method*. *The Journal of Bone & Joint Surgery*, 79(8), pp.1243–1258.

Asif, I.M. et al., 2014. In vitro bioactivity of titanium-doped bioglass. *Journal of Materials Science: Materials in Medicine*, 25(8), pp.1865–1873.

Attawia, M.A., Devin, J.E. & Laurencin, C.T., 1995. Immunofluorescence and Confocal Laser-Scanning Microscopy Studies of Osteoblast Growth and Phenotypic-Expression in 3-Dimensional Degradable Synthetic Matrices. *Journal of Biomedical Materials Research*, 29(7), pp.843–848.

Ayers, R.A. et al., 1999. Effect of nitinol implant porosity on cranial bone ingrowth and apposition after 6 weeks. *Journal of Biomedical Materials Research*, 45(1), pp.42–47.

Baker, B.M. & Chen, C.S., 2012. Deconstructing the third dimension - how 3D culture microenvironments alter cellular cues. *Journal of Cell Science*, 125(13), pp.3015–3024.

Ball, M. et al., 2008. The effect of different surface morphology and roughness on osteoblast-like cells. *Journal of biomedical materials research. Part A*, 86(3), pp.637–647.

Banerjee, A. et al., 2009. Hypothesis testing, type I and type II errors. *Industrial Psychiatry Journal*, 18(2), pp.127–131.

Bari, C. De & Dell'Accio, F., 2007. Mesenchymal stem cells in

rheumatology: a regenerative approach to joint repair. *Clinical Science*, 113(8), pp.339–348.

Barrias, C.C. et al., 2005. Proliferation, activity, and osteogenic differentiation of bone marrow stromal cells cultured on calcium titanium phosphate microspheres. *Journal of Biomedical Materials Research - Part A*, 72(1), pp.57–66.

Barrias, C.C., Ribeiro, C.C. & Barbosa, M. a., 2004. Adhesion and Proliferation of Human Osteoblastic Cells Seeded on Injectable Hydroxyapatite Microspheres. *Key Engineering Materials*, 254–256, pp.877–880.

Bauer, T.W. & Muschler, G.F., 2000. Bone graft materials. An overview of the basic science. *Clinical orthopaedics and related research*, 371(1), pp.10–27.

Baxter, M.A. et al., 2004. Study of telomere length reveals rapid aging of human marrow stromal cells following in vitro expansion. *Stem cells*, 22(5), pp.675–682.

Beattie, J.H. & Avenell, a, 1992. Trace element nutrition and bone metabolism. *Nutrition research reviews*, 5(1), pp.167–188.

Bellantuono, I., Aldahmash, A. & Kassem, M., 2009. Aging of marrow stromal (skeletal) stem cells and their contribution to age-related bone loss. *Biochimica et Biophysica Acta - Molecular Basis of Disease*, 1792(4), pp.364–370.

Berrier, A.L. & Yamada, K.M., 2007. Cell–Matrix Adhesion. *Journal of cellular physiology*, 213(1), pp.565–573.

Berry, C.C. et al., 2004. The influence of microscale topography on fibroblast attachment and motility. *Biomaterials*, 25(26), pp.5781–5788.

Bidan, C.M. et al., 2013. Geometry as a Factor for Tissue Growth: Towards Shape Optimization of Tissue Engineering Scaffolds.

Advanced Healthcare Materials, 2(1), pp.186–194.

Bidan, C.M. et al., 2016. Gradual conversion of cellular stress patterns into prestressed matrix architecture during in-vitro tissue growth. *Journal of royal society interface*, 13, p.20160136.

Bidan, C.M., Wang, F.M. & Dunlop, J.W.C., 2013. A three-dimensional model for tissue deposition on complex surfaces. *Computer Methods in Biomechanics and Biomedical Engineering*, 16(10), pp.1056–1070.

Biggs, M.J.P. et al., 2006. Regulation of Implant Surface Cell Adhesion: Characterization and Quantification of S-phase Primary Osteoblast Adhesions on Biomimetic Nanoscale Substrates. *Anticancer Research*, 11(4), pp.1609–1612.

Biggs, M.J.P. et al., 2007. The effects of nanoscale pits on primary human osteoblast adhesion formation and cellular spreading. *Journal of Materials Science: Materials in Medicine*, 18(2), pp.399–404.

Binamé, F. et al., 2010. What makes cells move: requirements and obstacles for spontaneous cell motility. *Molecular bioSystems*, 6(4), pp.648–661.

Bissett, H. et al., 2015. Titanium and zirconium metal powder spheroidization by thermal plasma processes. *Journal of the Southern African Institute of Mining and Metallurgy*, 115(10), pp.937–942.

Le Blanc, K. & Pittenger, M., 2005. Mesenchymal stem cells: progress toward promise. *Cytotherapy*, 7(1), pp.36–45.

Bobis, S., Jarocha, D. & Majka, M., 2006. Mesenchymal stem cells: characteristics and clinical applications. *Folia histochemica et cytobiologica / Polish Academy of Sciences, Polish Histochemical and Cytochemical Society*, 44(4), pp.215–230.

Bobyn, J.D. et al., 1980. The Optimum Pore Size for the Fixation of Porous-Surfaced Metal Implants by the Ingrowth of Bone. *Clin Orthop Relat Res*, 150, pp.263–270.

Bock, N. et al., 2011. Electrospraying, a reproducible method for production of polymeric microspheres for biomedical applications. *Polymers*, 3(1), pp.131–149.

Borden, M. et al., 2003. Structural and human cellular assessment of a novel microsphere-based tissue engineered scaffold for bone repair. *Biomaterials*, 24(4), pp.597–609.

Bortot, M.B., Prastalo, S. & Prado, M., 2012. Production and Characterization of Glass Microspheres for Hepatic Cancer Treatment. *Procedia Materials Science*, 1, pp.351–358.

Boukhechba, F. et al., 2009. Human primary osteocyte differentiation in a 3D culture system. *Journal of Bone and Mineral Research*, 24(11), pp.1927–1935.

Boyle, W.J., Simonet, W.S. & Lacey, D.L., 2003. Osteoclast differentiation and activation. , 423(May), pp.337–342.

Brink, M., 1997. The influence of alkali and alkaline earths on the working range for bioactive glasses. *Journal of Biomedical Materials Research*, 36(1), pp.109–117.

Bruder, S.P. et al., 1998. Bone regeneration by implantation of purified, culture-expanded human mesenchymal stem cells. *Journal of Orthopaedic Research*, 16(2), pp.155–162.

Bruder, S.P. et al., 1998. Mesenchymal stem cells in osteobiology and applied bone regeneration. *Clinical orthopaedics and related research*, (355S), pp.S247–S256.

Bruder, S.P., Fink, D.J. & Caplan, A.I., 1994. Mesenchymal stem cells in bone development, bone repair, and skeletal regeneration therapy. *Journal of Cellular Biochemistry*, 56(3),

pp.283–294.

Brüggemann, D., Frohnmayer, J.P. & Spatz, J.P., 2014. Model systems for studying cell adhesion and biomimetic actin networks. *Beilstein journal of nanotechnology*, 5(1), pp.1193–1202.

Burchardt, H., 1983. The Biology of Bone-Graft Repair. *Clinical Orthopaedics and Related Research*, (174), pp.28–42.

Buzea, C., Pacheco, I.I. & Robbie, K., 2007. Nanomaterials and nanoparticles: sources and toxicity. *Biointerphases*, 2(4), p.MR17-R71.

Calori, G.M. et al., 2011. The use of bone-graft substitutes in large bone defects: Any specific needs? *Injury*, 42(SUPPL. 2), pp.S56–S63.

Cao, W. & Hench, L.L., 1996. Bioactive materials. *Ceramics International*, 22(6), pp.493–507.

Caplan, A.I., 1987. Bone development and repair. *BioEssays : news and reviews in molecular, cellular and developmental biology*, 6(4), pp.171–175.

Caplan, A.I., 1991. Mesenchymal stem cells. *Journal of orthopaedic research : official publication of the Orthopaedic Research Society*, 9(5), pp.641–50.

Caplan, A.I., 2009. Why are MSCs therapeutic? New data: new insight. *The Journal of pathology*, 217, pp.318–324.

Chakrabarti, A.C. et al., 1992. Generation and characterization of iron- and barium-loaded liposomes. *Biochimica et Biophysica Acta*, 1108, pp.233–239.

Chan, B.P. et al., 2010. Mesenchymal stem cell-encapsulated collagen microspheres for bone tissue engineering. *Tissue engineering. Part C, Methods*, 16(2), pp.225–235.

Chan, O. et al., 2012. The effects of microporosity on osteoinduction of calcium phosphate bone graft substitute biomaterials. *Acta Biomaterialia*, 8(7), pp.2788–2784.

Chang, B.S. et al., 2000. Osteoconduction at porous hydroxyapatite with various pore configurations. *Biomaterials*, 21(12), pp.1291–1298.

Chang, Y.S. et al., 1998. Influence of various structure treatments on histological fixation of titanium implants. *Journal of Arthroplasty*, 13(7), pp.816–825.

Choueka, J. et al., 1995. Effect of annealing temperature on the degradation of reinforcing fibers for absorbable implants. *Journal of Biomedical Materials Research*, 29(11), pp.1309–1315.

Clupper, D.C. et al., 2004. Bioactive evaluation of 45S5 bioactive glass fibres and preliminary study of human osteoblast attachement. *Journal of Materials Science: Materials in Medicine*, 15, pp.803–808.

Clupper, D.C., Hench, L.L. & Mecholsky, J.J., 2004. Strength and toughness of tape cast bioactive glass 45S5 following heat treatment. *Journal of the European Ceramic Society*, 24(10–11), pp.2929–2934.

Coathup, M.J. et al., 2012. Effect of increased strut porosity of calcium phosphate bone graft substitute biomaterials on osteoinduction. *Journal of Biomedical Materials Research - Part A*, 100 A(6), pp.1550–1555.

Coathup, M.J. et al., 2013. The effect of particle size on the osteointegration of injectable silicate-substituted calcium phosphate bone substitute materials. *Journal of Biomedical Materials Research - Part B Applied Biomaterials*, 101 B(6), pp.902–910.

Coathup, M.J. et al., 2011. The osteoinductivity of silicate-substituted calcium phosphate. *The Journal of bone and joint surgery. American volume*, 93(23), pp.2219–26.

Conzone, S.D. et al., 2002. In vitro and in vivo dissolution behavior of a dysprosium lithium borate glass designed for the radiation synovectomy treatment of rheumatoid arthritis. *Journal of Biomedical Materials Research*, 60(2), pp.260–268.

Conzone, S.D. & Day, D.E., 2008. Preparation and properties of porous microspheres made from borate glass. *Journal of Biomedical Materials Research - Part A*, 88(2), pp.531–542.

Cormack, A.N. & Tilocca, A., 2012. Structure and Biological Activity of Glasses and Ceramics. *Philosophical Transactions Series A Mathematical, Physical, and Engineering Sciences*, 370(1963), pp.1271–1280.

Cowan, C.M. et al., 2004. Adipose-derived adult stromal cells heal critical-size mouse calvarial defects. *Nature biotechnology*, 22(5), pp.560–567.

Crockett, J.C. et al., 2011. Bone remodelling at a glance. *Journal of cell science*, 124, pp.991–998.

Currey, J.D., Brear, K. & Zioupos, P., 1996. The effects of ageing and changes in mineral content in degrading the toughness of human femora. *Journal of Biomechanics*, 29(2), pp.257–260.

Curtis, A.S.G. et al., 2004. Cells React to Nanoscale Order and Symmetry in Their Surroundings. *IEEE Transactions on Nanobioscience*, 3(1), pp.61–65.

Dalby, M.J., 2007. Cellular response to low adhesion nanotopographies. *International Journal of Nanomedicine*, 2(3), pp.373–381.

Dalby, M.J. et al., 2004. Investigating filopodia sensing using arrays

of defined nano-pits down to 35 nm diameter in size. *International Journal of Biochemistry and Cell Biology*, 36(10), pp.2015–2025.

Dalby, M.J., McCloy, D., Robertson, M., Wilkinson, C.D.W., et al., 2006. Osteoprogenitor response to defined topographies with nanoscale depths. *Biomaterials*, 27(8), pp.1306–1315.

Dalby, M.J., McCloy, D., Robertson, M., Agheli, H., et al., 2006. Osteoprogenitor response to semi-ordered and random nanotopographies. *Biomaterials*, 27(15), pp.2980–2987.

Dalby, M.J. et al., 2007. The control of human mesenchymal cell differentiation using nanoscale symmetry and disorder. *Nat Mater*, 6(12), pp.997–1003.

Dalby, M.J. et al., 2005. The control of human mesenchymal cell differentiation using nanoscale symmetry and disorder. *Journal of Dental Research*, 84(5), pp.407–413.

Dalby, M.J., Gadegaard, N. & Wilkinson, C.D.W., 2008. The response of fibroblasts to hexagonal nanotopography fabricated by electron beam lithography. *Journal of Biomedical Materials Research - Part A*, 84(4), pp.973–979.

Damien, C.J. & Parsons, J.R., 1991. Bone graft and bone graft substitutes: A review of current technology and applications. *Journal of Applied Biomaterials*, 2(3), pp.187–208.

Damien, E. et al., 2003. A preliminary study on the enhancement of the osteointegration of a novel synthetic hydroxyapatite scaffold in vivo. *Journal of biomedical materials research. Part A*, 66(2), pp.241–246.

Dempster, D.W. et al., 1986. A simple method for correlative light and scanning electron microscopy of human iliac crest bone biopsies: qualitative observations in normal and osteoporotic subjects. *Journal of bone and mineral research : the official*

journal of the American Society for Bone and Mineral Research, 1(1), pp.15–21.

Devin, J.E., Attawia, M. a & Laurencin, C.T., 1996. Three-dimensional degradable porous polymer-ceramic matrices for use in bone repair. *Journal of biomaterials science. Polymer edition*, 7(8), pp.661–9.

Diamond, T. et al., 1991. Does iron affect osteoblast function? Studies in vitro and in patients with chronic liver disease. *Calcified tissue international*, 48(6), pp.373–9.

Dimitriou, R. et al., 2011. Bone regeneration: current concepts and future directions. *BMC medicine*, 9(16), pp.1–10.

Dimitriou, R., Tsiridis, E. & Giannoudis, P. V., 2005. Current concepts of molecular aspects of bone healing. *Injury*, 36(12), pp.1392–1404.

Dodd, C. a et al., 1988. Allograft versus autograft bone in scoliosis surgery. *The Journal of bone and joint surgery. British volume*, 70(3), pp.431–434.

von Doernberg, M.-C. et al., 2006. In vivo behavior of calcium phosphate scaffolds with four different pore sizes. *Biomaterials*, 27(30), pp.5186–5198.

Dong, J. et al., 2001. In vivo evaluation of a novel porous hydroxyapatite to sustain osteogenesis of transplanted bone marrow-derived osteoblastic cells. *Journal of biomedical materials research*, 57(2), pp.208–216.

Doube, M. et al., 2010. BoneJ: Free and extensible bone image analysis in ImageJ. *Bone*, 47(6), pp.1076–1079.

Ducy, P. et al., 1996. Increased bone formation in osteocalcin-deficient mice. *Nature*, 382(6590), pp.448–452.

Eklou-Kalonji, E., Denis, I. & Pointillart, A., 1997. Influence of high

concentrations of extracellular calcium on the proliferation and differentiation of porcine osteoblasts in culture . *Reprod. Nutr. Dev.*, 37(3), pp.375–376.

Elliott, H. et al., 2015. Myosin II controls cellular branching morphogenesis and migration in three dimensions by minimizing cell-surface curvature. *Nature cell biology*, 17(2), pp.137–47.

Evans, E.A. & Calderwood, D.A., 2007. Forces and Bond Dynamics in Cell Adhesion. *Science*, 316, pp.1148–1153.

Even-Ram, S. et al., 2007. Myosin IIA regulates cell motility and actomyosin-microtubule crosstalk. *Nature cell biology*, 9(3), pp.299–309.

Feng, B. et al., 2011. The effect of pore size on tissue ingrowth and neovascularization in porous bioceramics of controlled architecture in vivo. *Biomedical Materials*, 6(1), p.15007.

Fischer, E.M. et al., 2003. Bone formation by mesenchymal progenitor cells cultured on dense and microporous hydroxyapatite particles. *Tissue engineering*, 9(6), pp.1179–88.

Flautre, B. et al., 2001. Porous HA ceramic for bone replacement: Role of the pores and interconnections - Experimental study in the rabbit. *Journal of Materials Science: Materials in Medicine*, 12(8), pp.679–682.

Florencio-Silva, R. et al., 2015. Biology of Bone Tissue: Structure, Function, and Factors That Influence Bone Cells. *BioMed Research International*, 2015(Article ID 421746), p.17 pages.

Follet, H. et al., 2004. The degree of mineralization is a determinant of bone strength: A study on human calcanei. *Bone*, 34(5), pp.783–789.

France, L.A. et al., 2012. Transient serum exposure regimes to

support dual differentiation of human mesenchymal stem cells. *Journal of Tissue Engineering and Regenerative Medicine*, 8(8), pp.652–663.

Franks, K. et al., 2002. The effect of MgO on the solubility behavior and cell proliferation in a quaternary soluble phosphate based glass system. *Journal of Materials Science: Materials in Medicine*, 13(6), pp.549–556.

Franks, K., Abrahams, I. & Knowles, J.C., 2000. Development of soluble glasses for biomedical use part I: In vitro solubility measurement. *Journal of Materials Science: Materials in Medicine*, 11(10), pp.609–614.

Friedenstein, A.J. et al., 1974. Precursors for fibroblasts in different populations of hematopoietic cells as detected by the in vitro colony assay method. *Experimental hematology*, 2(2), pp.83–92.

Friedenstein, A.J., Piatetzky-Shapiro, I.I. & Petrakova, K. V, 1966. Osteogenesis in transplants of bone marrow cells. *Journal of embryology and experimental morphology*, 16(3), pp.381–390.

Fu, H. et al., 2013. Evaluation of bone regeneration in implants composed of hollow HA microspheres loaded with transforming growth factor??1 in a rat calvarial defect model. *Acta Biomaterialia*, 9(3), pp.5718–5727.

Fu, H. et al., 2012. Long-term conversion of 45S5 bioactive glass-ceramic microspheres in aqueous phosphate solution. *Journal of Materials Science: Materials in Medicine*, 23(5), pp.1181–1191.

Fu, H., Rahaman, M.N. & Day, D.E., 2010. Effect of process variables on the microstructure of hollow hydroxyapatite microspheres prepared by a glass conversion method. *Journal of the American Ceramic Society*, 93(10), pp.3116–3123.

Fu, Q. et al., 2010. In vivo evaluation of 13-93 bioactive glass

scaffolds with trabecular and oriented microstructures in a subcutaneous rat implantation model. *Journal of Biomedical Materials Research - Part A*, 95(1), pp.235–244.

Fujibayashi, S. et al., 2003. A comparative study between in vivo bone ingrowth and in vitro apatite formation on Na2O-CaO-SiO2 glasses. *Biomaterials*, 24(8), pp.1349–1356.

Fujibayashi, S. et al., 2004. Osteoinduction of porous bioactive titanium metal. *Biomaterials*, 25(3), pp.443–450.

Galois, L. & Mainard, D., 2004. Bone ingrowth into two porous ceramics with different pore sizes: An experimental study. *Acta Orthopaedica Belgica*, 70(6), pp.598–603.

Gálvez, P. et al., 2014. Enhancing Effect of Glucose Microspheres in the Viability of Human Mesenchymal Stem Cell Suspensions for Clinical Administration. *Pharmaceutical Research*, 31(12), pp.3515–28.

Gao, P. et al., 2016. Beta-tricalcium phosphate granules improve osteogenesis in vitro and establish innovative osteo-regenerators for bone tissue engineering in vivo. *Scientific Reports*, 6, p.23367.

Gauthier, O. et al., 1998. Macroporous biphasic calcium phosphate ceramics: Influence of macropore diameter and macroporosity percentage on bone ingrowth. *Biomaterials*, 19(1–3), pp.133–139.

Geiser, M. et al., 2005. Ultrafine particles cross cellular membranes by nonphagocytic mechanisms in lungs and in cultured cells. *Environmental Health Perspectives*, 113(11), pp.1555–1560.

Gerhardt, L.-C. & Boccaccini, A.R., 2010. Bioactive Glass and Glass-Ceramic Scaffolds for Bone Tissue Engineering. *Materials*, 3(7), pp.3867–3910.

Giannoudis, P. V & Einhorn, T. a, 2009. Bone morphogenetic proteins in musculoskeletal medicine. *Injury*, 40 Suppl 3, pp.S1-3.

Giard, D.J. et al., 1977. Virus production with a newly developed microcarrier system. *Applied and Environmental Microbiology*, 34(6), pp.668–672.

Gibson, G., 1998. Active role of chondrocyte apoptosis in endochondral ossification. *Microscopy Research and Technique*, 43(2), pp.191–204.

Giuliani, N. et al., 2013. New Insights into Osteogenic and Chondrogenic Differentiation of Human Bone Marrow Mesenchymal Stem Cells and Their Potential Clinical Applications for Bone Regeneration in Pediatric Orthopaedics. *Stem Cells International*, 2013.

Goh, T.K.-P. et al., 2013. Microcarrier culture for efficient expansion and osteogenic differentiation of human fetal mesenchymal stem cells. *BioResearch open access*, 2(2), pp.84–97.

Gough, J.E. et al., 2002. Synthesis, degradation, and in vitro cell responses of sodium phosphate glasses for craniofacial bone repair. *Journal of Biomedical Materials Research*, 59(3), pp.481–489.

Gough, J.E., Jones, J.R. & Hench, L.L., 2004. Nodule formation and mineralisation of human primary osteoblasts cultured on a porous bioactive glass scaffold. *Biomaterials*, 25(11), pp.2039–2046.

Graham, T.R. & Kozlov, M.M., 2010. Interplay of proteins and lipids in generating membrane curvature. *Current Opinion in Cell Biology*, 22(4), pp.430–436.

Granero-moltó, F. et al., 2012. Regenerative Effects of Transplanted Mesenchymal Stem Cells in Fracture Healing. *Stem Cells*, 27(8),

pp.1887–1898.

Granja, P.L. et al., 2004. Preparation and Characterization of Injectable Chitosan-Hydroxyapatite Microspheres. *Key Engineering Materials*, 254–256, pp.573–576.

Graziano, A. et al., 2007. Concave Pit-Containing Scaffold Surfaces Improve Stem Cell-Derived Osteoblast Performance and Lead to Significant Bone Tissue Formation. *PLoS ONE*, 2(6), p.e496.

Graziano, A. et al., 2008. Scaffold's Surface Geometry Significantly Affects Human Stem Cell Bone Tissue Engineering. *Journal of cellular physiology*, 214(1), pp.166–172.

Green, S.A. et al., 1992. Management of segmental defects by the Ilizarov intercalary bone transport method. *Clinical orthopaedics and related research*, (280), pp.136–142.

Guedes, J.C. et al., 2012. TiO(2)-doped phosphate glass microcarriers: a stable bioactive substrate for expansion of adherent mammalian cells. *Journal of Biomaterials Applications*, 28(1), pp.3–11.

Gundle, R., Joyner, C.J. & Triffitt, J.T., 1995. Human bone tissue formation in diffusion chamber culture in vivo by bone-derived cells and marrow stromal fibroblastic cells. *Bone*, 16(6), pp.597–601.

Habibovic, P. et al., 2008. Comparative in vivo study of six hydroxyapatite-based bone graft substitutes. *Journal of Orthopaedic Research*, 26(10), pp.1363–1370.

Hadjidakis, D.J. & Androulakis, I.I., 2006. Bone remodeling. *Annals of the New York Academy of Sciences*, 1092, pp.385–396.

Hansen, J.C. et al., 2007. Effect of surface nanoscale topography on elastic modulus of individual osteoblastic cells as determined by atomic force microscopy. *Journal of Biomechanics*, 40(13),

pp.2865–2871.

Haque, P. et al., 2013. Degradation properties and microstructural analysis of 40P2O5–24MgO–16CaO–16Na2O–4Fe2O3 phosphate glass fibres. *Journal of Non-Crystalline Solids*, 375, pp.99–109.

Harada, S. & Rodan, G. a, 2003. Control of osteoblast function and regulation of bone mass. *Nature*, 423(6937), pp.349–355.

Harburger, D.S. & Calderwood, D.A., 2009. Integrin signalling at a glance. *Journal of cell science*, 122(2009), pp.159–163.

Harrison, R. et al., 2016. *Autonomous magnetic labelling of functional mesenchymal stem cells for improved traceability and spatial control in cell therapy applications*,

Hasan, M.S. et al., 2012. Material characterisation and cytocompatibility assessment of quinternary phosphate glasses. *Journal of Materials Science: Materials in Medicine*, 23(10), pp.2531–2541.

Hauschka, P. V et al., 1989. Osteocalcin and matrix Gla protein: vitamin K-dependent proteins in bone. *Physiological reviews*, 69(3), pp.990–1047.

He, W. et al., 2008. Availability and toxicity of Fe(II) and Fe(III) in Caco-2 cells. *Journal of Zhejiang University SCIENCE B*, 9(9), pp.707–712.

He, W. et al., 2014. Proteomic comparison of 3D and 2D glioma models reveals increased HLA-E expression in 3D models is associated with resistance to NK cell-mediated cytotoxicity. *Journal of Proteome Research*, 13(5), pp.2272–2281.

Hench, L.L., 1991. Bioceramics: From Concept to Clinic. *Journal of the American Ceramic Society*, 74(7), pp.1487–1510.

Hench, L.L., 2013. Chronology of Bioactive Glass Development and Clinical Applications. *New Journal of Glass and Ceramics*, 3(2),

pp.67–73.

Hench, L.L., 2009. Genetic design of bioactive glass. *Journal of the European Ceramic Society*, 29(7), pp.1257–1265.

Hench, L.L., 2015. Opening paper 2015- Some comments on Bioglass: Four Eras of Discovery and Development. *Biomedical glasses*, 1(1), pp.1–11.

Hench, L.L., 2006. The story of Bioglass. *Journal of Materials Science: Materials in Medicine*, 17(11), pp.967–978.

Hench, L.L. & Jones, J.R., 2015. Bioactive Glasses: Frontiers and Challenges. *Frontiers in Bioengineering and Biotechnology*, 3(November), pp.1–12.

Hench, L.L. & Paschall, H. a, 1973. Direct chemical bond of bioactive glass-ceramic materials to bone and muscle. *Journal of biomedical materials research*, 7(3), pp.25–42.

Hing, K. a et al., 2002. Mediation of bone ingrowth in porous hydroxyapatite bone graft substitutes. *Journal of biomedical materials research. Part A*, 68, pp.187–200.

Hing, K. a et al., 1999. Quantification of bone ingrowth within bone-derived porous hydroxyapatite implants of varying density. *Journal of materials science. Materials in medicine*, 10(10/11), pp.663–670.

Hong, S.J., Yu, H.S. & Kim, H.W., 2009. Tissue engineering polymeric microcarriers with macroporous morphology and bone-bioactive surface. *Macromolecular Bioscience*, 9(7), pp.639–645.

Hoppe, A., Güldal, N.S. & Boccaccini, A.R., 2011. A review of the biological response to ionic dissolution products from bioactive glasses and glass-ceramics. *Biomaterials*, 32(11), pp.2757–2774.

Hossain, K.M.Z., Patel, U. & Ahmed, I., 2014. Development of microspheres for biomedical applications: a review. *Progress in Biomaterials*, 4(1), pp.1–19.

Hsu, F.Y. et al., 2005. An in vivo study of a bone grafting material consisting of hydroxyapatite and reconstituted collagen. *Journal of Materials Science: Materials in Medicine*, 16(4), pp.341–345.

Huang, X. et al., 2010. The effect of the shape of mesoporous silica nanoparticles on cellular uptake and cell function. *Biomaterials*, 31(3), pp.438–448.

Hulbert, S.F. et al., 1970. Potential of ceramic materials as permanently implantable skeletal prostheses. *Journal of biomedical materials research*, 4, pp.433–456.

Iacono, M. V., 2007. Osteoporosis: A National Public Health Priority. *Journal of Perianesthesia Nursing*, 22(3), pp.175–183.

ISO 10993-12:2009, 2009. *Biological evaluation of medical devices —Part 12: Sample preparation and reference materials*,

ISO 10993-14:2009, 2009. *Biological Evaluation of Medical Devices – Part 14: Identification and quantification of degradation products from ceramics*,

ISO 10993-5:2009, 2009. *Biological Evaluation of Medical Devices – Part5: Tests for in vitro Cytotoxicity.*,

Itälä, A. et al., 2003. Molecular biologic comparison of new bone formation and resorption on microrough and smooth bioactive glass microspheres. *Journal of biomedical materials research. Part B, Applied biomaterials*, 65(1), pp.163–70.

Itälä, A.I. et al., 2001. Pore diameter of more than 100 microm is not requisite for bone ingrowth in rabbits. *Journal of biomedical materials research*, 58(6), pp.679–683.

Jaiswal, N. et al., 1997. Osteogenic differentiation of purified,

culture-expanded human mesenchymal stem cells in vitro. *Journal of Cellular Biochemistry*, 64(2), pp.295–312.

Jaiswal, N. et al., 1997. Osteogenic differentiation of purified, culture-expanded human mesenchymal stem cells in vitro. *Journal of cellular biochemistry*, 64(2), pp.295–312.

Jian, Y.-T. et al., 2015. Effect of Pore Size and Porosity on the Biomechanical Properties and Cytocompatibility of Porous NiTi Alloys. *Plos One*, 10(6), p.e0128138.

Johnstone, B. et al., 1998. In vitro chondrogenesis of bone marrow-derived mesenchymal progenitor cells. *Experimental cell research*, 238(1), pp.265–72.

Johnstone, S.A. et al., 2015. Comparison of human olfactory and skeletal MSCs using osteogenic nanotopography to demonstrate bone-specific bioactivity of the surfaces. *Acta Biomaterialia*, 13, pp.266–276.

Jones, J.R., 2013. Review of bioactive glass: From Hench to hybrids. *Acta Biomaterialia*, 23(S), pp.S53–S82.

Jones, J.R., Ehrenfried, L.M. & Hench, L.L., 2006. Optimising bioactive glass scaffolds for bone tissue engineering. *Biomaterials*, 27(7), pp.964–973.

Juin, P. et al., 1998. Induction of a caspase-3-like activity by calcium in normal cytosolic extracts triggers nuclear apoptosis in a cell-free system. *Journal of Biological Chemistry*, 273(28), pp.17559–17564.

Jung, S. et al., 2012. Large-scale production of human mesenchymal stem cells for clinical applications. *Biotechnology and Applied Biochemistry*, 59(2), pp.106–120.

Kanis, J.A. et al., 2013. European guidance for the diagnosis and management of osteoporosis in postmenopausal women.

Osteoporosis International, 24(1), pp.23–57.

Kanis, J.A. et al., 1994. The diagnosis of osteoporosis. *Journal of bone and mineral research : the official journal of the American Society for Bone and Mineral Research*, 9(8), pp.1137–41.

Kantawong, F. et al., 2009. Whole proteome analysis of osteoprogenitor differentiation induced by disordered nanotopography and mediated by ERK signalling. *Biomaterials*, 30(27), pp.4723–4731.

Karageorgiou, V. & Kaplan, D., 2005. Porosity of 3D biomaterial scaffolds and osteogenesis. *Biomaterials*, 26(27), pp.5474–5491.

Karaoz, E. et al., 2010. Protection of rat pancreatic islet function and viability by coculture with rat bone marrow-derived mesenchymal stem cells. *Cell death & disease*, 1, p.e36.

Karlsson, K.H. & Hupa, L., 2008. Thirty-five years of guided tissue engineering. *Journal of Non-Crystalline Solids*, 354(2–9), pp.717–721.

Kasper, G. et al., 2007. Mesenchymal stem cells regulate angiogenesis according to their mechanical environment. *Stem cells*, 25, pp.903–910.

Kasten, P. et al., 2008. Porosity and pore size of b-tricalcium phosphate scaffold can influence protein production and osteogenic differentiation of human mesenchymal stem cells: An in vitro and in vivo study. *Acta Biomaterialia*, 4(6), pp.1904–1915.

Kaye, B.H. et al., 1997. The effect of shape on intermethod correlation of techniques for characterizing the size distribution of powder .1. Correlating the size distribution measured by sieving, image analysis, and diffractometer methods. *Particle & Particle Systems Characterization*, 14(5), pp.219–224.

Keaveny, T.M. et al., 2001. BIOMECHANICS OF TRABECULAR BONE.

Kelly, R.N. & Kazanjian, J., 2006. Commercial reference shape standards use in the study of particle shape effect on laser diffraction particle size analysis. *AAPS PharmSciTech*, 7(2), p.E49.

Kern, S. et al., 2006. Comparative analysis of mesenchymal stem cells from bone marrow, umbilical cord blood, or adipose tissue. *Stem cells (Dayton, Ohio)*, 24(5), pp.1294–301.

Kilian, K.A. et al., 2010. Geometric cues for directing the differentiation of mesenchymal stem cells. *Proceedings of the National Academy of Sciences of the United States of America*, 107(11), pp.4872–7.

Kim, H.-W., Gu, H.-J. & Lee, H.-H., 2007. Microspheres of collagen-apatite nanocomposites with osteogenic potential for tissue engineering. *Tissue Engineering*, 13(5), pp.965–973.

Kim, H.D. & Valentini, R.F., 2002. Retention and activity of BMP-2 in hyaluronic acid-based scaffolds in vitro. *Journal of Biomedical Materials Research*, 59(3), pp.573–584.

Kim, K.K. & Pack, D.W., 2006. *Microspheres for Drug Delivery*,

Kim, M.-K. et al., 2015. Cytotoxicity, Uptake Behaviors, and Oral Absorption of Food Grade Calcium Carbonate Nanomaterials. *Nanomaterials*, 5(4), pp.1938–1954.

Kim, T.K. et al., 2006. Gas foamed open porous biodegradable polymeric microspheres. *Biomaterials*, 27(2), pp.152–159.

Klawitter, J.J. et al., 1976. An evaluation of bone growth into porous high density polyethylene. *Journal of Biomedical Materials Research*, 10(2), pp.311–323.

Klenke, F.M. et al., 2007. Impact of pore size on the vascularization and osseointegration of ceramic bone substitutes in vivo.

Journal of Biomedical Materials Research - Part A, 85(3), pp.777–786.

Klimek, K. et al., 2016. 'false' cytotoxicity of ions-adsorbing hydroxyapatite - Corrected method of cytotoxicity evaluation for ceramics of high specific surface area. *Materials Science and Engineering C*, 65, pp.70–79.

Kliment, C.R. et al., 2011. A novel method for accurate collagen and biochemical assessment of pulmonary tissue utilizing one animal. *International Journal of Clinical and Experimental Pathology*, 4(4), pp.349–355.

Klingemann, H., Matzilevich, D. & Marchand, J., 2008. Mesenchymal stem cells - Sources and clinical applications. *Transfusion Medicine and Hemotherapy*, 35(4), pp.272–277.

Knowles, J.C., 2003. Phosphate based glasses for biomedical applications. *Journal of Materials Chemistry*, 13(10), p.2395.

Knowles, J.C., Franks, K. & Abrahams, I., 2001. Investigation of the solubility and ion release in the glass system K2O-Na2O-CaO-P2O5. *Glass*, 22, pp.3091–3096.

Knychala, J. et al., 2013. Pore geometry regulates early stage human bone marrow cell tissue formation and organisation. *Annals of Biomedical Engineering*, 41(5), pp.917–930.

Kokubun, S., Kashimoto, O. & Tanak, Y., 1994. Histological Ingrowth Process Verification into Spacer Porous for of Bone Bonding and Hydroxyapatite Cervical Laminoplasty. *Tohoku J. Exp. Med.*, 173, pp.337–344.

Kolk, A. et al., 2012. Current trends and future perspectives of bone substitute materials - From space holders to innovative biomaterials. *Journal of Cranio-Maxillofacial Surgery*, 40(8), pp.706–718.

Kollmannsberger, P. et al., 2011. The physics of tissue patterning and extracellular matrix organisation: how cells join forces. *Soft Matter*, 7(20), pp.9549–9560.

Komlev, V.S. et al., 2003. Porous spherical hydroxyapatite and fluorhydroxyapatite granules: Processing and characterization. *Science and Technology of Advanced Materials*, 4(6), pp.503–508.

Krabbe, C., Zimmer, J. & Meyer, M., 2005. Neural transdifferentiation of mesenchymal stem cells--a critical review. *APMIS : acta pathologica, microbiologica, et immunologica Scandinavica*, 113(11–12), pp.831–44.

Kranz, R.L., 1979. Crack-crack and crack-pore interactions in stressed granite. *International Journal of Rock Mechanics and Mining Sciences and*, 16(1), pp.37–47.

Kuboki, Y. et al., 1998. BMP-induced osteogenesis on the surface of hydroxyapatite with geometrically feasible and nonfeasible structures: topology of osteogenesis. *Journal of biomedical materials research*, 39(2), pp.190–199.

Kühne, J.H. et al., 1994. Bone formation in coralline hydroxyapatite. Effects of pore size studied in rabbits. *Acta orthopaedica Scandinavica*, 65(3), pp.246–252.

Kular, J. et al., 2012. An overview of the regulation of bone remodelling at the cellular level. *Clinical Biochemistry*, 45(12), pp.863–873.

Labbaf, S. et al., 2011. Spherical bioactive glass particles and their interaction with human mesenchymal stem cells in vitro. *Biomaterials*, 32(4), pp.1010–1018.

Lakhkar, N.J., 2014. *Phosphate Glass Microspheres as Cell Microcarrier Substrates for Bone Tissue Engineering Applications*.

Lakhkar, N.J. et al., 2015. Titanium phosphate glass microcarriers induce enhanced osteogenic cell proliferation and human mesenchymal stem cell protein expression. *Journal of Tissue Engineering*, 6, pp.1–14.

Lakhkar, N.J. et al., 2012. Titanium phosphate glass microspheres for bone tissue engineering. *Acta Biomaterialia*, 8(11), pp.4181–4190.

Lam, S., 2008. What You Need To Know About Osteoporosis. *International Osteoporosis Foundation*, 24(10), pp.36–41.

Lancaster, M.A. et al., 2014. Cerebral organoids model human brain development and microcephaly. *Movement Disorders*, 29(2), pp.185–185.

Lareu, R.R. et al., 2010. Essential modification of the Sircol Collagen assay for the accurate quantification of collagen content in complex protein solutions. *Acta Biomaterialia*, 6(8), pp.3146–3151.

Lei, B. et al., 2011. Unique physical–chemical, apatite-forming properties and human marrow mesenchymal stem cells (HMSCs) response of sol–gel bioactive glass microspheres. *Journal of Materials Chemistry*, 21(34), pp.12725–12734.

Leonardi, E. et al., 2010. Response of human bone marrow stromal cells to a resorbable P2O5-SiO2-CaO-MgO-Na2O-K2O phosphate glass ceramic for tissue engineering applications. *Acta Biomaterialia*, 6(2), pp.598–606.

Lerner, U.H., 2006. Bone remodeling in post-menopausal osteoporosis. *Journal of dental research*, 85(7), pp.584–595.

Lew, K.-S. et al., 2012. Macroporous bioceramics: A remarkable material for bone regeneration. *Journal of Biomaterials Applications*, 27(3), pp.345–358.

Lew Androwski, K. et al., 2003. Quantitative Measures of Osteoinductivity of a Porous. *TISSUE ENGINEERING*, 9(1), pp.85–93.

Li, M., Wilkinson, D. & Patchigolla, K., 2005. Comparison of particle size distributions measured using different techniques. *Particulate Science and Technology*, 23(3), pp.265–284.

Li, R., Clark, A.E. & Hench, L.L., 1991. An investigation of bioactive glass powders by sol-gel processing. *Journal of applied biomaterials*, 2(4), pp.231–239.

Liang, C.Z. et al., 2012. Dual delivery for stem cell differentiation using dexamethasone and bFGF in/on polymeric microspheres as a cell carrier for nucleus pulposus regeneration. *Journal of Materials Science: Materials in Medicine*, 23(4), pp.1097–1107.

Liang, W. et al., 2008. Bioactive borate glass scaffold for bone tissue engineering. *Journal of Non-Crystalline Solids*, 354(15–16), pp.1690–1696.

Lieben, L., 2016. Bone: The circadian clock controls bone remodelling. *Nat Rev Rheumatol*, 12(3), pp.132–133.

Liebergall, M. et al., 2013. Stem cell-based therapy for prevention of delayed fracture union: a randomized and prospective preliminary study. *Molecular therapy : the journal of the American Society of Gene Therapy*, 21(8), pp.1631–8.

Lin, S.T. et al., 1994. Development of bioabsorbable glass fibres. *Biomaterials*, 15(13), pp.1057–1061.

Liu, X., Rahaman, M.N. & Fu, Q., 2011. Oriented bioactive glass (13-93) scaffolds with controllable pore size by unidirectional freezing of camphene-based suspensions: Microstructure and mechanical response. *Acta Biomaterialia*, 7(1), pp.406–416.

Liu, Z.-J., Zhuge, Y. & Velazquez, O.C., 2009. Trafficking and

differentiation of mesenchymal stem cells. *Journal of cellular biochemistry*, 106(6), pp.984–991.

Lo, Y.-P. et al., 2016. Three-dimensional spherical spatial boundary conditions differentially regulate osteogenic differentiation of mesenchymal stromal cells. *Scientific reports*, 6(February), p.21253.

Lorch, I.J., 1949. Alkaline phosphatase and the mechanism of ossification. *The Journal of bone and joint surgery. British volume*, 31B(1), pp.94–99.

Lotfi, M., Nejib, M. & Naceur, M., 2013. Cell Adhesion to Biomaterials : Concept of Biocompatibility. *Advances in Biomaterials Science and Biomedical Applications*, pp.207–240.

Lu, J.X. et al., 1999. Role of interconnections in porous bioceramics on bone recolonization in vitro and in vivo. *Journal of Materials Science: Materials in Medicine*, 10(2), pp.111–120.

Luo, Y.-R., 2007. *Comprehensive handbook of chemical bond energies*, CRC press.

Lutolf, M.P., Gilbert, P.M. & Blau, H.M., 2009. Designing materials to direct stem-cell fate. *Nature*, 462(7272), pp.433–41.

MačKović, M. et al., 2012. Bioactive glass (type 45S5) nanoparticles: In vitro reactivity on nanoscale and biocompatibility. *Journal of Nanoparticle Research*, 14(7).

Maeno, S. et al., 2005. The effect of calcium ion concentration on osteoblast viability, proliferation and differentiation in monolayer and 3D culture. *Biomaterials*, 26(23), pp.4847–4855.

Malda, J. & Frondoza, C.G., 2006. Microcarriers in the engineering of cartilage and bone. *Trends in Biotechnology*, 24(7), pp.299–304.

Manikandan, S. et al., 2006. Degradation behaviour of borosilicate glass: some studies. *Anti-Corrosion Methods and Materials*, 53(5), pp.303–309.

Mankani, M.H. et al., 2001. In vivo bone formation by human bone marrow stromal cells: effect of carrier particle size and shape. *Biotechnology and bioengineering*, 72(1), pp.96–107.

Martinelli, J.R. et al., 2010. Synthesis and characterization of glass-ceramic microspheres for thermotherapy. *Journal of Non-Crystalline Solids*, 356(44–49), pp.2683–2688.

Mastrogiacomo, M. et al., 2006. Role of scaffold internal structure on in vivo bone formation in macroporous calcium phosphate bioceramics. *Biomaterials*, 27(17), pp.3230–3237.

Matassi, F. et al., 2011. New biomaterials for bone regeneration. *Clinical Cases in Mineral and Bone Metabolism*, 8(1), pp.21–24.

McBeath, R. et al., 2004. Cell shape, cytoskeletal tension, and RhoA regulate stem cell lineage commitment. *Developmental Cell*, 6(4), pp.483–495.

McClung, M.R., 2015. Bisphosphonate therapy: how long is long enough? *Osteoporosis international : a journal established as result of cooperation between the European Foundation for Osteoporosis and the National Osteoporosis Foundation of the USA*, 26(5), pp.1455–1457.

McMahon, H.T. & Gallop, J.L., 2005. Membrane curvature and mechanisms of dynamic cell membrane remodelling. *Nature*, 438(7068), pp.590–596.

McMurray, R.J. et al., 2011. Nanoscale surfaces for the long-term maintenance of mesenchymal stem cell phenotype and multipotency. *Nat Mater*, 10(8), pp.637–644.

McMurray, R.J., Dalby, M.J. & Tsimbouri, P.M., 2010. Using

biomaterials to study stem cell mechanotransduction, growth and differentiation. *Journal of tissue engineering and regenerative medicine*, 4(7), pp.524–531.

Meinel, L. et al., 2005. Silk implants for the healing of critical size bone defects. *Bone*, 37(5), pp.688–698.

Mendes, S.C. et al., 2002. Bone tissue-engineered implants using human bone marrow. , 8(6), pp.911–920.

Murphy, C.M., Haugh, M.G. & O'Brien, F.J., 2010. The effect of mean pore size on cell attachment, proliferation and migration in collagen-glycosaminoglycan scaffolds for bone tissue engineering. *Biomaterials*, 31(3), pp.461–466.

Nagase, M. et al., 1987. An analytical study of the inflammation induced by a calcium phosphate ceramic. *The KITAKANTO Medical Journal*, 37(1), pp.101–106.

Nagase, M. et al., 1992. Toxicity of silica-containing calcium phosphate glasses demonstrated in mice. *Biomaterials*, 13(3), pp.172–175.

Nagatoya, K. et al., 2014. Effects of raloxifene on bone metabolism in postmenopausal women on chronic hemodialysis. *Clinical and Experimental Nephrology*, 19(5), pp.939–946.

Nakamura, I. et al., 2012. Regulation of osteoclast function. *Modern Rheumatology*, 22(2), pp.167–177.

Nandi, S.K. et al., 2010. Orthopaedic Applications of Bone Graft. *Indian Journal of Medical Research*, 132(July), pp.15–30.

Nelson, C.M. et al., 2005. Emergent patterns of growth controlled by multicellular form and mechanics. *Proceedings of the National Academy of Sciences of the United States of America*, 102(33), pp.11594–11599.

Ng, K.W., Leong, D.T.W. & Hutmacher, D.W., 2005. The challenge

to measure cell proliferation in two and three dimensions. *Tissue Engineering*, 11(1–2), pp.182–191.

Le Nihouannen, D. et al., 2005. Ectopic bone formation by microporous calcium phosphate ceramic particles in sheep muscles. *Bone*, 36(6), pp.1086–1093.

O'Donnell, S. et al., 2006. Strontium ranelate for preventing and treating postmenopausal osteoporosis. *The Cochrane database of systematic reviews*, (4), p.CD005326.

Okamoto, T. et al., 2002. Clonal heterogeneity in differentiation potential of immortalized human mesenchymal stem cells. *Biochemical and Biophysical Research Communications*, 295(2), pp.354–361.

de Oliveira, A.A.R. et al., 2013. Synthesis, characterization and cytocompatibility of spherical bioactive glass nanoparticles for potential hard tissue engineering applications. *Biomedical materials (Bristol, England)*, 8(2), p.25011.

Olszta, M.J. et al., 2007. Bone structure and formation: A new perspective. *Materials Science and Engineering R: Reports*, 58(3–5), pp.77–116.

Oonishi, H. et al., 1999. Comparative bone growth behavior in granules of bioceramic materials of various sizes. *Journal of biomedical materials research*, 44(1), pp.31–43.

Oonishi, H. et al., 1997. Particulate bioglass compared with hydroxyapatite as a bone graft substitute. *Clinical orthopaedics and related research*, (334), pp.316–325.

Oonishi, H. et al., 2000. Quantitative comparison of bone growth behavior in granules of Bioglass®, A-W glass-ceramic, and hydroxyapatite. *Journal of Biomedical Materials Research*, 51(1), pp.37–46.

Orozco, L. et al., 2011. Intervertebral disc repair by autologous mesenchymal bone marrow cells: a pilot study. *Transplantation*, 92(7), pp.822–828.

Orozco, L. et al., 2013. Treatment of knee osteoarthritis with autologous mesenchymal stem cells: a pilot study. *Transplantation*, 95(12), pp.1535–1541.

Owen M, F.A., 1988. Stromal stem cells: marrow- derived osteogenic precursors. *Ciba foundation symposium*, 136(3), pp.42–60.

Ozdemir, T. et al., 2013. Substrate curvature sensing through Myosin IIa upregulates early osteogenesis. *Integrative biology : quantitative biosciences from nano to macro*, 5(11), pp.1407–1416.

Pampaloni, F., Reynaud, E.G. & Stelzer, E.H.K., 2007. The third dimension bridges the gap between cell culture and live tissue. *Nature reviews. Molecular cell biology*, 8(10), pp.839–845.

Panchalingam, K.M. et al., 2015. Bioprocessing strategies for the large-scale production of human mesenchymal stem cells: a review. *Stem Cell Research & Therapy*, 6(1), p.225.

Park, J.-H. et al., 2014. Preparation of in situ hardening composite microcarriers: calcium phosphate cement combined with alginate for bone regeneration. *Journal of biomaterials applications*, 28(7), pp.1079–84.

Park, J.-H.H. et al., 2013. Microcarriers Designed for Cell Culture and Tissue Engineering of Bone. *Tissue Engineering Part B: Reviews*, 19(2), pp.172–90.

Park, J.S. et al., 2010. Osteogenic differentiation of human mesenchymal stem cells using RGD-modified BMP-2 coated microspheres. *Biomaterials*, 31(24), pp.6239–6248.

Park, J.Y. et al., 2009. Study of cellular behaviors on concave and convex microstructures fabricated from elastic PDMS membranes. *Lab on a Chip*, 9, pp.2043–2049.

Parsons, A.J. et al., 2009. Phosphate Glass Fibre Composites for Bone Repair. *Journal of Bionic Engineering*, 6(4), pp.318–323.

Parsons, A.J. et al., 2004. Synthesis and degradation of sodium iron phosphate glasses and their in vitro cell response. *Journal of Biomedical Materials Research - Part A*, 71(2), pp.283–291.

Patel, N. et al., 2002a. A comparative study on the in vivo behavior of hydroxyapatite and silicon substituted hydroxyapatite granules. *Journal of Materials Science: Materials in Medicine*, 13(12), pp.1199–1206.

Patel, N. et al., 2002b. A comparative study on the in vivo behavior of hydroxyapatite and silicon substituted hydroxyapatite granules. *Journal of Materials Science: Materials in Medicine*, 13(12), pp.1199–1206.

Patel, N. et al., 2005. In vivo assessment of hydroxyapatite and silicate-substituted hydroxyapatite granules using an ovine defect model. *Journal of Materials Science: Materials in Medicine*, 16(5), pp.429–440.

Patel, N. et al., 2002. The in vivo response of phase pure hydroxyapatite and carbonate substituted hydroxyapatite granules of varying size ranges. *14th International Symposium on Ceramics in Medicine-Annual Meeting of the International Society for Ceramics in Medicine BIOCERAMICS'01 (ISCM)*, 218–220, pp.383–386.

Patel, Z.S. et al., 2008. Dual delivery of an angiogenic and an osteogenic growth factor for bone regeneration in a critical size defect model. *Bone*, 43(5), pp.931–940.

Peister, a et al., 2004. Stable transfection of MSCs by

electroporation. *Gene therapy*, 11, pp.224–228.

Penttinen, R.P.K., 2011. *Cell interaction with bioactive glasses and ceramics*, Woodhead Publishing Limited.

Perez, R.A. et al., 2011. Porous hydroxyapatite and gelatin/hydroxyapatite microspheres obtained by calcium phosphate cement emulsion. *Journal of Biomedical Materials Research - Part B Applied Biomaterials*, 97 B(1), pp.156–166.

Petrie, R.J. & Yamada, K.M., 2015. Fibroblasts Lead the Way: A Unified View of 3D Cell Motility. *Trends in Cell Biology*, 25(11), pp.666–674.

Pittenger, M.F., 1999. Multilineage Potential of Adult Human Mesenchymal Stem Cells. *Science*, 284(5411), pp.143–147.

Pruksakorn, D. et al., 2010. Metabolic alteration of HepG2 in scaffold-based 3-D culture: Proteomic approach. *Proteomics*, 10(21), pp.3896–3904.

Quent, V.M.C. et al., 2010. Discrepancies between metabolic activity and DNA content as tool to assess cell proliferation in cancer research. *Journal of Cellular and Molecular Medicine*, 14(4), pp.1003–1013.

Rachner, T.D., Khosla, S. & Hofbauer, L.C., 2011. Osteoporosis: Now and the future. *The Lancet*, 377(9773), pp.1276–1287.

R Core Team, 2016. R: A Language and Environment for Statistical Computing.

Rahamana, M.N. et al., 2013. Bioactive glass in tissue engineering. *Journal of Materials Science: Materials in Medicine*, 24(1), pp.669–676.

Rashidi, H. et al., 2012. Differences in the pattern and regulation of mineral deposition in human cell lines of osteogenic and non-osteogenic origin. *Cells Tissues Organs*, 195(6), pp.484–494.

Reichert, C. et al., 2013. Resorption behavior of a nanostructured bone substitute: in vitro investigation and clinical application. *Journal of Orofacial Orthopedics*, 74(2), pp.165–175.

Repetto, G., del Peso, A. & Zurita, J.L., 2008. Neutral red uptake assay for the estimation of cell viability/cytotoxicity. *Nature protocols*, 3(7), pp.1125–31.

Rezwan, K. et al., 2006. Biodegradable and bioactive porous polymer/inorganic composite scaffolds for bone tissue engineering. *Biomaterials*, 27(18), pp.3413–3431.

Ripamonti, U., 2009. Biomimetism, biomimetic matrices and the induction of bone formation. *Journal of Cellular and Molecular Medicine*, 13(9B), pp.2953–2972.

Ripamonti, U., 1996. Osteoinduction in porous hydroxyapatite implanted in heterotopic sites of different animal models. *Biomaterials*, 17(1), pp.31–35.

Ripamonti, U., 2003. Sculpturing the architecture of mineralized tissues: Soluble, insoluble and geometric signals. *European Cells and Materials*, 5(SUPPL. 2), pp.29–30.

Ritchie, R.O., 2011. The conflicts between strength and toughness. *Nature Materials*, 10(11), pp.817–822.

Roberts, T.T. & Rosenbaum, A.J., 2012. Bone grafts, bone substitutes and orthobiologics: the bridge between basic science and clinical advancements in fracture healing. *Organogenesis*, 8(4), pp.114–24.

Romberg, R.W. et al., 1986. Inhibition of hydroxyapatite-crystal growth by bone-specific and other calcium-binding proteins. *Biochemistry*, 25(5), pp.1176–1180.

Roodman, G.D., 1999. Cell biology of the osteoclast. *Experimental Hematology*, 27(8), pp.1229–1241.

Rumpler, M. et al., 2008. The effect of geometry on three-dimensional tissue growth. *Journal of The Royal Society Interface*, 5(27), pp.1173–1180.

Salih, V. et al., 2000. Development of soluble glasses for biomedical use part II: The biological response of human osteoblast cell lines to phosphate-based soluble glasses. *Journal of Materials Science: Materials in Medicine*, 11(10), pp.615–620.

Santini, M.T. et al., 2004. MG-63 human osteosarcoma cells grown in monolayer and as three-dimensional tumor spheroids present a different metabolic profile: A 1H NMR study. *FEBS Letters*, 557(1–3), pp.148–154.

Saralidze, K., Koole, L.H. & Knetsch, M.L.W., 2010. Polymeric microspheres for medical applications. *Materials*, 3(6), pp.3537–3564.

Scarano, A. et al., 2014. Experimental evaluation in rabbits of the effects of thread concavities in bone formation with different titanium implant surfaces. *Clinical Implant Dentistry and Related Research*, 16(4), pp.572–581.

Scheuer, L. & Black, S., 2004. Bone Development. In *The Juvenile Skeleton*. Academic Press, 2004, pp. 23–45.

Schumann, P. et al., 2009. Consequences of seeded cell type on vascularization of tissue engineering constructs in vivo. *Microvascular Research*, 78(2), pp.180–190.

Sene, F.F., Martinelli, J.R. & Okuno, E., 2008. Synthesis and characterization of phosphate glass microspheres for radiotherapy applications. *Journal of Non-Crystalline Solids*, 354(42–44), pp.4887–4893.

Seo, C.H. et al., 2011. The effect of substrate microtopography on focal adhesion maturation and actin organization via the RhoA/ROCK pathway. *Biomaterials*, 32(36), pp.9568–9575.

Sepulveda, P. & Hench, L.L., 2002. Bioactive Hierarchical Structures for Genetic Control of Bone Morphogenesis. *Materials Research*, 5(3), pp.243–246.

Sharmin, N. et al., 2013. Effect of boron addition on the thermal, degradation, and cytocompatibility properties of phosphate-based glasses. *BioMed Research International*, 2013.

Sharmin, N. et al., 2014. Effect of boron oxide addition on fibre drawing, mechanical properties and dissolution behaviour of phosphate-based glass fibres with fixed 40, 45 and 50 mol% P2O5. *Journal of Biomaterials Applications*, 29(5), pp.639–653.

Sheng, Y.W. et al., 2012. Effect of spheroidization of Ti-6Al-4V powder on characteristics and rheological behaviors of gelcasting slurry. *Procedia Engineering*, 36, pp.299–306.

Shi, X. et al., 2011. Hydrolysis and biomineralization of porous PLA microspheres and their influence on cell growth. *Colloids and Surfaces B: Biointerfaces*, 85(1), pp.73–80.

Skelton, K.L. et al., 2007. Effect of ternary phosphate-based glass compositions on osteoblast and osteoblast-like proliferation, differentiation and death in vitro. *Acta Biomaterialia*, 3(4), pp.563–572.

Soriano-Souza, C.A. et al., 2015. Chlorhexidine-loaded hydroxyapatite microspheres as an antimicrobial delivery system and its effect on in vivo osteo-conductive properties. *Journal of Materials Science: Materials in Medicine*, 26(4).

Sottile, V. & Thomson, A., 2003. In Vitro Osteogenic Differentiation of Human ES Cells. *Cloning and Stem Cells*, 5(2), pp.149–155.

Squillaro, T., Peluso, G. & Umberto Galderisi, 2016. Clinical Trials with Mesenchymal Stem Cells : An Update . PubMed Commons. *Cell Transplantation*, 25(5), pp.829–848.

Stenderup, K. et al., 2003. Aging is associated with decreased maximal life span and accelerated senescence of bone marrow stromal cells. *Bone*, 33(6), pp.919–926.

Sul, Y.T. et al., 2002. Qualitative and quantitative observations of bone tissue reactions to anodised implants. *Biomaterials*, 23(8), pp.1809–1817.

Sun, R., Lu, Y. & Chen, K., 2009. Preparation and characterization of hollow hydroxyapatite microspheres by spray drying method. *Materials Science and Engineering C*, 29(4), pp.1088–1092.

Sung, K.E. et al., 2013. Understanding the Impact of 2D and 3D Fibroblast Cultures on In Vitro Breast Cancer Models. *PLoS ONE*, 8(10), p.e76373.

Suzuki, S. et al., 2011. A Study of Fine Particle Spheroidization Process by Elevated-Pressure Pure Oxygen Flame. In *Proceedings of the ASME/JSME 2011 8th Thermal Engineering Joint Conference*. pp. 1–7.

Szabadkai, G. & Duchen, M.R., 2008. Mitochondria: the hub of cellular Ca2+ signaling. *Physiology (Bethesda)*, 23, pp.84–94.

Takemoto, M. et al., 2005. Mechanical properties and osteoconductivity of porous bioactive titanium. *Biomaterials*, 26(30), pp.6014–6023.

Tamai, N. et al., 2002. Novel hydroxyapatite ceramics with an interconnective porous structure exhibit superior osteoconduction in vivo. *Journal of Biomedical Materials Research*, 59(1), pp.110–117.

Taylor, A.F., 2002. Osteoblastic glutamate receptor function regulates bone formation and resorption. *Journal of Musculoskeletal Neuronal Interactions*, 2(3), pp.285–290.

Teitelbaum, S.L., 2000. Bone Resorption by Osteoclasts. *Science*,

289(5484), pp.1504–1508.

Teitelbaum, S.L. & Ross, F.P., 2003. Genetic regulation of osteoclast development and function. *Nature reviews Genetics*, 4(8), pp.638–49.

Teixeira, L.N. et al., 2012. The influence of pore size on osteoblast phenotype expression in cultures grown on porous titanium. *International Journal of Oral and Maxillofacial Surgery*, 41(9), pp.1097–1101.

Tian, X.-F. et al., 2008. Comparison of osteogenesis of human embryonic stem cells within 2D and 3D culture systems. *Scandinavian journal of clinical and laboratory investigation*, 68(1), pp.58–67.

Tollemar, V. et al., 2012. Stem cells, growth factors and scaffolds in craniofacial regenerative medicine. *Cell*, 149(4), pp.727–729.

Torquato, S., Truskett, T.M. & Debenedetti, P.G., 2000. Is Random Close Packing of Spheres Well Defined? *Physical Review Letters*, 84(10), pp.2064–2067.

Tran, G.T. et al., 2009. Growth hormone: does it have a therapeutic role in fracture healing? *Expert opinion on investigational drugs*, 18(7), pp.887–911.

Trounson, A. & McDonald, C., 2015. Stem Cell Therapies in Clinical Trials: Progress and Challenges. *Cell Stem Cell*, 17(1), pp.11–22.

Tsigkou, O. et al., 2014. Monodispersed bioactive glass submicron particles and their effect on bone marrow and adipose tissue-derived stem cells. *Advanced Healthcare Materials*, 3(1), pp.115–125.

Tsimbouri, P.M. et al., 2013. A genomics approach in determining nanotopographical effects on MSC phenotype. *Biomaterials*,

34(9), pp.2177–2184.

Turner, L.-A. & Dalby, M.J., 2014. Nanotopography – potential relevance in the stem cell niche. *The Royal Society of Chemistry*, pp.154–194.

Tzioupis, C.C. & Giannoudis, P. V, 2006. The Safety and Efficacy of Parathyroid Hormone (PTH) as a Biological Response Modifier for the Enhancement of Bone Regeneration. *Current drug safety*, 1(2), pp.189–203.

Väänänen, H.K. et al., 2000. The cell biology of osteoclast function. *Journal of cell science*, 113 (Pt 3, pp.377–381.

Vacanti, J.P. et al., 1988. Selective cell transplantation using bioabsorbable artificial polymers as matrices. *Journal of Pediatric Surgery*, 23(1), pp.3–9.

Valerio, P. et al., 2009. Effects of extracellular calcium concentration on the glutamate release by bioactive glass (BG60S) preincubated osteoblasts. *Biomedical materials*, 4(4), p.45011.

Valério, P. et al., 2007. BG60S dissolution interferes with osteoblast calcium signals. *Journal of Materials Science: Materials in Medicine*, 18(2), pp.265–271.

Varshneya, A.K., 2013. *Fundamentals of inorganic glasses*, Elsevier.

Vogel, V. & Sheetz, M., 2006. Local force and geometry sensing regulate cell functions. *Nature Reviews Molecular Cell Biology*, 7(4), pp.265–275.

Walters, N.J. & Gentleman, E., 2015. Evolving insights in cell-matrix interactions: Elucidating how non-soluble properties of the extracellular niche direct stem cell fate. *Acta Biomaterialia*, 11(1), pp.3–16.

Wang, F. et al., 1998. Reciprocal interactions between beta1-integrin and epidermal growth factor receptor in three-

dimensional basement membrane breast cultures: a different perspective in epithelial biology. *Proceedings of the National Academy of Sciences of the United States of America*, 95(25), pp.14821–14826.

Wang, J.R. et al., 2014. Nanotopology potentiates growth hormone signalling and osteogenesis of mesenchymal stem cells. *Growth Hormone and IGF Research*, 24(6), pp.245–250.

Wang, Q. et al., 2006. Preparation of hollow hydroxyapatite microspheres. *Journal of Materials Science: Materials in Medicine*, 17(7), pp.641–646.

Wang, S. et al., 2013. Nanoporosity significantly enhances the biological performance of engineered glass tissue scaffolds. *Tissue Eng Part A*, 19(13–14), pp.1632–1640.

Wang, W. et al., 2009. 3D spheroid culture system on micropatterned substrates for improved differentiation efficiency of multipotent mesenchymal stem cells. *Biomaterials*, 30(14), pp.2705–2715.

Wang, Z. et al., 2010. Role of the porous structure of the bioceramic scaffolds in bone tissue engineering. In *Nature Proceedings*.

Weaver, V.M. et al., 1997. Reversion of the malignant penotype of human breast cells in three-dimensional cutlure and in vivo by integrin blocking antibodies. *J.Cell Biol.*, 137(1), pp.231–245.

Weinberg, E.D., 2006. Iron loading: A risk factor for osteoporosis. *BioMetals*, 19(6), pp.633–635.

Weiner, S., Traub, W. & Wagner, H.D., 1999. Lamellar bone: structure-function relations. *Journal of structural biology*, 126(3), pp.241–255.

Weitzmann, M.N., 2013. The Role of Inflammatory Cytokines, the RANKL/OPG Axis, and the Immunoskeletal Interface in

Physiological Bone Turnover and Osteoporosis. *Scientifica*, 2013, p.125705.

Werner, M. et al., 2017. Surface Curvature Differentially Regulates Stem Cell Migration and Differentiation via Altered Attachment Morphology and Nuclear Deformation. *Advanced Science*, 4(2), p.1600347.

van Wezel, A.L., 1967. Growth of cell-strains and primary cells on micro-carriers in homogeneous culture. *Nature*, 216(5110), pp.64–65.

Wilkinson, A. et al., 2011. Biomimetic microtopography to enhance osteogenesis in vitro. *Acta Biomaterialia*, 7(7), pp.2919–2925.

Wu, T.J. et al., 2004. Studies on the microspheres comprised of reconstituted collagen and hydroxyapatite. *Biomaterials*, 25(4), pp.651–658.

Xia, T. et al., 2006. Comparison of the abilities of ambient and manufactured nanoparticles to induce cellular toxicity according to an oxidative stress paradigm. *Nano Letters*, 6(8), pp.1794–1807.

Xiong, L. et al., 2015. BMP2-loaded hollow hydroxyapatite microspheres exhibit enhanced osteoinduction and osteogenicity in large bone defects. *International Journal of Nanomedicine*, 10, pp.517–526.

Xynos, I.D. et al., 2000. Bioglass ®45S5 stimulates osteoblast turnover and enhances bone formation in vitro: Implications and applications for bone tissue engineering. *Calcified Tissue International*, 67(4), pp.321–329.

Xynos, I.D. et al., 2001. Gene-expression profiling of human osteoblasts following treatment with the ionic products of Bioglass® 45S5 dissolution. *Journal of Biomedical Materials Research*, 55(2), pp.151–157.

Xynos, I.D. et al., 2000. Ionic products of bioactive glass dissolution increase proliferation of human osteoblasts and induce insulin-like growth factor II mRNA expression and protein synthesis. *Biochemical and biophysical research communications*, 276(2), pp.461–465.

Yamasaki, K. & Hagiwara, H., 2009. Excess iron inhibits osteoblast metabolism. *Toxicology Letters*, 191(2–3), pp.211–215.

Yang, J. et al., 2014. Nanotopographical induction of osteogenesis through adhesion, bone morphogenic protein cosignaling, and regulation of microRNAs. *ACS Nano*, 8(10), pp.9941–9953.

Ylänen, H. et al., 2000. Effect of immersion in SBF on porous bioactive bodies made by sintering bioactive glass microspheres. *Journal of Non-Crystalline Solids*, 275(1), pp.107–115.

Yu, X. et al., 1997. Properties and structure of sodium-iron phosphate glasses. *Journal of Non-Crystalline Solids*, 215(1), pp.21–31.

Yuan, H. et al., 2002. A comparison of the osteoinductive potential of two calcium phosphate ceramics implanted intramuscularly in goats. *Journal of Materials Science: Materials in Medicine*, 13(12), pp.1271–1275.

Yuan, H., De Bruijn, J.D., et al., 2001. Bone induction by porous glass ceramic made from Bioglass® (45S5). *Journal of Biomedical Materials Research*, 58(3), pp.270–276.

Yuan, H., Yang, Z., et al., 2001. Material-dependent bone induction by calcium phosphate ceramics: A 2.5-year study in dog. *Biomaterials*, 22(19), pp.2617–2623.

Yuan, X. et al., 2015. A novel culture system for modulating single cell geometry in 3D. *Acta Biomaterialia*, 24, pp.228–240.

Z. Károly & Szépvölgyi, J., 2005. Plasma spheroidization of ceramic particles. *Chemical Engineering and Processing: Process Intensification*, 44(2), pp.221–224.

Zadpoor, A. a., 2015. Bone tissue regeneration: the role of scaffold geometry. *Biomaterials Science*, 3(2), pp.231–245.

Zaheer, S., LeBoff, M. & Lewiecki, E.M., 2015. Denosumab for the Treatment of Osteoporosis. *Expert Opin Drug Metab Toxicol.*, 11(3), pp.37–54.

Zhang, D. et al., 2009. Predicting physical and chemical properties of bioactive glasses from chemical composition. Part 3: In vitro reactivity. *Glass Technology*, 50(1), pp.1–8.

Zhao, Y. et al., 2016. A combinatorial variation in surface chemistry and pore size of three-dimensional porous poly(ε-caprolactone) scaffolds modulates the behaviors of mesenchymal stem cells. *Materials Science and Engineering C*, 59, pp.193–202.

Zimmermann, G. & Moghaddam, A., 2011. Allograft bone matrix versus synthetic bone graft substitutes. *Injury*, 42(SUPPL. 2), pp.S16–S21.

Zioupos, P. & Currey, J.D., 1998. Changes in the Stiffness, Strength, and Toughness of Human Cortical Bone With Age. *Bone*, 22(1), pp.57–66.

Appendices

Appendix 1

The pH of conditioned medium from different microsphere (MS) conditions and control was measured using Whatman pH meter up to two decimal places, calibrated using standards for pH 7 and pH 10 (Thermo scientific).

The results shown in Figure A-1 showed that throughout the 22 days of conditioning the pH remains between 8 and 9. There was an increase in pH for all conditions from day 13 to 16, which may be due to a measurement error. By the end of 22 days of conditioning, there were no significant differences between any of the conditions.

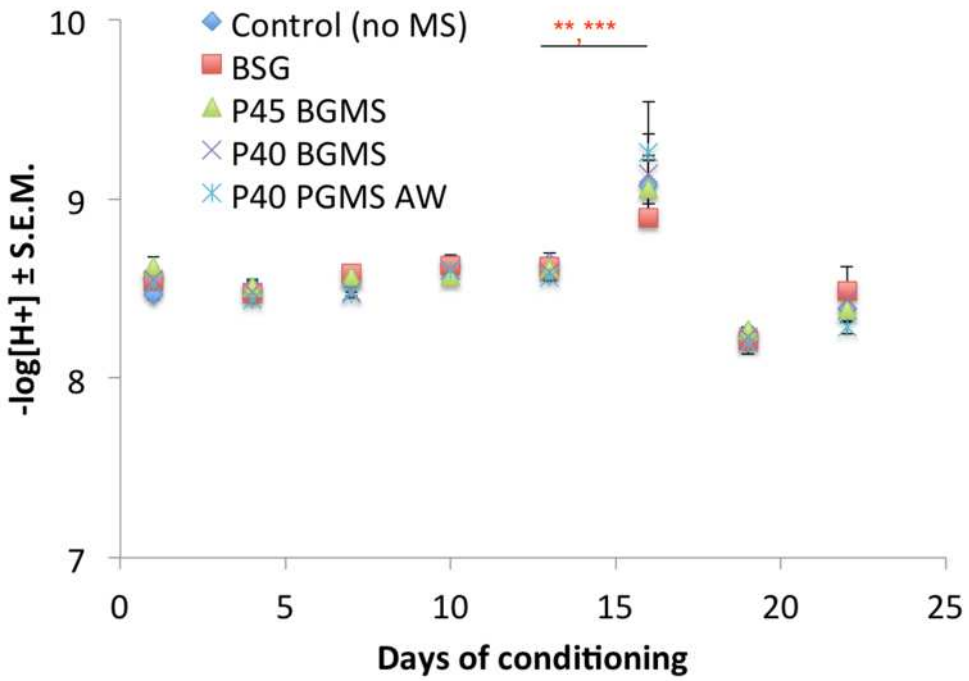

Figure A-1: Measurement of pH of media eluted with different glass MS over 22 days of conditioning.

Appendix 2

Validation study for DNA assay

Human MSCs were different cell seeding rates of 2,000, 5,000, 10,000, 25,000, 60,000 and 100,000 cells well^{-1} on 2D and borosilicate microspheres (BSG,) in 6 replicates for each condition. After 10 h, medium was removed and 500 µl of distilled water was added to each well. The samples were then freeze thawed at -80^{0}C three times and only half (n=3) of these thawed replicates were further sonicated. The DNA quantification was then performed for all samples using Pico Green assay.

The results, see Figure A-2, indicated that for 2D-sonication seemed to be negatively affecting DNA measurements but in case of 2D-no sonication and 3D-sonication conditions there seemed to be a proportional increase in DNA content with increasing cell numbers (with overlapping means in both conditions). In 3D-no sonication condition, differences were not measurable at 10,000, 25,000 and 60,000 cells/well, suggesting that only freeze-thaw was not sufficient to rupture all the cells in 3D sample. Based on these results, on 3D samples, DNA assay was always performed after freeze thawing and sonication and on 2D samples, it was performed after freeze thawing.

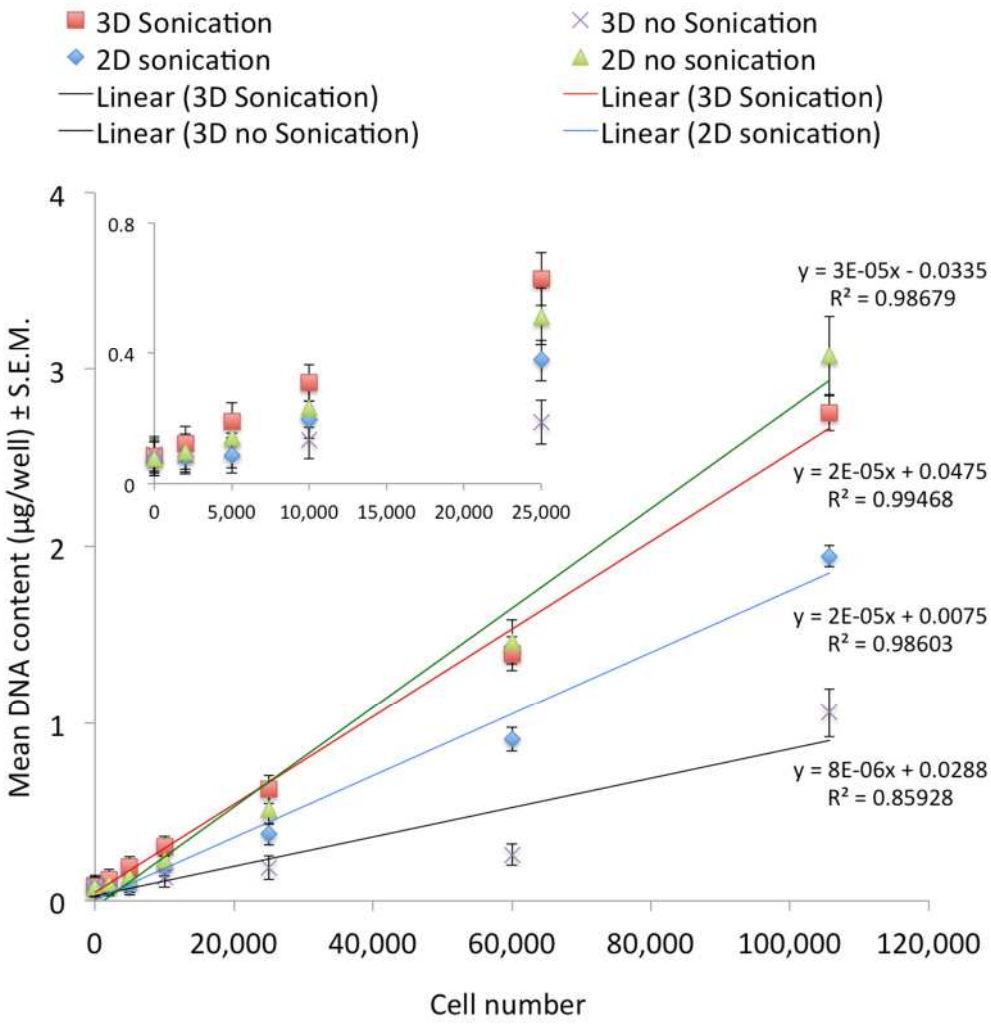

Figure A-2: Validation of DNA quantification on 2D and 3D systems.

Validation study for ALP activity assay

The cell lysates from above samples were also used to assess the effect of sonication on alkaline phosphatase activity measurements for 2D and 3D samples. The results, see Figure A-3, showed that 2D samples with no sonication had more ALP activity than the sonication 2D samples, indicating a possible negative effect of sonication. On the other hand in 3D, there was no negative effect of sonication on ALP activity. Moreover, the non-sonicated samples did not show a linear increase in absorbance with increasing in cell numbers between 5,000 to 25,000 cell seeding. This confirmed that

sonication was essential for complete homogenisation of 3D agglomerate to accurately measure ALP activity of 3D sample.

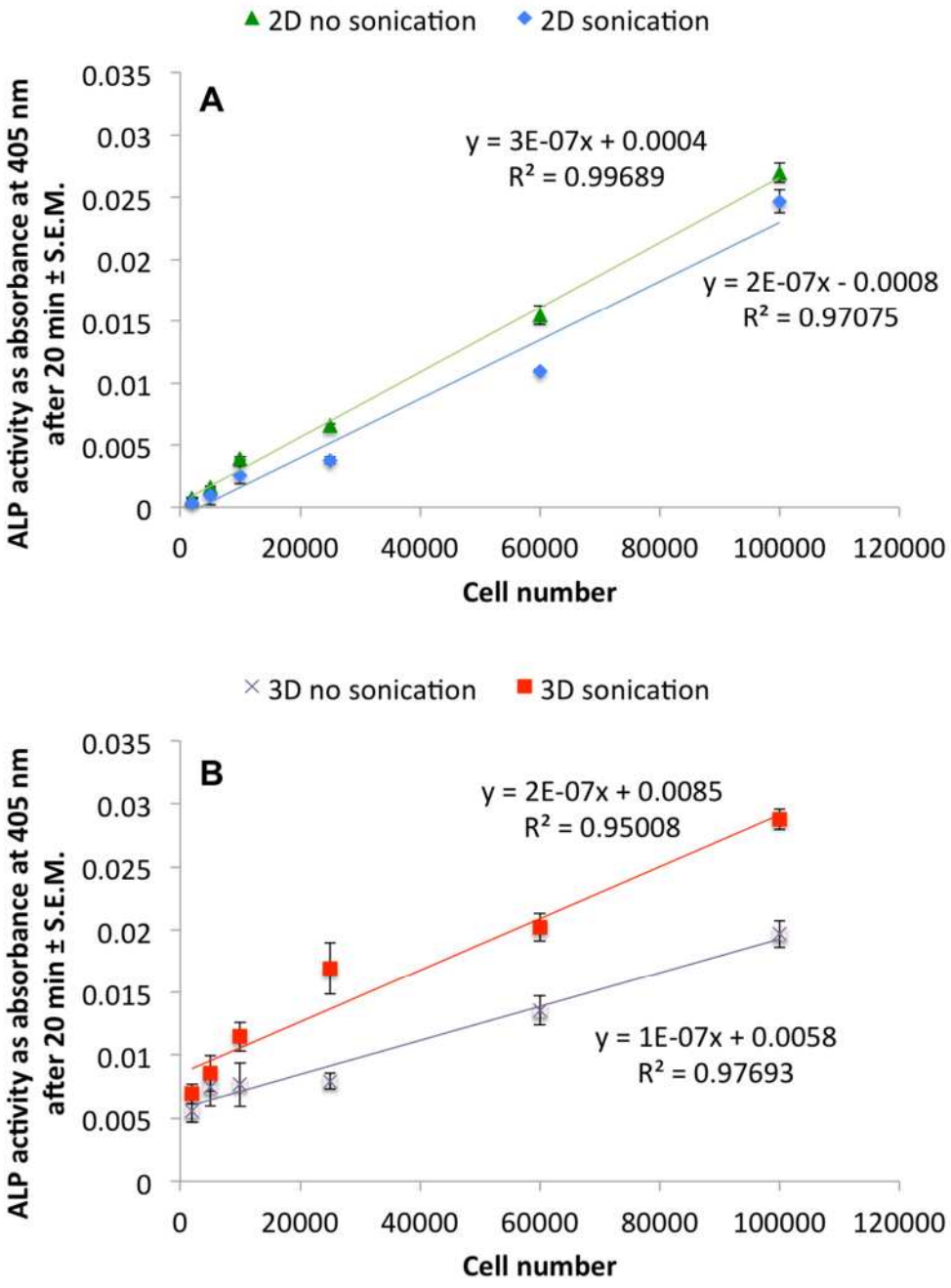

Figure A-3: Validation of ALP activity assessments on (A) 2D and (B) 3D culture systems.

Appendix 3

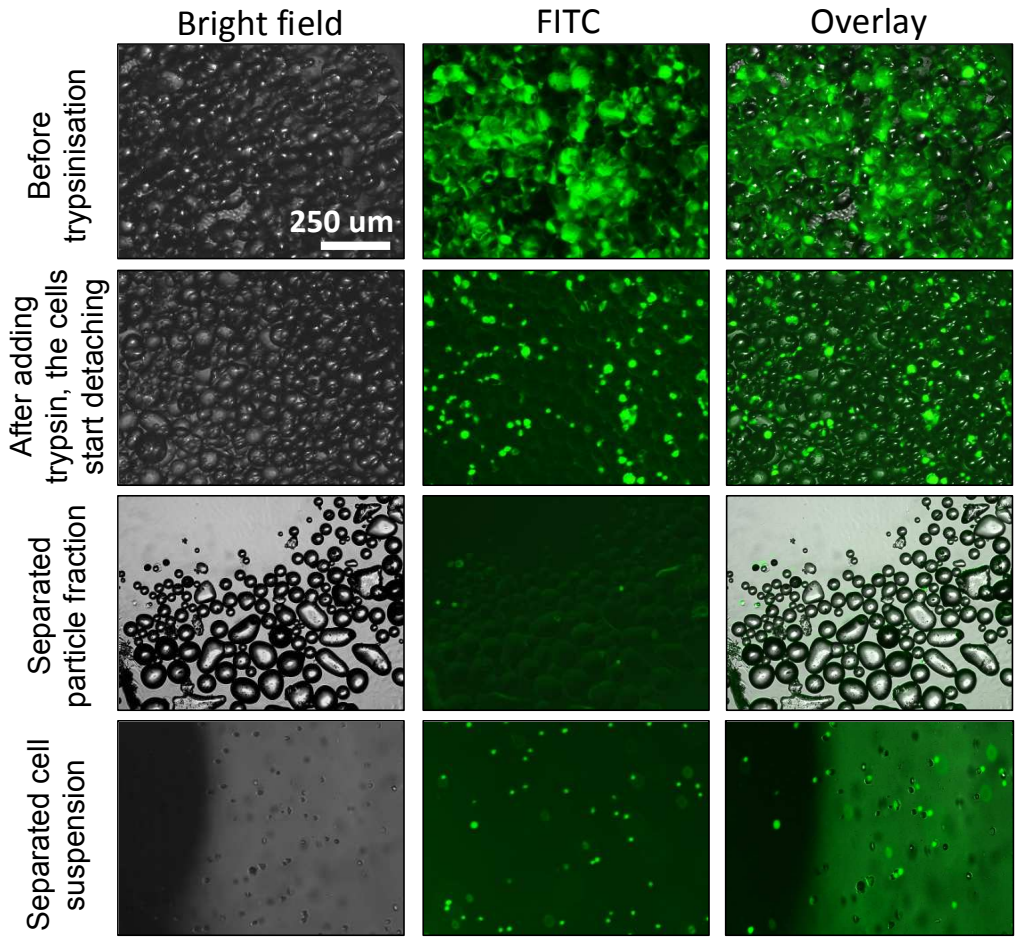

Figure A-4: Trypsinisation of cells on 3D samples. Green signal represents GFP-hMSCs.

Appendix 4

The standard curve made from Rat-tail collagen Type 1 is shown in Figure A-5, A-B.

To confirm that the Sirius Red stain was able to penetrate the 3D agglomerated samples, a 3D sample was stained with Sirius Red, cryo-sectioned and visualised under the light microscope. The image validates that (Figure A-5, C-E) that the dye was able to penetrate inside the 3D agglomerate and the method for collagen quantification of 3D samples was reliable.

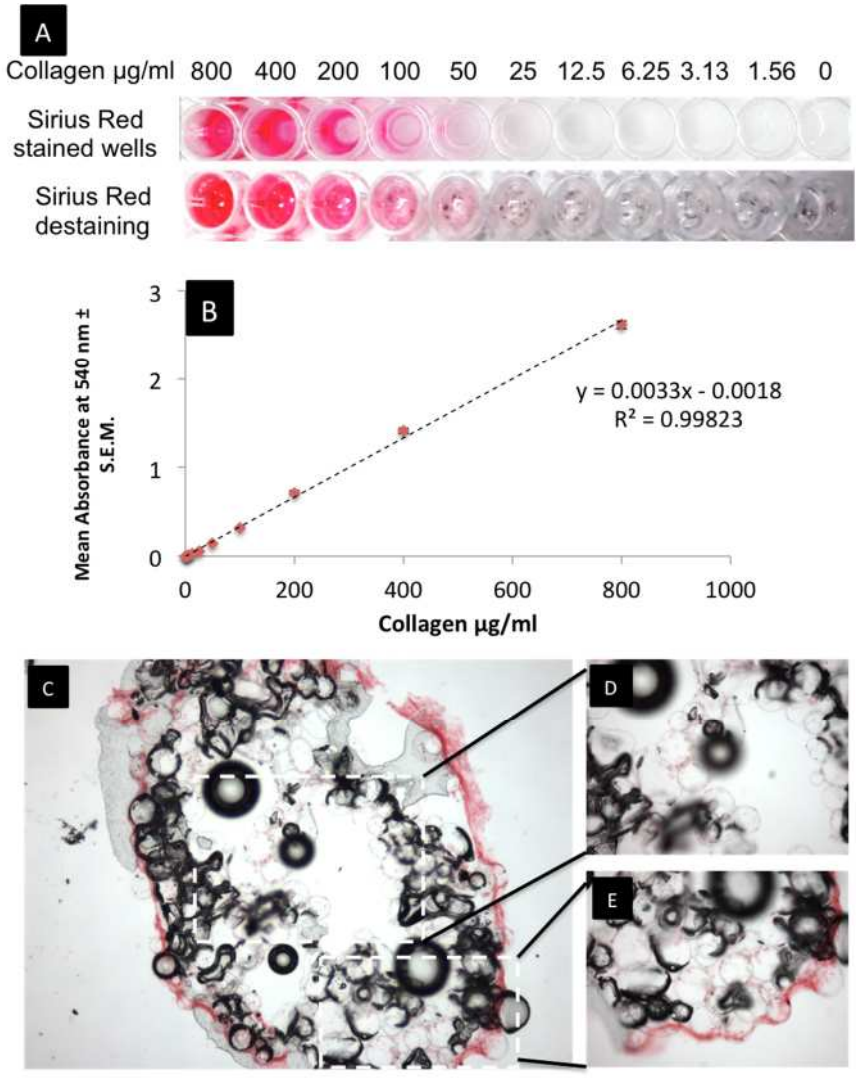

Figure A-5: Collagen standard curve (A-B) and validation of Sirius Red quantification on 3D samples (C-E). BSG loaded with hMSCs and cultured for 7 days in normal growth medium. On day 7, 3D sample was fixed in 4% PFA, stained with 0.1% Sirius Red in distilled water for 30 min and cryo-sectioned before visualising under microscope.

Appendix 5

GFP-hMSCs were seeded at 10,000 cells cm^{-2} in a 96-well plate. On day 4, fresh medium containing barium sulphate (1.5 µl/ml) was added and on day 6 and 7, images were captured using Nikon Eclipse TS100. Since Ba loading was found to be better after 3 days (see Figure A-6), therefore, same protocol was used for Ba loading in cells present on AG6 P40 PGMS AW.



Figure A-6: Barium loading on human MSCs. Scale bar- 62.5 µm.